

Growth of Two Dimensional (2D) Materials and its Applications in Nanoelectronic Devices

by
Mahendra Pawar
10PP17A26044

A thesis submitted to the
Academic of Scientific & Innovative Research
for the award of the degree of
DOCTOR OF PHILOSOPHY
in
SCIENCE

Under the supervision of

Dr. T. G. Ajithkumar
Research Guide

Dr. Dattatray J. Late
Research Co-guide



CSIR-National Chemical Laboratory
Pune



Academy of Scientific and Innovative Research
AcSIR Headquarters, CSIR HRDC campus
Sector 19, Kamla Nehru Nagar,
Ghaziabad, U.P. - 201 002, India

September 2021

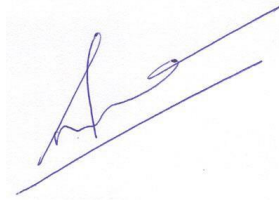
Certificate

This is to certify that the work incorporated in this Ph.D. thesis entitled, “Growth of Two Dimensional (2D) Materials and its Applications in Nanoelectronic Devices”, submitted by Mahendra Pawar to the Academy of Scientific and Innovative Research (AcSIR) in fulfilment of the requirements for the award of the Degree of Doctor of Philosophy in Science, embodies original research work carried-out by the student. We, further certify that this work has not been submitted to any other University or Institution in part or full for the award of any degree or diploma. Research material(s) obtained from other source(s) and used in this research work have been duly acknowledged in the thesis. Image(s), illustration(s), figure(s), table(s) etc., used in the thesis from other source(s), have also been duly cited and acknowledged.



(Mahendra Pawar)

Date: 01/09/2021



(Dr. T. G. Ajithkumar)

Date: 01/09/2021



(Dr. Dattatray J. Late)

Date: 01/09/2021

STATEMENTS OF ACADEMIC INTEGRITY

I, Mahendra S. Pawar, a Ph.D. student of the Academy of Scientific and Innovative Research (AcSIR) with Registration No. 10PP17A26044 hereby undertake that, the thesis entitled “Growth of Two Dimensional (2D) Materials and its Applications in Nanoelectronic Devices” has been prepared by me and that the document reports original work carried out by me and is free of any plagiarism in compliance with the UGC Regulations on “*Promotion of Academic Integrity and Prevention of Plagiarism in Higher Educational Institutions (2018)*” and the CSIR Guidelines for “*Ethics in Research and in Governance (2020)*”.



Signature of the Student

Date: 01/09/2021

Place: Pune

It is hereby certified that the work done by the student, under my supervision, is plagiarism-free in accordance with the UGC Regulations on “*Promotion of Academic Integrity and Prevention of Plagiarism in Higher Educational Institutions (2018)*” and the CSIR Guidelines for “*Ethics in Research and in Governance (2020)*”.



Signature of the Supervisor

Name: Dr. T. G. Ajithkumar

Date: 01/09/2021

Place: Pune



Signature of the Co-supervisor

Name: Dr. Dattatray J. Late

Date: 01/09/2021

Place: Pune

Acknowledgement

This thesis becomes a reality with the kind support and help of many individuals. I would like to express my sincere thanks to all of them.

The foremost and heartfelt gratitude must be prolonged to my supervisor, **Dr. T. G. Ajithkumar and Dr. Dattatray J. Late**, who has the endurance to allow me and my space but the foresight to press me when obligatory. He has cultivated me a lot, not only in the research field but also about living a beautiful life which I never anticipated from a mentor. I could never wish for a better supervisor, nor a truer friend, I'll miss the long and fruitful discussion in group meeting as well as during the group party. And I will persist great fan of his coolness, kind hearted with very supportive nature and excellent communication skills.

I wish to express my sincere thanks to the Doctoral Advisory Committee members, **Dr. Mahesh Dharne, Dr. Jayaraj Nithyanandhan, and Dr. Suresh Gokhale** for their encouragement, timely suggestions during the DAC meetings.

I take this opportunity to thank current and former directors of CSIR-NCL for establishing all the scientific infrastructure and facilities to carry out high quality research work. I would like to acknowledge SAO and AcSIR coordinators from CSIR-NCL for their indispensable support. The requisite support from the current and former Head of the Physical and Materials Chemistry Division is acknowledged. I sincerely thank to CMC division for the characterization facility and their staff especially Dr. Deo, Dr. Gholap, Dr. Vrushali, Harsha, Venkatesh, Sheetal, Tushar and Pankaj for their generous support. I am thankful to Council of Scientific & Industrial Research (CSIR), New Delhi for the financial assistance.

I express my heartiest gratitude towards **Dr. C. S. Gopinath, Dr. Janardan Kundu, Dr. Arup Rath, Dr. C. P. Vinod, Dr. Aparna Deshpande** (IISER Pune), **Dr. Sucharita Sinha** (BARC, Mumbai) **Prof. Mahendra More** (SPPU Pune), **Prof. Sandesh Jadkar** (SPPU Pune), **Prof. Sanjay Dhole** (SPPU Pune), **Prof. Avinash Kumbhar** (SPPU Pune), **Dr. Bharat Kale** (C-MET Pune), **Dr. Pravin Walke** (Mumbai university), **Dr. Anil Singh** (BARC, Mumbai) for their kind help at different parts of my research journey.

I also appreciate the help from my current and former labmates especially Srilatha, Urmila, Disha, Manisha, Dr. Amit, Dr. Prashant, Swapnil, Pooja, Pratik, Onkar, Shraddha, Amol, Prof. Gorax Gote, and Dr. Nitin. Thanks for your support as colleagues and friends.

Beyond the group there are a plethora of people at CSIR-NCL who contribute to an environment which is both scientifically and otherwise beautiful. I am thankful to, Rangarajan, Srikant, Debranjana, Ashish, Prasenjit, Satish, Praveen, Thripuranthanka, Yogita, Sharad, Preeti, Zinoy, Sudhakar, Sharad, Arun, Farsa Ram, Prashant, Prabhakar, Nitin, Himanshu, Siboo, Kranti, Inderjeet, Ravi, and Dr. Naresh for their help in the research work. I am pleased to meet and befriend many other people at CSIR-NCL from various parts of India. I thank to them for the moments spent together at CSIR-NCL during the sports meet and cultural programs. I always cherish the beautiful moments spent with my friends from Department of Physics, SPPU Pune. Many thanks to Prashant, Shabbir, Balu, Krishna, Sameer, Ambadas, Amit, Nilesh Saykar, Dnyaneshwar, Gaurav, Ravindra, Vishal, Nilesh Pawar, Rupali, Shruti, Dhanya, Chaitali, Pallavi for being a part of unforgettable memories at Pune.

I would like to express my deep sense of gratitude towards my family for their endless support, love and care. I want to give special regards to my family for standing by me during difficult times. Thank you for always being there for me and your support gives me the strength I need to keep going. At the end, I dedicate this thesis to my family specially my mother (**Akka**) and I am happy to make them feel proud.

Mahendra Pawar

List of Abbreviations

0D	Zero Dimensional
1D	One Dimensional
2D	Two Dimensional
3D	Three Dimensional
TMDCs	Transition Metal Dichalcogenides
XRD	X-Ray Diffraction
XPS	X-ray Photoelectron Spectroscopy
UV-Vis	Ultra Violet - Visible Spectroscopy
AFM	Atomic Force Microscopy
SEM	Scanning Electron Microscope
FESEM	Field Emission Scanning Electron Microscope
TEM	Transmission Electron Microscope
HR-TEM	High Resolution Transmission Electron Microscope
SAED	Selected Area Electron Diffraction
CVD	Chemical Vapor Deposition
PLD	Pulsed Laser Deposition
RH	Relative Humidity
FET	Field Effect Transistor
FE	Field Emission
ITO	Indium Tin Oxide
vdW	Van der Waals
EQE	External Quantum Efficiency

Chemical Notations

DI	Deionized
V ₂ O ₅	Vanadium Pentoxide

$C_{12}H_{27}N$	Dodecylamine
DMF	Dimethylformamide
NMP	N-Methyl-2-Pyrrolidone
BP	Black Phosphorous
h-BN	Hexagonal Boron nitride
Na_2SO_4	Sodium Sulfate
$NaBH_4$	Sodium borohydride
$SnSe_2$	Tin Diselenide
$PtSe_2$	Platinum Diselenide
H_2PtCl_6	Chloroplatinic acid
$C_6H_{12}N_4$	Hexamethylenetetramine
$(NH_4)_6Mo_7O_{24}$	Ammonium heptamolybdate
$Cd(NO_3)_2$	Cadmium nitrate
CH_4N_2S	Thiourea
CH_3OH	Methanol

List of Symbol

g	Gram
mg	Milligram
h	Hour
ml	Milliliter
min	Minute
s	second
M	Molar
mmol	Mill mole
ms	Millisecond
μs	Microsecond
μA	Microampere

mA	Milliampere
nA	Nano ampere
MΩ	Mega ohm
Å	Angstrom
W	Watt
mW	Milliwatt
nm	Nano meter
ppm	Parts per million
rpm	Revolutions per minute
%	Percentage

Table of Contents

Preface	1-3
Chapter 1	
Introduction to 2D materials	4-34
1.1 Introduction to Nanomaterials	5-7
1.2 Introduction to 2D Materials	7-12
1.2.1 Graphene	8-10
1.2.2 Transition metal dichalcogenides	10-11
1.2.3 Black phosphorus	11-12
1.3 Devices based on 2D materials	12-24
1.3.1 Field effect transistor	12-15
1.3.2 Photodetector	16-18
1.3.3 Humidity and gas sensor	18-21
1.3.4 Energy storage devices	21-24
1.4 Conclusions and Objectives of the Thesis	25-26
1.5 References	27-34
Chapter 2	
Synthesis methods and Device Fabrication	35-62
2.1 Synthesis methods of 2D materials	36-40
2.1.1 Micromechanical exfoliation	36-37
2.1.2 Liquid exfoliation	37-38
2.1.3 Li-ion Intercalation	38-39
2.1.4 Chemical vapor deposition	39-40
2.1.5 Wet chemical synthesis	40
2.2 Device Fabrication	40-52
2.2.1 Field Emission Study	40-42
2.2.2 Field Effect Transistor	42-45
2.2.3 Humidity Sensor	45-48
2.2.4 Photodetector	48-52
2.3 Characterization Techniques	52-59
2.3.1 X-Ray Diffraction	52-53
2.3.2 Raman Spectroscopy	53-55
2.3.3 X-Ray Photoelectron Spectroscopy	55-56
2.3.4 UV-Visible Spectroscopy	56
2.3.5 Atomic Force Microscopy	56-57
2.3.6 Scanning Electron Microscopy	57-58
2.3.7 Transmission Electron Microscopy	58-59
2.4 References	60-62
Chapter 3	
Ultra-thin V₂O₅ Nanosheet based Humidity Sensor, Photodetector and its	
Enhanced Field Emission Properties	63-84
3.1 Introduction	64-65
3.2 Experimental section	65-66

3.3	Result and discussions	66-76
3.3.1	Material characterization	66-68
3.3.2	Humidity sensor	69-71
3.3.3	Photodetector	71-73
3.3.4	Field Emission	73-76
3.4	Conclusions	76
3.5	References	77-84

Chapter 4

Humidity Sensing and Photodetection Behavior of Electrochemically Exfoliated		
Atomically Thin-Layered Black Phosphorus Nanosheets		85-108
4.1	Introduction	86-87
4.2	Experimental section	87-88
4.3	Result and discussions	88-100
4.3.1	Material characterization	88-92
4.3.2	Field effect transistor	92-95
4.3.3	Humidity sensor	95-97
4.3.4	Photodetector	97-100
4.4	Conclusions	100
4.5	References	101-108

Chapter 5

High-Performance Sensing Behavior Using Electronic Ink of 2D SnSe₂ Nanosheets		109-132
5.1	Introduction	110-111
5.2	Experimental section	111-112
5.3	Result and discussions	112-125
5.3.1	Material characterization	112-119
5.3.2	Humidity sensor	119-121
5.3.3	NH ₃ Gas sensor	121-125
5.4	Conclusions	125
5.5	References	126-132

Chapter 6

Temperature dependent Raman Spectroscopy investigations of PtSe₂

Nanosheets synthesized by wet Chemistry and its Sensor application	133-150
6.1 Introduction	134-135
6.2 Experimental section	135-136
6.3 Result and discussions	136-145
6.3.1 Material characterization	136-140
6.3.2 Temperature dependent Raman spectroscopic investigations	140-143
6.3.3 Humidity sensor and Photodetector	143-145
6.4 Conclusions	145
6.5 References	146-150
Chapter 7	
MoS₂ and CdMoS₄ nanostructure based UV light Photodetectors	151-168
7.1 Introduction	152-153
7.2 Experimental section	153-154
7.3 Result and discussions	154-162
7.3.1 Material characterization	154-159
7.3.2 MoS ₂ nanosheets based photodetector	159-160
7.3.3 CdMoS ₄ nanostructures based photodetector	160-162
7.4 Conclusions	162-163
7.5 References	164-168
Chapter 8	
Summary & Future Perspectives	169-173
8.1 Summary	169-172
8.2 Future Perspectives	172-173
Abstract	174
List of Publications	175-177
Erratum	178

Preface

This thesis presents the growth of 2D materials such as V_2O_5 , Black Phosphorus (BP), $SnSe_2$, $PtSe_2$ and MoS_2 using various top down and bottom up approaches. Further, use of these materials for nanoelectronic device applications i.e. Field Effect Transistor, Humidity/gas sensor and Photodetector. The thesis consists of total number of seven chapters in which preparation and fabrication of these 2D materials are reported along with different performance parameters of the devices are also investigated. The third working chapter deals with the synthesis and characterization of V_2O_5 nanosheets and investigation of device performance under light irradiation and/or in the presence of humidities. The fourth chapter is based on the electrochemical exfoliation of BP nanosheets and their utilization in nanoelectronic devices. The fifth chapter, illustrates that thickness dependent study of the liquid exfoliated $SnSe_2$ nanosheets and its impact on the performance parameter of the fabricated device. In the sixth chapter, humidity sensing behaviour of the $PtSe_2$ nanosheets along with photo sensor study are investigated. The seventh and last working chapter is about the synthesis of MoS_2 and $CdMoS_4$ nanostructures, fabrication of photodetector device and study the cyclic photoresponse under the UV light.

Chapter 1: Introduction

This chapter deals with the brief introduction to 2D materials like Graphene and Graphene like other 2D inorganic layered materials. It also discusses their applications in various nanoelectronic, optoelectronic and energy storage devices.

Chapter 2: Synthesis methods and Device Fabrication

In this chapter details about the material synthesis, their characterization using various microscopic and spectroscopic techniques and fabrication of nanoelectronic devices are explained.

Chapter 3: Ultra-thin V_2O_5 Nanosheets based Humidity Sensor, Photodetector and its Enhanced Field Emission Properties

This project deals with the synthesis of V_2O_5 nanosheets by simple hydrothermal method. The structural, morphological and optical investigations of the as synthesized V_2O_5 nanosheets were characterized by using Raman Spectroscopy, Scanning Electron Microscopy, UV-Vis Spectroscopy etc. The humidity sensing behaviours were investigated in the range of 11-97% of relative humidity (RH) at room temperature with maximum sensitivity of $\sim 45.3\%$. We also

demonstrated the V_2O_5 nanosheets based photodetector with sensing response time of ~ 65 sec and recovery time of ~ 75 sec were observed. We also studied field emission (FE) properties for the V_2O_5 nanosheets at a base pressure of $\sim 1 \times 10^{-8}$ mbar. The turn on field required to draw emission current density of $1 \mu A/cm^2$ and $10 \mu A/cm^2$ is found to be ~ 1.15 V/ μm and ~ 1.72 V/ μm respectively. We achieved field emission current density of $1532 \mu A/cm^2$ at an applied field of 3.2 V/ μm also the field enhancement factor calculated from the Fowler – Norheim (F-N) equation is found to be 8530 and 3530 for low field and high field regions respectively. Our results open up several avenues towards utilization of V_2O_5 nanosheets for various nanoelectronic device applications.

Chapter 4: Humidity Sensing and Photodetector Behavior of Atomically Thin-Layered Black Phosphorus Nanosheets Synthesized Using Electrochemical Exfoliation

This project deals with the synthesis of atomically thin Black Phosphorous nanosheets using electrochemical exfoliation. The surface morphology and thickness of the nanosheets were identified using AFM, TEM, and Raman spectroscopy. The black phosphorus nanosheets thick film device was used for the humidity sensing application with exposure to different humidities. The response time of the thick film humidity sensor was found to be ~ 101 sec and the recovery time of ~ 26 sec with sensitivity factor $\sim 521\%$. Further, the black phosphorus nanosheets based FET device was fabricated by using the photolithography tool shows good mobility of ~ 7.3 $cm^2/Vsec$ and on/off ratio of $\sim 10^4$. The UV light irradiation on the black phosphorus nanosheets shows good response time with high sensitivity. To summarize, the results show that the few layer thick film of black phosphorus nanosheets sample exhibits creditable sensitivity and better recovery time to be used in humidity sensor and photodetector applications.

Chapter 5: High-Performance Sensing Behavior Using Electronic Inks of 2D SnSe₂ Nanosheets

Most of the recent research work on layered chalcogenides is understandably focused on single atomic layers. However, it is uncertain if the single layer units are most ideal structures for enhanced gas-solid interactions. To probe this concern, we have synthesized few layer thick SnSe₂ nanosheets ink using liquid exfoliation method. The morphology, thickness/layering and elemental analysis of the sheets were characterized by using SEM, TEM, AFM, Raman spectroscopy and by XPS. The two dimensional (2D) SnSe₂ nanosheets sensor device with different thicknesses was assessed for the humidity and gas sensing performances with exposure to humidity in different conditions. The results show that compared to the bulk /

thicker counterpart, sensor device of few SnSe₂ layers exhibit excellent sensitivity, recovery and ability to be tune the sensing performance with thickness and can be used in lab on chip devices.

Chapter 6: Temperature-dependent Raman spectroscopy and sensor applications of PtSe₂ nanosheets synthesized by wet chemistry

We report on a wet chemistry method used to grow PtSe₂ nanosheets followed by thermal annealing. The SEM and TEM analysis confirms the formation of PtSe₂ nanosheets. Furthermore, XRD, Raman, XPS and SAED patterns were used to analyze the crystal structure and to confirm the formation of the PtSe₂ phase. The temperature-dependent Raman spectroscopy investigations were carried out on PtSe₂ nanosheets deposited on Si substrates in the temperature range 100-506 K. The shifts in Raman active E_g and A_{1g} modes as a function of temperature were monitored. The temperature coefficient for both modes was calculated and was found to match well with the reported 2D transition metal dichalcogenides. A PtSe₂ nanosheets-based sensor device was tested for its applicability as a humidity sensor and photodetector. The humidity sensor based on PtSe₂ nanosheets showed an excellent recovery time of ~5s, indicating the great potential of PtSe₂ for future sensor devices.

Chapter 7: MoS₂ and CdMoS₄ nanostructure based UV light Photodetectors

We have developed MoS₂ nanosheets and CdMoS₄ hierarchical nanostructures based UV light photodetector. The surface morphologies of the prepared samples were investigated using Field Emission Scanning Electron Microscopy (SEM) and Transmission Electron Microscopy (TEM). The performance parameters for the present photodetectors are investigated under the illumination of UV light having wavelength ~385 nm. Upon illumination, the CdMoS₄ based photodetector device showed better response to UV light compared to MoS₂ device in terms of photoresponsivity, response time (~72 sec) and recovery time (~94 sec). Our results reveals that CdMoS₄ hierarchical nanostructures are useful for enhancing the device performance.

Chapter 8: Summary and Future Perspectives

In this concluding chapter, the key observations and results evolved from each working chapter are summarized. It also highlights the point that why achieved outcomes are significant and the scope of these 2D materials in next generation nanoelectronic devices. It also cover short note on future perspectives as well as the opportunity of progress in the field of 2D materials.

Chapter 1: Introduction to 2D Materials

1.1 Introduction to Nanomaterials

The study of materials with at least one dimension in the nanometre scale is known as nanomaterials and it is also considered as key field in the material science.¹ At this scale, there are certain properties such as (physical, chemical and mechanical) changes which are connected to the number of atoms or molecules developing the material. The nature of these materials can be crystalline, polycrystalline, amorphous which can be attributed to metal, semiconductor, ceramics or polymers. In the last two decades, the researchers have prepared hundreds of nanostructured materials with different dimensions so the need to classify them has been increased.

Classification of Materials

In 1995 Gleiter² has given the first idea to classify these nanostructured materials and the same was then explained by Skorokhod in 2000.³ But, the structures like fullerenes, nanotubes and nanoflowers were not explained by them. Then, Skorokhod with his co-worker⁴ developed modified classification scheme to distinguish zero dimensional (0D), one dimensional (1D), two dimensional (2D) and three dimensional (3D) materials.

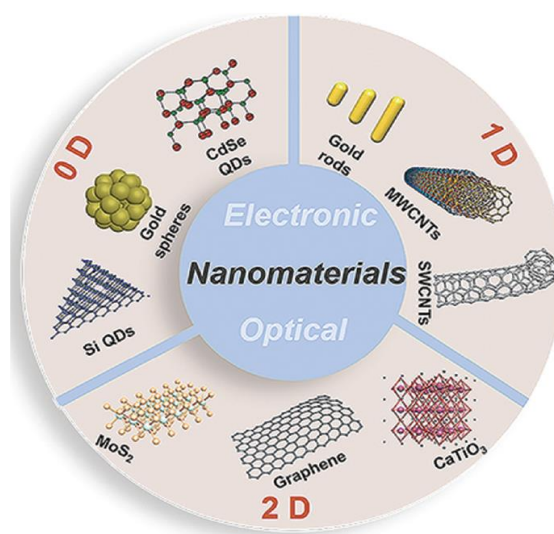


Figure 1.1: Classification of nanomaterials with dimensions: Zero Dimension (0D), One Dimension (1D), Two Dimension (2D).⁵

The classification of these nanostructured materials is based on the number of dimensions of a material, which are outside the nanoscale (<100 nm) range. The Figure 1.1 gives the classification of nanomaterials based on their dimensions.

0D Materials

In 0D materials, all the dimensions are measured within the nanoscale. The common examples of 0D nanomaterials are nanoparticles, quantum dots, core shell quantum dots, hollow sphere and so on. The various research groups have synthesized 0D materials by different physical and chemical methods. The quantum dots has intensively studied in light emitting diodes, solar cells, single electron transistor.⁶⁻⁸

1D Materials

In 1D materials, one dimension is outside the nanoscale and other two dimensions are within the nanoscale. This class of material includes nanotubes, nanorods, and nanowires. The breakthrough work by Iijima in 1D nanotube⁹ it has gathered significant attention in various electronic and optoelectronics device application.

2D Materials

In 2D materials, two dimensions are outside the nanoscale and only one dimension is within the nanoscale. This class of material exhibits nanosheets, nanofilms, nanodiscs and nanocoatings. After the discovery of Graphene from bulk Graphite, 2D materials¹⁰ has become principal area in the field of materials physics and chemistry. The lack of bandgap in Graphene allowed researchers to discover new 2D materials such as TMDCs, Transition metal oxides, layered double hydroxides, h-BN, monoelemental 2D materials i.e. (BP, Silicenes), metal organic frameworks, covalent organic frameworks. These 2D materials possesses sizable bandgap when bulk materials are scaled down to single-layers. This makes them potential

candidate in electronic/optoelectronics, energy storage, catalysis applications. Figure 1.2 shows the schematic illustration of different kinds of 2D materials beyond Graphene.

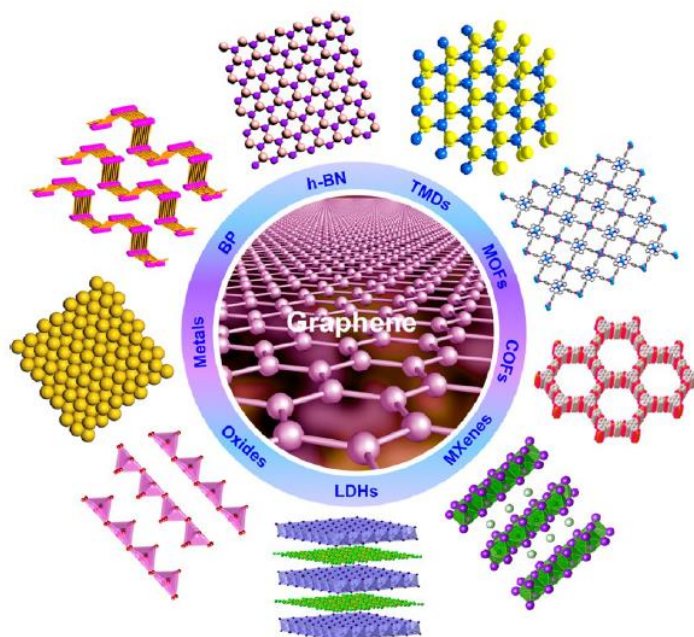


Figure 1.2: Schematic illustration of different kinds of Materials.¹¹

3D Materials

In 3D materials none of the three dimensions are confined to the nanoscale. This class of materials contain bulk powders, bulk crystals, nanoflowers, nanocones and nanopillars. It is well known that, the behaviours of nanostructured materials highly subjected on the sizes, shapes, morphologies and dimensionality of the material, these are the key factors which decides the decisive performance of the device and application. Thus, it is required to synthesize 3D materials with controlled morphology and structure.

1.2 Introduction to 2D materials

In 1966, Frindt et al. successfully showed that these materials could be mechanically or chemically exfoliated into single or few layers.¹² The interesting fact about 2D materials is it expands each year with over 200 2D compounds that can be effortlessly isolated into atomically

monolayers.^{13,14} In case of layered materials, the sheets are attached via weak van der Waals (vdW) interactions which could be easily exfoliated in order to obtain one or few-layer nanosheets using top down approach.^{15,16} These exfoliated 2D nanosheets displays superior electronic and optical properties different from their 3D bulk counterpart due to the presence of well-defined crystal structure with few surface dangling bonds. These 2D materials also possesses tunable band gap i.e. direct bandgap in single layer and indirect bandgap in bulk form. This transition from indirect bandgap to direct band gap happens only when bulk layered crystals are exfoliated down to single-layers. The change of bandgap in these 2D layered crystals is governed by strong photoluminescence, strong exciton binding energies makes these materials suitable aspirant for optoelectronics device applications such as solar cells, photodetector, light emitting diodes.^{17,18} There exists plenty of materials in periodic table having unique electronic and transport properties with the possibility to create one-atom thick or few-atom thick 2D layered materials. The 2D materials mainly deals with Graphene, TMDC's, Black Phosphorous, h-BN, MXenes. Among these, Graphene is the most celebrated and studied material till date.

1.2.1 Graphene

Since the discovery of Graphene from Graphite bulk crystal by K. S. Novoselov, A. K. Geim using the micromechanical exfoliation method, the 2D materials have showed potential in various device applications. Monolayer graphite is a sp^2 bonded one-atom-thick piece of carbon atoms, which exhibits numerous properties, such as ultrahigh charge-carrier mobility ($\sim 10,000 \text{ cm}^2\text{V}^{-1}\text{s}^{-1}$),¹⁰ quantum hall effect,¹⁹ high surface area ($2630 \text{ m}^2\text{g}^{-1}$),²⁰ excellent optical transparency ($\sim 97.7\%$),²¹ excellent thermal conductivity ($4000 \text{ Wm}^{-1} \text{ K}^{-1}$).²² The fascinating thing about Graphene is it's band structure and the linear dispersion at the k point provides us new phenomenon i.e. anomalous room-temperature quantum hall effect which opened up new window known as "Fermi-Dirac" Physics. The high mechanical strength in single layer

graphite is due to the presence of strong C-C bond and chemical inertness is due to the lack of dangling bonds in the basal plane.²³ Because of these extraordinary properties, it has attracted much attention for next generation devices such as field effect transistors,^{24,26} supercapacitors,^{20,27} solar cells^{28,29} and sensors.^{30,31} The semi-metallic nature and lack of bandgap results in small on/off ratio in Graphene FET's that limits its application in optoelectronic devices.³² The defects in Graphene layers greatly impact the transport properties so to overcome this researchers have developed various methods to grow appropriate Graphene layers. The methods consists of liquid exfoliation, micromechanical exfoliation, CVD, and MBE but failed to grow Graphene layers over entire substrate.

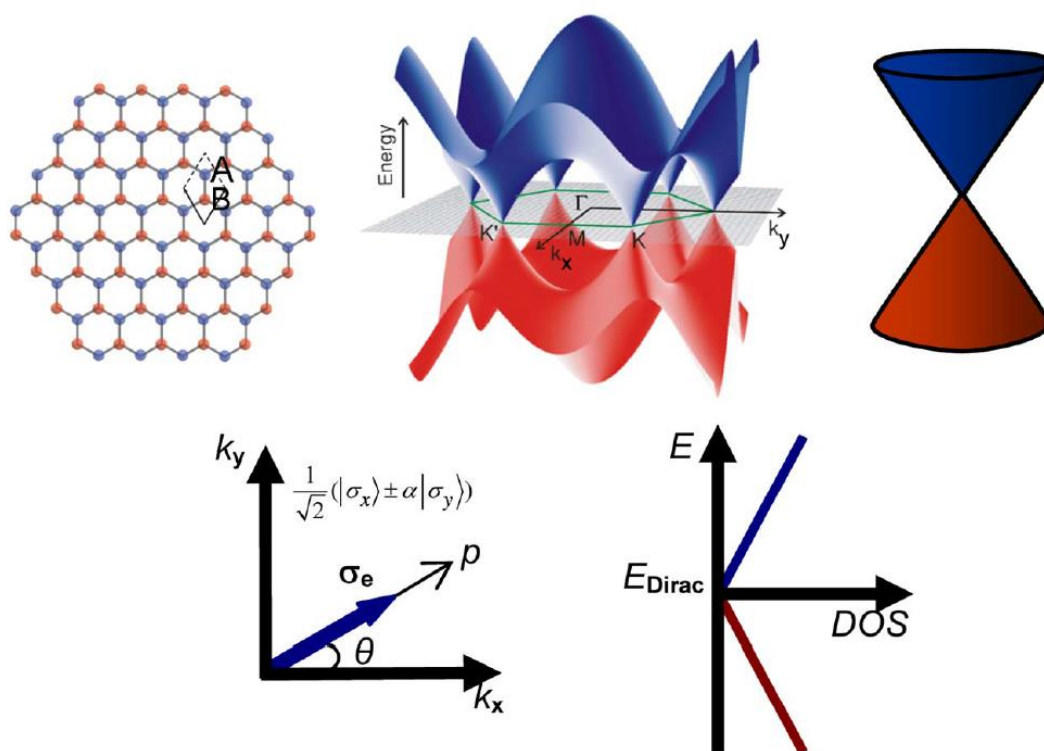


Figure 1.3: Graphene lattice, band structure, lattice dispersion at low energies and density of states dependence on energy.²³

It has inspired researchers to discover various 2D layered materials having comparable structure features but facile electronic and optical characteristics, like TMDC's e.g. (MoS₂,

WS₂, MoSe₂, WSe₂ and so on),³³⁻³⁵ h-BN,³⁶ Black Phosphorus (BP),³⁷ have also been explored in recent years.

1.2.2 Transition Metal Dichalcogenides (TMDCs)

These TMDCs compound consisting of a generalized formula MX₂ where M is transition metal from the group IV, group V, or group VI and X be the chalcogen atom such as S, Se, Te. The TMDCs are layered materials in which there is strong intralayer bonding and weak interlayer bonding present. In 2D TMDCs system, the atomically thin sheet comprises of three atomic layers in which transition metal is stuffed among two chalcogen atoms. There are large number of synthetic methods have been developed by the researchers such as micromechanical exfoliation,¹⁰ liquid exfoliation,¹⁶ ion-intercalation and exfoliation,^{38,39} CVD,⁴⁰⁻⁴² PLD,¹⁷ wet-chemical syntheses,⁴³⁻⁴⁵ etc., for the synthesis of ultrathin 2D materials. In the recent years, researchers have made attempts to prepare high quality uniform 2D TMDCs films with thickness control using ALD, MOCVD and HWCVD. The films prepared using deposition techniques are not only uniform all over the wafer but also are analogous in performance to the materials synthesized through other top down/bottom up approaches. The distinct feature is broadening the bandgap with decreasing number of layers due to the quantum confinement effect. In 2010, Heinz et al. observed strong photoluminescence in monolayer MoS₂ which strongly indicates transition from indirect bandgap to a direct band gap in MoS₂.⁴⁶ The weak vdW interaction between each layer and high surface area provides potential for energy storage and gas sensing applications. The property i.e. large surface to volume ratio of 2D TMDCs helps to enhance sensitivity, response time, recovery time and low power consumption. Due to their unique structural features i.e. lack of dangling bonds and outstanding electronic (excellent ohmic contact), optical, mechanical, and thermal properties the ultrathin 2D TMDCs become a key class of materials in various fields of science. Based on these fascinating properties, these

2D materials are widely used in variety of applications, such as nanoelectronic devices,^{18,47} energy storage and conversion,⁴⁸⁻⁵⁰ sensors,^{51,52} catalysis.⁵³⁻⁵⁵

1.2.3 Black Phosphorous (BP)

The field of 2D materials is constantly growing research area, and it is not just limited to Graphene and TMDCs. Recently, monoelemental BP which is layered allotrope of the element Phosphorous has received enormous attention in researchers all over the world in numerous fields. In common, phosphorus has three allotropes, i.e. white, red and black. Among these, white and red phosphorous are extensively utilized in explosives and security contests. The BP is a layered *p-type* semiconductor synthesized from red phosphorous under high temperature and pressure. It also shows an interesting phase transformation under different pressure conditions.

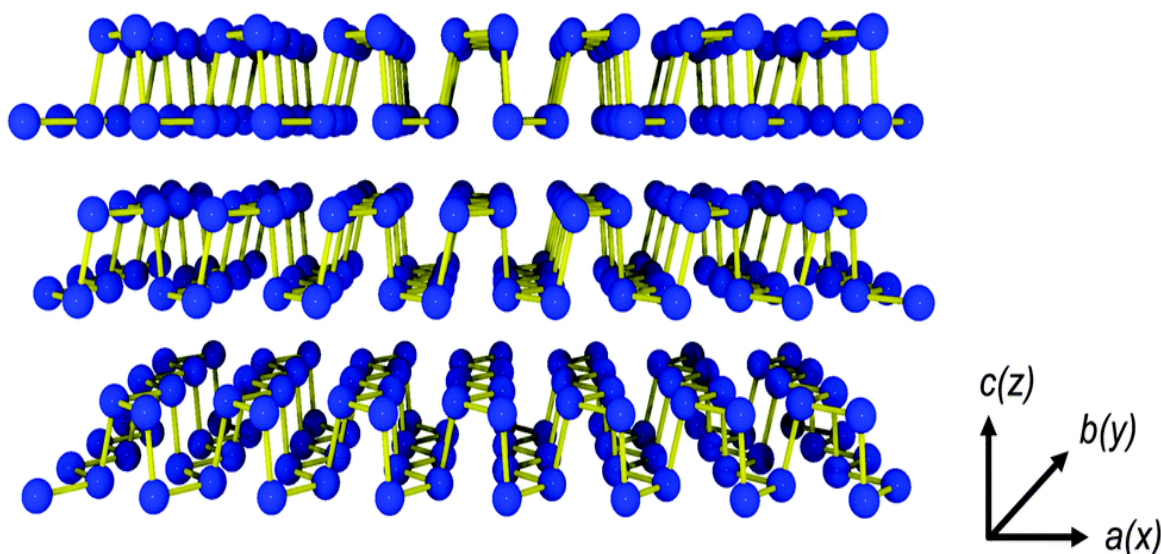


Figure 1.4: Crystal structure of few-layer BP.⁵⁶

When the pressure is around 5 GPa, the phase changes to semiconducting rhombohedral from semiconducting orthorhombic, and at about 10 GPa it changes to metallic simple cubic phase. The unit cell of BP comprises of eight atoms, which contributes to a calculated density of 2.69 g cm^{-3} . It also consists of two layers of BP and every phosphorous atom is bonded among three

adjacent atoms at 2.18 \AA .⁵⁷ The bulk BP possesses a direct bandgap of 0.3 eV and 2.1 eV in the single-layer with mobility values upto $1000 \text{ cm}^2/\text{Vs}$.⁵⁸ These excellent semiconducting properties of BP appealed the possibility to use atomically thick nanosheet in various nanoelectronics and broadband photodetection applications.⁵⁹⁻⁶¹

1.3 Devices based on 2D materials

These 2D materials due to their extraordinary structural, physical, electronic and optical properties have received enormous interest in various applications such as electronic, optoelectronic, catalysis, energy storage and so on. In this part, I will discuss few applications of 2D materials such as Field Effect Transistor, photodetector, humidity and gas sensor, energy storage devices.

1.3.1 Field Effect Transistor

The observation of high charge carrier mobility in Graphene based FET attracted researchers to work in electronics application.

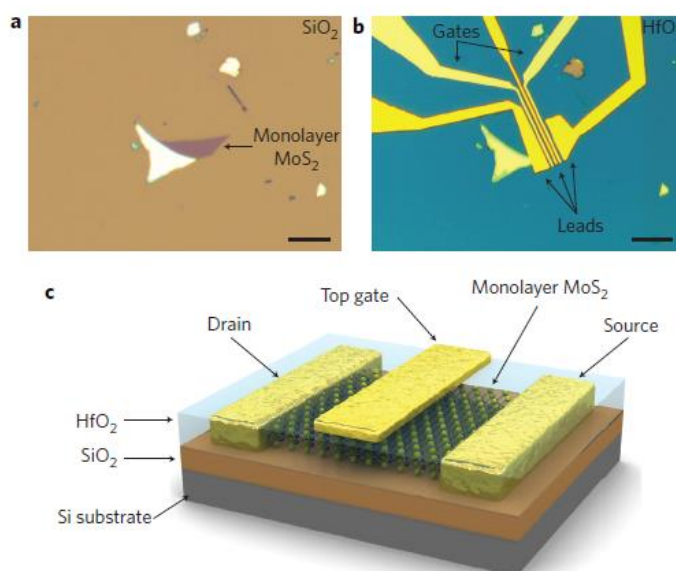


Figure 1.5: (a) optical image, (b) optical image of the MoS₂ based device and on the top 30 nm HfO₂ is coated using ALD for mobility booster purpose, (c) Device schematic for the single layer MoS₂.⁴⁷

In this, A.K. Geim and K. S. Novoselov observed charge carrier mobility $\sim 10,000 \text{ cm}^2/\text{Vs}$ for the micromechanically exfoliated Graphene based FET.¹⁰ The absence of band gap in Graphene results in small on/off ratios which makes Graphene unsuitable for electronic device applications. There are some TMDCs with semiconducting nature possesses bandgap within 1-2.2 eV makes them ideal materials for FET's. Previously researchers have reported charge carrier mobility $\sim 0.5\text{-}3 \text{ cm}^2/\text{Vs}$ for MoS₂ based FET's. In 2011 Kis et al. has used HfO₂ as gate dielectric to demonstrate single layer MoS₂ transistor exhibits charge carrier mobility 217 cm^2/Vs and on/off ratio $\sim 1 * 10^8$ with low power dissipation.⁴⁷

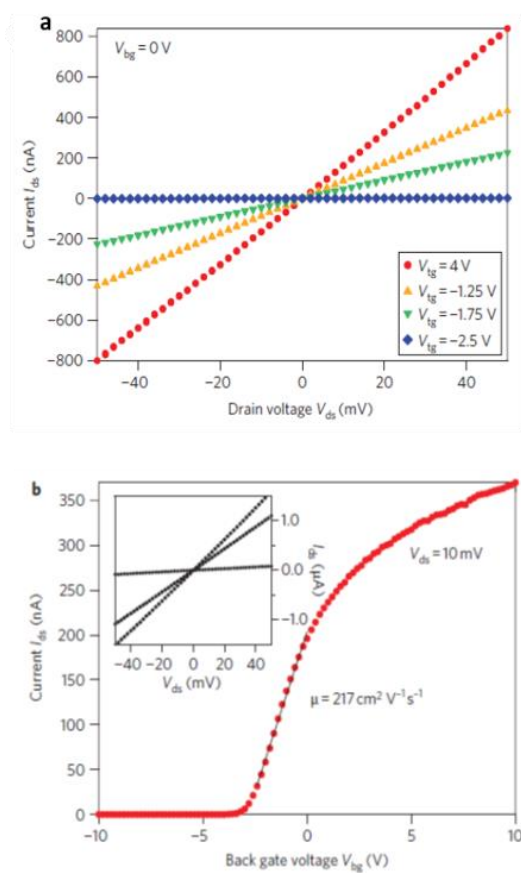


Figure 1.6: (a) output characteristics curve, (b) transfer characteristics curve for the single layer MoS₂ based devices.⁴⁷

Later, researchers found new approach to grow large area monolayers using CVD method in order to achieve high carrier mobility with fine control over layers. The CVD grown monolayer

MoSe₂ has been reported by Ajayan et al. which display that MoSe₂ monolayers work as an *n*-type with a mobility of 50 cm²/Vs and on/off ratio of 10⁶.

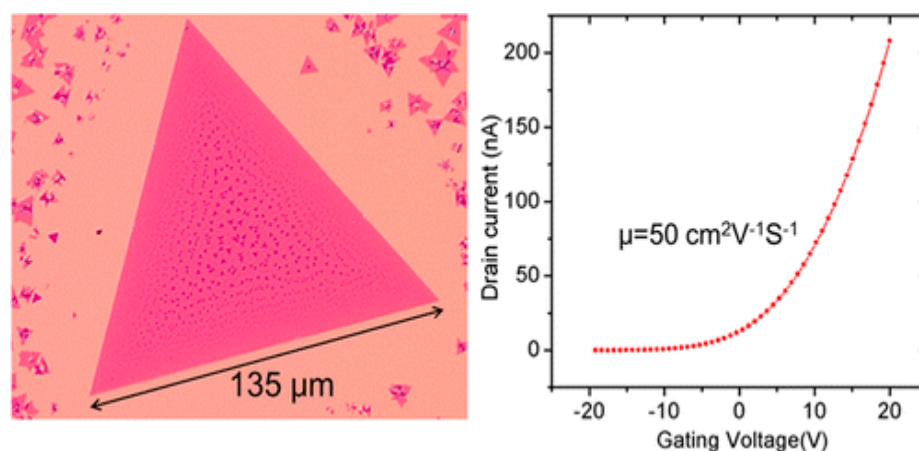


Figure 1.7: Optical image, typical I_{ds} as function of V_g plot for the CVD grown monolayer MoSe₂.⁶²

The profound outcome of this method results in large area, uniform and highly crystalline nature of as grown monolayer MoSe₂.⁶² The MoSe₂ single layers also prepared using micromechanical exfoliation by Stefano et al.⁶³ fabricated back gated FET. The device has showed on/off ratios larger than 10⁶.

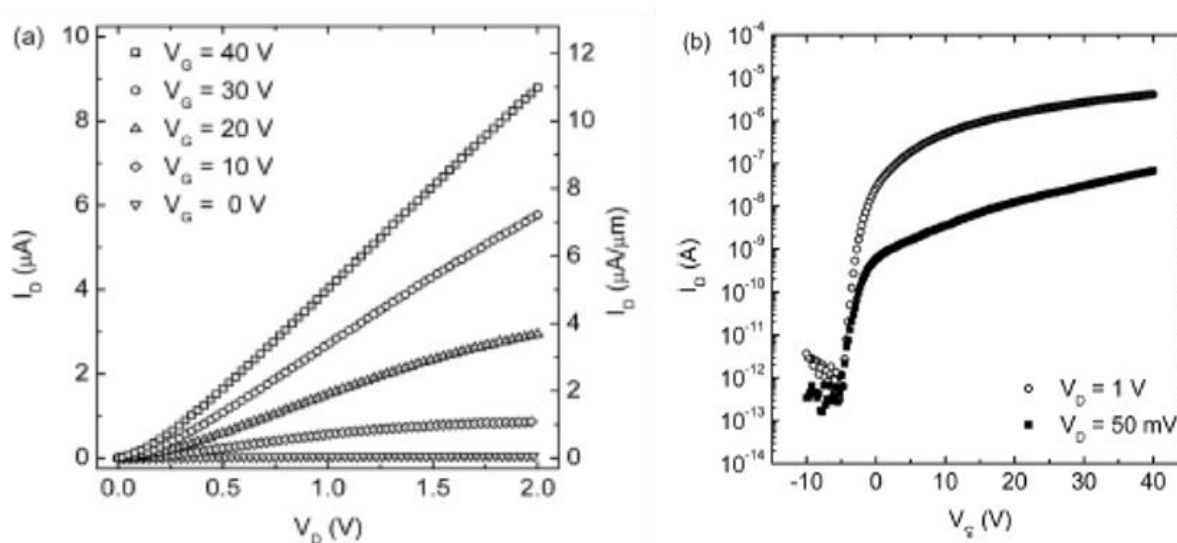


Figure 1.8: (a) (I_D - V_D) curves measured at various V_g values, (b) I_D - V_g curve measured at $V_D = 50$ mV.⁶³

They also measured intrinsic conductivity and mobility of the MoSe₂ as a function of gate bias. The temperature dependence study reveals that the mobility increases with decreasing the temperature, suggesting that the phonon scattering dominates the temperature.

In 2014, Song et al. fabricated few layer BP FET device using micromechanical exfoliation method. This is the first report on low frequency noise (LFN) analysis where they observed reduction in current fluctuations in few layer BP device resulting from Al₂O₃ passivation. In order to support these observations the measurements were carried out on thermally annealed devices before and after the passivation of Al₂O₃.⁵⁹

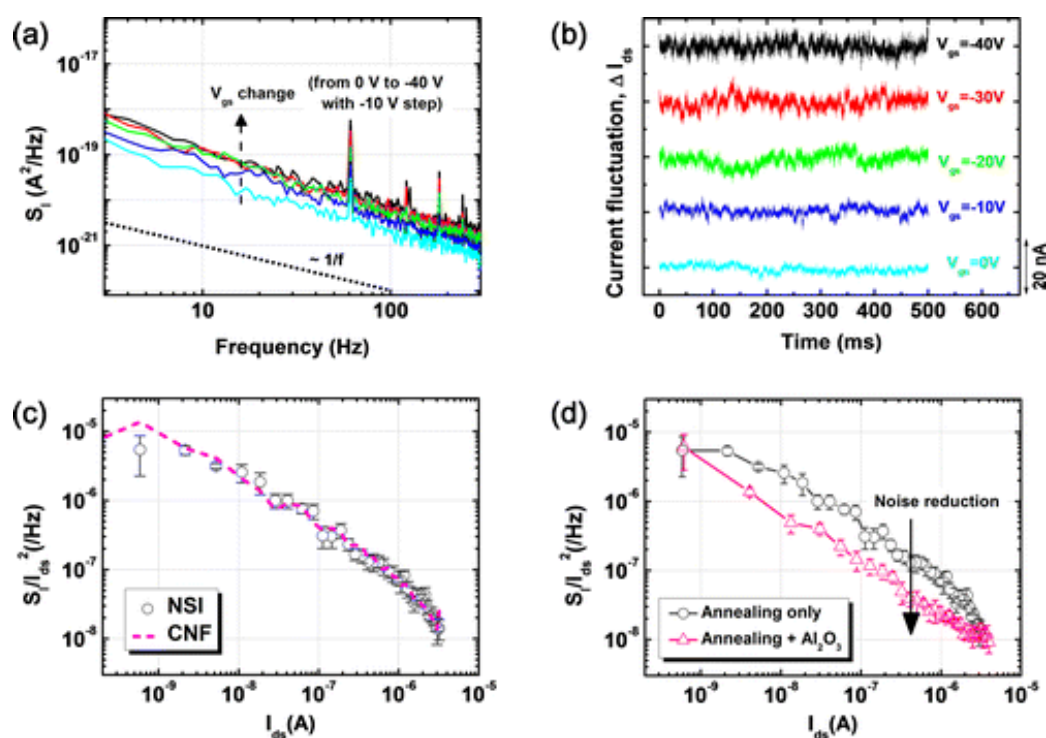


Figure 1.9: Low frequency noise characteristics of the few layer BP FET (noise reduction due to Al₂O₃ passivation represented).⁵⁹

The main advantage of (LFN) method is that it can be practiced irrespective of area size of the interface in the device study. The Figure 1.9(d) shows the reduction in the noise level after Al₂O₃ passivation over few layer BP FETs which indicates that the trap sites triggers charge fluctuation are reduced by Al₂O₃ passivation.

1.3.2 Photodetector

The direct bandgap of MoS₂ proposes that it might be suitable candidate for optical devices. In this regard Kis et al. has fabricated phototransistor based on single layer MoS₂.

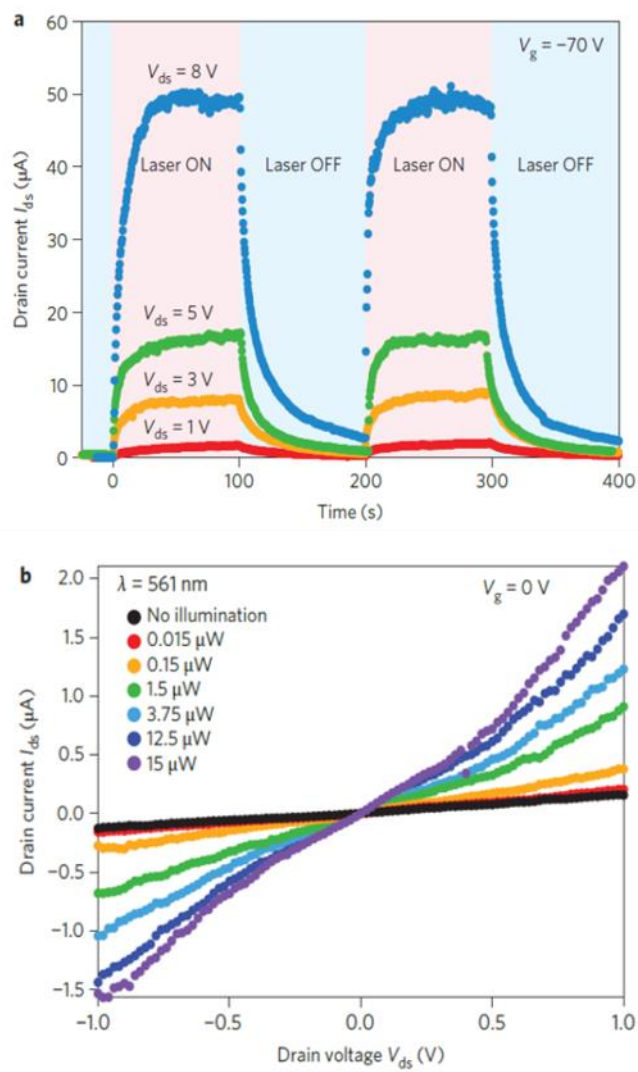


Figure 1.10: (a) Time-resolved photo response measured for various V_{ds} values and $P_{inc} = 4.25\ \mu\text{W}$. (b) output curves measured in dark also with various light intensities.⁶⁴

The fabricated phototransistor showed improved charge carrier mobility with Photoresponsivity of $\sim 880\text{ A/W}$ at a wavelength of 561 nm and photo response in the 460-600 nm range.⁶⁴ The electrical and optoelectronic properties are greatly affected by the presence of

sulfur vacancies or defects occurred during synthesis process. Considering this issue, Li et al. and co-workers synthesized highly crystalline monolayer MoSe₂ using CVD method.

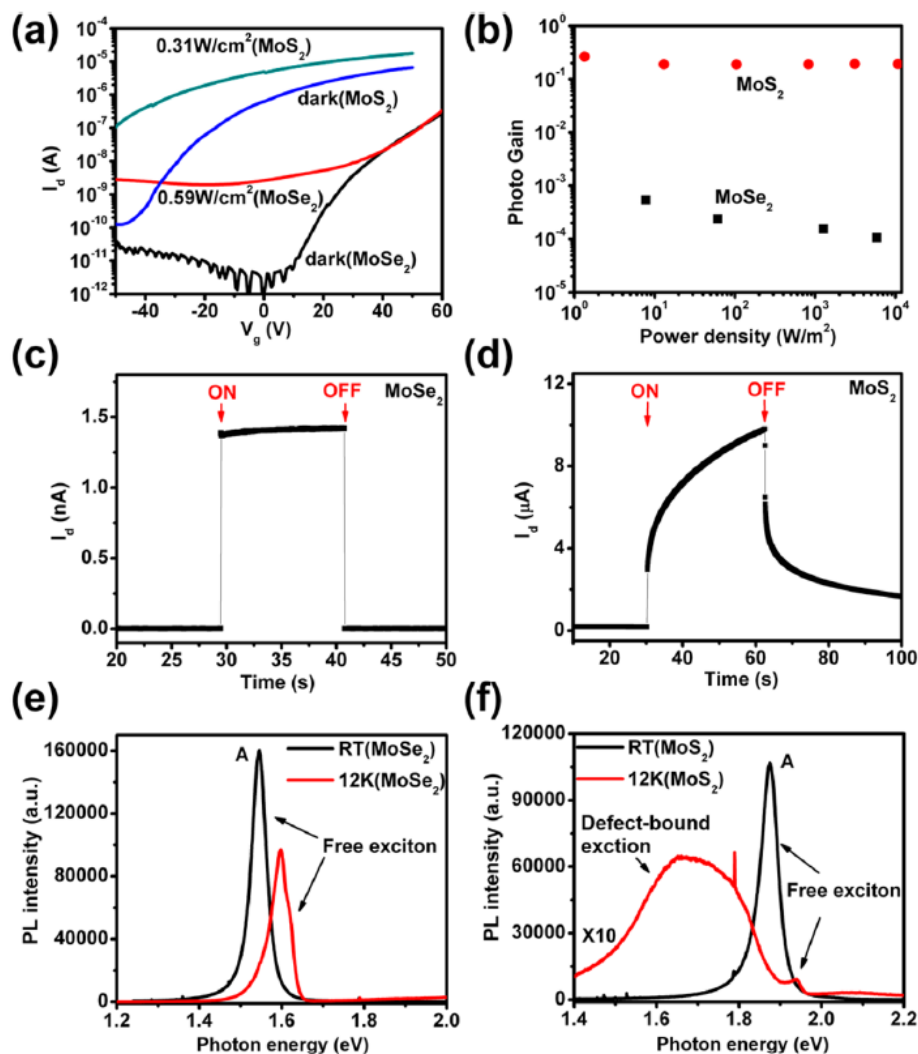


Figure 1.11: Optical properties of CVD grown monolayer MoSe₂ and MoS₂. (a) I_d - V_g transfer characteristics, (b) power density dependence of photogain at $V_{ds} = 1\text{V}$, (c,d) Time resolved photocurrents of the photodetector, (e,f) PL plots for single layer MoSe₂ and MoS₂ recorded at room temperature and 12 K respectively.⁶⁵

In 2014, Wee et al. has fabricated phototransistors on monolayer WSe₂ grown using CVD contacted with metals having various work-function values. The group has thoroughly investigated the effect of schottky contact on the optical properties of the devices.

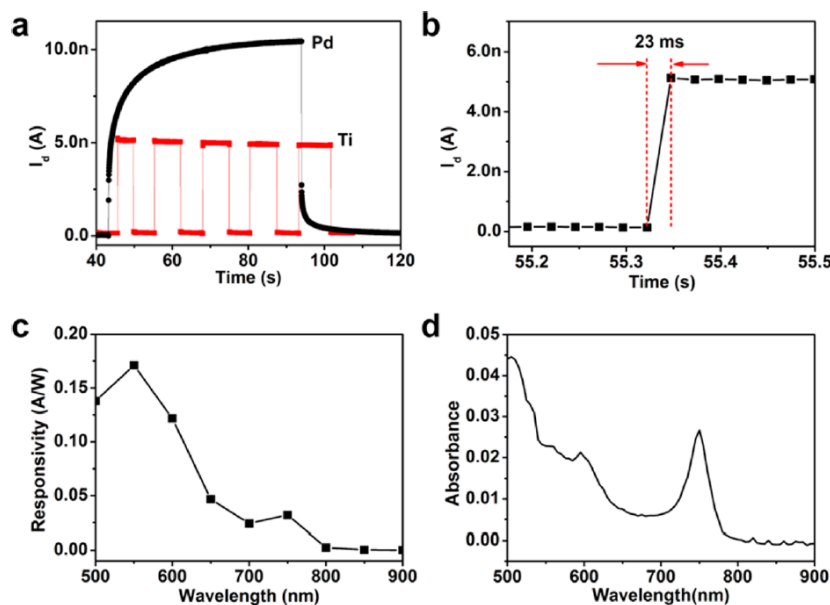


Figure 1.12: (a) Photoswitching behaviors of the Pd- and Ti- contacted phototransistors, (b) photoswitching rate of the Ti-contacted photodetector, (c) wavelength dependence of the photoresponsivity and (d) absorbance spectrum of CVD grown monolayer WSe_2 .⁶⁶

The response and recovery time were found to be less than 23 ms for the WSe_2 phototransistor when contacted with Ti metal. They also observed highly stable performance of the device even after 6 months in ambient conditions.⁶⁶

1.3.3 Humidity and Gas Sensor

The existence of 2D structure, high surface area and excellent electrical properties of 2D materials especially graphene received massive interest in various sensing applications such as humidity and gas sensor. The inkjet printed graphene via liquid exfoliation utilized for humidity sensing was reported by Hasan et al. The group has come with novel approach where they have integrated graphene with CMOS micro-electro-mechanical-system micro hotplate for humidity sensor device. They observed the percolating networks in the sensing layers which are reduced upon exposure of water vapors which results in increased resistivity with reproducible response of the fabricated sensor. The obtained results reveals that the suitable

volume of graphene ink onto CMOS system has potential in next generation devices i.e. internet of things and low cost humidity sensors.⁶⁷

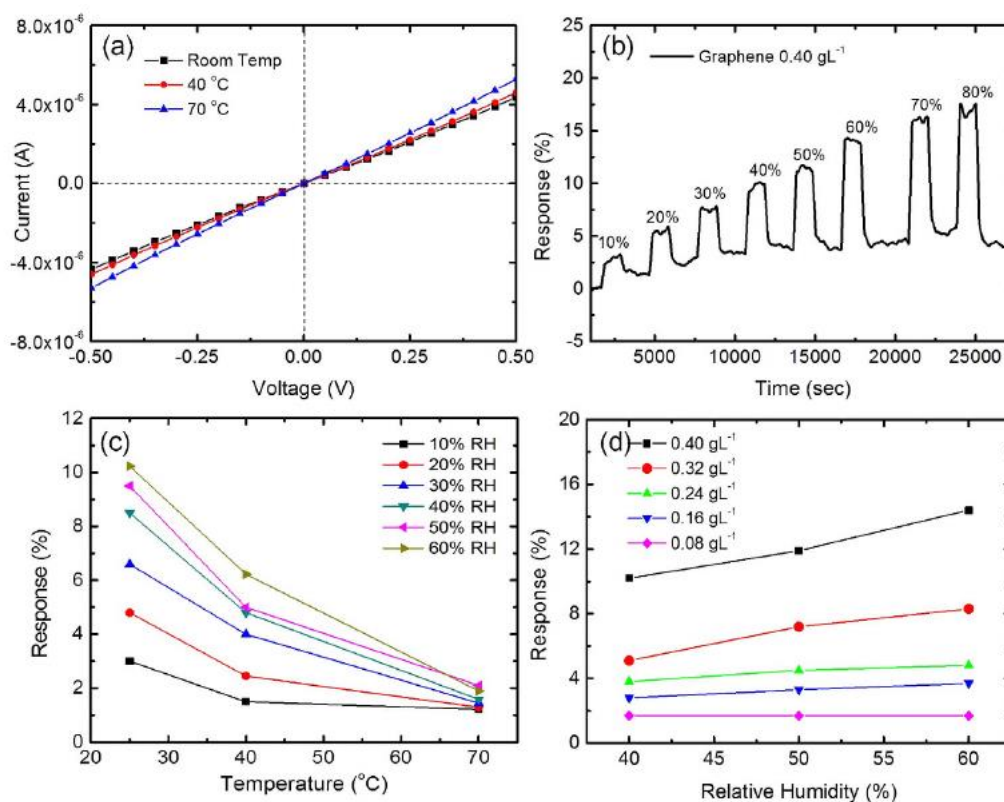


Figure 1.13: (a) *I-V* characteristics recorded at three different temperature, (b) Sensing response with eight different RH levels at RT, (c) Sensing response under three different Temperature conditions and (d) Sensing response varies with amount of Graphene deposited.⁶⁷

The presence of weak vdW interaction and high surface area in single layer MoS₂ provides potential in sensing application. In 2014 Late et al. has fabricated single and few layer MoS₂ FET based sensors.⁵² The single and few layer sample has been prepared by micromechanical exfoliation method and tested for various gases such as NO₂ and NH₃. The sensing performance have been studied for the prepared samples for the various relative humidities ranging from 4%-84%. The Figure 1.14 presents the comparative sensing behavior of bi and few layer MoS₂ device upon exposure to ammonia and nitrogen dioxide gas.

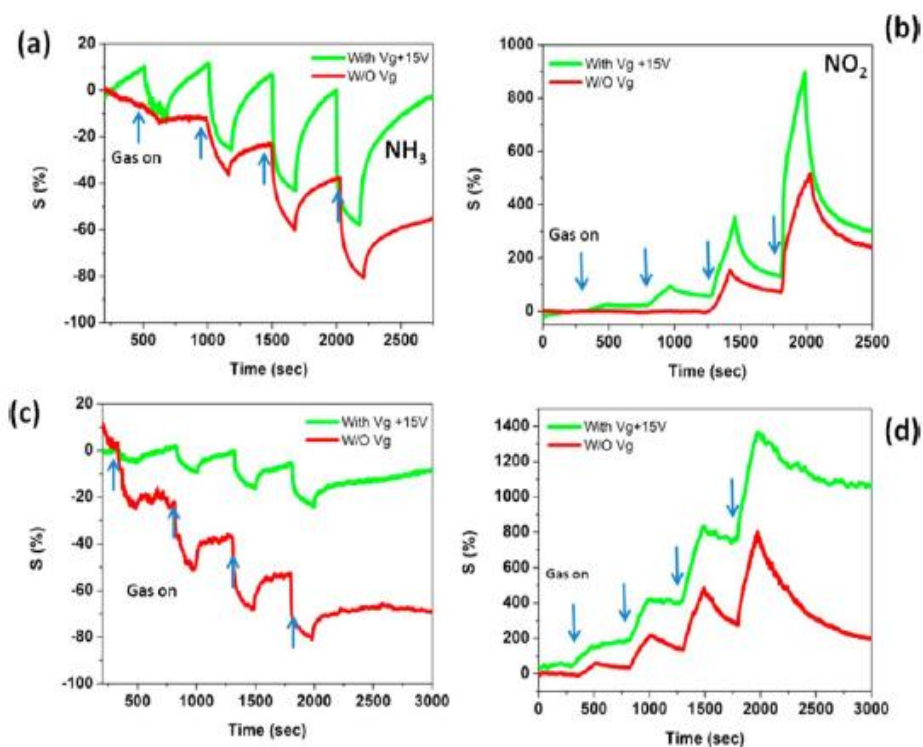


Figure 1.14: Comparative sensing behavior with and without applying back gate voltage (+15 V) for two-layer (a) NH_3 , (b) NO_2 gas and five-layer MoS_2 (c) NH_3 and (d) NO_2 gas (for 100, 200, 500, 1000 ppm).⁵²

The monolayer WS_2 is the less explored material from 2D family on their optical and sensing properties. It possess favorable band structure, wide operating range over temperature and high thermal stability makes WS_2 a promising candidate for applications in nanoelectronic devices. Huo et al. synthesized and fabricated WS_2 nanoflake based FET from the bulk crystal and thoroughly investigated optoelectronic and sensing properties. Upon red light (633 nm) illumination, the WS_2 nanoflake device achieved response time (<20 ms), photoresponsivity 5.7 A/W) and EQE (1118 %) respectively. On the other hand, the photoresponse under ethanol and NH_3 gas reaches to maximum in terms of photoresponsivity (884 A/W) and EQE (1.7×10^5 %). The reason behind response enhancement is adsorption of ethanol and NH_3 molecules which eventually donates electron to the device under light illumination. Thus, leads to

generate more number of photo-induced electrons per incident photons. The effect of gas molecules such as O_2 , NH_3 , Ethanol on photo responsive parameters shown in Figure 1.14.⁶⁸

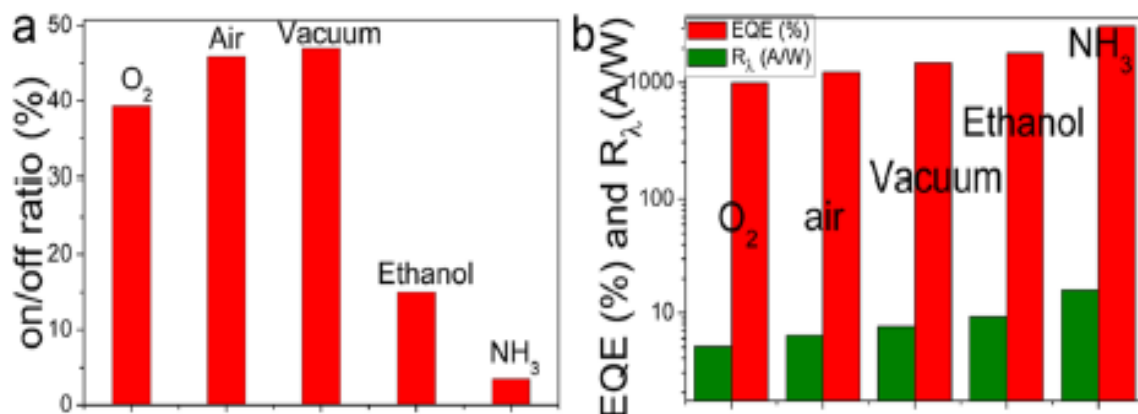


Figure 1.15: Effect of gas molecules on photo-responsive parameters (a) photosensitive on/off ratio, (b) photoresponsivity and EQE of the multilayer WS_2 nanoflake based device.⁶⁸

1.3.4 Energy Storage Devices

There are two important types of energy storage devices such as supercapacitors and Li-ion Batteries. These 2D materials possess high surface to volume ratio and good conductivity, hence some layered materials are suitable candidates for the energy storage applications.

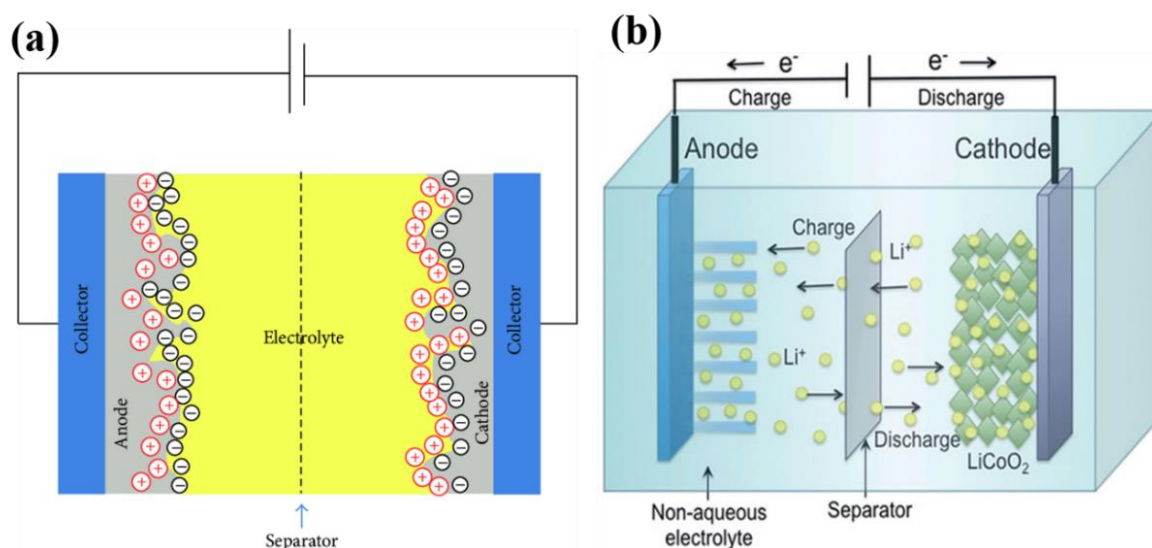


Figure 1.16: Schematic diagrams for (a) supercapacitor⁶⁹ and (b) Li-ion batteries.⁷⁰

The supercapacitors based on 2D materials gained much interest because of high power density, ultrafast charge-discharging rates and excellent cyclic stability. The Figure 1.16 (a) and (b) present the schematic diagrams for supercapacitor and Li-ion batteries. In 2015, Balasingam et al. has reported few layer MoSe₂ nanosheets using hydrothermal method and studied their electrochemical charge storage behaviour.⁷¹ The MoSe₂ nanosheet electrode exhibited a maximum specific capacitance of 198.9 Fg⁻¹ and the symmetric device showed 49.7 F/g at a scan rate of 2 mV/s. The two-dimensional MoSe₂ nanosheets showed high specific capacitance with good cyclic stability, which makes it a promising electrode material for supercapacitor applications.⁷¹

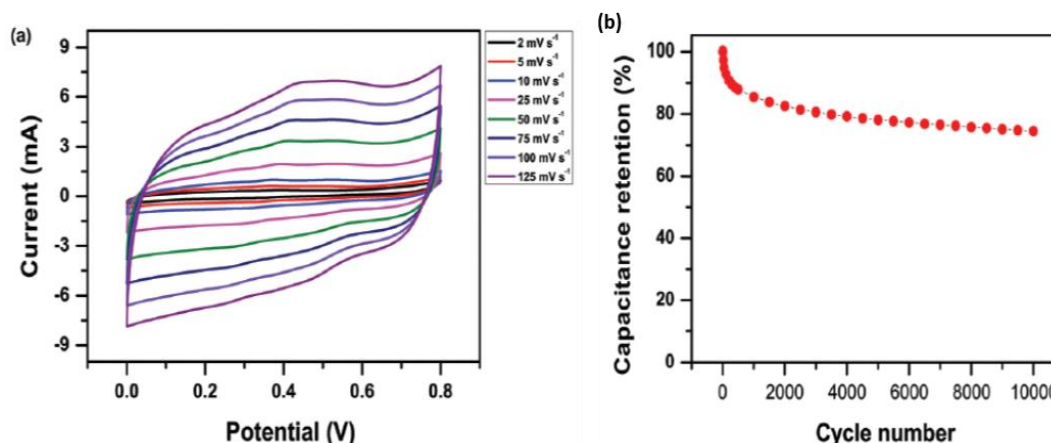


Figure 1.17: (a) cyclic voltammograms of MoSe₂ nanosheets in 0.5 M H₂SO₄ electrolyte measured at different scan rates ranging from 2 to 125 mV/s, (b) specific capacitance retention of the MoSe₂ nanosheets as a function of the cycle number.⁷¹

As mentioned earlier, 2D materials possess large surface to volume ratio hence it can provide active sites which makes it quite challenging to explore these materials for hydrogen evolution. Recently, Jing et al. has synthesized SnS₂ nanosheets using solvothermal method in the presence of PVP. They have suggested that the role of PVP is to inhibit the growth of SnS₂ nanosheets along (001) direction and protect the product from agglomeration. These

nanosheets exhibit high hydrogen evolution activity of $1.06 \text{ mmol h}^{-1}\text{g}^{-1}$ under sunlight, much higher than that of the SnS_2 with different morphologies and P25-TiO_2 .⁷²

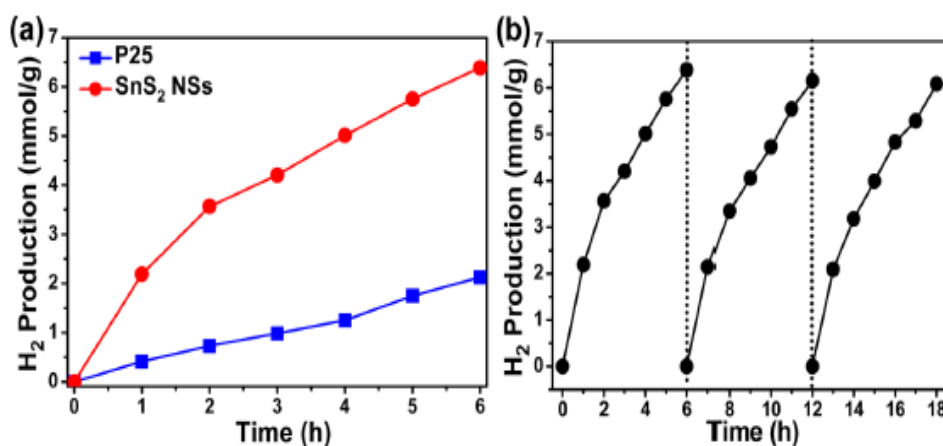


Figure 1.18: (a) comparison of the hydrogen evolution rate on commercial P25-TiO_2 and SnS_2 nanosheets, (b) cyclic H_2 production curve for SnS_2 nanosheets.⁷²

In contrast to other 2D materials, Black Phosphorous (BP) possesses indirect bandgap (0.3 eV) in bulk and direct bandgap (2.1 eV) in single layer.

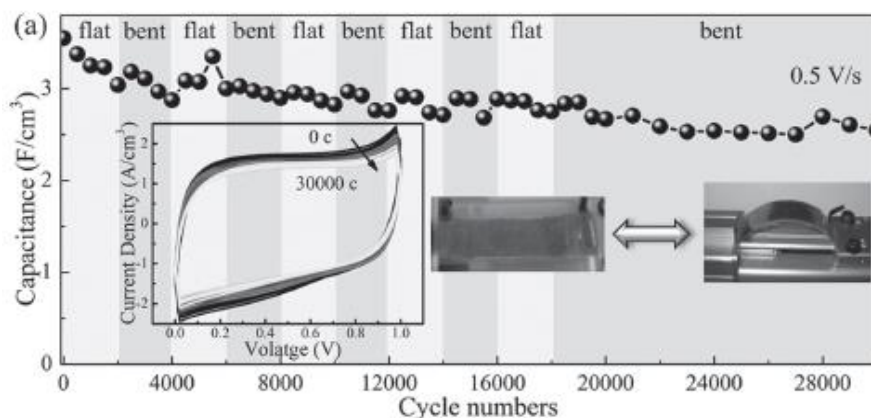


Figure 1.19: (a) Cyclic stability measurements for BP device carried out in flat and bent conformation set up.⁷³

The recent studies revealed that BP exhibits large specific surface area which makes it good candidate as electrode material. In 2016, Hao et al. has synthesized BP flakes using liquid exfoliation method.

Further, they have utilized these nanoflake as flexible electrode material and achieved excellent electrochemical energy storage. These devices have been found to deliver high specific capacitance of 45.8 Fg^{-1} at a scan rate of 0.01 V/s with outstanding mechanical flexibility and cyclic stability over 30,000 cycles.⁷³ Like other 2D TMDCs, tellurides such as WTe_2 and MoTe_2 are attracting interest in electronics and optoelectronics device applications.

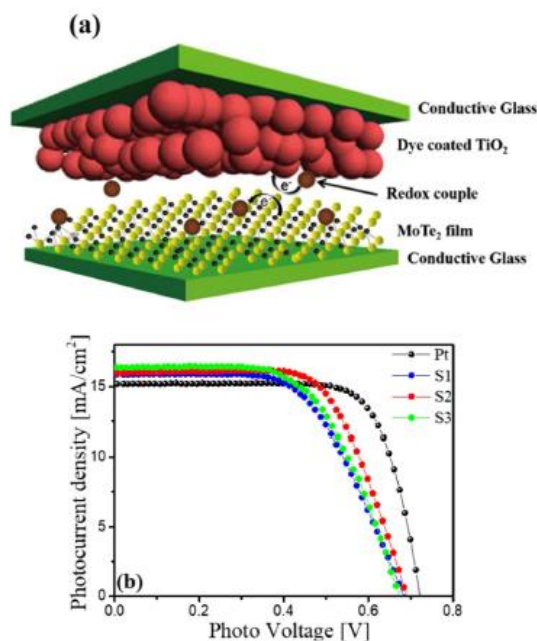


Figure 1.20: Schematic diagram of the electro catalytic mechanism in DSSC using MoTe_2 counter electrodes (CEs) (b) Photocurrent-voltage plots of dye sensitized solar cells (DSSCs) for various CEs measured at AM 1.5 G illumination.⁷⁴

Hussain et al. have prepared MoTe_2 films using sputtering technique followed by annealing process and used them as (CEs) in DSSCs.⁷⁴ The MoTe_2 CE device showed 7.25% power conversion efficiency under solar simulator with light illumination of 100 mW/cm^2 also it exhibited good electro catalytic performance and low charge transfer resistance at the electrolyte-electrode interface.

1.4 Conclusions and Objectives of the Thesis

In conclusion, this chapter provided brief information about the classification of nanomaterials especially 2D materials including graphene, TMDCs and Black Phosphorous. It explains the unique properties of 2D materials and their limitations especially zero bandgap in graphene restricts their application in optoelectronic devices. Like graphene, other 2D materials have been investigated via various synthetic approaches and explored by the researchers all over the world. This chapter has covered the materials utilized in device applications such as FET, Photodetector, Sensor, Energy storage of 2D materials in the literature review section. The study on many other 2D materials with unique synthesis approach is still lacking and needs to explore. With the above-mentioned information in hand, this thesis discuss the growth of 2D materials with new synthesis route for nanoelectronic devices in brief. If the present literature are considered, CVD grown monolayers of TMDCs are widely studied and device characteristics have been investigated. Hence, the devices fabricated on 2D materials with novel synthesis method are indeed important.

The third chapter deals with the synthesis of V_2O_5 nanosheets and their utilization in humidity sensor, photodetector and field emission. The simple hydrothermal route was implemented and devices fabricated on ITO substrates. The photodetector device showed better response to UV light and emission current density of 1.5 mA/cm^2 with turn on field $1.18 \text{ V}/\mu\text{m}$ has been achieved through field emission studies. *In the fourth chapter*, BP nanosheets are obtained with the help of electrochemical exfoliation method for FET, photodetector and humidity sensor applications. The *p-type* nature of BP was confirmed through transfer and output characteristics. The humidity sensor device exhibited excellent sensitivity with good response and recovery time. *The fifth chapter* discusses the synthesis of SnSe_2 nanosheets using liquid exfoliation method. The liquid exfoliation process is divided into two steps, in the first step ultrasonication of SnSe_2 bulk crystal followed by centrifugation (second step) to achieve

uniform layers of SnSe₂. The devices were fabricated for the samples centrifuged at 1000, 3000 and 5000 rpm and comparative sensing behavior has been demonstrated. The new route for the synthesis of PtSe₂ nanosheets was developed in the *chapter 6*. Initially PtSe complex was obtained then growth of PtSe₂ nanosheets on Si substrate via thermal annealing is achieved. The as grown samples are then used for humidity sensor and photodetector purpose. The devices showed excellent response to water molecules and green light in terms of response and recovery time. *In seventh chapter*, MoS₂ and CdMoS₄ nanostructure based UV light photodetectors study has been demonstrated. The results reveals that the CdMoS₄ device shows better response to UV light when compared with MoS₂ device.

1.5 References

- 1) Ozin, G. A.; Arsenault, A. C. *Nanochemistry*, RSC Publishing, Cambridge, UK, **2005**.
- 2) Gleiter, H. Nanostructured materials: basic concepts and microstructure. *Acta Mater.* **2000**, *48*, 1.
- 3) Skorokhod, V. V.; Uvarova, I. V.; Ragulya, A. V. Physico-chemical kinetics in nanostructured systems. *Kyiv: Academperiodica* **2001**, *1*, 180.
- 4) Pokropivny, V. V.; Skorokhod, V. V. Classification of nanostructures by dimensionality and concept of surface forms engineering in nanomaterial science. *Mater. Sci. Eng., C* **2007**, *27*, 990.
- 5) Yin, J.; Huang, Y.; Hameed, S.; Zhou, R.; Xie, L.; Ying, Y. Large scale assembly of nanomaterials: mechanisms and applications. *Nanoscale* **2020**, *12*, 17571.
- 6) Stouwdam, J. W.; Janssen, R. A. Red, green, and blue quantum dot LEDs with solution processable ZnO nanocrystal electron injection layers. *J. Mater. Chem.* **2008**, *18*, 1889.
- 7) Lee, W.; Kang, S. H.; Kim, J. Y.; Kolekar, G. B.; Sung, Y. E.; Han, S. H. TiO₂ nanotubes with a ZnO thin energy barrier for improved current efficiency of CdSe quantum-dot-sensitized solar cells. *Nanotechnology* **2009**, *20*, 335706.
- 8) Mokerov, V. G.; Fedorov, Y. V.; Velikovski, L. E.; Scherbakova, M. Y. New quantum dot transistor. *Nanotechnology* **2001**, *12*, 552.
- 9) Iijima, S. Helical microtubules of graphitic carbon. *Nature* **1991**, *354*, 56.
- 10) Novoselov, K. S.; Geim, A. K.; Morozov, S. V.; Jiang, D.; Zhang, Y.; Dubonos, S. V.; Grigorieva, I. V.; Firsov, A. A. Electric field effect in atomically thin carbon films. *Science* **2004**, *306*, 666-669.
- 11) Zhang, H. Ultrathin two-dimensional nanomaterials. *ACS Nano* **2015**, *9*, 9451-9469.
- 12) Frindt, R.F. Single crystals of MoS₂ several molecular layers thick. *J. Appl. Phys.* **1966**, *37*, 1928-1929.

- 13) Butler, S. Z.; Hollen, S. M.; Cao, L.; Cui, Y.; Gupta, J. A.; Gutiérrez, H. R.; Heinz, T. F.; Hong, S. S.; Huang, J.; Ismach, A. F.; Johnston-Halperin, E. Progress, challenges, and opportunities in two-dimensional materials beyond graphene. *ACS Nano* **2013**, *7*, 2898-2926.
- 14) Duan, X.; Wang, C.; Pan, A.; Yu, R.; Duan, X. Two-dimensional transition metal dichalcogenides as atomically thin semiconductors: opportunities and challenges. *Chem. Soc. Rev.* **2015**, *44*, 8859-8876.
- 15) Halim, U.; Zheng, C. R.; Chen, Y.; Lin, Z.; Jiang, S.; Cheng, R.; Huang, Y.; Duan, X. A rational design of cosolvent exfoliation of layered materials by directly probing liquid-solid interaction. *Nat. Commun.* **2013**, *4*, 1-7.
- 16) Coleman, J. N.; Lotya, M.; O'Neill, A.; Bergin, S. D.; King, P. J.; Khan, U.; Young, K.; Gaucher, A.; De, S.; Smith, R. J.; Shvets, I. V.; Two-dimensional nanosheets produced by liquid exfoliation of layered materials. *Science* **2011**, *331*, 568-571.
- 17) Late, D. J.; Shaikh, P. A.; Khare, R.; Kashid, R. V.; Chaudhary, M.; More, M. A.; Ogale, S. B. Pulsed laser-deposited MoS₂ thin films on W and Si: field emission and photoresponse studies. *ACS Appl. Mater. Interfaces.* **2014**, *6*, 15881.
- 18) Wang, Q. H.; Kalantar-Zadeh, K.; Kis, A.; Coleman, J. N.; Strano, M. S. Electronics and optoelectronics of two-dimensional transition metal dichalcogenides. *Nat. Nanotechnol.* **2012**, *7*, 699.
- 19) Zhang, Y.; Tan, Y. W.; Stormer, H. L.; Kim, P. Experimental observation of the quantum Hall effect and Berry's phase in graphene. *Nature* **2005**, *438*, 201.
- 20) Stoller, M. D.; Park, S.; Zhu, Y.; An, J.; Ruoff, R. S. Graphene-based ultracapacitors. *Nano Lett.* **2008**, *8*, 3498-3502.

- 21) Nair, R. R.; Blake, P.; Grigorenko, A. N.; Novoselov, K. S.; Booth, T. J.; Stauber, T.; Peres, N. M.; Geim, A. K. Fine structure constant defines visual transparency of graphene. *Science* **2008**, *320*, 1308.
- 22) Balandin, A. A.; Ghosh, S.; Bao, W.; Calizo, I.; Teweldebrhan, D.; Miao, F.; Lau, C.N. Superior thermal conductivity of single-layer graphene. *Nano Lett.* **2008**, *8*, 902.
- 23) Wu, Y.; Farmer, D. B.; Xia, F.; Avouris, P. Graphene electronics: Materials, devices, and circuits. *Proc. IEEE* **2013**, *101*, 1620.
- 24) Geim, A. K. Graphene: status and prospects. *Science* **324**, 2009, 1530.
- 25) Schwierz, F. Graphene Transistors. *Nat. Nanotech.* **2010**, *5*, 487.
- 26) Liao, L.; Bai, J.; Cheng, R.; Lin, Y.; Jiang, S.; Qu, Y.; Huang, Y.; Duan, X. F. Sub-100 nm Channel Length Graphene Transistors. *Nano Lett.* **2010**, *10*, 3952.
- 27) Vivekchand, S. R. C.; Rout, C. S.; Subrahmanyam, K. S.; Govindaraj, A.; Rao, C. N. R. Graphene-Based Electrochemical Supercapacitors. *J. Chem. Sci.* **2008**, *120*, 9.
- 28) Arco, L. G.; Zhang, Y.; Schlenker, C. W.; Ryu, K.; Thompson, M. E.; Zhou, C. Continuous, Highly Flexible and Transparent Graphene Films by Chemical Vapor Deposition for Organic Photovoltaics. *ACS Nano* **2010**, *4*, 2865.
- 29) Yang, N.; Zhai, J.; Wang, D.; Chen, Y.; Jiang, L. Two-Dimensional Graphene Bridges Enhanced Photoinduced Charge Transport in Dye-Sensitized Solar Cells. *ACS Nano* **2010**, *4*, 887.
- 30) Ghosh, A.; Late, D. J.; Panchakarla, L.S.; Govindaraj, A.; Rao C. N. R. NO₂ and Humidity Sensing Characteristics of Few-Layer Graphene. *J. Exp. Nanosci.* **2009**, *4*, 313.
- 31) Dan, Y. P.; Lu, Y.; Kybert, N. J.; Luo, Z.; Johnson, A. T. C. Intrinsic Response of Graphene Vapor Sensors. *Nano Lett.* **2009**, *9*, 1472.

- 32) Neto, A. C.; Guinea, F.; Peres, N. M.; Novoselov, K. S.; Geim, A. K. The electronic properties of graphene. *Rev. Mod. Phys.* **2009**, *81*, 109.
- 33) Chhowalla, M.; Shin, H. S.; Eda, G.; Li, L. J.; Loh, K. P.; Zhang, H. The chemistry of two-dimensional layered transition metal dichalcogenide nanosheets. *Nat. Chem.* **2013**, *5*, 263.
- 34) Xu, M.; Liang, T.; Shi, M.; Chen, H. Graphene-like two-dimensional materials. *Chem. Rev.* **2013**, *113*, 3766.
- 35) Chhowalla, M.; Liu, Z.; Zhang, H. Two-dimensional transition metal dichalcogenide (TMD) nanosheets. *Chem. Soc. Rev.* **2015**, *44*, 2584.
- 36) Lin, Y.; Williams, T. V.; Connell, J. W. Soluble, exfoliated hexagonal boron nitride nanosheets. *J. Phys. Chem. Lett.* **2009**, *1*, 277.
- 37) Liu, H.; Du, Y.; Deng, Y.; Peide, D. Y. Semiconducting black phosphorus: synthesis, transport properties and electronic applications. *Chem. Soc. Rev.* **2015**, *44*, 2732.
- 38) Dines, M. B. Lithium intercalation via n-butyllithium of the layered transition metal dichalcogenides. *Mater. Res. Bull.* **1975**, *10*, 287.
- 39) Viculis, L. M.; Mack, J. J.; Mayer, O. M.; Hahn, H. T.; Kaner, R. B. Intercalation and exfoliation routes to graphite nanoplatelets. *J. Mater. Chem.* **2005**, *15*, 974-8.
- 40) Reina, A.; Jia, X.; Ho, J.; Nezich, D.; Son, H.; Bulovic, V.; Dresselhaus, M. S.; Kong, J. Large area, few-layer graphene films on arbitrary substrates by chemical vapor deposition. *Nano Lett.* **2008**, *9*, 30.
- 41) Lee, Y. H.; Zhang, X. Q.; Zhang, W.; Chang, M. T.; Lin, C. T.; Chang, K. D.; Yu, Y. C.; Wang, J. T.; Chang, C. S.; Li, L. J.; Lin, T. W. Synthesis of large-area MoS₂ atomic layers with chemical vapor deposition. *Adv. Mater.* **2012**, *24*, 2320.

- 42) Song, L.; Ci, L.; Lu, H.; Sorokin, P. B.; Jin, C.; Ni, J.; Kvashnin, A. G.; Kvashnin, D. G.; Lou, J.; Yakobson, B. I.; Ajayan, P. M. Large scale growth and characterization of atomic hexagonal boron nitride layers. *Nano Lett.* **2010**, *10*, 3209.
- 43) Yoo, D.; Kim, M.; Jeong, S.; Han, J.; Cheon, J. Chemical synthetic strategy for single-layer transition-metal chalcogenides. *J. Am. Chem. Soc.* **2014**, *136*, 14670.
- 44) Mahler, B.; Hoepfner, V.; Liao, K.; Ozin, G. A. Colloidal synthesis of 1T-WS₂ and 2H-WS₂ nanosheets: applications for photocatalytic hydrogen evolution. *J. Am. Chem. Soc.* **2014**, *136*, 1412.
- 45) Choucair, M.; Thordarson, P.; Stride, J. A. Gram-scale production of graphene based on solvothermal synthesis and sonication. *Nat. Nanotechnol.* **2009**, *30*.
- 46) Mak, K. F.; Lee, C.; Hone, J.; Shan, J.; Heinz, T. F. Atomically thin MoS₂: a new direct-gap semiconductor. *Phys. Rev. Lett.* **2010**, *105*, 136805.
- 47) Radisavljevic, B.; Radenovic, A.; Brivio, J.; Giacometti, I. V.; Kis, A. Single-layer MoS₂ transistors. *Nat. Nanotechnol.* **2011**, *6*, 147-150.
- 48) Zhu, J.; Yang, D.; Yin, Z.; Yan, Q.; Zhang, H. Graphene and graphene-based materials for energy storage applications. *Small* **2014**, *10*, 3480.
- 49) Cao, X.; Shi, Y.; Shi, W.; Rui, X.; Yan, Q.; Kong, J.; Zhang, H. Preparation of MoS₂-coated three-dimensional graphene networks for high-performance anode material in lithium-ion batteries. *Small* **2013**, *9*, 3433.
- 50) Gu, X.; Cui, W.; Li, H.; Wu, Z.; Zeng, Z.; Lee, S. T.; Zhang, H.; Sun, B. A Solution-processed hole extraction layer made from ultrathin MoS₂ nanosheets for efficient organic solar cells. *Adv. Energy Mater.* **2013**, *3*, 1262.
- 51) Schedin, F.; Geim, A. K.; Morozov, S. V.; Hill, E. W.; Blake, P.; Katsnelson, M. I.; Novoselov, K. S. Detection of individual gas molecules adsorbed on graphene. *Nat. Mater.* **2007**, *6*, 652.

- 52) Late, D. J.; Huang, Y. K.; Liu, B.; Acharya, J.; Shirodkar, S. N.; Luo, J.; Yan, A.; Charles, D.; Waghmare, U. V.; Dravid, V. P.; Rao, C. N. Sensing behavior of atomically thin-layered MoS₂ transistors. *ACS Nano* **2013**, *7*, 4879-4891.
- 53) Qu, L.; Liu, Y.; Baek, J. B.; Dai, L. Nitrogen-doped graphene as efficient metal-free electrocatalyst for oxygen reduction in fuel cells. *ACS Nano* **2010**, *4*, 1321.
- 54) Lukowski, M. A.; Daniel, A. S.; Meng, F.; Forticaux, A.; Li, L.; Jin, S. Enhanced hydrogen evolution catalysis from chemically exfoliated metallic MoS₂ nanosheets. *J. Am. Chem. Soc.* **2013**, *135*, 10274.
- 55) Chen, J.; Wu, X. J.; Yin, L.; Li, B.; Hong, X.; Fan, Z.; Chen, B.; Xue, C.; Zhang, H. One-pot synthesis of CdS nanocrystals hybridized with single-layer transition-metal dichalcogenide nanosheets for efficient photocatalytic hydrogen evolution. *Angew. Chem. Int. Ed.* **2015**, *127*, 1226.
- 56) Liu, H.; Du, Y.; Deng, Y.; Peide, D. Y. Semiconducting black phosphorus: synthesis, transport properties and electronic applications. *Chem. Soc. Rev.* **2015**, *44*, 2732.
- 57) Xia, F.; Wang, H.; Jia, Y. Rediscovering black phosphorus as an anisotropic layered material for optoelectronics and electronics. *Nat. Commun.* **2014**, *5*, 1.
- 58) Liu, H.; Neal, A. T.; Zhu, Z.; Luo, Z.; Xu, X.; Tomanek, D.; Ye, P. D. Phosphorene: An Unexplored 2D Semiconductor with a High Hole Mobility. *ACS Nano* **2014**, *8*, 4033.
- 59) Na, J.; Lee, Y. T.; Lim, J. A.; Hwang, D. K.; Kim, G.; Choi, W. K.; Song, Y. Few Layer Black Phosphorus Field-Effect Transistors with Reduced Current Fluctuation. *ACS Nano* **2014**, *8*, 11753.
- 60) Buscema, M.; Groenendijk, D. J.; Steele, G. A.; Zant, H. S. J.; Castellanos-Gomez, A. Photovoltaic Effect in Few Layer Black Phosphorus P-N Junctions Defined by Local Electrostatic Gating. *Nat. Commun.* **2014**, *5*, 4651.

- 61) Buscema, M.; Groenendijk, D. J.; Blanter, S. I.; Steele, G. A.; Zant, H. S. J.; Castellanos-Gomez, A. Fast and Broadband Photoresponse of Few-Layer Black Phosphorus Field-Effect Transistors. *Nano Lett.* **2014**, *14*, 3347-3352.
- 62) Wang, X.; Gong, Y.; Shi, G.; Chow, W. L.; Keyshar, K.; Ye, G.; Vajtai, R.; Lou, J.; Liu, Z.; Ringe, E.; Tay, B. K.; Ajayan, P. M. Chemical vapor deposition growth of crystalline monolayer MoSe₂. *ACS Nano* **2014**, *8*, 5125.
- 63) Larentis, S.; Fallahazad, B.; Tutuc, E. Field-effect transistors and intrinsic mobility in ultra-thin MoSe₂ layers. *Appl. Phys. Lett.* **2012**, *101*, 223104.
- 64) Lopez-Sanchez, O.; Lembke, D.; Kayci, M.; Radenovic, A.; Kis, A. Ultrasensitive photodetectors based on monolayer MoS₂. *Nat. Nanotechnol.* **2013**, *8*, 497.
- 65) Chang, Y. H.; Zhang, W.; Zhu, Y.; Han, Y.; Pu, J.; Chang, J. K.; Hsu, W. T.; Huang, J. K.; Hsu, C. L.; Chiu, M. H.; Takenobu, T.; Li, H.; Wu, C-I.; Chang, W-H.; Wee, A. T. S.; Li, L-J. Monolayer MoSe₂ grown by chemical vapor deposition for fast photodetection. *ACS Nano* **2014**, *8*, 8582.
- 66) Zhang, W.; Chiu, M. H.; Chen, C. H.; Chen, W.; Li, L. J.; Wee, A.T.S. Role of metal contacts in high-performance phototransistors based on WSe₂ monolayers. *ACS Nano* **2014**, *8*, 8653.
- 67) Santra, S.; Hu, G.; Howe, R. C. T.; De Luca, A.; Ali, S. Z.; Udrea, F.; Gardner, J. W.; Ray, S. K.; Guha, P.K.; Hasan, T. CMOS integration of inkjet-printed graphene for humidity sensing. *Sci. Rep.* **2015**, *5*, 1.
- 68) Huo, N.; Yang, S.; Wei, Z.; Li, S. S.; Xia, J. B.; Li, J. Photoresponsive and gas sensing field-effect transistors based on multilayer WS₂ nanoflakes. *Sci. Rep.* **2014**, *4*, 1.
- 69) Saleem, A. M.; Desmaris, V.; Enoksson, P. Performance enhancement of carbon nanomaterials for supercapacitors. *J. Nanomater.* **2016**.

-
- 70) Winter, M.; Brodd, R. J. 2004. What are batteries, fuel cells, and supercapacitors? *Chem. Rev.* **2004**, *104*, 4245-4270.
- 71) Balasingam, S. K.; Lee, J. S.; Jun, Y. Few-layered MoSe₂ nanosheets as an advanced electrode material for supercapacitors. *Dalton Trans.* **2015**, *44*, 15491.
- 72) Yu J.; Xu C. Y.; Ma, F. X.; Hu, S. P.; Zhang, Y. W.; Zhen, L. Monodisperse SnS₂ nanosheets for high-performance photocatalytic hydrogen generation. *ACS Appl. Mater. Interfaces.* **2014**, *6*, 22370.
- 73) Hao, C.; Yang, B.; Wen, F.; Xiang, J.; Li, L.; Wang, W.; Zeng, Z.; Xu, B.; Zhao, Z.; Liu, Z.; Tian, Y. Flexible All-Solid-State Supercapacitors based on Liquid-Exfoliated Black-Phosphorus Nanoflakes. *Adv. Mater.* **2016**, *28*, 3194.
- 74) Hussain, S.; Patil, S. A.; Vikraman, D.; Mengal, N.; Liu, H.; Song, W.; An, K. S.; Jeong, S. H.; Kim, H. S.; Jung, J. Large area growth of MoTe₂ films as high performance counter electrodes for dye-sensitized solar cells. *Sci. Rep.* **2018**, *8*, 29.

Chapter 2

Synthesis Methods and Device Fabrication

2.1 Synthesis of 2D Materials

The preparation of 2D materials via facile, feasible and reliable methods are of great significance for the investigation of its distinctive structural, physical characteristics. The researchers around the world have developed various approaches to synthesize these materials i.e. top down and bottom up approach. The top down approach consists of micromechanical exfoliation, liquid exfoliation, and ion intercalation methods. It is based on the isolation of bulk crystals into one atom thick sheets of 2D materials where several driving forces plays key role to diminish the weak vdW force among the stacked layers. The other way of preparing 2D layered sheets is bottom up approach which consists of CVD, PLD, and wet chemical synthesis. It depends on the direct preparation of 2D nanomaterials using different precursors via chemical reactions under various synthesis parameters. In this section, I discuss in brief various methods to synthesize these 2D materials along with their advantages and disadvantages.

2.1.1 Micromechanical Exfoliation

In this method the bulk crystals of (Graphite, MoS₂, BP, MoSe₂, GaSe) placed on the centre of the adhesive tape, and the other two sides of adhesive tape is adhered on the crystal surface. Then, the scotch tape from the top surface is detached from the crystal which takes out some layers from the bulk crystal. In order to obtain thin layers the above process can be repeated several times and can be transferred onto the substrate. Further, the scotch tape with thin flakes is placed onto the target i.e. SiO₂/Si substrate. At last, the scotch tape is taken off from the substrate and monolayer or few-layer flakes can be obtained on the SiO₂/Si wafer. The exfoliated flakes are then observed on the wafer with the help of optical microscope. In 2004, A. K. Geim and K. S. Novoselov awarded with noble prize for the discovery of Graphene from bulk graphite crystal.² Later on, single layers of other 2D materials such as h-BN, MoS₂, WS₂, MoSe₂, GaSe, SnSe₂ has been produced from bulk layered crystals. During mechanical

exfoliation process no chemical reaction occurs so the same crystal structure remains on the substrate.

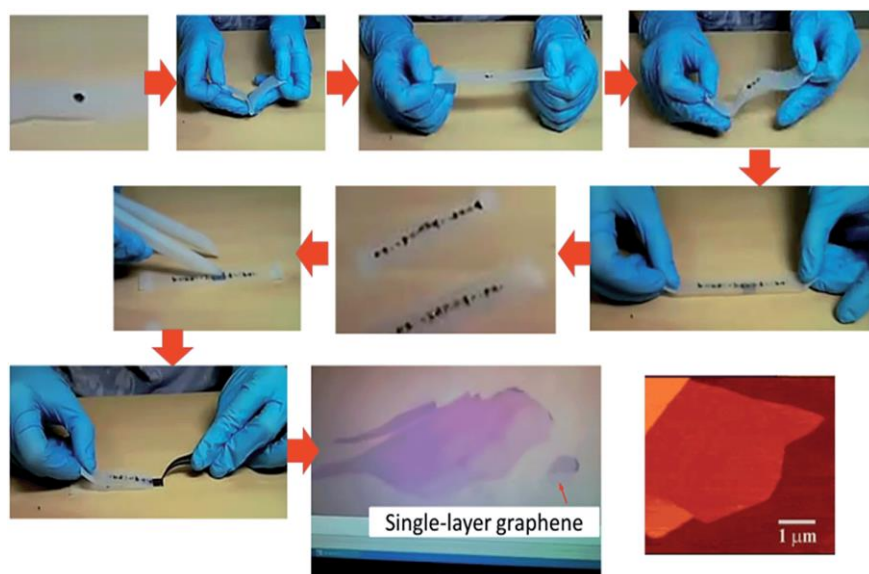


Figure 2.1: Preparation of single layer Graphene from Graphite using micromechanical exfoliation method.¹

The 2D ultrathin sheets obtained possess excellent quality with lateral dimensions up to tens of micrometer which are best fit for potential in electronic devices. There are several limitations to this approach i.e. difficult to control the size, shape and thickness of the material. It does not meet the real practical applications because the production yield is low. This method is appropriate only to those materials which bulk crystals are existing. At last, to meet the real world applications the production yield and growth control must be improved.

2.1.2 Liquid Exfoliation

This method is used to obtain single or few layer sheets of 2D materials from bulk crystals which are dispersed using ultrasonication in solvents, such as NMP and DMF.³ The advantage of using this method is it can disrupt the weak vdW interaction among the neighboring layers, but cannot suppress the covalent bonding. Here, the solvent plays a vital role in stabilizing the isolated layers and hindering their restacking and gathering.

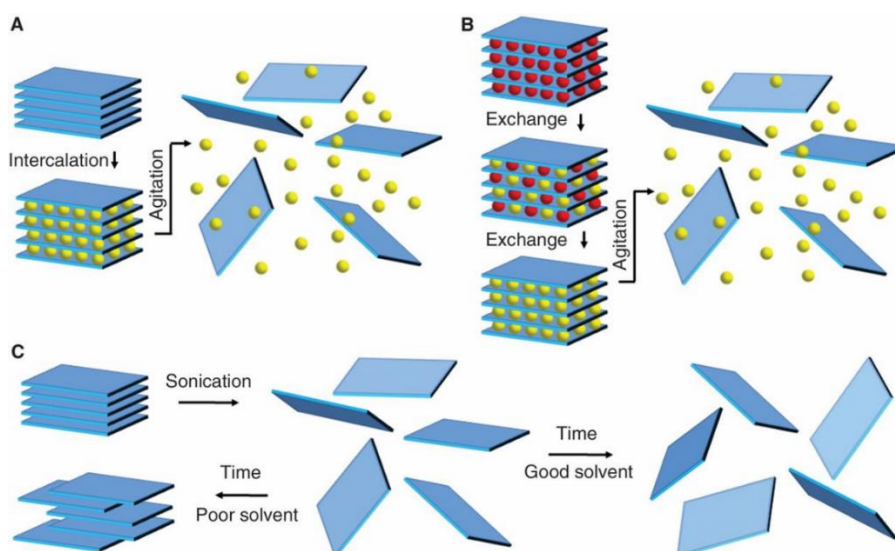


Figure 2.2: Schematic depiction of liquid exfoliation mechanism.³

It was found that the efficiency of exfoliation increases if the surface tension between the bulk crystal and the solvent matches also it minimizes the energy. There are few parameters which plays pivotal role in exfoliation process such as power of sonication, the liquid medium used to disperse 2D layers and the rate of centrifugation. Initially, bulk crystal of 2D materials are dispersed in particular solvent via ultrasonication process. During ultrasonication, the growth and breakdown of the microbubbles in solvents which is accredited to the cavitation-induced pressure pulsations. The cavitation results in high-speed microjets and shock waves, leads to produce normal and shear forces on bulk crystals. The cavitation and shear forces shows a major role in the exfoliation of bulk material to achieve single/few layers of 2D materials. The yield and lateral dimensions of the 2D nanosheets obtained by this method is more compared to micromechanical exfoliation approach but still low but not suitable for the practical applications.

2.1.3 Li-ion Intercalation

This method is somewhat similar to liquid exfoliation only difference is intercalates are used. In this process, Li-ions intercalate into the layers of bulk crystal which results in the weakening

of vdW interaction among the layers. The n-butyl lithium and metal naphthalenide are the most used common intercalates in the exfoliation method. During ion intercalation the cations such as (Li, Na, K) intercalates into the interlayer spacing between the layers which weakens the vdW interactions results into the exfoliation flakes into the solution. The single or few layer sheets are obtained after centrifuging the intercalated compounds. This method has been used to synthesize atomically thin nanosheets of 2D materials such as (MoS_2 , WS_2 , TiS_2 , NbSe_2 , and MoSe_2). The advantage of this method is that it can induce phase change of 2D TMDCs from semiconducting (2H) to metallic (1T) phase during exfoliation process.⁴⁻⁵

2.1.4 Chemical Vapor Deposition

In this method, the reaction is carried out at high temperature and in the presence of inert carrier gas, where different precursors are heated upto their evaporation point which then react on the surface of the wafer (SiO_2/Si) to produce large area one-atom thick 2D sheets.

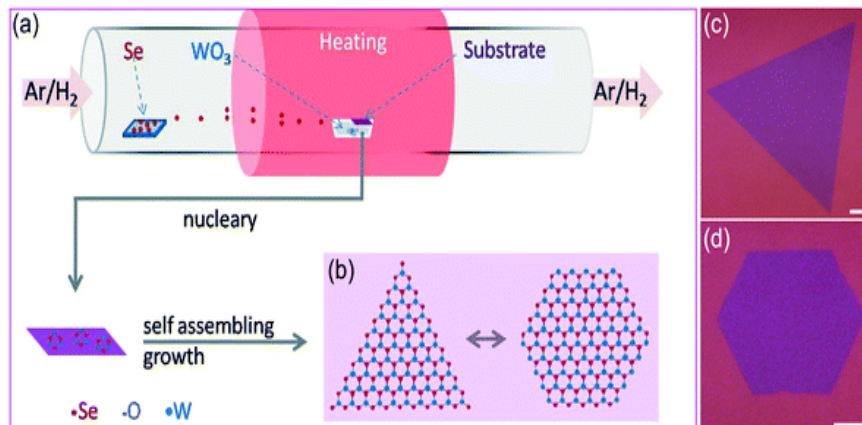


Figure 2.3: Monolayer WSe_2 using CVD setup (a) A schematic (b) structural models with triangular and hexagonal shapes. (c and d) optical microscopy images of WSe_2 flakes, respectively. (Scale bars, 10 μm)⁹

It allows researchers to produce high quality, large area films on the specific substrates which provides excellent electronic and optoelectronic properties. Through this method, monolayer flakes with different shapes such as triangular, hexagonal, circular, rectangular were grown on

SiO₂/ Si substrates. The growth mechanism for monolayer with various shape mainly depends on four key process parameters: (1) gas flow rate (2) growth temperature (3) substrates used and (4) the precursor ratio of M:X powder (where M = Mo, W and X = Se, S etc.). The monolayer triangles of TMDCs are formed when the precursor ratio i.e. M:X was kept (1:2). Upto this time, CVD technique has been effectively employed to grow various TMDC's films such as MoS₂, MoSe₂, h-BN, WS₂, SnSe₂ and so on.⁶⁻⁹ The large area growth of some 2D materials has been achieved holding the great promise for practical applications. The main challenge is how to grow these materials on arbitrary substrates to avoid the complicated transfer process.

2.1.5 Wet Chemical Synthesis

This method includes hydrothermal/solvothermal, templated synthesis, and soft colloidal synthesis. In this method, the reactions are carried out with different precursors at certain experimental conditions. This method has been established to remain operative for the preparation of various nanostructures of 2D materials like single layer graphite, MoS₂, SnS₂, MoSe₂, and VS₂ and so on.¹⁰⁻¹² The advantage of this method is it allows to produce high yield with low cost also easy to control dimension and nature of the synthesized nanomaterials. There are few parameters such as reaction temperature, reaction time, precursor's concentration and solvent which decides the final product. In this case, it is difficult to produce single layers of 2D materials because any of the reaction parameter affects the product.

2.2 Device Fabrication

2.2.1 Field Emission Study

The term field emission is defined as “the emission of electrons from the surface of a condensed phase into vacuum in the presence of high electric field”. This phenomenon i.e. extraction of electrons from the surface of solid was first observed by W. Wood in 1897.¹³ The FE is the

quantum mechanical phenomenon, where electrons cross the potential barrier due to high field of $\sim 10^7$ V/cm in the metal or semiconducting materials. In FE, we measure emission current (I) and electric potential (V) applied between the anode and cathode. These measured quantities are related to current density (J) and electric field (E) through following equations (1) and (2) respectively,

$$J = IA \quad \dots\dots (1)$$

$$E = \beta V \quad \dots\dots (2)$$

Where, A is the emitter area and β is the field enhancement factor. The modified Fowler-Nordheim (F-N) theory¹⁴ was used to characterize the dependence of emission current density over applied field (J-E) which is given in equation (3),

$$J = \lambda_M a \phi^{-1} E^2 \beta^2 \exp\left(-\frac{b \phi^{\frac{3}{2}}}{\beta E} v_F\right) \quad \dots\dots (3)$$

The field enhancement factor (β) depends upon the emitter geometry and it is expressed as, $\beta = h/r$, where h is the height and r be the radius of the curvature of the tip surface. The important aspects of the material to be a potential candidate as an emitter are:

- 1) It should possess low turn on field: It is defined as “the field required to withdraw a current density of $1 \mu\text{A}/\text{cm}^2$ ”.
- 2) It should achieve high emission current density at lower operating field
- 3) It should provide highly stable emission current over a long period of time.

The details about the FE measurements and the FE system described below:

All the FE measurements were carried out at room temperature in the planer “Diode” assembly in an all metal ultrahigh vacuum (UHV) chamber at a base pressure of $\sim 1 \times 10^{-8}$ mbar. A typical ‘diode’ configuration consists of a phosphor coated semitransparent screen as an anode. This

assembly also referred as close proximity configuration where, anode and cathode are held parallel to each other with small separation. In order to investigate the FE properties, 2D nanosheets were sprinkled onto a piece of carbon tape ($0.3 \text{ cm} \times 0.3 \text{ cm}$). The carbon tape was then pasted onto a copper rod holder (diameter $\sim 50 \text{ mm}$), which acted as a cathode.

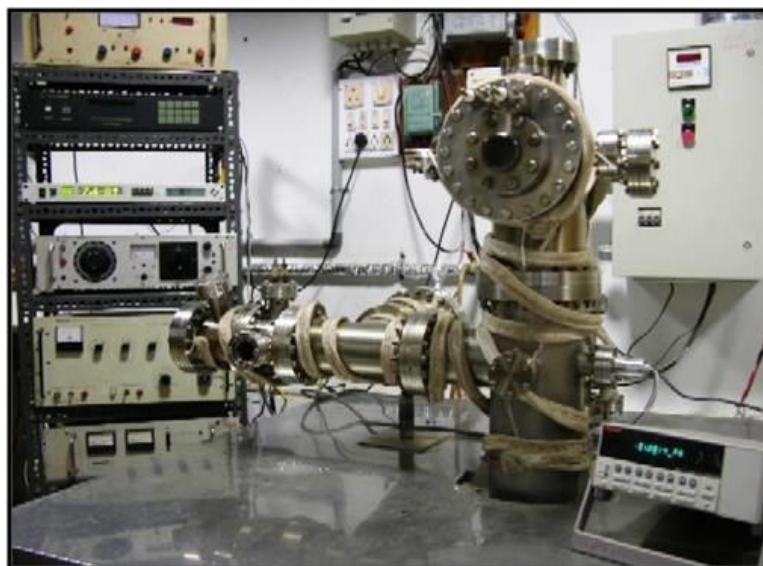


Figure 2.4: UHV Field emission measurement system.

The FE investigations are performed in planar diode configuration under ultra-high vacuum (10^{-8} mbar) with anode-cathode separation of 0.2 cm. The emission current density - applied field and I-t measurements were carried out using Keithley (6514) electrometer by sweeping DC voltage applied to cathode with a step of 40V (0 - 40 KV, Spellman, U.S.). The field emission current stability was recorded at present current value of $1 \mu\text{A}$ using computer controlled data acquisition system.

2.2.2 Transistor Device Fabrication

The FET is a device where, charge flowing through it is governed with the help of applied electric field. Basically, it is a three terminal device consists of source, drain and gate. The region where output current flows from the material is positioned among source and drain called as channel. These FET's can be divided into two types based on the type of majority

charge carriers considered as n-channel or p-channel FET's. The type i.e. (n-channel/p-channel) can be evaluated with the help of transfer and output curves of the device. In 1926,¹⁵ the early concept about FET was outlined in paper published by Lilienfield and the second by Heil in 1935.¹⁶ The method/principle proposed by Lilienfield the first metal-oxide-semiconductor (MOS)FET was invented at the Bell laboratory in 1959. It is well known that FET's form the basis of electronic components market such as MOS integrated circuits, photodetectors and biosensors. As predicted in Moore's law (1965) the size of the fabricated FET's are scaled down over several decades. Therefore, investigators are mostly centering on expansion of additional highly-integrated chips with lesser FETs. The FET's fabricated from traditional approaches faces major difficulties such as high leakage current and instability of the device due to surface roughness that inhibits industry from upholding the rate of development. In order to achieve high performance and device downscaling process 2D materials such graphene, TMDCs, BP are being used. The 2D materials with thickness control, ease of fabrication and dangling bond free surfaces makes them potential candidate in nanoelectronic devices when compared with other materials.

There are several performance parameters which supports to the evaluation of FET devices and these are described below:

Contrast (on/off) ratio: It is obtained by dividing ON state and the OFF state output currents. The factor which affects the on/off ratio is the leakage current. A higher contrast ratio indicates a more efficient ON/OFF operation within the FET.

Field Effect mobility (μ): It characterizes how fast charge carriers move under the application of electric field. The field effect mobility can be calculated from the following equation (4),

$$\mu_{FE} = \frac{dI_D}{dV_G} \left[\frac{L}{WC_i V_D} \right] \dots\dots (4)$$

Where, d_{ID}/d_{VG} is the transconductance, C_i is capacitance of SiO_2 , V_D represents drain voltage, L and W signifies the length and width of the channel. Transconductance is the term used to relate the current flowing through output of the device to the voltage across input of a device. The reciprocal of the resistance gives the value of conductance and it is denoted by symbol 'S'. The mobility factor can be improved by doping the materials with metal nanoparticles through chemical doping. In addition to this novel methods have been reported to achieve low cost FET with high transmittance of the device.^{17,18} The performance of the FET device can be enhanced by combining h-BN with high *k-dielectric* HfO_2 in insulating materials. The role of h-BN here is to minimize the surface roughness of the channel and dielectric HfO_2 is used to enhance the effective gate capacitance.¹⁹ The 2D TMDCs possesses similar lattice parameter for few compounds such as MoS_2 , WS_2 , MoSe_2 , WSe_2 and are thus suitable for heterostructures formation.²⁰ The p-n junctions formed through these heterostructures are imperative physical devices for the construction of different kinds of FETs.

Sub Threshold swing: It is an importance measure of the performance of the FET device as it controls the ratio between on-state current and off-state current. It is also defined as the change in the gate voltage (V_G) required to change the drain current (I_{DS}) by one order of magnitude. The formula for sub threshold swing is given in equation (5),

$$S = n \left(\frac{KT}{q} \right) \ln(10) \quad \dots (5)$$

Where, KT be the thermal voltage, q be the charge and n is the ideality factor. The sub threshold swing plays vital role in achieving high on/off ratio at low power supply voltage which is limited by diffusion of charge carriers and is ≥ 60 mV/dec at room temperature. Further, lowering the sub threshold swing value would results in decrease of the power supply voltage, energy dissipation and minimum energy point voltage for ultralow power circuits.

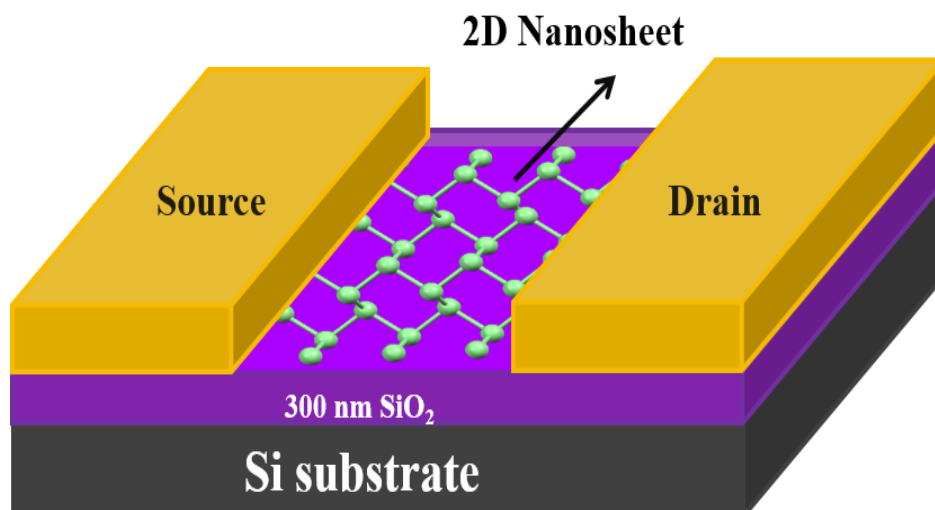


Figure 2.5: Schematic of the FET device.

For device fabrication, the optical lithography technique was employed to fabricate FET device, on which Ti/Au (30 nm/70 nm) metals was deposited on the patterned electrodes by thermal evaporator. The 2D nanosheet samples were then drop casted onto the electrode. The devices were then subsequently heated at 200°C in the presence of Ar environment to 2h. The electrical characterization of the devices was carried using Keithley 4200 semiconductor analyzer.

2.2.3 Humidity Sensor

It is basically a device that senses and answers to several kind of input from the surrounding environments and converts into signal that is compatible with electronic circuits. The input signal may be in the form of water vapor, light, gas molecules, heat and many other. The present section deals with the humidity sensor, photodetector and their fabrication process.

General Background

In the recent years, humidity has gained much interest in various fields such as agriculture, industry and some domestic applications though it is common component in the environment.²¹⁻²³ The humidity sensor with different working conditions and mechanisms have

been investigated so far in order to sense humidity/water vapors. The key requirements for the material to be excellent humidity sensor are excellent sensitivity, quick response, good reproducibility, resistant to impurities, simple structure and low cost. The term *humidity* represents the amount of water vapor in the atmosphere /gas, it plays vital role in the well-being of humans or animals. Humidity consists of two types' absolute humidity and relative humidity, in this sections we focus on relative humidity. Absolute humidity is defined as "It is a measure of water vapor in the air" and it is expressed as grams per cubic metre.

Relative humidity is the "ratio of amount of water vapor in the air to the greatest amount possible at the same temperature". It is expressed in terms of percentage and temperature is taken into consideration. Humidity sensor is a device which responds to humidity/water vapor present in the atmosphere and converts it into electrical properties. The humidity sensors are classified into two main types i.e. resistive and capacitive respectively. In the resistive type, resistance of the sensor changes due to adsorption of water molecules on the surface of materials. The capacitive type consists of two metal electrodes separated by thin layer of nonconducting film. The water vapors/molecules adsorbs on the film also the molecules makes contact with the metal electrodes it leads to voltage change which then gives rise to change in the capacitance. The resistive type sensor also divided into two groups i.e. electronic and ionic. In case of ionic type, as humidity increases resistance of the device decreases and the parameters which affects the performance are microstructure and intrinsic impedance of the materials. However, in electronic type-the resistance of the device increases/decreases depending upon the type of semiconductor whether it is *n-type* or *p-type*. The performance parameters of any type of humidity sensor is characterized by sensitivity, response and recovery time, stability and selectivity.

Performance parameters:

- 1) **Sensitivity:** It is ratio of variation in the electrical resistance of a sensor material upon exposure to relative humidity to the resistance of the sensor in low humidity. The formula for the sensitivity presented in equation (6),

$$S = \left(\frac{R_H - R_L}{R_L} \right) \dots\dots (6)$$

Where, R_H be the resistance in high humidity and R_L be the resistance in low humidity.

- 2) **Response Time:** It is defined as the time required by the device to attain 90% of its saturation value of resistance upon exposure to relative humidities.
- 3) **Recovery Time:** The time taken by the sensor to return to 90% of its baseline resistance value upon exposure to lower humidity.
- 4) **Stability:** The ability of a sensor to produce reproducible results for a long period of time without showing a drift in the sensor performance.

Preparation of salt solutions with Relative Humidity:

The response of the device as a function of RH was performed by introducing the device inside the closed RH levels. We used saturated salt solutions of lithium chloride, magnesium chloride, potassium carbonate, sodium bromide, potassium iodide, sodium chloride, potassium chloride and potassium sulfate in order to attain various RH environments. These saturated salt solutions possess approximate relative humidities of 11%, 32%, 43%, 57%, 69%, 75%, 85% and 97% respectively.

Fabrication of the Devices

The ITO (Indium Tin Oxide) substrate was used to fabricate sensing devices (humidity and gas). Initially, we made scratch at the centre on the conducting surface with the help of glass cutter with separation between source and drain were $\sim 100\mu\text{m}$. The contacts were made using silver paint. For device preparation the as synthesized powder sample was dispersed into the ethanol and then ultrasonicated for 10 min, and subsequently drop casted between the source

and drain. The devices were subsequently annealed in vacuum furnace at 200°C to improve the contact resistance.

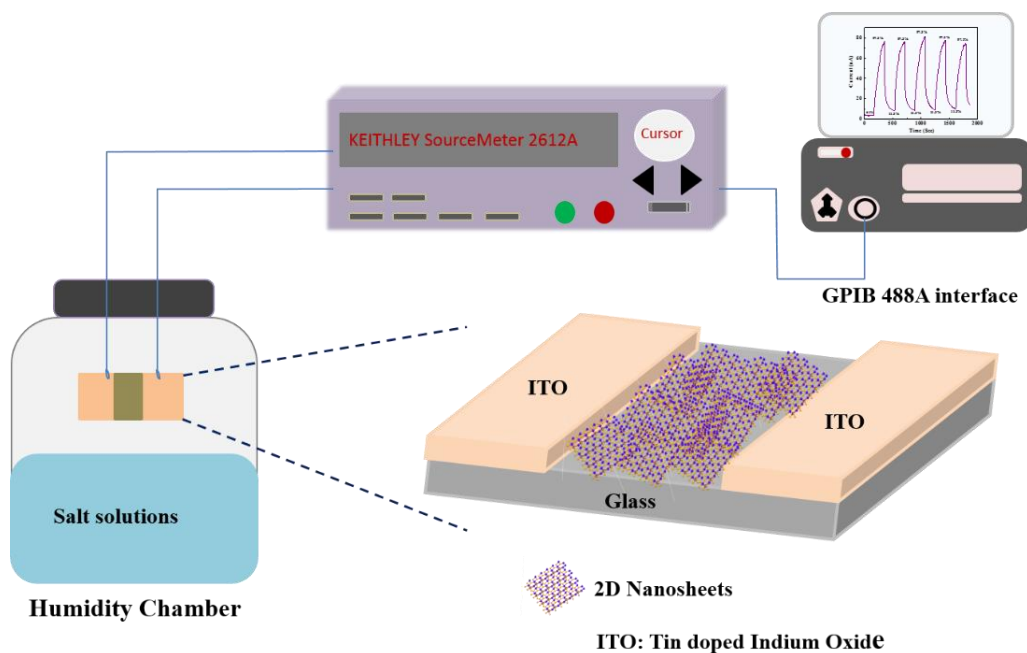


Figure 2.6: Schematic of the experimental set up for measurement of humidity sensor.

The Keithley 2612A system source meter was used to perform all the electrical characterizations. The source meter was connected to a computer via GPIB 488A interface. The experimental set up used for the humidity sensor purpose shown in Figure 2.6.

NH₃ Sensing test

The NH₃ gas which we used for test was 1% NH₃ balanced by 99% N₂ cylinder purchased from Vadilal Chemical Ltd (Pune, India). The gas was then injected into chamber through mass flow controllers to control the NH₃ gas flow rate which was varied from 20 sccm to 100 sccm. All the sensing measurements were performed at room temperature and at atmospheric pressure.

2.2.4 Photodetection

Photodetector is the device that converts incident light into an electrical signal. Like, FET's Photodetectors are fundamental components in the present miniaturized electronic industry.^{24,25}

The photodetectors which operate from visible to near-infrared wavelength are widely utilized in various applications such as optical communications system and biomedical imaging.^{26,27}

The detection of ultraviolet light can be used in environment monitoring, space science, territory intrusions and military reconnaissance. Since the discovery of graphene in 2004 by A. K. Geim and K. S. Novoselov, the 2D materials have attracted great deal of attention in photodetector application due to strong light-matter interactions, thickness dependent bandgap, high transparency and excellent charge carrier mobility. There are different types of photodetectors available: Photodiode, Phototransistors, Photoconductors, Photomultipliers and pyroelectric detectors.

Photodiode: It is a semiconductor p-n junction device which converts light into electric signal, it generally operates in reverse bias mode and intrinsic layer is present between the p and n region. When the photon with high energy incident on depletion region, electrons gets released from the atom results into the formation of electron hole pairs. The depletion energy will have built in electric field which moves e-h away from the junction gives rise to photocurrent

Phototransistor: It is a semiconductor device that detects light and modify the current flowing among the emitter and collector according to the level of light it takes. In this case, when light falls on the base of the phototransistor will induce a small current, which is then amplified by normal transistor action results in considerably large amount of current. The phototransistor device provide a current i.e. 50 to 100 times that of photodiode.

Photoconductors:

When the light falls upon the semiconductor material part of the light gets absorbed, transmitted and scattered. If the photon with energy equal or greater than the bandgap of the semiconductor material (e-h) pairs get produced. These (e-h) pairs can be parted through the application of

electric field through external supply which causes electrons and holes to be transported. This results in generation of photocurrent of the device.

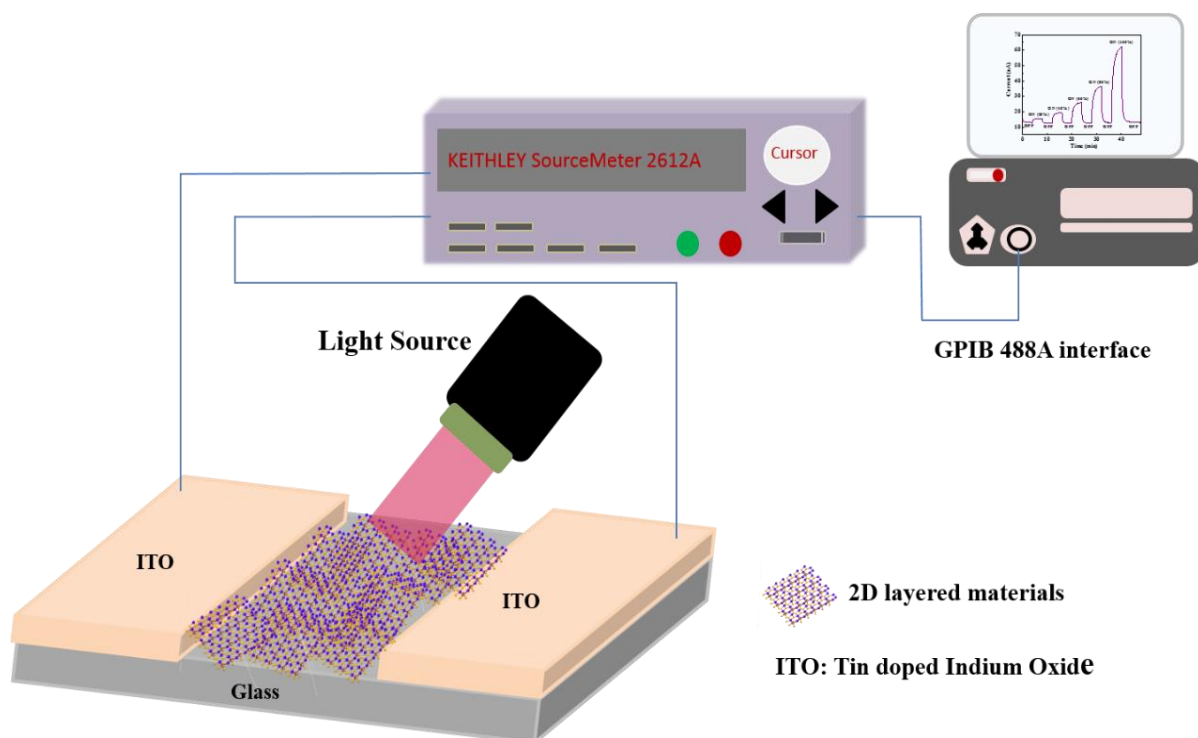


Figure 2.7: Schematic of the experimental set up for measurement of photodetector.

The work presented in this thesis on 2D materials based photodetectors is more on photoconductive sensors. To investigate the photodetection property we used HAMAMATSU (Model name: L9566-01A-02) UV light source. All the measurements were carried out at room temperature and in identical conditions. Figure 2.7 shows the experimental set up used for the photodetector study.

Pyroelectric Detectors: These are the sensors generally used to detect infrared light and works on the phenomenon called pyroelectric effect. Such detectors do not respond directly to light but only to the produced heat. These detectors has many applications in fire detection, satellite based infrared detection and it also shows broader spectral response in energy meters compared with the photodiode.

Photomultipliers: Basically, it is a photomultiplier tube (PMT) that converts incident light into an electrical signal. The basic working principle is explained here: When light enters PMT it passes through input window and strikes photocathode. The electrons gets excited from photocathode into vacuum and are accelerated and focused by the focusing electrodes onto the dynode. These electrons are then multiplied by means of secondary electron emission at each successive dynodes. The multiplied secondary electrons emitted from the last dynode are collected at the anode. These PMTs require devoted optimization for the use in cryogenic detector.

The performance of the fabricated photodetector is characterized by various parameters and the decisive performance parameters are listed below:

- 1) **Photoresponsivity:** Photoresponsivity is the output signal of the detector produced in response to given incident radiant power. It is the ratio of photocurrent generated to the power density of light. The modified definition for the responsivity when it includes the frequency and wavelength dependence termed as spectral responsivity. The photoresponsivity can be calculated using equation (7),

$$R = \frac{I_p}{P} \quad \dots\dots (7)$$

Where, R be the photoresponsivity, I_p presents generated photocurrent and P be the power density of incident light.

- 2) **Quantum Efficiency:** The ability of the detector to convert incident photons into electrons is termed as quantum efficiency. It is the ratio of number of electrons produced per incident photons. The expression for the quantum efficiency is given in equation (8),

$$\eta = R \left(\frac{hc}{e\lambda} \right) \quad \dots\dots (8)$$

Where, η be the quantum efficiency, R be the photoresponsivity, λ be the wavelength and e be the charge of the electron.

- 3) **Detectivity:** It is important parameter used to characterize the performance of the detector, if this factor is larger it is more appropriate for identifying weak signals. It is the reciprocal of noise-equivalent power and shown in equation (9),

$$D = \frac{1}{NEP} \quad \dots\dots (9)$$

The specific detectivity is the ratio of square root of the detector area to the noise equivalent power and denoted as D^*

$$D^* = \frac{\sqrt{A}}{NEP} \quad \dots\dots (10)$$

2.3 Characterization Techniques

With this knowledge in hand, we have synthesized various 2D materials and characterized them with the help of microscopic and spectroscopic techniques. These characterization techniques are used for gathering structural, morphological optical and chemical states information associated with the 2D materials. The characterization techniques utilized are listed below:

2.3.1 Powder X-Ray Diffraction

The XRD is widely used to study the crystal structure and phase of the materials. The diffraction pattern is obtained from the X-Ray beam which is incident on the sample under investigation. It gives diffraction pattern for the bulk material of crystalline solid rather than a single crystal. The diffraction pattern determines the purity of the sample as well as the composition of any impurities present. When the monochromatic X-Ray beam incident on the crystalline solid, part of the light gets diffracted and interfere constructively or destructively as per the atomic arrangements present in the material. In crystalline solid, atoms are arranged in highly ordered structure hence they interfere constructively means waves are in phase and there will be some resultant energy leaving behind the solid crystal. The constructive interference

occurs only when the path difference is an integral multiple of wavelength (λ) known as Bragg's law of diffraction. The Bragg's law is represented by the equation (11),

$$2d \sin \theta = n\lambda \quad \dots (11)$$

Where, d be the interplanar distance between the two planes, θ is the incident angle, λ be the wavelength of X-Ray and n is an integer. The intensities of diffracted rays are plotted as a function of angle θ and obtained diffraction pattern is used to identify the crystal structure of the sample. The Bragg's equation is used to derive Scherer's formula and shown in equation (12),

$$t = \frac{k\lambda}{\beta \cos \theta} \quad \dots (12)$$

Where, t be the crystallite size, k be the constant depends on the crystalline shape, and β is FWHM of the peak. This width of the diffraction peak is used to calculate the crystallite size using Scherer's equation. This equation is useful for the identification of crystal phase and to observe the growth and development of the nanocrystallites.

2.3.2 Raman Spectroscopy

Raman spectroscopy is very powerful and nondestructive technique to characterize structural, optical and mechanical properties of the 2D layered materials. It is based on the inelastic scattering of light with matter also capable of probing amorphous and crystalline solids. When the light incident on the sample, part of the light gets absorbed, transmitted and scattered from the materials. The scattered light consists of two type i.e. elastic and inelastic scattering. In case of elastic scattering the energy of incident light is same as that of emitted photon with different direction also known as Rayleigh scattering. The intensity of the Rayleigh scattered light is usually in the range of 0.1% to 0.01% to that of radiation source. The inelastic scattering also termed as Raman scattering where, energy of the emitted photons is different or lower than the energy of the incident photons. It is divided into two parts i.e. Stokes scattering and Anti-Stokes

scattering. The Figure 2.8 presents the various states involved in the Raman spectroscopy through energy level diagram.

Stokes Scattering: If the molecule in the final vibrational state is more energetic than the initial state, then the emitted photon shifts to lower energy and the shift is known as Stokes shift.

Anti-Stokes Scattering: If the molecule in the last vibrational state is less energetic than the first state, then the emitted photon shifts to upper energy and the shift is known as Anti-Stokes shift.

In this study, our interest is to collect the intensity of the Raman scattered light which is determined by the change in polarizability. This intensity is then collected by the detector which is plotted as a function of wavenumber and is proportional to its momentum in units of reciprocal centimeters. The observed peaks in the Raman spectrum are attributed to the number of symmetry allowed Raman active modes.

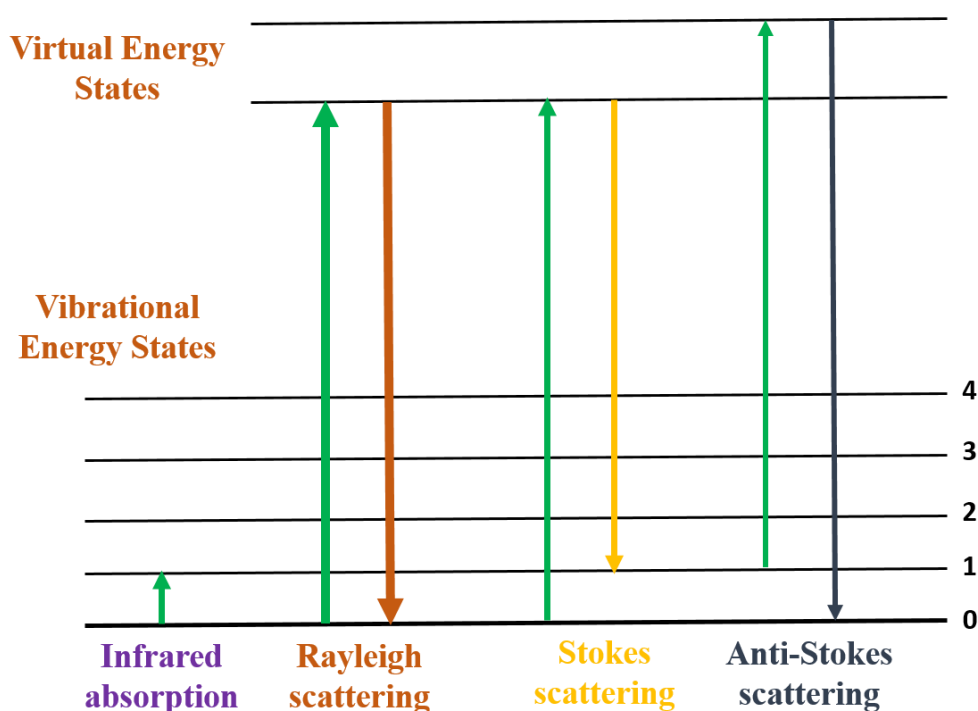


Figure 2.8: Energy level diagram showing various states involved in the Raman Spectroscopy.

The peak in the Raman spectra relates to one or more vibrational modes of the solid. It provides very useful information including strength of interatomic and intermolecular bonds,

mechanical strain in a solid, composition of multicomponent matter and degree of crystallinity of solid. It employs the Raman Effect for substances analysis including solid, liquid and gases. Through this technique, highly complex materials such as biological organisms and human tissue can also be analyzed.

2.3.3 X-Ray Photoelectron Spectroscopy

In 1960s the first XPS was developed by Siegbahn and his research group and later in 1981, he was awarded with Nobel Prize in Physics for his work with XPS. This technique is used to perform surface analysis of the materials and accomplished by irradiating sample with monochromatic X-Rays and further analyzing energy of the emitted electrons. These photons have limited penetrating power of the order of 1-10 μm in a solid which then interacts with the atoms presents in the surface region causing electrons to be emitted by the photoelectric effect. The maximum kinetic energy associated with these emitted photons given by the equation (13),

$$K.E. = h\nu - B.E. - \phi \quad \dots (13)$$

Where, $h\nu$ be the energy of the photon, B.E. is the binding energy of the atomic orbital from which the electrons originates and ϕ be the workfunction of the spectrometer. As we all know that, XPS is an ultra-high vacuum technique so the sample to be analyzed has first to be evacuated. In general, when sample is irradiated with X-Rays (~ 1.5 keV), the electrons absorbs enough amount of energy and gets ejected from the sample with certain kinetic energy. The energy of the ejected electrons is then detected by the detector and plotted as a function of number of electrons produced. The energy required to eject the electrons which are farther from nucleus is less and hence binding energy is lower for higher orbitals. This techniques is widely used to determine the elemental composition, oxidation states, overall electronic structure and thickness of the film. The materials such as inorganic compounds, metal alloys, semiconductors, polymers, catalysts, glasses and ceramics are also analyzed using XPS technique.

2.3.4 UV-Visible Spectroscopy

The UV-Vis spectroscopy is used to obtain the qualitative and quantitative information about the given compound or molecule. It allows us to measure how much a given compound absorbs light and it is carried out by measuring the intensity of light that passes through the sample w.r.t. the intensity of the light from reference sample. This spectrophotometer measures the amount of light transmitted through the sample given by Beer-Lambert's law in equation (14),

$$I = I_0 e^{-\epsilon cl} \quad \dots (14)$$

Where, I be the transmitted light intensity, I_0 be the incident light intensity, ϵ be the molar absorptivity, c be the sample's concentrations and l is the cuvette path length. The UV-Vis spectrophotometer consists of light source (Deuterium or tungsten lamp), a monochromator (diffraction grating) and detector (PMT's or photodiodes). When light passes through the sample, the material absorbs energy and part of the light gets transmitted. The transmitted light from the sample further reaches to the detector which then records the intensity of the transmitted light. The major use of the instrument is to investigate the optical properties of the materials.

2.3.5 Atomic Force Microscopy

This tool is very helpful for the measurement of the thickness and surface roughness of the sample with very high resolution on the order of fractions of nm. It also provides various types of surface measurements such as force measurement, topographic imaging and mechanical properties to the needs of scientists and engineer. AFM consists of cantilever with a very sharp tip to scan over a sample surface and detector. In general, AFM works in three different modes having unique advantages and disadvantages: contact mode, non-contact mode and tapping mode. The working principle of AFM divides into three steps:

- 1) Surface sensing: As the cantilever tip approaches the surface of the material, the attractive force between the surface and the tip cause the cantilever to deflect near the

surface. When the cantilever is brought even closer to the surface, such that the tip makes contact with it, repulsive force becomes dominant and causes the cantilever to deflect away from the surface.

- 2) Detection of cantilever deflection: The deflection in the cantilever are detected with the help of Laser beam by reflecting an incident beam off the flat top of the cantilever. The slight deflection in the cantilever causes change in the direction of the reflected beam and this minor change is monitored through position-sensitive photodiode (PSPD). Hence, when AFM tip approaches close to the sample surface, the subsequent cantilever deflection is recorded by PSPD detector.
- 3) Imaging: At last, with PSPD information AFM generates accurate topographic map of the surface by using a feedback loop to control the height of the tip above the surface- thus maintaining constant laser position.

2.3.6 Scanning Electron Microscopy

The SEM provides information about surface morphology, chemical composition and crystalline structure of the materials. It uses a focused beam of high-energy electrons to produce a different kinds of signals at the surface of solid sample. These signals consists of secondary electrons, back scattered electrons (BSEs), X-Rays, auger electrons and visible light. The secondary electrons are used for the imaging purpose while BSEs give rapid phase discrimination of the sample. The secondary electrons originates due to inelastic interaction between the electron beam and the sample whereas, BSEs are reflected back after elastic interaction between the electron beam and the sample. The secondary electrons possess low energy (~50 eV) which confines their mean free path in solid sample. These secondary electrons are detected by the Everhart-Thornley detector. This whole process depends on a raster-scanned primary beam. The number of secondary electrons reaching the detector decides the brightness of the signal/image. Nowadays, modern SEM provide resolution between 1-20

nm and the resolution of present microscope depends on many factors such as electron spot size and interaction volume of the electron beam with the sample.

In addition to this, the chemical/elemental composition present in the material also identified using energy dispersive X-Ray analysis (EDAX) technique in SEM. The energies of the X-rays are characteristic of the difference in energy between the two shells and of the atomic structure of the element from which they are emitted and thus allows the elemental/chemical composition of the specimen to be measured.

2.3.7 Transmission Electron Microscopy

In 1931, German Scientists Max Knoll and Ernst Ruska developed first TEM and thereafter it has become common tool that is used worldwide by scientists and engineers. This technology provides information about the crystalline nature, morphology, structure and stress in given sample. For the operation purpose, it requires very thin specimen (<100 nm) that are semitransparent to electrons. The conventional electron microscopes operates in ultra-high vacuum (10^{-5} torr or less) with thermionic guns capable of accelerating the electrons through a selected potential difference in the range of 40-200 kV. In TEM, the electrons emitted due to thermionic emission are accelerated in the form of electron beam which then transmits through specimen. This transmitted beam is focused by the objective lens into an image on phosphor screen or charge coupled device (CCD) camera. The image strikes the phosphor screen and light is produced, letting the operator to observe the image. The area from which fewer electrons are transmitted appears darker while the lighter areas of the image indicate those areas of the sample that more electrons were transmitted through. It allows researchers to view specimen to the atomic level, which is less than 1 nm and thus TEM has added advantage of greater resolution. The crystallinity of the sample can be studied through SAED pattern, also quality/nature of the prepared material can be analyzed.

This chapter provided the details about various synthesis methods and overview about the nanoelectronic devices and their fabrication. It also explain outcomes of each synthetic approach and the processes involved during the growth of 2D materials. Moreover, it gives background about various devices such as Field Emission, FET, and Photodetector and humidity sensor. It briefly enlighten the various performance parameters which plays pivotal role in deciding the performance of the fabricated nanoelectronic devices.

2.4 References

- 1) Yi, M.; Shen Z. A. review on mechanical exfoliation for the scalable production of graphene. *J. Mater. Chem. A* **2015**, *3*, 11700.
- 2) Novoselov, K. S.; Geim, A. K.; Morozov, S. V.; Jiang, D.; Zhang, Y.; Dubonos, S. V.; Grigorieva, I. V.; Firsov, A. A. Electric field effect in atomically thin carbon films. *Science* **2004**, *306*, 666-669.
- 3) Nicolosi, V.; Chhowalla, M.; Kanatzidis, M. G.; Strano, M. S.; Coleman, J. N. Liquid exfoliation of layered materials. *Science* **2013**, *340*, 1226419.
- 4) Dines, M. B. Lithium intercalation via n-butyllithium of the layered transition metal dichalcogenides. *Mater. Res. Bull.* **1975**, *10*, 287.
- 5) Viculis, L. M.; Mack, J. J.; Mayer, O. M.; Hahn, H. T.; Kaner, R. B. Intercalation and exfoliation routes to graphite nanoplatelets. *J. Mater. Chem.* **2005**, *15*, 974-8.
- 6) Reina, A.; Jia, X.; Ho, J.; Nezich, D.; Son, H.; Bulovic, V.; Dresselhaus, M. S.; Kong, J. Large area, few-layer graphene films on arbitrary substrates by chemical vapor deposition. *Nano Lett.* **2008**, *9*, 30.
- 7) Lee, Y. H.; Zhang, X. Q.; Zhang, W.; Chang, M. T.; Lin, C. T.; Chang, K. D.; Yu, Y. C.; Wang, J. T.; Chang, C. S.; Li, L. J.; Lin, T. W. Synthesis of large-area MoS₂ atomic layers with chemical vapor deposition. *Adv. Mater.* **2012**, *24*, 2320.
- 8) Song, L.; Ci, L.; Lu, H.; Sorokin, P. B.; Jin, C.; Ni, J.; Kvashnin, A. G.; Kvashnin, D. G.; Lou, J.; Yakobson, B. I.; Ajayan, P. M. Large scale growth and characterization of atomic hexagonal boron nitride layers. *Nano Lett.* **2010**, *10*, 3209.
- 9) Wang, X.; Li, Y.; Zhuo, L.; Zheng, J.; Peng, X.; Jiao, Z.; Xiong, X.; Han, J.; Xiao, W. Controllable growth of two-dimensional WSe₂ using salt as co-solvent. *CrystEngComm*, **2018**, *20*, 6267.

- 10) Yoo, D.; Kim, M.; Jeong, S.; Han, J.; Cheon, J. Chemical synthetic strategy for single-layer transition-metal chalcogenides. *J. Am. Chem. Soc.* **2014**, *136*, 14670.
- 11) Mahler, B.; Hoepfner, V.; Liao, K.; Ozin, G. A. Colloidal synthesis of 1T-WS₂ and 2H-WS₂ nanosheets: applications for photocatalytic hydrogen evolution. *J. Am. Chem. Soc.* **2014**, *136*, 1412.
- 12) Choucair, M.; Thordarson, P.; Stride, J. A. Gram-scale production of graphene based on solvothermal synthesis and sonication. *Nat. Nanotechnol.* **2009**, *30*.
- 13) Wood, R. W. A new form of cathode discharge and the production of X-rays, together with some notes on diffraction. Preliminary communication. *Phys. Rev.* **1897**, *5*, 1.
- 14) Forbes, R.G. Use of a spreadsheet for Fowler-Nordheim equation calculations, *J. Vac. Sci. Technol. B: Microelectron. Nanom. Struct.* **1999**, *17*, 534.
- 15) Edgar, L.J. Method and apparatus for controlling electric currents. *U.S. Patent 1*, **1930**, 745,175.
- 16) Heil, O. Improvements in or relating to electrical amplifiers and other control arrangements and devices. *British Patent*, **1935**, 439, 10.
- 17) Schmidt, V.; Riel, H.; Senz, S.; Karg, S.; Riess, W.; Gösele, U. Realization of a silicon nanowire vertical surround-gate field-effect transistor. *Small* **2006**, *2*, 85.
- 18) Di, C. A.; Wei, D.; Yu, G.; Liu, Y.; Guo, Y.; Zhu, D. Patterned graphene as source/drain electrodes for bottom-contact organic field-effect transistors. *Adv. Mater.* **2008**, *20*, 3289.
- 19) Roy, T.; Tosun, M.; Kang, J. S.; Sachid, A. B.; Desai, S. B.; Hettick, M.; Hu, C. C.; Javey, A. Field-effect transistors built from all two-dimensional material components. *ACS Nano* **2014**, *8*, 6259.
- 20) Xie, L. M. Two-dimensional transition metal dichalcogenide alloys: preparation, characterization and applications. *Nanoscale* **2015**, *7*, 18392.

- 21) Kulwicki, B. M. Humidity sensors. *J. Am. Ceram. Soc.* **1991**, *74*, 697.
- 22) Yamazoe, N.; Shimizu, Y. Humidity sensors: principles and applications. *Sens. Actuators*, **1986**, *10*, 379.
- 23) Seiyama, T.; Yamazoe, N.; Arai, H. 1983. Ceramic humidity sensors. *Sens. Actuators*, **1983**, *4*, 85.
- 24) Liu, H. C.; Song, C. Y.; SpringThorpe, A. J.; Cao, J. C. Terahertz quantum-well photodetector. *Appl. Phys. Lett.* **2004**, *84*, 4068.
- 25) Assefa, S.; Xia, F.; Vlasov, Y. A. Reinventing germanium avalanche photodetector for nanophotonic on-chip optical interconnects. *Nature* **2010**, *464*, 80.
- 26) Koppens, F. H. L.; Mueller, T.; Avouris, P.; Ferrari, A. C.; Vitiello, M. S.; Polini, M. Photodetectors based on graphene, other two-dimensional materials and hybrid systems. *Nat. Nanotechnol.* **2014**, *9*, 780.
- 27) Li, J.; Niu, L.; Zheng, Z.; Yan, F. Photosensitive graphene transistors. *Adv. Mater.* **2014**, *26*, 5239.

Chapter 3

Ultra-thin V₂O₅ Nanosheet based Humidity Sensor, Photodetector and its Enhanced Field Emission Properties

The paper based on this chapter is published in RSC Advances

M. Pawar et al. *RSC Adv.* **2015**, *5*, 88796.

3.1 Introduction

Since the invention of graphene, atomically thin 2D materials have attracted enormous interest because of their unique electrical, optical and mechanical properties in device applications^{1,2}. The 2D materials such as graphene, MoS₂, WS₂, MoSe₂, WSe₂, Black Phosphorous⁵⁸ etc. and metal oxides materials such as MoO₃, WO₃, MnO₂ were invented for various applications including humidity sensor³⁻⁸, photodetector⁹⁻²³, transistor²⁴, gas sensor^{25,26}, solar cell⁴³⁻⁴⁶, supercapacitor⁴⁷⁻⁵⁰, catalyst for water splitting^{51,52}.

Humidity sensors have been developed to measure and monitor the environmental humidity that plays an important role in the agriculture, food as well as medical industry along with human activities²⁷. The layered V₂O₅ is most stable oxide as compared with other oxides of vanadium. It has high surface to volume ratio and high oxidation state at nanoscale geometry; recently nanostructure V₂O₅ has been used in various application including field emission^{29-30, 59-62}, supercapacitor³¹⁻³⁴, Li ion battery³⁵, transistor³⁶, Photodetector³⁷ etc. Various methods of synthesis of V₂O₅ nanostructures have been reported till date including hydrothermal^{28,53,54}, electrospinning^{55,56}, polycondensation method⁵⁷. Among them, hydrothermal method is extensively utilized for the preparation of V₂O₅ nanostructures because of economical and highly pure product. In hydrothermal method morphology of the materials can be tuned by the hydrothermal temperatures which can be kept slightly below the melting point of the reactants and also by varying the concentration of solvents.

The nanostructure V₂O₅ possesses direct bandgap of 2.2 eV to 2.7 eV in the visible light region which inspires to investigate the optoelectronic properties such as photodetection³⁷, optical waveguide³⁹, and high speed photoelectric switches³⁸. In this paper, we report V₂O₅ nanosheet based humidity sensor with superior performance with fast response and recovery time along with the high sensitivity. We also demonstrated the photodetector based on V₂O₅ nanosheet

with fast response time ~ 65 sec and recovery time of ~ 75 sec to UV light. We have also done the field emission measurement for V_2O_5 nanosheets. We achieved turn on field to be 1.15 V/ μm and highest current density of ~ 1532 $\mu\text{A}/\text{cm}^2$ at 3.2 V/ μm with high field enhancement factor of ~ 8580 shows applications in flat panel displays, electron emitter etc.

3.2 Experimental Section

Materials

Commercially available Vanadium (V) Oxide (Sigma-Aldrich, 99.99%) and Dodecylamine ($C_{12}H_{27}N$) (Sigma-Aldrich, $\geq 99\%$) were utilized for the preparation of V_2O_5 nanosheets. For humidity sensing measurements the salts were obtained from the Thomas Baker chemicals Pvt. Ltd. Mumbai (India).

Synthesis of V_2O_5 Nanosheets:

The V_2O_5 nanosheets were prepared using simple hydrothermal method for that 15 mM of V_2O_5 and 7.5 mM of $C_{12}H_{27}N$ were mixed with 5 ml of ethanol stirred for 2 h. To this mixture 15 ml of water was added and stirring was continued for further 48 h, then the mixture was transferred into the 50 ml autoclave which then heated in oven at 180°C for 7 days. The obtained black precipitate was finally washed with ethanol for several times followed by centrifugation and the precipitate was then dried in a vacuum furnace at 80°C for 12 h.

Characterization Details

The structural investigations were carried out from Raman Spectroscopy with Horiba JY Lab HR 800 instrument by Ar laser having $\lambda=632.5$ nm. The spectrometer operated in geometry called the back scattering with detector utilized was synapse CCD detector. The surface morphology were investigated by using FESEM with HITACHI S-4800 instrument and TEM images were captured using FEI TECNAI G2-20 (TWIN, The Netherlands) instrument

operating at 200 KV. A UV-Vis spectrum was recorded using Shimadzu (UV-3600) Plus UV-Vis-NIR Spectrophotometer in the wavelength range 200-1300 nm.

3.3 Results and Discussion

3.3.1 Material Characterization

Figure 3.1(a) shows the typical side view of the V_2O_5 single-layer nanosheets and figure 3.1(b) shows the top view. Figure 3.1(c) shows the typical experimental set-up used for the UV photodetection.

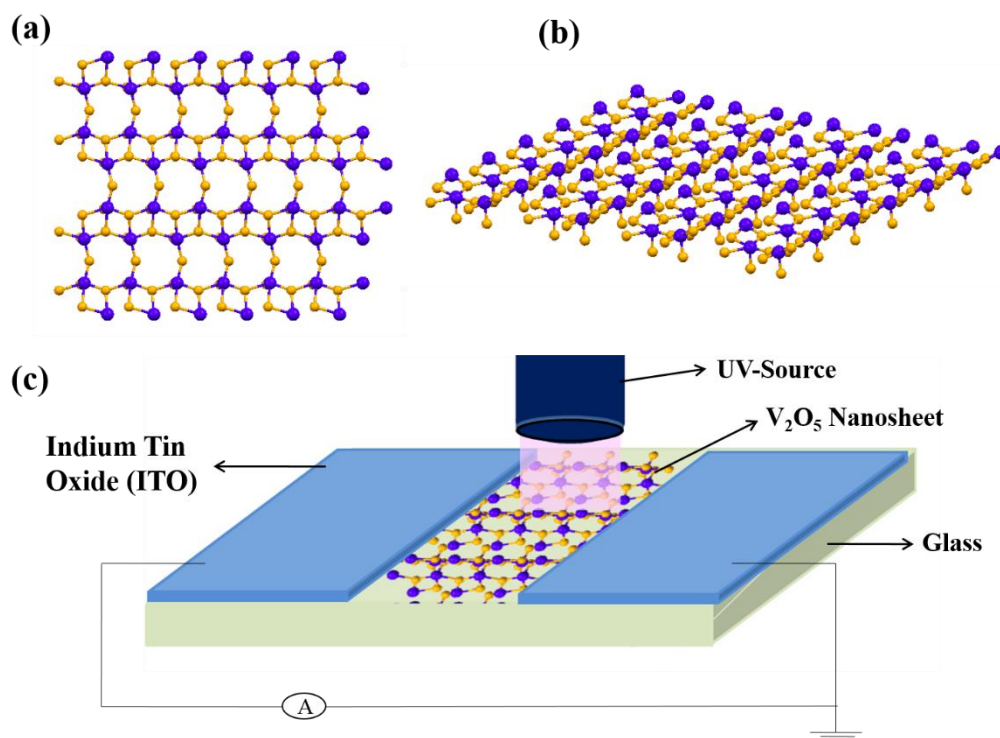


Figure 3.1: Schematics for V_2O_5 nanosheets (a) side view, (b) top view and (c) photodetection experimental set up.

The Raman Spectrum for V_2O_5 nanosheets as well as for the bulk V_2O_5 material were shown in Figure 3.2. The observed Raman spectra for V_2O_5 nanosheets is similar to that reported previously in literature^{28,41-42}. The Raman shift corresponds to different modes of vibrations are 143, 194, 286, 408, 525, 693 and 993 cm^{-1} . The Raman spectra are found to be slightly

down shifted to V_2O_5 nanosheets as compared to the V_2O_5 bulk material due to decrease in interlayer bonding. The Raman mode 993 and 693 cm^{-1} corresponds to the stretching modes of $V=O$ terminal oxygen and V_2-O i.e. doubly coordinated oxygen bonds respectively which is triply coordinated oxygen bonds. The Raman mode observed at 525 cm^{-1} corresponds to the stretching mode of V_3-O i.e. triply coordinated oxygen bonds. The bending vibration of the $V=O$ bonds arises for the 408 and 286 cm^{-1} modes.

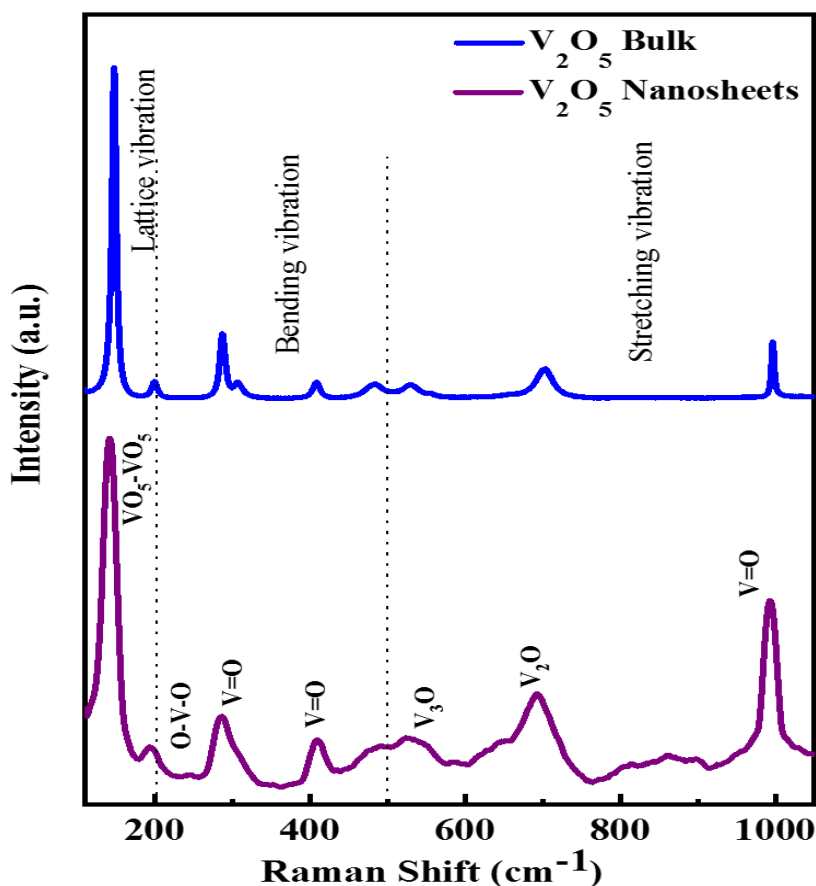


Figure 3.2: Raman spectrum for the as obtained V_2O_5 nanosheets and bulk powder.

The Raman mode frequency 143 and 194 cm^{-1} corresponds to the external VO_5-VO_5 modes. Figure 3.3(a-d) shows the typical FESEM images of the as synthesized V_2O_5 nanosheets which indicates that the high yield of nanosheets synthesized by using hydrothermal method. Typical FESEM images show V_2O_5 nanosheets with lateral dimensions in few tens of micrometer. Figure 3.4(a-f) shows the TEM images of V_2O_5 nanosheets and inset of 3.4(e) shows the

HRTEM image taken from the V_2O_5 nanosheet which depicts the interplanar distance between the two plane is ~ 0.35 nm, which corresponds to (210) plane of the V_2O_5 . The Figure 3.4(f) presents the SAED pattern which exhibits crystalline nature of the V_2O_5 nanosheets.

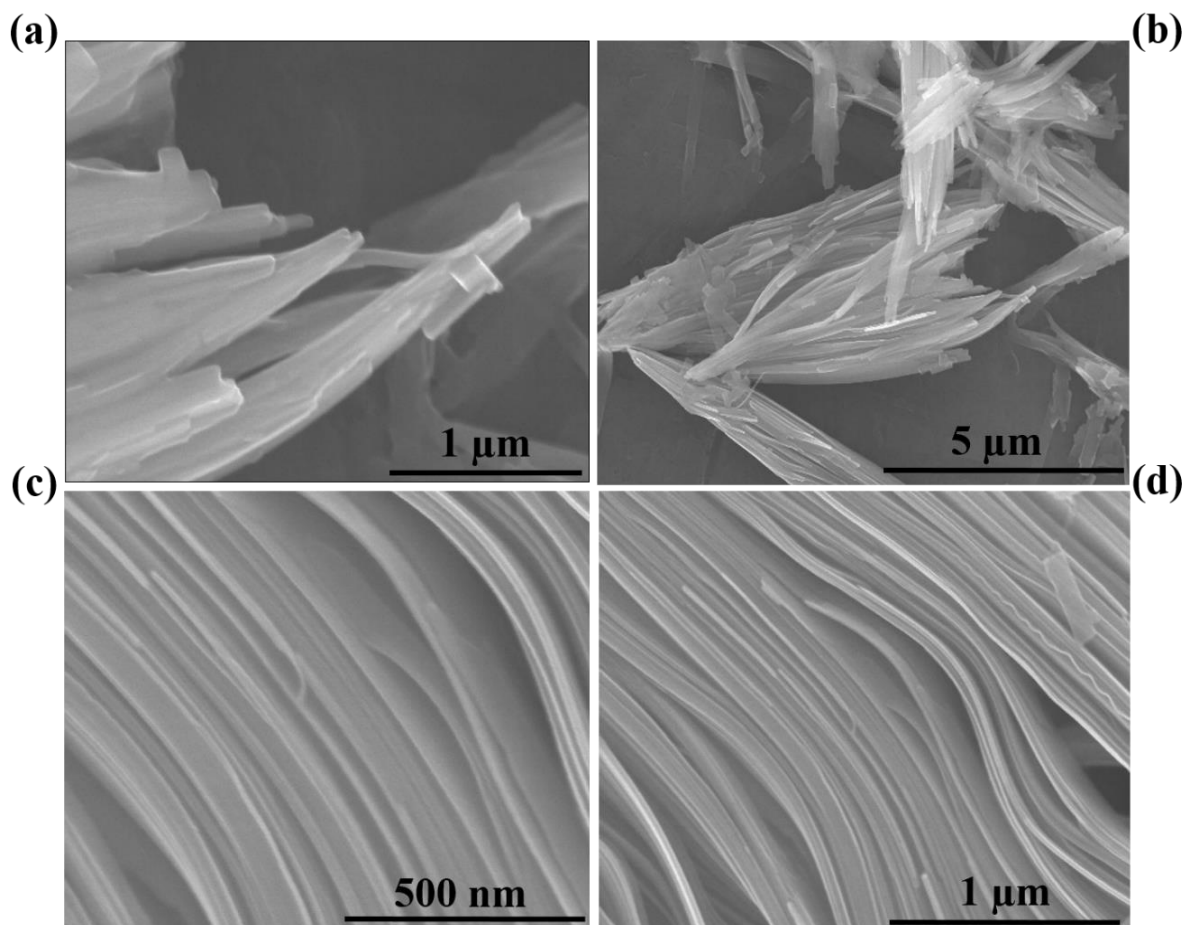


Figure 3.3: (a-d) FESEM images of as synthesized V_2O_5 nanosheets by using hydrothermal method.

To investigate the optical properties of the V_2O_5 nanosheets, we recorded the UV-Vis Spectrum as shown in Figure 3.5. In parallel we also investigated the UV-Vis spectrum for the Bulk V_2O_5 powder. The spectrum represents the major absorption bands for V_2O_5 nanosheets and for V_2O_5 bulk powder are 442 nm and 435 nm respectively. It is well known that the absorption band above 440 nm corresponds to the band gap of V_2O_5 .

3.3.2 Humidity Sensor

The V_2O_5 nanosheets synthesized by using simple hydrothermal method were used to further investigate the humidity sensing performance.

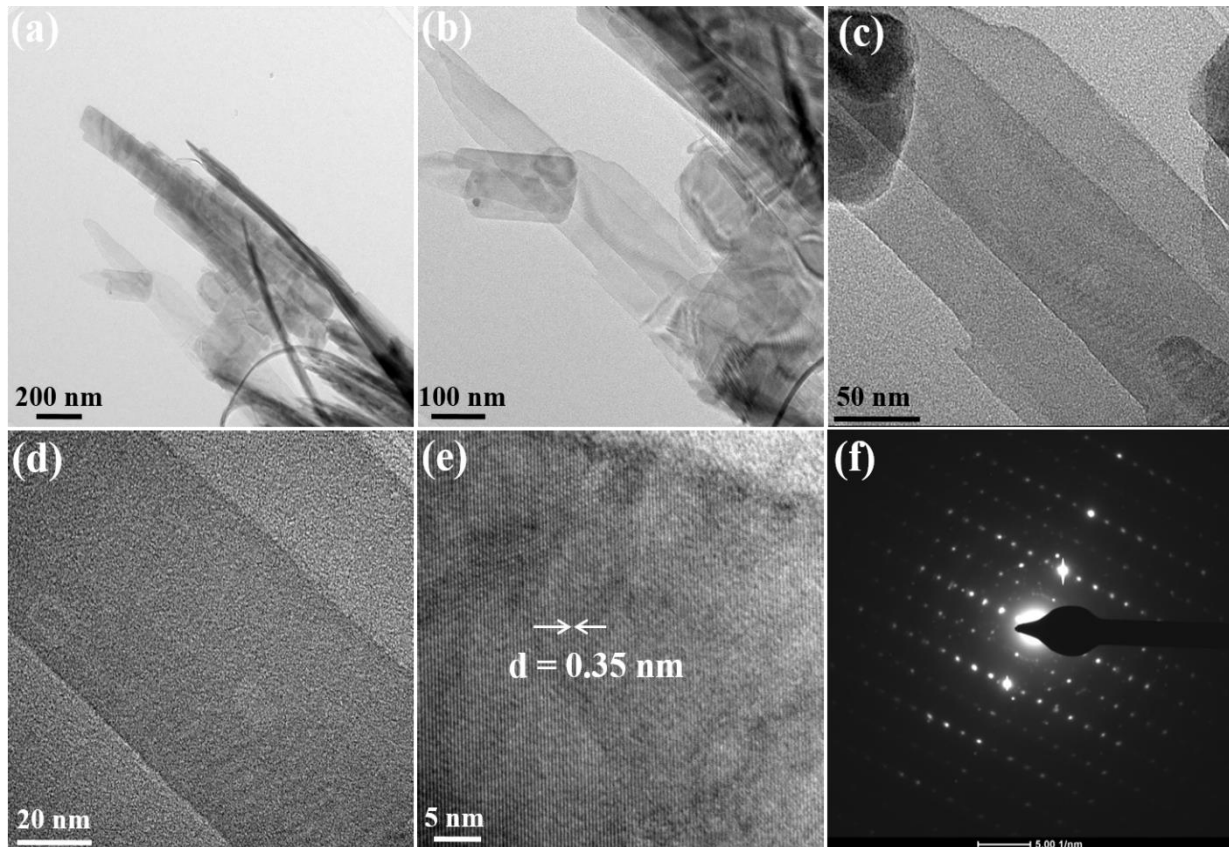


Figure 3.4: (a-d) Typical low magnification TEM images, (e) HRTEM image taken at 5 nm, (f) corresponding SAED pattern showing crystalline nature of as synthesized V_2O_5 nanosheets.

Figure 3.6(a) presents the I-V curves of V_2O_5 sensor device in various RH levels. The (I-V) curves displays that the current decreases with the increase in RH value. Figure 3.6(b) shows the resistance vs RH plot for the V_2O_5 nanosheet based sensor device. The obtained plot represents that the resistance increases with the increasing RH levels. The sensitivity Vs RH plot was also presented in figure 3.6(c). The sensitivity of the device varies with the water molecules adsorbed on the V_2O_5 nanosheet.

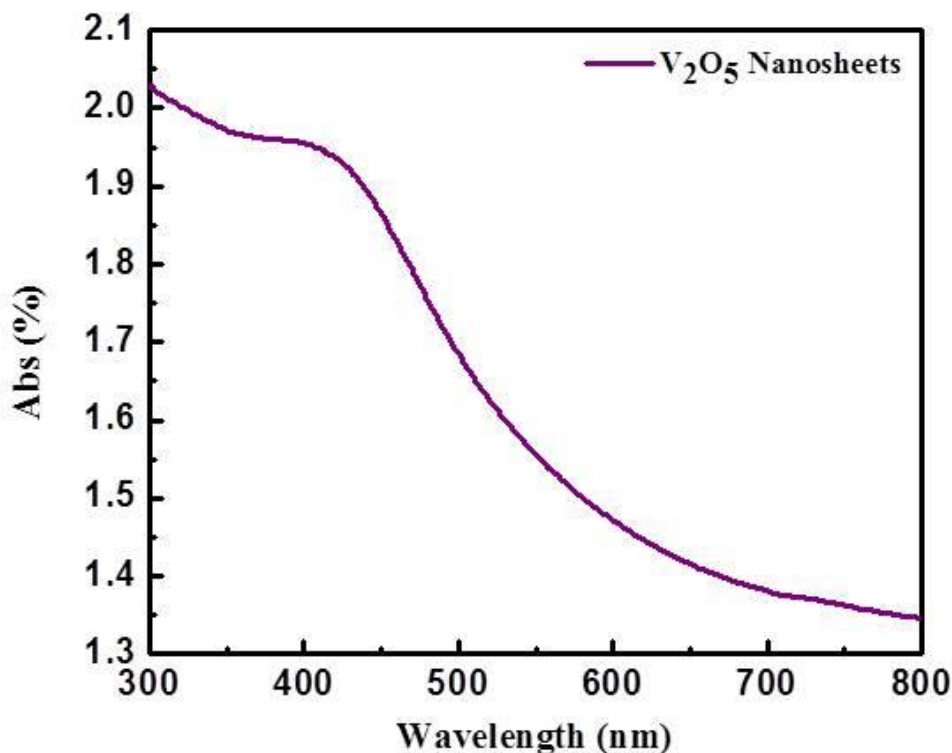


Figure 3.5: UV-Vis spectra of V₂O₅ nanosheets.

We observed the positive sensitivity for the presented V₂O₅ nanosheet based sensor with increased RH levels. The sensitivity for V₂O₅ nanosheet sensor is defined as $S = \frac{R_H}{R_A} - 1$, where R_H and R_A is the resistances of the device to the humidity and in air respectively. The positive sensitivity indicates that the H₂O molecules present in the saturated salts acts as an electron acceptor results in the p-type doping. The adsorbed water molecules on the V₂O₅ nanosheet shifts the Fermi level closer to the valence band edge. The highest sensitivity was calculated to be 45.3% for the V₂O₅ nanosheets based sensor device. The response and recovery time for the V₂O₅ nanosheet based sensor device were shown in figure 3.6(d). The cycles of 11.3% and 97.3% RH were used to record the response and recovery time. The I-t measurements were carried out for several cycles to check the reproducibility in the response and recovery time. The response and recovery time for the V₂O₅ nanosheets sensor were found to be 4 min. and 5 min. respectively.

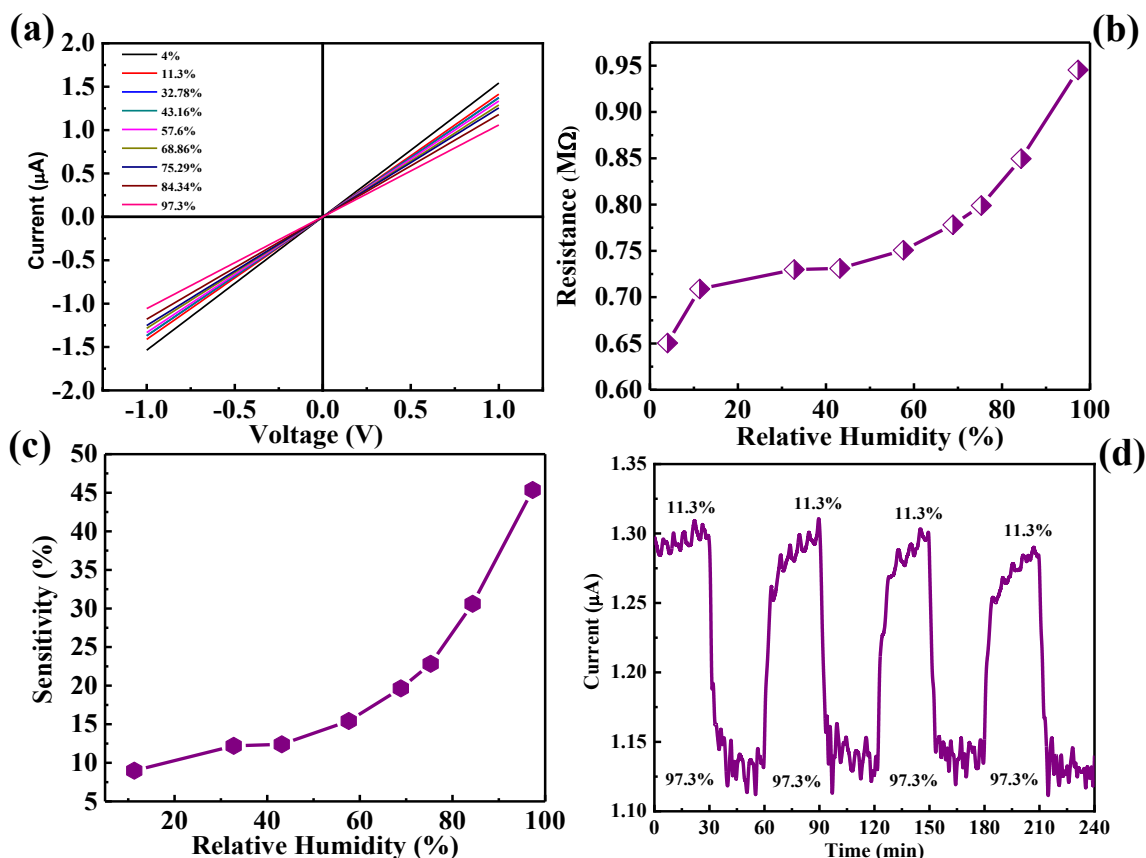


Figure 3.6: (a) *I-V* characteristics, (b) resistance vs. RH, (c) sensitivity vs. RH and (d) *I-t* plot for as obtained V_2O_5 nanosheets based sensor device.

The slow desorption of water molecules from the V_2O_5 nanosheets results into long recovery time and the hydrophilic nature of nanosheets leads to immediate adsorption of water molecules on the surface of nanosheets gives rise to faster response.⁶⁴ Another reason is due to the thickness of V_2O_5 nanosheets layer, thicker the sheet recovery will be more because desorption of H_2O molecules is difficult in the thick sheets so recovery time will be less in case of thin sheets.

3.3.3 Photodetector

The V_2O_5 nanosheets synthesized by using simple hydrothermal method were also used for UV light photodetection. Figure 3.7(a) presents the (*I-V*) plots for the V_2O_5 nanosheet device with power density of UV light used upto 200 mW/cm^2 .

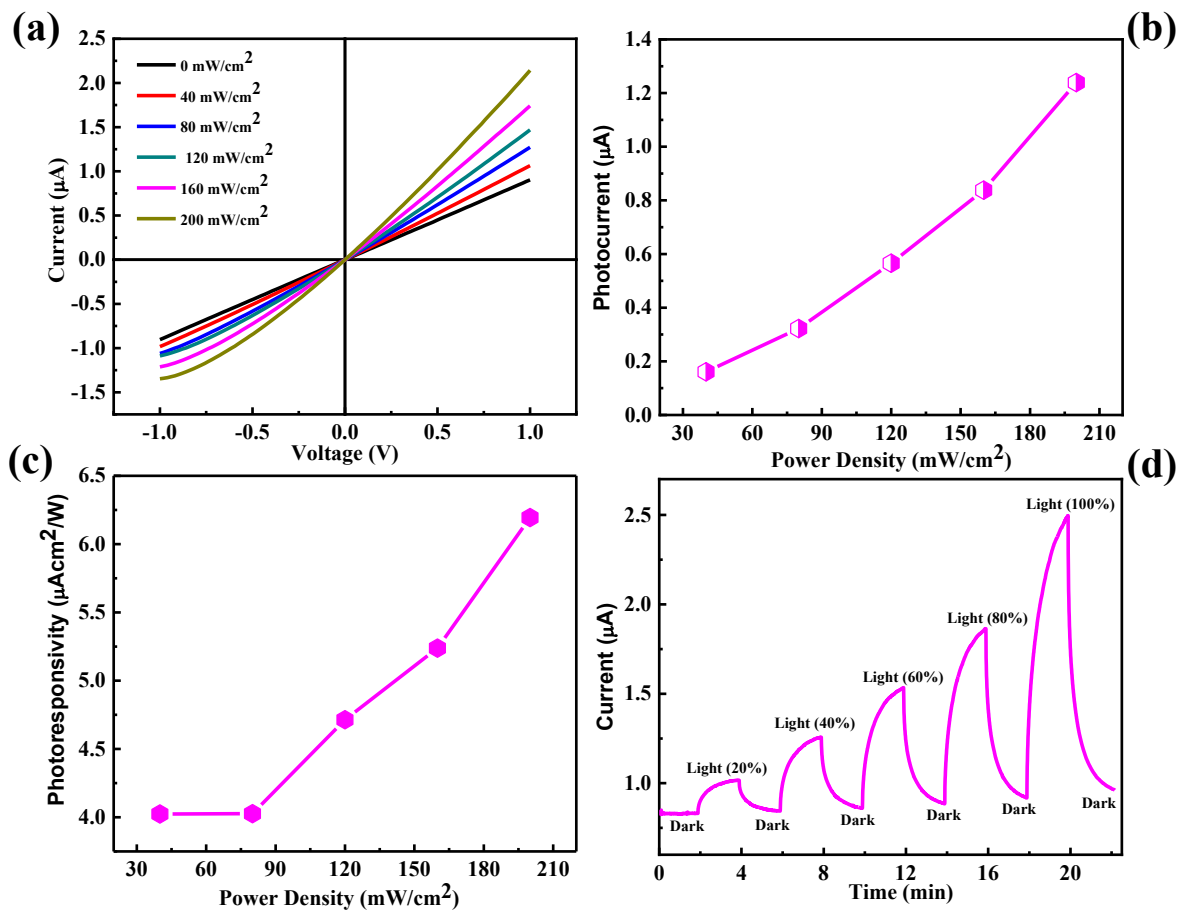


Figure 3.7: (a) *I-V* characteristics, (b) photocurrent vs. power density, (c) photo responsivity vs. power density and (d) *I-t* plot under the illumination of UV light from 0 mW/cm^2 to 200 mW/cm^2 .

We observed that the current increases with the increasing power density of UV light. Photocurrent as a function of power density plot were shown in Figure 3.7(b) which indicates that the photocurrent increases with the increasing power density. Photocurrent is the difference in the current recorded in the light illumination condition and the current recorded in the dark condition. Figure 3.7(c) shows the photoresponsivity vs power density plot. The photoresponsivity is defined as the ratio of photocurrent to power density. We observed that the photoresponsivity increases with the increasing power density. We observed the maximum photoresponsivity of $\sim 6.1946 \mu\text{Acm}^2/\text{W}$ for 200 mW/cm^2 power density. When the device is irradiated with UV light, the electrons from the valence gets excited to conduction band results

in the formation of (e-h) pairs. These generated (e-h) pairs then transported to electrodes through external supply before recombination which gives rise to photocurrent. The photocurrent response of the V₂O₅ nanosheets photodetector is shown in Figure 3.7(d), which is measured under the 365 nm light illumination with on and off cycles at applied bias voltage of 1V. The Response and recovery time with the V₂O₅ nanosheets based sensor is ~65 sec and ~75 sec respectively.

3.3.4 Field Emission

As synthesized V₂O₅ nanosheets were also used to study FE properties. Figure 3.8(a) shows the FE current density as a function of applied electric field (J-E) for V₂O₅ nanosheets. From the plot it is clear that current density exponentially increases with applied field, representing that electron emission follows the Fowler–Nordheim (F-N) theory. The turn on and threshold field were found to be 1.15 and 1.72 V/μm respectively for V₂O₅ nanosheets. From the same plot, we also achieved maximum current density of 1532 μA/cm² at 3.2 V/μm. Our findings reveal that the obtained values for turn-on and threshold field are much lesser than the values reported in the literature for different V₂O₅ nanostructures. As noticed from the SEM image, most of the V₂O₅ nanosheets are randomly oriented, it could be expected that some of them will protrude outside the substrate surface, which act as potential emitting sites. The dependence of field electron emission current density over applied field (J-E) is further characterized by modified Fowler-Nordheim (F-N) theory⁶³ using the following equation:

$$J = \lambda_M a \phi^{-1} E^2 \beta^2 \exp\left(-\frac{b \phi^2}{\beta E} v_F\right) \quad \dots\dots\dots (1)$$

Where J is the emission current density, E is the applied average electric field, a and b are constants, typically 1.54×10^{-6} A eV V⁻² and 6.83 eV^{-3/2} Vnm⁻¹, respectively, φ is the work function of the emitter material, λ_M be the macroscopic pre-exponential correction factor, v_F is

value of the principal Schottky-Nordheim barrier function (a correction factor), and β is the field enhancement factor.

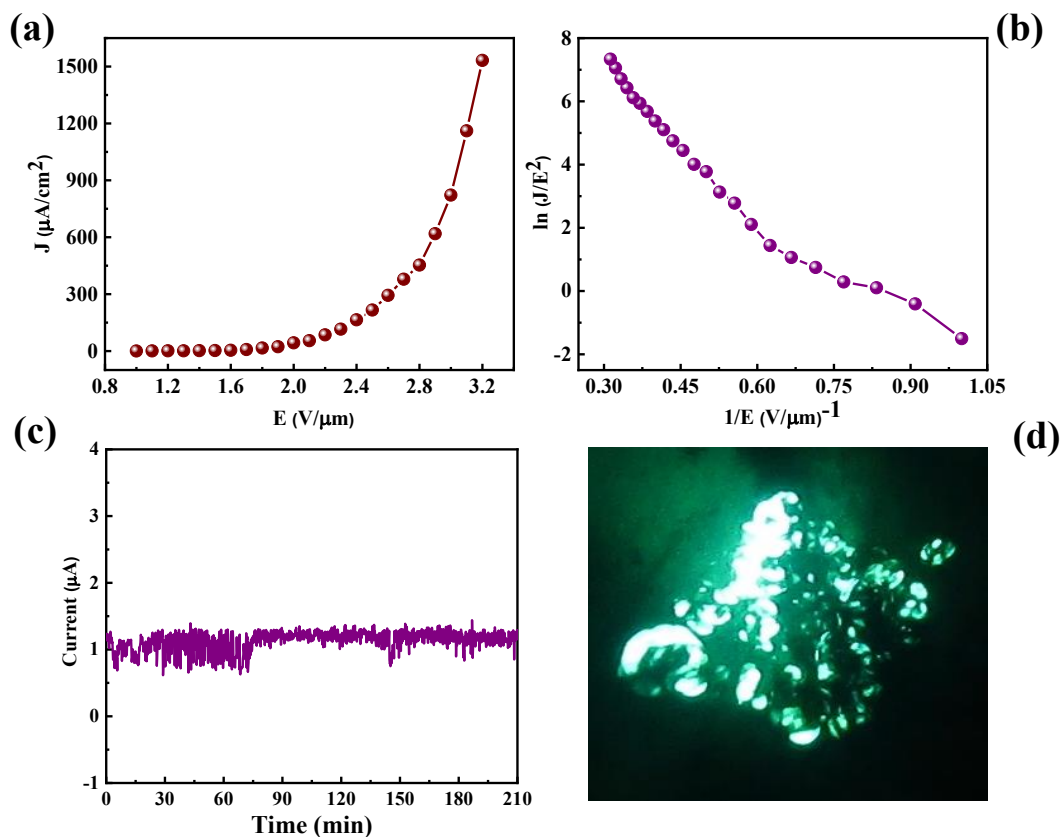


Figure 3.8: FE properties of V_2O_5 nanosheets, (a) emission current density vs. applied electric field (J - E plot), (b) (F - N) plot showing nonlinear behavior indicating field electron emission from semiconducting material, (c) FE long term current stability (I - t plot), (d) FE pattern recorded at current density of $50 \text{ mA}/\text{cm}^2$.

The graph of $\ln(J/E^2)$ versus $(1/E)$ obtained from the J - E characteristics, known as a (F - N) plot. The corresponding F - N plot is shown in Figure 3.8(b). In our case, the F - N plot appears to be nonlinear and F - N plots with such nonlinear behavior have been observed for different semiconducting metal oxides. This behavior in the F - N plot further determined by taking two discrete slopes in the high-field and low-field regions (see Figure 3.8(b)). The field

enhancement factors (β) are calculated from the slope of the low-field and the high-field regions of the F-N plot, using the following equation (2),

$$\beta = \frac{6.8 \times 10^3 \times \phi^{\frac{3}{2}}}{slope} \quad \dots\dots\dots (2)$$

It is found to be 8580 and 3538 for low field region and high field region, separately. For the application purpose in FE based devices, emission current stability stands as key parameter. The emission current versus time (I-t) plot were performed at a base pressure of $\sim 1 \times 10^{-8}$ mbar presented in Figure 3.8(c). The average emission current is seen to remain stable at pre-set value of $\sim 1 \mu\text{A}$ over three and half hour. The emission current is seen to be stable over the duration of measurement and characterized by fluctuation in the form of “spike”. The appearance of the “spikes” in the emission current is attributed to the adsorption, desorption, and migration of the residual gas molecules on the emitter surface. The striking feature of the observed FE behavior is that the average emission current remains nearly constant over the entire duration and shows no signs of degradation. It is key feature mainly from the real-world application of the emitter material as an electron source. Typical FE image, taken at emission current of $\sim 50 \mu\text{A}/\text{cm}^2$, is shown in inset of Figure 3.8(d). It displays many small spots, conforming to the emission from the most protruding sites of V_2O_5 nanosheets. We observed emission current fluctuation which are proportionate with the progressive deviations in the intensity of these tiny spots, displayed in the I-t plot. The comparison of FE properties between the as-synthesized product and various V_2O_5 nanostructures is shown in table 1.

Sr. No.	Morphology	Turn-on Field (at $10 \mu\text{A}/\text{cm}^2$)	Max. Current density at applied field	References
1	Nanofiber-Bundles	$\sim 1.84 \text{ V}/\mu\text{m}$	$213 \mu\text{A}/\text{cm}^2$ at $3.3 \text{ V}/\mu\text{m}$	60

2	Centimeter long nanowires	$\sim 2.82 \text{ V}/\mu\text{m}$	14 mA/cm^2 at 4.42 $\text{V}/\mu\text{m}$	61
3	Vertically aligned nanowires	$\sim 8.30 \text{ V}/\mu\text{m}$	1.8 mA/cm^2 at 18 $\text{V}/\mu\text{m}$	29
4	Nanotubes array	$\sim 6.35 \text{ V}/\mu\text{m}$	2.1 mA/cm^2 at 9.20 $\text{V}/\mu\text{m}$	62
5	Nanorods array	$\sim 6.3 \text{ V}/\mu\text{m}$	2.31 mA/cm^2 at 10 $\text{V}/\mu\text{m}$	30
6	Nanosheets	$\sim 1.72 \text{ V}/\mu\text{m}$	1.53 mA/cm^2 at 3.2 $\text{V}/\mu\text{m}$	Present

Table 1: Comparison of FE properties of various nanomaterials.

3.4 Conclusions

In conclusion, we present the preparation of V_2O_5 nanosheets and their characterization using few microscopy and spectroscopic techniques. We have investigated device performance for V_2O_5 nanosheets in the presence of water vapors having RH ranging from 11-97%. The maximum sensitivity of $\sim 45.3\%$ and response time of ~ 4 min. and recovery time ~ 5 min. were observed for the fabricated sensor device. Further, the as synthesized V_2O_5 nanosheet showed good performance towards UV photodetector with response time of ~ 65 s and maximum photoresponsivity of $\sim 6.2 \mu\text{A}/\text{cm}^2/\text{W}$. The FE properties were studied in planar diode assembly at base pressure of $\sim 1 \times 10^{-8}$ mbar. The turn on field required to draw an emission current density of $1 \mu\text{A}/\text{cm}^2$ and $10 \mu\text{A}/\text{cm}^2$ is found to be 1.15 and 1.72 $\text{V}/\mu\text{m}$ respectively which is very less as compared to previous reports for different V_2O_5 nanostructures. We achieved emission current density of $1532 \mu\text{A}/\text{cm}^2$ at 3.2 $\text{V}/\mu\text{m}$ and also high field enhancement factor 8580 and 3538 for low field and high field region. Our findings open up many windows and key success in the direction of the use of other oxide nanosheet materials with layered structure for various energy harvesting, optoelectronics and nanoelectronics device applications including sensors, photodetector, flat panel displays, electron emitter and transistor.

3.5 References

- 1) Wang, Q. H.; Kalantar-Zadeh, K.; Kis, A.; Coleman, J. N.; Strano, M. S. Electronics and Optoelectronics of Two Dimensional Transition Metal Dichalcogenides. *Nat. Nanotechnol.* **2012**, *7*, 699-712.
- 2) Buscema, M.; Island, J. O.; Groenendijk, D. J.; Blanter, S. I.; Steele, G. A.; Zant, V. D.; H. S. J.; Castellanos-Gomez, A. Photocurrent Generation with Two-Dimensional Van der Waals Semiconductors. *Chem. Soc. Rev.* **2015**, *44*, 3691-3718.
- 3) Li, Z.; Zhang, H.; Zheng, W.; Wang, W.; Huang, H.; Wang, C.; MacDiarmid, A. G.; Wei, Y. Highly Sensitive and Stable Humidity Nanosensors based on LiCl Doped TiO₂ Electrospun Nanofibers. *J. Am. Chem. Soc.* **2008**, *130*, 5036-5037.
- 4) Bi, H.; Yin, K.; Xie, X.; Ji, J.; Wan, S.; Sun, L.; Terrones, M.; Dresselhaus, M. S. Ultrahigh Humidity Sensitivity of Graphene Oxide. *Sci. Rep.* **2013**, *3*, 2714.
- 5) Chu, J.; Peng, X.; Feng, P.; Sheng, Y.; Zhang, J. Study of Humidity Sensors based on Nanostructured Carbon Films Produced by Physical Vapor Deposition. *Sensors Actuators, B Chem.* **2013**, *178*, 508-513.
- 6) Kulkarni, M. V.; Apte, S. K.; Naik, S. D.; Ambekar, J. D.; Kale, B. B. Ink-jet Printed Conducting Polyaniline based Flexible Humidity Sensor. *Sensors Actuators, B Chem.* **2013**, *178*, 140-143.
- 7) Su, P. G.; Lu, Z. M. Flexibility and Electrical and Humidity Sensing Properties of Diamine-Functionalized Graphene Oxide Films. *Sensors Actuators, B Chem.* **2015**, *211*, 157-163.
- 8) Tang, Q. Y.; Chan, Y. C.; Zhang, K. Fast Response Resistive Humidity Sensitivity of polyimide/multiwall Carbon Nanotube Composite Films. *Sensors Actuators, B Chem.* **2011**, *152*, 99-106.

- 9) Xia, F.; Mueller, T.; Lin, Y.-M.; Valdes-Garcia, A.; Avouris, P. Ultrafast Graphene Photodetector. *Nat. Nanotechnol.* **2009**, *4*, 839-843.
- 10) Yu, S. H.; Lee, Y.; Jang, S. K.; Kang, J.; Jeon, J.; Lee, C.; Lee, J. Y.; Kim, H.; Hwang, E.; Lee, S.; Cho, J. H. Dye-Sensitized MoS₂ Photodetector with Enhanced Spectral Photoresponse. *ACS Nano* **2014**, *8*, 8285-8291.
- 11) Chang, Y.; Zhang, O. W.; Zhu, O. Y.; Han, Y.; Pu, J.; Chang, J.; Hsu, W. Monolayer MoSe₂ Grown by Chemical Vapor Deposition for Fast Photodetection. *ACS Nano* **2014**, *8*, 8582-8590.
- 12) Huo, N.; Yang, S.; Wei, Z.; Li, S.-S.; Xia, J. B.; Li, J. Photoresponsive and Gas Sensing Field-Effect Transistors based on Multilayer WS₂ Nanoflakes. *Sci. Rep.* **2014**, *4*, 5209.
- 13) Late, D. J.; Shaikh, P. A.; Khare, R.; Kashid, R. V.; Chaudhary, M.; More, M. A.; Ogale, S. B. Pulsed Laser-Deposited MoS₂ Thin Films on W and Si: Field Emission and Photoresponse Studies. *ACS Appl. Mater. Interfaces* **2014**, *6*, 15881-15888.
- 14) Lei, S.; Ge, L.; Liu, Z.; Najmaei, S.; Shi, G.; You, G.; Lou, J.; Vajtai, R.; Ajayan, P. M. Synthesis and Photoresponse of Large GaSe Atomic Layers. *Nano Lett.* **2013**, *13*, 2777-2781.
- 15) Lei, S.; Sobhani, A.; Wen, F.; George, A.; Wang, Q.; Huang, Y.; Dong, P.; Li, B.; Najmaei, S.; Bellah, J.; Gupta, G.; Mohite, A. D.; Ge, L.; Lou, J.; Halas, N. J.; Vajtai, R.; Ajayan, P. Ternary CuIn₇Se₁₁ : Towards Ultra-Thin Layered Photodetectors and Photovoltaic Devices. *Adv. Mater.* **2014**, *26*, 7666-7672.
- 16) Lopez-Sanchez, O.; Lembke, D.; Kayci, M.; Radenovic, A.; Kis, A. Ultrasensitive Photodetectors Based on Monolayer MoS₂. *Nat. Nanotechnol.* **2013**, *8*, 497-501.
- 17) Wang, J.; Gudiksen, M. S.; Duan, X.; Cui, Y.; Lieber, C. M. Highly Polarized Photoluminescence and Photodetection from Single Indium Phosphide Nanowires. *Science* **2001**, *293*, 1455-1457.

-
- 18) Xia, J.; Huang, X.; Liu, L. Z.; Wang, M.; Wang, L.; Huang, B.; Zhu, D. D.; Li, J. J.; Gu, C. Z.; Meng, X. M. CVD Synthesis of Large-area, Highly Crystalline MoSe₂ Atomic Layers on Diverse Substrates and Application to Photodetectors. *Nanoscale* **2014**, *6*, 8949-8955.
- 19) Zhang, C.; Wang, S.; Yang, L.; Liu, Y.; Xu, T.; Ning, Z.; Zak, A.; Zhang, Z.; Tenne, R.; Chen, Q. High-Performance Photodetectors for Visible and near-Infrared Lights based on Individual WS₂ Nanotubes. *Appl. Phys. Lett.* **2012**, *100*, 243101.
- 20) Liu, K.; Sakurai, M.; Aono, M. ZnO-Based Ultraviolet Photodetectors. *Sensors* **2010**, *10*, 8604-8634.
- 21) Hu, L.; Yan, J.; Liao, M.; Wu, L.; Fang, X. Ultrahigh External Quantum Efficiency from Thin SnO₂ Nanowire Ultraviolet Photodetectors. *Small* **2011**, *7*, 1012-1017.
- 22) Guo, D.Y.; Shan, C.X.; Qu, S.N.; Shen, D.Z. Highly Sensitive Ultraviolet Photodetectors Fabricated from ZnO Quantum Dots/Carbon Nanodots Hybrid Films. *Sci. Rep.* **2014**, *4*, 7469.
- 23) Deng, K.; Lu, H.; Shi, Z.; Liu, Q.; Li, L. Flexible Three-Dimensional SnO₂ Nanowire Arrays: Atomic Layer Deposition-Assisted Synthesis, Excellent Photodetectors, and Field Emitters. *ACS Appl. Mater. Interfaces* **2013**, *5*, 7845-7851.
- 24) Late, D. J.; Liu, B.; Luo, J.; Yan, A.; Matte, H. S. S. R.; Grayson, M.; Rao, C. N. R.; Dravid, V. P. GaS and GaSe Ultrathin Layer Transistors. *Adv. Mater.* **2012**, *24*, 3549-3554.
- 25) Galstyan, V.; Comini, E.; Faglia, G.; Sberveglieri, G. TiO₂ Nanotubes: Recent Advances in Synthesis and Gas Sensing Properties. *Sensors (Basel)*. **2013**, *13*, 14813-14838.

- 26) Late, D. J.; Huang, Y. K.; Liu, B.; Acharya, J.; Shirodkar, S. N.; Luo, J.; Yan, A.; Charles, D.; Waghmare, U. V.; Dravid, V. P.; Rao, C. N. R. Sensing Behavior of Atomically Thin-Layered MoS₂ Transistors. *ACS Nano* **2013**, *7*, 4879-4891.
- 27) Li, G.; Pang, S.; Jiang, L.; Guo, Z.; Zhang, Z. Environmentally Friendly Chemical Route to Vanadium Oxide Single-Crystalline Nanobelts as a Cathode Material for Lithium-Ion Batteries. *J. Phys. Chem. B* **2006**, *110*, 9383.
- 28) Niederberger, M.; Muhr, H. J.; Krumeich, F.; Bieri, F.; Günther, D.; Nesper, R. Low-Cost Synthesis of Vanadium Oxide Nanotubes via Two Novel Non-Alkoxide Routes. *Chem. Mater.* **2000**, *12*, 1995-2000.
- 29) Wu, M. C.; Lee, C. S. Field Emission of Vertically Aligned V₂O₅ Nanowires on an ITO Surface Prepared with Gaseous Transport. *J. Solid State Chem.* **2009**, *182*, 2285-2289.
- 30) Chen, W.; Zhou, C.; Mai, L.; Liu, Y.; Qi, Y.; Dai, Y. Field Emission from V₂O₅,*n*H₂O Nanorod Arrays. *J. Phys. Chem. C* **2008**, *112*, 2262-2265.
- 31) Cao, L.; Zhu, J.; Li, Y.; Xiao, P.; Zhang, Y.; Zhang, S.; Yang, S. Ultrathin Single-Crystalline Vanadium Pentoxide Nanoribbon Constructed 3D Networks for Superior Energy Storage. *J. Mater. Chem. A* **2014**, *2*, 13136.
- 32) Kim, D.; Yun, J.; Lee, G.; Ha, J. S. Fabrication of High Performance Flexible Microsupercapacitor Arrays with Hybrid Electrodes of MWNT/V₂O₅ Nanowires Integrated with a SnO₂ Nanowire UV Sensor. *Nanoscale* **2014**, *6*, 12034-12041.
- 33) Myung, S.; Lee, M.; Kim, G. T.; Ha, J. S.; Hong, S. Large Scale Surface Programmed Assembly of Pristine Vanadium Oxide Nanowire based devices. *Adv. Mater.* **2005**, *17*, 2361-2364.
- 34) Wang, Y.; Cao, G. Synthesis and Enhanced Intercalation Properties of Nanostructured Vanadium Oxides. *Chem. Mater.* **2006**, *18*, 2787-2804.

- 35) Mai, L.; Dong, F.; Xu, X.; Luo, Y.; An, Q.; Zhao, Y.; Pan, J.; Yang, J. Cucumber - Like V_2O_5 /poly(3,4ethylenedioxythiophene) & MnO_2 Nanowires with Enhanced Electrochemical Cyclability. *Nano Lett.* **2013**, *13*, 740-745.
- 36) Kim, G. T.; Muster, J.; Krstic, V.; Park, J. G.; Park, Y. W.; Roth, S.; Burghard, M. Field-Effect Transistor Made of Individual V_2O_5 Nanofibers. *Appl. Phys. Lett.* **2000**, *76*, 1875.
- 37) Chen, R. S.; Wang, W. C.; Chan, C. H.; Hsu, H. P.; Tien, L. C.; Chen, Y. J. Photoconductivities in Monocrystalline Layered V_2O_5 Nanowires Grown by Physical Vapor Deposition. *Nanoscale Res. Lett.* **2013**, *8*, 443.
- 38) Lu, J.; Hu, M.; Tian, Y.; Guo, C.; Wang, C.; Guo, S.; Liu, Q. Fast visible light photoelectric switch based on ultralong single crystalline V_2O_5 Nanobelt. *Opt. Express* **2012**, *20*, 6974.
- 39) Yan, B.; Liao, L.; You, Y.; Xu, X.; Zheng, Z.; Shen, Z.; Ma, J.; Jong, L.; Yu, T. Single-Crystalline V_2O_5 Ultralong Nanoribbon Waveguides. *Adv. Mater.* **2009**, *21*, 2436-2440.
- 40) Parida, M. R.; Vijayan, C.; Rout, C. S.; Sandeep, C. S. S.; Philip, R.; Deshmukh, P. C. Room Temperature Ferromagnetism and Optical Limiting in V_2O_5 Nanoflowers Synthesized by a Novel Method. *J. Phys. Chem. C* **2011**, *115*, 112-117.
- 41) Das, E.; Eckert, H.; Hu, H.; Wachs, I. E.; Walzer, J. F.; Feher, F. J. Bonding States of Surface Vanadium(V) Oxide Phases on Silica: Structural Characterization by ^{51}V NMR and Raman Spectroscopy. *J. Phys. Chem.* **1993**, *97*, 8240-8243.
- 42) Baddour-Hadjean, R.; Pereira-Ramos, J. P.; Navone, C.; Smirnov, M. Raman Microspectrometry Study of Electrochemical Lithium Intercalation into Sputtered Crystalline V_2O_5 Thin Films. *Chem. Mater.* **2008**, *20*, 1916-1923.

- 43) Miao, X.; Tongay, S.; Petterson, M. K.; Berke, K.; Rinzler, A. G.; Appleton, B. R.; Hebard, A. F. High Efficiency Graphene Solar Cells by Chemical Doping. *Nano Lett.* **2012**, *12*, 2745-2750.
- 44) Bach, U.; Lupo, D.; Comte, P.; Moser, J. E.; Weissörtel, F.; Salbeck, J.; Spreitzer, H.; Grätzel, M. Solid-state dye-sensitized mesoporous TiO₂ solar cells with high photon-to-electron conversion efficiencies. *Nature* **1998**, *395*, 583-585.
- 45) Hu, J.; Gordon, R. G. Textured fluorine-doped ZnO films by atmospheric pressure chemical vapor deposition and their use in amorphous silicon solar cells. *Sol. Cells* **1991**, *30*, 437-450.
- 46) Tai, S. Y.; Liu, C. J.; Chou, S. W.; Chien, F. S. S.; Lin, J. Y.; Lin, T. W. Few-layer MoS₂ nanosheets coated onto multi-walled carbon Nanotubes as a low-cost and highly electrocatalytic counter electrode for dye-sensitized solar cells. *J. Mater. Chem.* **2012**, *22*, 24753-24759.
- 47) Chen, S.; Zhu, J.; Wu, X.; Han, Q.; Wang, X. Graphene Oxide MnO₂ Nanocomposites for Supercapacitors. *ACS Nano* **2010**, *4*, 2822-2830.
- 48) Cao, L.; Yang, S.; Gao, W.; Liu, Z.; Gong, Y.; Ma, L.; Shi, G.; Lei, S.; Zhang, Y.; Zhang, S.; Vajtai, R.; Ajayan, P. M. Direct Laser-Patterned Micro-Supercapacitors from Paintable MoS₂ Films. *Small* **2013**, *9*, 2905-2910.
- 49) Yoon, S.; Kang, E.; Kim, J. K.; Lee, C. W.; Lee, J. Development of high-performance supercapacitor electrodes using novel ordered mesoporous tungsten oxide materials with high electrical conductivity. *Chem. Commun. (Camb)*. **2011**, *47*, 1021-1023.
- 50) Liu, C.; Yu, Z.; Neff, D.; Zhamu, A.; Jang, B. Z. Graphene-Based Supercapacitor with an Ultrahigh Energy Density. *Nano Lett.* **2010**, *10*, 4863-4868.
- 51) Maeda, K.; Domen, K. Solid Solution of GaN and ZnO as a Stable Photocatalyst for Overall Water Splitting under Visible Light. *Chem. Mater.* **2010**, *22*, 612-623.

- 52) Chen, Z.; Cummins, D.; Reinecke, B. N.; Clark, E.; Sunkara, M. K.; Jaramillo, T. F. Core shell MoO₃ MoS₂ Nanowires for Hydrogen Evolution: A Functional Design for Electrocatalytic Materials. *Nano Lett.* **2011**, *11*, 4168-4175.
- 53) Livage, J. Hydrothermal Synthesis of Nanostructured Vanadium Oxides. *Materials (Basel)* **2010**, *3*, 4175-4195.
- 54) Liu, J.; Wang, X.; Peng, Q.; Li, Y. Vanadium Pentoxide Nanobelts: Highly Stable and Selective Ethanol Sensor. *Adv. Mater.* **2005**, *17*, 764-767.
- 55) Yu, D.; Chen, C.; Xie, S.; Liu, Y.; Park, K.; Zhou, X.; Zhang, Q.; Li, J.; Cao, G. Mesoporous vanadium Pentoxide nanofibers with significantly enhanced Li-ion storage properties by electrospinning. *Energy Environ. Sci.* **2011**, *4*, 858.
- 56) Mai, L.; Xu, L.; Han, C.; Xu, X.; Luo, Y.; Zhao, S.; Zhao, Y. Electrospun Ultralong Hierarchical Vanadium Oxide Nanowires with High Performance for Lithium Ion Batteries. *Nano Lett.* **2010**, *10*, 4750-4755.
- 57) Yu, H. Y.; Kang, B. H.; Pi, U. H.; Park, C. W.; Choi, S. Y.; Kim, G. T. V₂O₅ nanowire-based nanoelectronic devices for helium detection. *Appl. Phys. Lett.* **2005**, *86*, 1-3.
- 58) Late, D. J. Temperature Dependent Phonon Shifts in Few-Layer Black Phosphorus. *ACS Appl. Mater. Interfaces* **2015**, *7*, 5857-5862.
- 59) Suryawanshi, S.R.; Kolhe, P. S.; Rout, C.S.; Late, D. J.; More, M. A. Spectral Analysis of the Emission Current Noise Exhibited by Few Layer WS₂ Nanosheets Emitter. *Ultramicroscopy* **2015**, *149*, 51-57.
- 60) Dewangan, K.; Sinha, N. N.; Chavan, P. G.; Sharma, P. K.; Pandey, A. C.; More, M. A.; Joag, D. S.; Munichandraiah, N.; Gajbhiye, N. S. Synthesis and Characterization of Self-Assembled Nanofiber-Bundles of V₂O₅: their Electrochemical and Field Emission Properties. *Nanoscale* **2012**, *4*, 645-651.

- 61) Zhai, T.; Liu, H.; Li, H.; Fang, X.; Liao, M.; Li, L.; Zhou, H.; Koide, Y.; Bando, Y.; Golberg, D. Centimeter-Long V_2O_5 Nanowires: From Synthesis to Field-Emission, Electrochemical, Electrical Transport, and Photoconductive Properties. *Adv. Mater.* **2010**, *22*, 2547-2552.
- 62) Zhou, C.; Mai, L.; Liu, Y.; Qi, Y.; Dai, Y.; Chen, W. Synthesis and Field Emission Property of $V_2O_5 \cdot nH_2O$ Nanotube Arrays. *J. Phys. Chem. C* **2007**, *111*, 8202-8205.
- 63) Forbes, R. G. Use of a Spreadsheet for Fowler-Nordheim Equation Calculations, *J. Vac. Sci. Technol. B: Microelectron. Nanom. Struct.* **1999**, *17*, 534.
- 64) Zhang, Z.; Hu, C.; Xiong, Y.; Yang, R.; Wang, Z. Synthesis of Ba-doped CeO_2 Nanowires and their Application as Humidity Sensors. *Nanotechnology* **2007**, *18*, 465504.

Chapter 4

Humidity Sensing and Photodetection Behavior of Electrochemically Exfoliated Atomically Thin-Layered Black Phosphorus Nanosheets

The paper based on this chapter is published in ACS Applied Materials and Interfaces

M. Pawar et al. *ACS Appl. Mater. Interfaces*. **2016**, 8, 11548.

4.1 Introduction

Two-dimensional (2D) graphene has attracted much attention because of its potential for use in next generation devices such as FET,¹⁻⁵ supercapacitors,⁶⁻⁸ solar cells,⁹⁻¹² and sensors.¹³⁻¹⁵ For gas sensors, the previous reports of conventional semiconducting metal oxide nanostructures indicates an amplified sensing concert due to the enhancement in the surface-to-volume ratio.^{16,17} Indeed, earlier papers on graphene nanosheets show exceptional sensing behavior with single molecule detection.¹³⁻¹⁵ Though, in addition to better surface-to-volume ratio and high sensitivity, additional crucial parameters needed for a superior gas sensor are the semiconducting nature^{17,18} and the easy accessibility of reactive sites for the redox reactions. The semiconductors are mainly fascinating due to their ability to manipulate the enhancement in sensing performance by tuning the optical and electronic properties.^{19,20} The zero band gap in graphene restricts its widespread applications in various nanoelectronics devices due to low on/off ratio. There is an emerging interest to search graphene-like other 2-D layered materials with semiconducting properties. Recently, there are a number of ultrathin layered 2D materials investigated by researchers, such as MoS₂,²¹⁻²⁸ WS₂,^{22,29-31} MoSe₂,³²⁻³⁴ WSe₂,^{33,35} gallium sulfide (GaS)^{23,36} gallium selenide (GaSe),^{23,36} and BP,³⁷⁻⁵⁰ among others. Among these materials, BP is found to be more thermodynamically stable under ambient environment. The BP is known to be a p-type semiconductor material and has been widely investigated recently for various nanoelectronics applications.^{40-45,47} Although the bulk BP material is the most thermodynamically stable phosphorus allotrope,⁵¹ and it can undergo electrochemical and ambient oxidation.^{52,53} More significantly, the bulk BP material possesses a direct bandgap (0.3eV). Surprisingly, for the 2D single-layer BP, the bandgap remains direct and becomes wider (2.2 eV).^{40,41} These excellent semiconducting properties of BP materials attracted the possibility to use this atomically thin layered nanosheet in various nanoelectronics and photonics applications which cover the entire range of spectrum.^{40-45,47} There are recent reports

in the literature on BP as a potentially viable and effective application in field effect transistors,^{40,42,43} photodetectors,^{44,45} field emissions,⁴¹ and so forth. Further, the literature reports do not emphasize on easy and one step synthesis and subtleties of humidity sensing performance of atomically thin BP layered materials. Herein, we have synthesized atomically thin nanosheets of BP using electrochemical exfoliation and show its excellent performance toward humidity sensor, photo detector, and field effect transistor. The sensing performance of BP nanosheets toward humidity has been studied to reveal the role of BP nanosheets in the interactions between solid and gas vapors.

4.2 Experimental Section

Synthesis of BP nanosheets using electrochemical exfoliation method

Bulk BP crystal was purchased from Smart Elements GmbH Ferrogasse 4/I A-U80 Wien GERMANY (purity 99.998%). The BP nanosheets were obtained using electrochemical exfoliation method for which BP bulk crystal taken as a working electrode. The bulk BP crystal was then attached to metal electrode in such a way that only the crystal will be submerged into the ionic solution of (0.5 M Na₂SO₄) also Pt wire acts as counter electrode. These two electrodes are kept parallel to each other and separated by a distance of 0.5 cm. Initially, the current was ~1 mA for the applied voltage of +7V to the working and counter electrodes. During the electrochemical exfoliation process, oxidation of water molecules takes place which then produces the •OH and •O radicals. These radicals further intercalates into the layers of the bulk BP crystal which weakens the vdW interaction among the bulk BP layered crystals. The oxidation of the radicals results into the release of O₂ gas which causes the BP interlayer to separate out. These isolated layers of BP were dispersed into the Na₂SO₄ solution and the reaction was continued for 90 min. The solution mixture was then transferred to glass beaker and kept stable for overnight to obtain the black color precipitate. The product was then washed using DI water through ultrasonication for 15 min followed by centrifugation process.

Thereafter, the obtained precipitate was then annealed in vacuum furnace for 3 h at 60°C in order to remove the solvent.

Characterization Details

The optical images were captured with the help of optical microscopy (Nikon Eclipse LV150NL). The imaging modes and objective used are bright field and 20X. The AFM images and height profile were studied using an ICON system (Bruker, Santa Barbara Ca.) in tapping mode. The LabRAM HR instrument was used to perform Raman spectroscopy using Ar laser (514.5 nm) in the back scattering geometry with laser power ~ 1 mW.

Transistor device Fabrication

The optical lithography technique was employed to fabricate a BP FET device,⁵³ on which titanium/gold (3 nm/70 nm) metals was deposited on the patterned electrodes by thermal evaporator. The BP nanosheet samples were then drop casted onto the electrode. The devices were then subsequently heated at 200°C for 2 h in the presence of Ar environment.

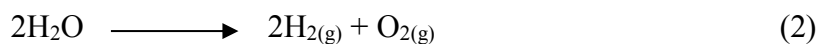
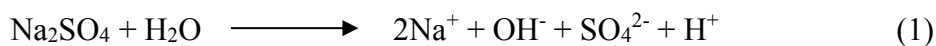
4.3 Results and Discussion

4.3.1 Material Characterization

Figure 4.1(a) and (b) shows the typical structure of BP nanosheets with one layer. The few layer atomically thin BP nanosheet samples were synthesized by a simple electrochemical exfoliation method. The experimental setup used for the synthesis of BP nanosheets is displayed in Figure 4.2. The obtained yield is in excess of 80 wt % which confirms that the method can be used on bulky scale for the synthesis of BP nanosheets. The major advantages of the electrochemical synthesis method involve the high product yield, high crystalline quality of the sample, fast synthesis process, it does not requires any additional catalyst, and importantly it is an inexpensive method to synthesize materials in large quantity.

The typical reactions occurring during electrochemical exfoliation are as follows:

Overall Reaction:



Cathode (Reduction):



Anode (Oxidation):

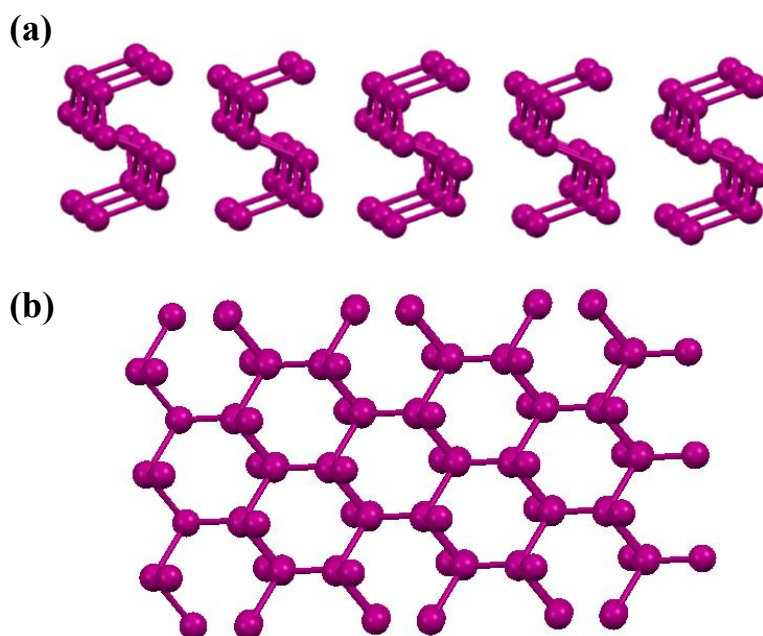
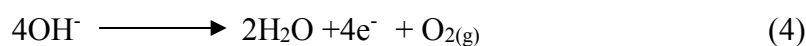


Figure 4.1: Representation of monolayer BP nanosheets (a) lateral sight and (b) top sight.

The optical images of few layer BP nanosheet deposited on Si substrate by drop casting method are shown in Figure 4.3 (a,b). Figure 4.3(c) presents AFM image of the thinnest BP nanosheet and Figure 4.3 (d) exhibits height profile plot of the BP nanosheet sample. In order to obtain precise thickness of the BP nanosheets we performed statistical analysis through AFM measurements, which shows that thickness of BP nanosheets varies from 1.4 to 10 nm which confirms the 3 to 15 layers of the nanosheets sample. Also, the lateral dimension of flakes were

found to be 0.5 to 30 μm . Figure 4.4(a,b) shows the low magnification TEM images of few layer BP nanosheet samples.

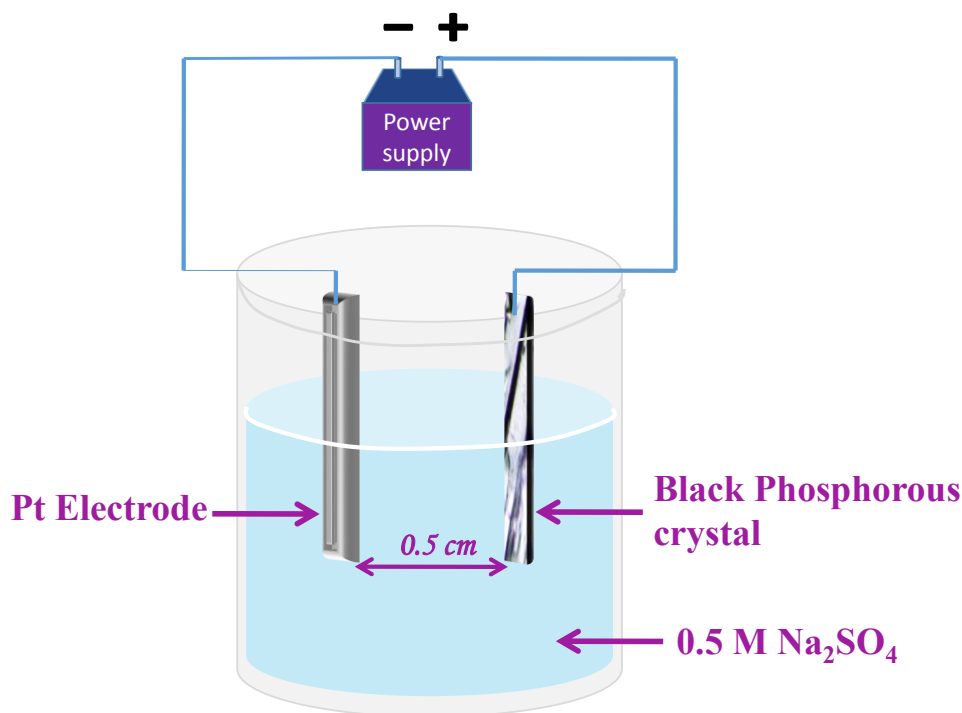


Figure 4.2: Experimental setup used for electrochemical exfoliation of BP nanosheets.

Figure 4.4(c) shows the SAED pattern of few layers BP nanosheets sample confirming the hexagonal structure.⁴¹ Figure 4.4(d) shows the HRTEM image depicting the inter atomic spacing to be ~ 0.25 nm. We have also noticed the amorphization of the BP nanosheets sample during TEM measurements. The Raman spectroscopy is a very powerful and accurate characterization technique for giving exact information about the various properties of the materials. The Raman spectroscopy is quite sensitive to the number of layers in the layered material systems, and our Raman spectroscopy results of BP nanosheet agree with the reported data in the literature.^{48,49} Figure 4.5 shows the comparative Raman spectra for the bulk BP single crystal and electrochemically exfoliated BP nanosheets sample. The Raman peaks A^1_g , B_{2g} and A^2_g were observed at 362, 437, and 466 cm^{-1} for the electrochemically exfoliated BP nanosheets sample. For the bulk samples the Raman peaks corresponds to A^1_g , B_{2g} and A^2_g mode were observed at 364, 440, and 468 cm^{-1} respectively.

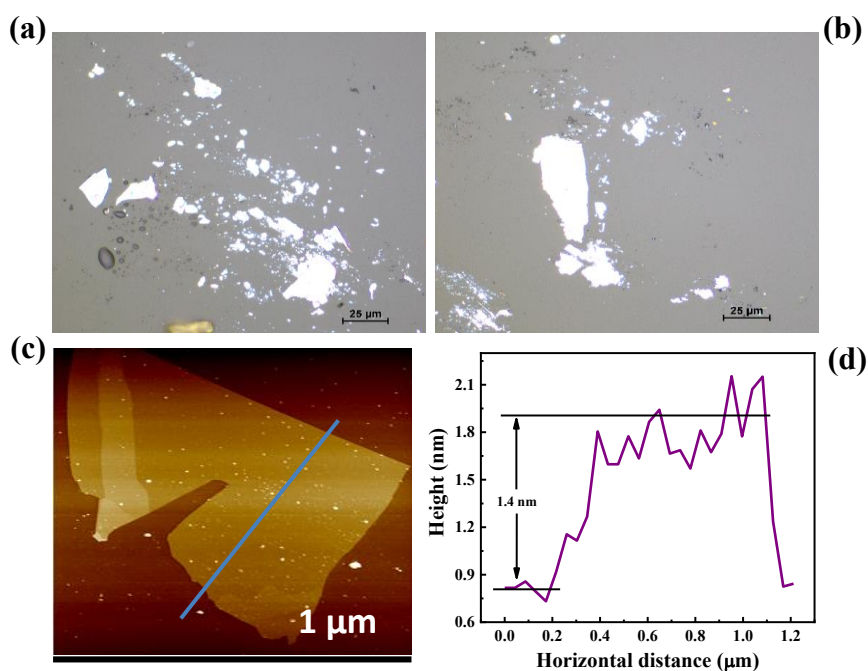


Figure 4.3: Electrochemically exfoliated of BP nanosheets, (a, b) optical images of nanosheets deposited on Si substrate, (c) typical AFM image of nanosheet, and (d) corresponding AFM height profile.

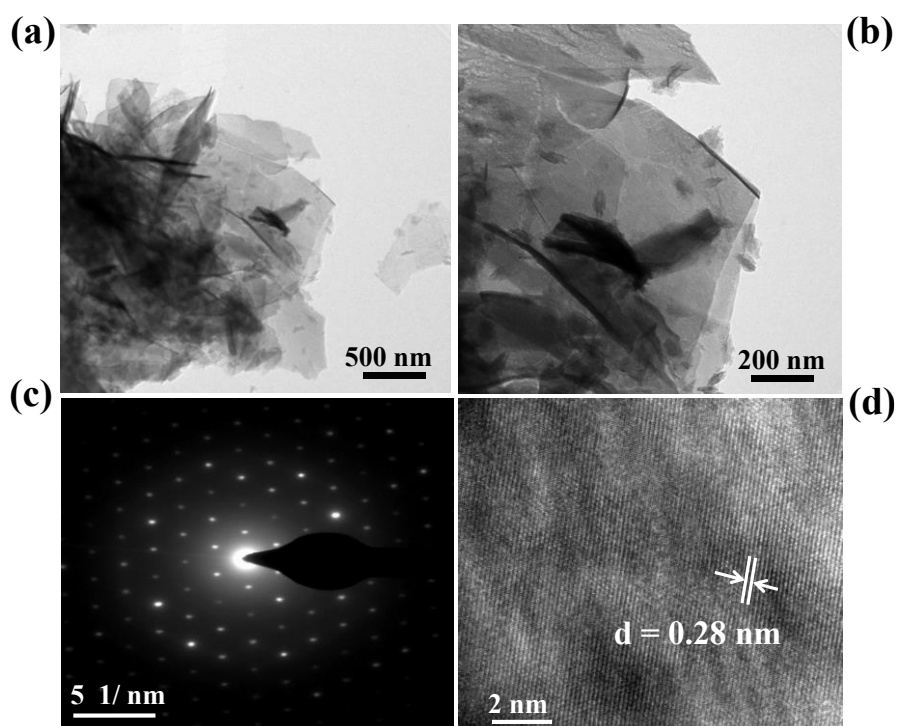


Figure 4.4: (a,b) Low resolution TEM images of electrochemically exfoliated of BP nanosheets. (c) SAED pattern of black phosphorus nanosheets and (d) HRTEM image of electrochemically exfoliated BP nanosheet.

Interestingly, for both the bulk and nanosheets sample the characteristic peaks which corresponds to the A^1_g , B_{2g} and A^2_g phonon modes of vibration originating from the in-plane (B_{2g} and A^2_g) and out-of-plane (A^1_g) vibrational mode were observed.⁴¹ This clearly indicates the good crystalline quality of the sample after the electrochemical exfoliation. Furthermore, the change in the peak shift, broadening clearly indicates the reduction in the size of BP sample. The FET device was fabricated by using standard optical lithography technique with electrodes patterned on 300 nm SiO_2/Si substrate with channel length $\sim 150 \mu\text{m}$ and channel width $\sim 5 \mu\text{m}$.

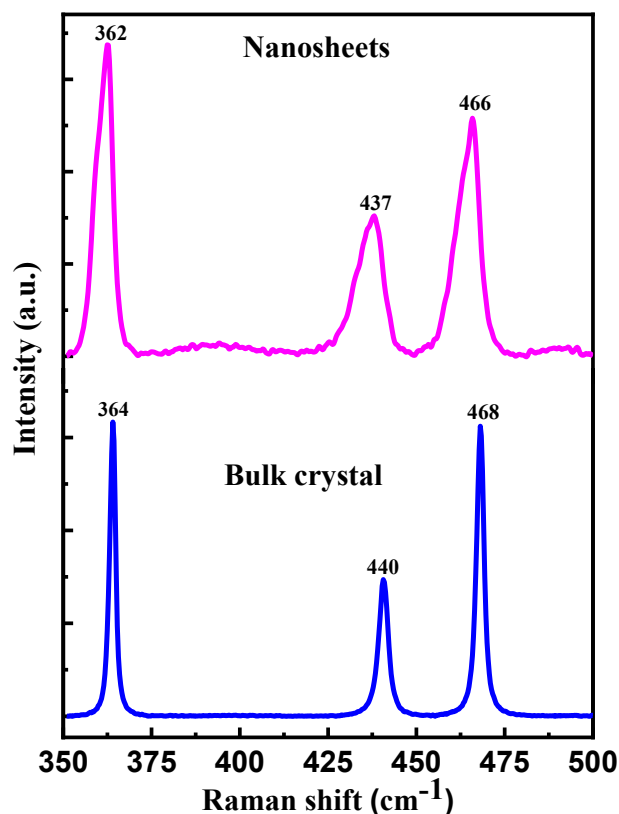


Figure 4.5: Comparative Raman spectra of bulk and electrochemically exfoliated BP nanosheets.

4.3.2 Field Effect Transistor

The as synthesized BP nanosheets sample were then dispersed into the ethanol solvent and then drop casted on the electrode geometry followed by the annealing of the device in Argon (Ar) for 2 h at 200°C .

The as synthesized BP nanosheets sample were then dispersed into the ethanol solvent and then drop casted on the electrode geometry followed by the annealing of the device in Argon (Ar) for 2 h at 200°C.

The typical schematic diagram of the BP FET device is shown in Figure 4.6(a). Figure 4.6(b) shows the typical optical photograph of the lithographically fabricated transistor device based on few layer BP nanosheets. The transistor characterization of the device was carried out in ambient conditions immediately after the annealing of the device using Keithley 4200 semiconductor analyzer. Figure 4.6(c) shows the representative linear output characteristics I_{ds} vs V_{ds} . The semilog transfer curves shown in Figure 4.6(d) of atomically thin BP nanosheets based FET shows *p-type* behavior.

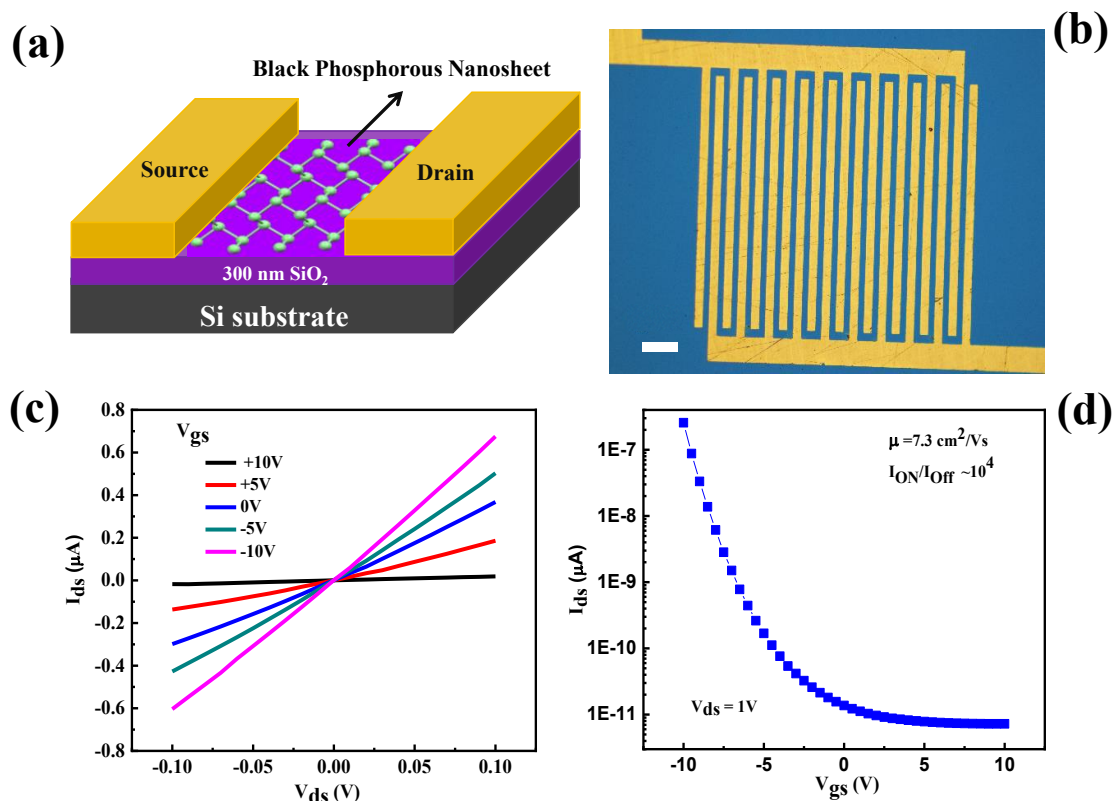


Figure 4.6: FET based on electrochemically exfoliated BP nanosheets (a) schematic diagram of the transistor device, (b) optical photograph of the photolithography prepared typical transistor device, (c) output characteristics of the transistor device, and (d) transfer characteristics of the transistor devices. Inset of (b) scale bar is 20 μm .

The I_{ds} - V_{gs} characteristics were performed at a bias ramp rate of 10 V/s in steps of 1 V. The field-effect mobility (μ) is obtained using this curve from the equation written below:^{54,55}

$$\mu_{FE} = \frac{dI_D}{dV_G} \left(\frac{L}{WC_iV_D} \right)$$

Where, dI_D/dV_G is the trans-conductance, C_i signifies capacitance of 300 nm thick SiO_2 (11 nF/cm²), V_D represents drain voltage, and L (150 μm) and W (5 μm) are the length and width of the channel, individually. The μ_{FE} and $I_{on/off}$ ratio of the BP device were found to be ~ 7.3 cm²/Vs and 10^4 respectively. The sub threshold swing of ~ 2 V/decade was calculated from the Figure 6(d).

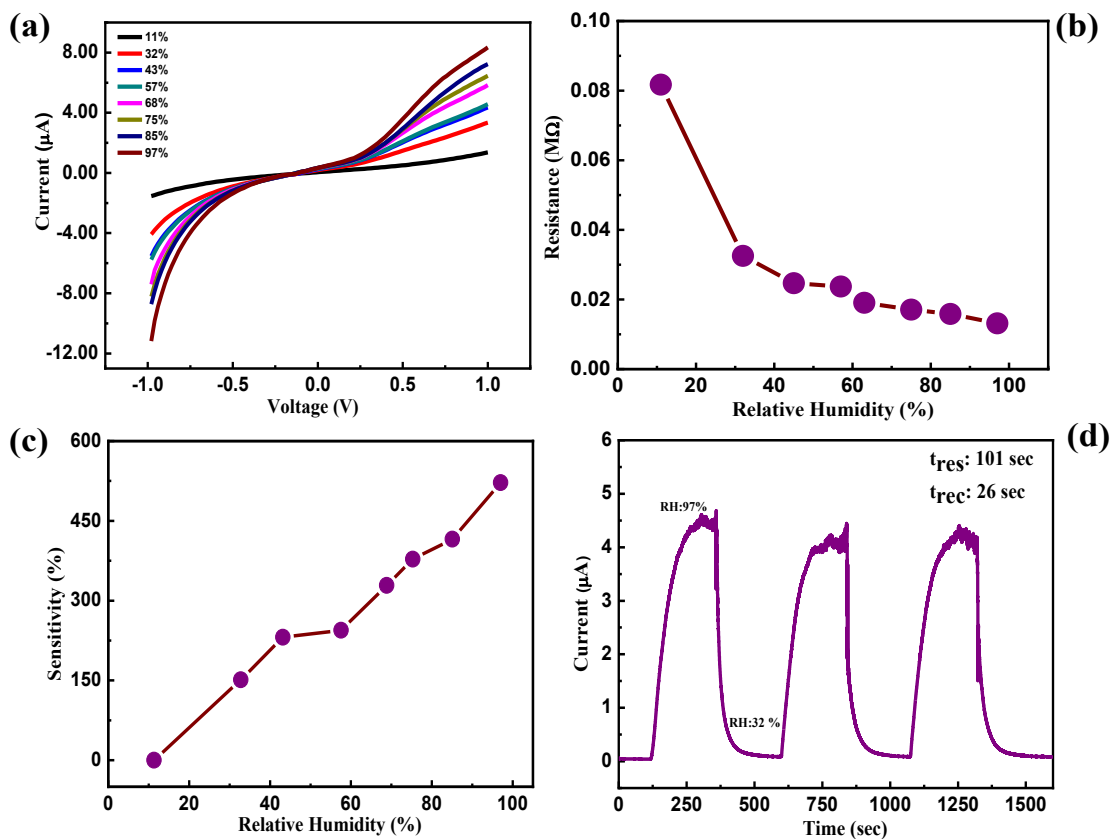


Figure 4.7: BP nanosheets (a) (I - V) characteristics at different RH, (b) resistance vs RH plot, (c) sensitivity vs RH plot, and (d) (I - t) plot for three cycles of humidity switching between 32% and 97%.

The values mentioned here for the μ_{FE} are belittle since we cannot ignore the contact resistances in our two-probe experiments. As a result, the actual mobility value is likely to be higher as per

the recent reports in the literature.^{40,42-45,47} It is noted that the BP transistor device kept in ambient, shows degradation in their performance with time.^{51,52}

4.3.3. Humidity Sensor

Further, the humidity sensing performance of atomically thin few layer BP nanosheets thick film sensor device were investigated. A recent literature reports concluded that single-layer BP device affect the performance of transistor device if kept in ambient.⁵¹⁻⁵² In this investigation, we have prepared thick film sensor device of few layer BP nanosheets sample and measured its I-V characteristics for various RH. It is observed that the slope of I-V increases as RH varies from 11% to 97%, as shown in Figure 4.7(a). The water vapor acts as e⁻ donor, hence the resistance of the device fabricated on BP nanosheets sample was observed to be decrease with the increasing RH as depicted in Figure 4.7(b). The results demonstrate that water molecules donates e⁻ to the BP sample where charge transfer takes place leads to change in the resistance of the device. The sensitivity vs RH plot shown in Figure 4.7(c) for BP sensor device. The sensitivity is obtained from the equation (1),

$$S = (R_{11} - R_{\Delta RH})/R_{\Delta RH} \quad \dots\dots\dots (1)$$

Where, R₁₁ and R_{ΔRH} are the resistances of the device in the 11% RH and change in relative humidity, individually. The maximum sensitivity value was observed to be ~521%. Figure 4.7(d) shows current-time (I-t) curve for the sensor device when the RH changes from 32% to 97%. From the I-t curve, it is clear that the response time of the thick film humidity sensor was found to be ~101 s, and the recovery time was found to be ~26 s which is comparable to other 2D inorganic layered materials such as MoS₂²⁶ and MoSe₂.³⁴ To see the repeatability in response and recovery time, we have carried out the I-t measurements for more than hundreds of cycles and three represented cycles were shown for the brevity. Moreover, the vibrant experimental results shown in Figure 4.7(d) indicate the good cyclic stability of the device depicting well-defined response to water molecules. It is expected that the atomically thin

nature of the sample shows quick response and fast recovery time which are the key important parameters for the advanced miniaturized next generation humidity sensor device. Remarkably, the bulk sample of BP is insensible toward the change of relative humidity; in that case, no noticeable change in the I-t plot could be observed under the alternating on/off cycle of the moisture due to the instability of the device as observed for the VS₂ based humidity sensor.⁵⁶ It is important to note that our BP nanosheets film humidity sensor device is quite thick, its properties are remarkably different from those of the bulk BP single crystal. For example, the resistance of our nanosheets film with few μm thicknesses in a low-humidity environment is on the order of a 0.081 M Ω at 11% RH, and in a high humidity environment, it is on the order of 0.013 M Ω at 97% RH. In the case of the bulk BP sample, the resistance is on the order of a few hundred ohms. This large difference is mainly attributed to the randomly stacked nanosheets in our thick film sensor device compared to a bulk single crystalline sample. The large channel resistance is a huge advantage for the sensing application purpose due to the ionic conduction through the absorbed water molecule layer can be measurable. This is not the case in bulk BP crystal due to its high conductance and instability at high current.⁵⁷ Briefly, the humidity sensing mechanism can be explained as follows. The sensitivity of the moisture is based on the top surface and side exposed P atoms. The electrons might move on the surface of the sheet along with side exposed atoms. In humidity sensing, water molecules get adsorbed on the surface of the nanosheet as well as on the side exposed atom. After water molecules adsorb on the surface of the nanosheet, an auto ionization reaction occurs, and the water molecule starts losing (H^+) protons and forms hydroxide ion (OH^-). This released proton then starts jumping from one to other water molecule results in the formation of hydronium ion. For relative humidity of (11%), the surface of the nanosheets gets partly covered by the water molecules so hopping of proton between neighboring sites of the water molecules results into slow charge transfer compared to higher humidity levels (97%). As it is expected that at higher

humidity level the surface of the nanosheets gets fully covered by the water molecules which increases the magnitude of charge transfer.⁵⁸ Interestingly, this results in an increase in the conductivity values, increasing the relative humidity levels. Therefore, proton acts as an effective carrier for the electrical conductivity. The suggested mechanism might also be influenced by the thickness of the sample and the operating conditions such as temperature, composition of gas phase, and hydroxylation of the nanosheet surface.

4.3.4 Photodetector

Figure 4.8(a) displays the I-V plots for the BP nanosheets under illumination of various intensities of UV light. The power densities were varied in the range from 0 to 200 mW/cm². It has been observed that for the few-layer BP nanosheets based photodetector, as the UV light intensity increases, the current of the device is found to increase. Figure 4.8(b) shows the photocurrent vs power density plot, and the equation to calculate photocurrent is $I_{ph} = I_{light} - I_{dark}$. The maximum photocurrent of $\sim 6.3451 \mu\text{A}$ was observed for the power density of $\sim 200 \text{ mW/cm}^2$. Figure 4.8(c) depicts the typical photoresponsivity Vs power density plot. The photoresponsivity can be calculated by using the following relation,⁵⁹

$$R = \frac{I_{ph}}{P_{light}}$$

Where, I_{ph} is the photocurrent and $P_{light} = W \times l \times L_{intensity}$, W is the width of the channel (1 cm), l is the channel length (300 μm), and $L_{intensity}$ is the light intensity. We observed that the decrease in photoresponsivity with the increasing power density. The maximum photoresponsivity of $\sim 1.51 \text{ mA/W}$ were noted for power density of 200 mW/cm^2 . Figure 4.8(d) shows the typical I-t cure for the illumination of UV light with 150 mW/cm^2 . To see the repeatability in the I-t cycle, we have carried out several hundred cycles, and the three representative cycles are shown for clarity. From the I-t plot response time and recovery time were found to be $\sim 15\text{s}$ and 30s , respectively.

The reported photo detector is more stable and reproducible under ambient conditions for more than a hundred cycles. The observed response and recovery times for the humidity sensor device were larger because of the charge trapping at the semiconductor interface. The main advantage of the present sensor and photodetector is that they perform at room temperature.

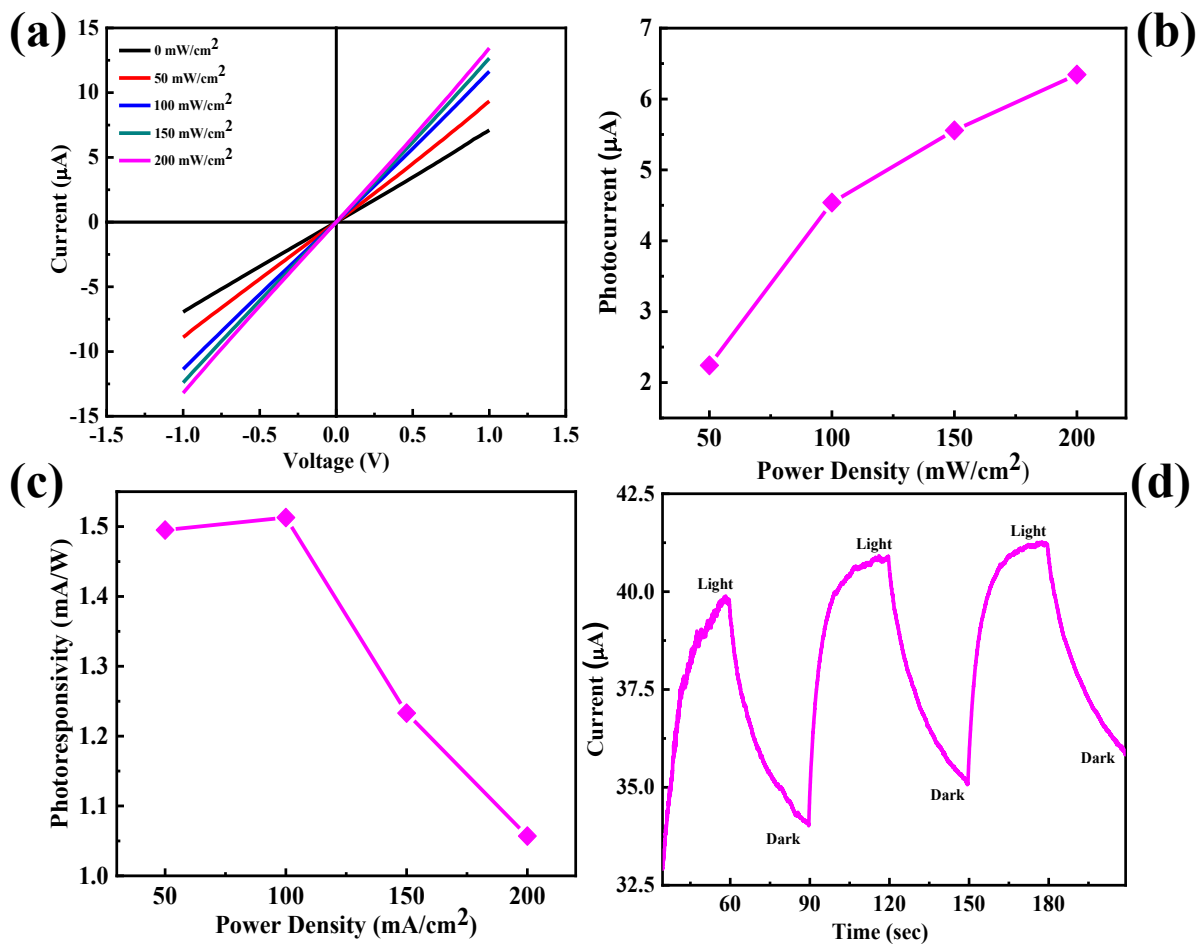


Figure 4.8: BP nanosheets (a) (I-V) characteristics at different UV light intensities. (b) Photocurrent Vs power density, (c) photoresponsivity Vs power density, and (d) I-t cycles on illumination of UV light of $150 \text{ mW}/\text{cm}^2$ and with applied bias of 2V .

It is also important to observe that the recovery of the device is not complete in all cycles, which is also found earlier in the graphene sensors^{13,60,61} and MoS_2 ,^{26,62,63} WS_2 ,⁶⁴ MoSe_2 ,³⁴ VS_2 ,⁵⁶ and other oxide-based sensors.^{65,66} Table 1 shows the comparative sensing data with the existing literature based on various nanomaterials.

Nanomaterial based sensors	Response Time (s)	Recovery Time (s)	Sensitivity (%)	Reference
Graphene Oxide	10.5	41	350	60
	20-30 (ms)	90-30 (ms)	–	61
MoS ₂	300	600	800	26
	90	110	–	62
WS ₂	5-10	600	400	64
MoSe ₂	150	540	1100	34
Black Phosphorus	60	30	150	67
	255	10	-99.17	70
VS ₂	30-40	12-50	3000	56
V ₂ O ₅	240	300	45.3	65
SnO ₂	120-170	20-60	3500	66
BP	101	26	521	Present work

Table 1: Comparative sensing data with the existing literature based on various nanomaterials.

Interestingly, we also notice that thin layer black phosphorus sample has better sensitivity, which seems counterintuitive. Our humidity sensor devices show better performance compared with the very recent report on the 55 nm thick BP nanosheet device toward NO₂ sensing⁶⁷ and BP thick film sensor.⁵⁷ It has been shown recently that the BP nanosheets are quite sensitive to the number of layers, metal contacts, and ambient conditions for field effect transistor characteristics,⁶⁸ and p-n junction diode.⁶⁹ The specific sensing mechanism is still under study and therefore complicated to understand right now, which requires further, more detailed investigation. The engineering of BP nanosheets with metal contacts, a controlled number of layers, and an oxygen-free environment might solve the issues related to better sensitivity, high mobility, and high ON/OFF ratio.

4.4 Conclusions

We report comprehensive suite electrochemical exfoliation of an atomically thin layer of BP nanosheets. We also present our investigation on few layer nanosheet thick film based BP photo detector, humidity sensor, and FET. In the case of the FET, it shows *p-type* behavior and the field effect mobility of $\sim 7.3 \text{ cm}^2/\text{Vs}$ and current ON/OFF ratio of $\sim 10^4$. The BP nanosheets based thick film sensor devices are more sensitive to water vapors and UV light. Further, BP based thick film devices open several avenues to improve the sensing performance and allow selective response to certain kinds of gases and humidities.

4.5 References and Notes

- 1) Novoselov, K. S.; Jiang, D.; Schedin, F.; Booth, T. J.; Khotkevich, V. V.; Morozov, S.V.; Geim, A. K. Two-dimensional Atomic Crystals. *Proc. Nat. Acad. Sci.* **2005**, *102*, 10451-10453.
- 2) Novoselov, K. S.; Geim, A. K.; Morozov, S. V.; Jiang, D.; Zhang, Y.; Dubonos, S. V.; Grigorieva, I. V.; Firsov, A. A. Electric Field Effect in Atomically Thin Carbon Films. *Science* **2004**, *306*, 666-669.
- 3) Novoselov, K. S.; Geim, A. K.; Morozov, S. V.; Jiang, D.; Katsnelson, M. I.; Grigorieva, I. V.; Dubonos, S.V.; Firsov, A. A. Two-Dimensional Gas of Massless Dirac Fermions in Graphene. *Nature* **2005**, *438*, 197-200.
- 4) Schwierz, F. Graphene Transistors. *Nat. Nanotech.* **2010**, *5*, 487-496.
- 5) Liao, L.; Bai, J.; Cheng, R.; Lin, Y.; Jiang, S.; Qu, Y.; Huang, Y.; Duan, X. F. Sub-100 nm Channel Length Graphene Transistors. *Nano Lett.* **2010**, *10*, 3952-3956.
- 6) Wang, Y.; Shi, Z. Q.; Huang, Y.; Ma, Y. F.; Wang, C. Y.; Chen, M. M.; Chen, Y. S. Supercapacitor Devices Based on Graphene Materials. *J. Phys. Chem. C* **2009**, *113*, 13103–13107.
- 7) Vivekchand, S. R. C.; Rout, C. S.; Subrahmanyam, K. S.; Govindaraj, A.; Rao, C. N. R. Graphene-Based Electrochemical Supercapacitors. *J. Chem. Sci.* **2008**, *120*, 9-13.
- 8) Stoller, M. D.; Park, S.; Zhu, Y.; An, J.; Ruoff, R. S. Graphene-Based Ultracapacitors. *Nano Lett.* **2008**, *8*, 3498-3502.
- 9) Arco, L. G.; Zhang, Y.; Schlenker, C. W.; Ryu, K.; Thompson, M. E.; Zhou, C. Continuous, Highly Flexible and Transparent Graphene Films by Chemical Vapor Deposition for Organic Photovoltaics. *ACS Nano* **2010**, *4*, 2865–2873.

- 10) Yang, N.; Zhai, J.; Wang, D.; Chen, Y.; Jiang, L. Two-Dimensional Graphene Bridges Enhanced Photo induced Charge Transport in Dye-Sensitized Solar Cells. *ACS Nano* **2010**, *4*, 887-894.
- 11) Jang, Y. H.; Xin, X.; Byun, M.; Jang, Y. J.; Lin, Z.; Kim, D. H. An Unconventional Route to High-Efficiency Dye-Sensitized Solar Cells via Embedding Graphitic Thin Films into TiO₂ Nanoparticle Photoanode. *Nano Lett.* **2012**, *12*, 479-485.
- 12) Li, X.; Zhu, H.; Wang, K.; Cao, A.; Wei, J.; Li, C.; Jia, Y.; Li, Z.; Li, X.; Wu, D. Graphene-On-Silicon Schottky Junction Solar Cells. *Adv. Mater.* **2010**, *22*, 2743-2748.
- 13) Ghosh, A.; Late, D. J.; Panchakarla, L. S.; Govindaraj, A.; Rao C. N. R. NO₂ and Humidity Sensing Characteristics of Few-Layer Graphene. *J. Exp. Nanosci.* **2009**, *4*, 313-322.
- 14) Schedin, F.; Geim, A. K.; Morozov, S. V.; Hill, E. W.; Blake, P.; Katsnelson, M. I.; Novoselov, K. S. Detection of Individual Gas Molecules Adsorbed On Graphene. *Nature Mater.* **2007**, *6*, 652-655.
- 15) Dan, Y. P.; Lu, Y.; Kybert, N. J.; Luo, Z.; Johnson, A. T. C. Intrinsic Response of Graphene Vapor Sensors. *Nano Lett.* **2009**, *9*, 1472-1475.
- 16) Fan, S.; Srivastava, A.; Dravid, V. P. Nanopatterned Polycrystalline ZnO for Room Temperature Gas Sensing. *Sens. Actuators, B* **2010**, *144*, 159-163.
- 17) Korotcenkov, G. Metal Oxides for Solid-State Gas Sensors: What Determines Our Choice? *Mat. Sci. Eng. B* **2007**, *139*, 1-23.
- 18) Doll, T.; Lechner, J.; Eisele, I.; Schierbaum, K.; Gopel, W. Ozone Detection in the ppb Range with Work Function Sensors Operating at Room Temperature. *Sens. Actuators, B* **1996**, *34*, 506-510.
- 19) Fan, S.; Srivastava, A.; Dravid, V. P. UV-Activated Room-Temperature Gas Sensing Mechanism of Polycrystalline ZnO. *Appl. Phys. Lett.* **2009**, *95*, 142106.

- 20) Peng, N.; Zhang, Q.; Lee, Y.; Tan, O.; Marzari, N. Gate Modulation in Carbon Nanotube Field Effect Transistors-Based NH₃ Gas Sensors. *Sens. Actuators, B* **2008**, *132*, 191-195.
- 21) Jariwala, D.; Sangwan, V. K.; Late, D. J.; Johns, J. E.; Dravid, V. P.; Marks, T. J.; Lauhon, L. J.; Hersam, M. C. Band-Like Transport in High Mobility Unencapsulated Single-Layer MoS₂ Transistors, *Appl. Phys. Lett.* **2013**, *102*, 173107.
- 22) Matte, H. S. S. R.; Gomathi, A.; Manna, A. K.; Late, D. J.; Datta, R.; Pati, S. K.; Rao, C. N. R. MoS₂ and WS₂ Analogues of Graphene. *Angew. Chem. Int. Ed.* **2010**, *49*, 4059-4062.
- 23) Late, D. J.; Liu, B.; Matte, H. S. S. R.; Rao, C. N. R.; Dravid, V. P. Rapid Characterization of Ultrathin Layers of Chalcogenides on SiO₂/Si Substrates. *Adv. Fun. Mater.* **2012**, *22*, 1894-1905.
- 24) Ghatak, S.; Pal, A. N.; Ghosh, A. Nature of Electronic States in Atomically Thin MoS₂ Field-Effect Transistors. *ACS Nano* **2011**, *5*, 7707-7712.
- 25) Late, D. J.; Liu, B.; Matte, H. S. S. R.; Dravid, V. P.; Rao, C. N. R. Hysteresis in Single-Layer MoS₂ Field Effect Transistors. *ACS Nano* **2012**, *6*, 5635- 5641.
- 26) Late, D. J.; Huang, Y.; Liu, B.; Luo, J.; Acharya, J.; Shirodkar, S. N.; Luo, J.; Yan, A.; Charles, D.; Waghmare, U. V.; Dravid, V. P.; Rao, C. N. R. Sensing Behavior of Atomically Thin-Layered MoS₂ Transistors. *ACS Nano* **2013**, *7*, 4879-4891.
- 27) Kashid, R. V.; Late, D. J.; Chou, S. S.; Huang, Y.; De, M.; Joag, D. S.; More, M. A.; Dravid, V. P. Enhanced Field-Emission Behavior of Layered MoS₂ Sheets. *Small* **2013**, *9*, 2730-2734.
- 28) Late, D. J.; Shaikh, P. A.; Khare, R.; Kashid, R. V.; Chaudhary, M.; More, M. A.; Ogale, S. B. Pulsed Laser Deposited MoS₂ Thin Films on W and Si: Field Emission and Photoresponse Studies. *ACS Appl. Mater. Interfaces* **2014**, *6*, 15881-15888.

- 29) Rout, C. S.; Joshi, P. D.; Kashid, R. V.; Joag, D. S.; More, M. A.; Simbeck, A. J.; Washington, M.; Nayak, S. K.; Late, D. J. Superior Field Emission Properties of Layered WS₂-RGO Nanocomposites. *Sci. Rep.* **2013**, *3*, 3282.
- 30) Braga, D.; Lezama, I. G.; Berger, H.; Morpurgo, A. F. Quantitative Determination of the Band Gap of WS₂ with Ambipolar Ionic Liquid Gated Transistors. *Nano Lett.* **2012**, *12*, 5218-5223.
- 31) Georgiou, T.; Jalil, R.; Belle, B. D.; Britnell, L.; Gorbachev, R. V.; Morozov, S. V.; Kim, Y. J.; Gholinia, A.; Haigh, S. J.; Makarovskiy, O.; Eaves, L.; Ponomarenko, L. A.; Geim, A. K.; Novoselov, K. S.; Mishchenko, A. Vertical Field Effect Transistor Based on Graphene-WS₂ Heterostructures for Flexible and Transparent Electronics. *Nat. Nanotechnol.* **2013**, *8*, 100-103.
- 32) Larentis, S.; Fallahazad, B.; Tutuc, E. Field Effect Transistors and Intrinsic Mobility in Ultrathin MoSe₂ Layers. *Appl. Phys. Lett.* **2012**, *101*, 223104.
- 33) Late, D. J.; Shirodkar, S. N.; Waghmare, U. V.; Dravid, V. P.; Rao, C. N. R. Thermal Expansion, Anharmonicity and Temperature-Dependent Raman Spectra of Single- and Few-Layer MoSe₂ and WSe₂. *ChemPhysChem.* **2014**, *15*, 1592-1598.
- 34) Late, D. J.; Doneux, T.; Bougouma, M. Single Layer MoSe₂ Based NH₃ Sensor, *Appl. Phys. Lett.* **2014**, *105*, 233103.
- 35) Allain, A.; Kis, A. Electron and Hole Mobilities in Single-Layer WSe₂. *ACS Nano* **2014**, *8*, 7180-7185.
- 36) Late, D. J.; Liu, B.; Luo, J.; Yan, A.; Matte, H. S. S. R.; Grayson, M.; Rao, C. N. R.; Dravid, V. P. GaS and GaSe Ultrathin Layer Transistors. *Adv. Mater.* **2012**, *24*, 3549-3554.
- 37) Warschauer, D. Electrical and Optical Properties of Crystalline Black Phosphorus. *J. Appl. Phys.* **1963**, *34*, 1853.

- 38) Nishii, T.; Maruyama, Y.; Inabe, T.; Shirotani, I. Synthesis and Characterization of Black Phosphorus Intercalation Compounds, *Synth. Met.* **1987**, *18*, 559-564.
- 39) Bridgman, P. M. Two New Modifications of Phosphorus. *J. Am. Chem. Soc.* **1914**, *36*, 1344-1363.
- 40) Li, L.; Yu, Y.; Ye, G. J.; Ge, Q.; Ou, X.; Wu, H.; Feng, D.; Chen, X. H.; Zhang, Y.; Black Phosphorus Field Effect Transistors. *Nat. Nanotech.* **2014**, *9*, 372- 377.
- 41) Wang, X.; Jones, A. M.; Seyler, K. L.; Tran, V.; Jia, Y.; Zhao, H.; Wang, H.; Yang, L.; Xu, X.; Xia, F., Highly Anisotropic and Robust Excitons in Monolayer Black Phosphorus, *Nat. Nanotechnol.* **2015**, *10*, 517-521.
- 42) Liu, H.; Neal, A. T.; Zhu, Z.; Luo, Z.; Xu, X.; Tomanek, D.; Ye, P. D. Phosphorene: An Unexplored 2D Semiconductor with a High Hole Mobility. *ACS Nano* **2014**, *8*, 4033- 4041.
- 43) Na, J.; Lee, Y. T.; Lim, J. A.; Hwang, D. K.; Kim, G.; Choi, W. K.; Song, Y. Few Layer Black Phosphorus Field-Effect Transistors with Reduced Current Fluctuation. *ACS Nano* **2014**, *8*, 11753- 11765.
- 44) Buscema, M.; Groenendijk, D. J.; Steele, G. A.; Zant, H. S. J.; Castellanos-Gomez, A. Photovoltaic Effect in Few Layer Black Phosphorus P-N Junctions Defined by Local Electrostatic Gating. *Nat. Comm.* **2014**, *5*, 4651- 4658.
- 45) Buscema, M.; Groenendijk, D. J.; Blanter, S. I.; Steele, G. A.; Zant, H. S. J.; Castellanos-Gomez, A. Fast and Broadband Photoresponse of Few-Layer Black Phosphorus Field-Effect Transistors. *Nano Lett.* **2014**, *14*, 3347-3352.
- 46) Du, Y.; Ouyang, C.; Shi, S.; Lei, M. Abinitio Studies on Atomic and Electronic Structures of Black Phosphorus. *J. Appl. Phys.* **2010**, *107*, 093718.
- 47) Qiao, J.; Kong, X.; Hu, Z.; Yang, F.; Ji, W. High Mobility Transport Anisotropy and Linear Dichroism in Few Layer Black Phosphorus. *Nat. Commun.* **2014**, *5*, 4475.

- 48) Zhang, S.; Yang, J.; Xu, R.; Wang, F.; Li, W.; Ghufran, M.; Zhang, Y.; Yu, Z.; Zhang, G.; Qin, Q.; Lu, Y. Extraordinary Photoluminescence and Strong Temperature/Angle-Dependent Raman Responses in Few-Layer Phosphorene. *ACS Nano* **2014**, *8*, 9590-9596.
- 49) Late, D. J., Temperature Dependent Phonon Shifts in Few-Layer Black Phosphorus, *ACS Appl. Mater. Interfaces* **2015**, *7*, 5857-5862.
- 50) Threlfall, R.E. 100 Years of Phosphorus Making: **1951**, 1851-1951. Oldbury: Albright and Wilson Ltd.
- 51) Ling, X.; Liang, L.; Huang, S.; Poretzky, A. A.; Geohegan, D. B.; Sumpter, B. G.; Kong, J.; Meunier, V.; Dresselhaus, M. S. Low Frequency Interlayer Breathing Modes in Few-Layer Black Phosphorus. *Nano Lett.* **2015**, *15*, 4080-4088.
- 52) Wood, J. D.; Wells, S. A.; Jariwala, D.; Chen, K.; Cho, E.; Sangwan, V. K.; Liu, X.; Lauhon, L. J.; Marks, T. J.; Hersam, M. C. Effective Passivation of Exfoliated Black Phosphorus Transistors against Ambient Degradation. *Nano Lett.* **2014**, *14*, 6964-6970.
- 53) Kim, J.; Liu, Y.; Zhu, W., Kim, S.; Wu, D.; Tao, L.; Dodabalapur, A.; Lai, K.; Akinwande, D. Toward Air Stable Multilayer Phosphorene Thin Films and Transistors. *Sci. Rep.* **2015**, *5*, 8989.
- 54) Late, D. J., Ghosh, A.; Subrahmanyam, K. S.; Panchakarla, L. S.; Krupanidhi, S. B.; Rao, C. N. R. Characteristics of Field Effect Transistors Based on Undoped and B-and N Doped Few-Layer Graphenes. *Solid State Comm.* **2010**, *150*, 734-738.
- 55) Li, L.; Ye, G. J.; Tran, Vy.; Fei, R.; Chen, G.; Wang, H.; Wang, J.; Watanabe, K.; Taniguchi, T.; Yang, L.; Chen, X. H.; Zhang, Y. Quantum Oscillations in a Two Dimensional Electron gas in Black Phosphorus Thin Films. *Nat. Nanotechnol.* **2015**, *10*, 608-613.

- 56) Feng, J.; Peng, L.; Wu, C.; Sun, X.; Hu, S.; Lin, C.; Dai, J.; Yang, Y.; Xie, Y. Giant Moisture Responsiveness of VS₂ Ultrathin Nanosheets for Novel Touchless Positioning Interface. *Adv. Mater.* **2012**, *24*, 1969-1974.
- 57) Yasaei, P.; Behranginia, A.; Foroozan, T.; Asadi, A.; Kim, K.; Khalili-Araghi, F.; Salehi-Khojin, A. Stable and Selective Humidity Sensing Using Stacked Black Phosphorus Flakes. *ACS Nano* **2015**, *9*, 9898-9905.
- 58) Farahani, H.; Wagiran, R.; Hamidon, M. N. Humidity Sensors Principle, Mechanism, and Fabrication Technologies: A Comprehensive Review. *Sensors* **2014**, *14*, 7881-7939.
- 59) Cao, Y.; Cai, K.; Hu, P.; Zhao, L.; Yan, T.; Zhang, X.; Wu, X.; Wang, K.; Zheng, H.; Strong Enhancement of Photoresponsivity with Shrinking the Electrodes Spacing in few Layer GaSe Photodetectors. *Sci. rep.* **2015**, *5*, 8130.
- 60) Bi, H.; Yin, K.; Xie, X.; Ji, J.; Wan, S.; Sun, L.; Terrones, M.; Dresselhaus, M. S.; Ultrahigh Humidity Sensitivity of Graphene Oxide. *Sci. Rep.* **2013**, *3*, 2714.
- 61) Borini, S.; White, R.; Wei, D.; Astley, M.; Haque, S.; Spigone, E.; Harris, N.; Kivioja, J.; Ryhanen, T.; Ultrafast Graphene Oxide Humidity Sensors. *ACS Nano* **2013**, *7*, 11166-11173.
- 62) Tan, Y.; Yu, K.; Yang, T.; Zhang, Q.; Cong, W.; Yin, H.; Zhang, Z.; Chen, Y.; Zhu, Z.; The Combinations of Hollow MoS₂ Micro@nano-spheres: One-step Synthesis, Excellent Photocatalytic and Humidity Sensing Properties. *J. Mater. Chem. C* **2014**, *2*, 5422-5430.
- 63) Kannan, P. K.; Late, D. J.; Morgan, H.; Rout, C. S.; Recent Developments in 2D Layered Inorganic Nanomaterials for Sensing. *Nanoscale* **2015**, *7*, 13293.

- 64) O'Brien, M.; Lee, K.; Morrish, R.; Berner, N.C.; McEvoy, N.; Wolden, C. A.; Duesberg, G. S. Plasma Assisted Synthesis of WS₂ For Gas Sensing Application, *ChemPhyLett.* **2014**, *615*, 6-10.
- 65) Pawar, M. S.; Bankar, P. K.; More, M. A.; Late, D. J.; Ultra-thin V₂O₅ Nanosheets Based Humidity Sensor, Photodetector and Its Enhanced Field Emission Properties. *RSC Adv.* **2015**, *5*, 88796 - 88804.
- 66) Kuang, Q.; Lao, C.; Wang, Z. L.; Xie, Z.; Zheng L.; High Sensitivity Humidity Sensor Based on a Single SnO₂ Nanowire. *J. Am. Chem. Soc.* **2007**, *129*, 6070-6071.
- 67) Abbas, A. N.; Liu, B.; Chen, L.; Ma, Y.; Cong, S.; Aroonyadet, N.; Kopf, M.; Nilges, T.; Zhou, C. Black Phosphorus Gas Sensors. *ACS Nano* **2015**, *9*, 5618-5624.
- 68) Perello, D. J.; Chae, S. H.; Song, S.; Lee, Y. H. High Performance n-Type Black Phosphorus Transistors with Type Control via Thickness and Contact Metal Engineering. *Nat. Commun.* **2015**, *6*, 7809.
- 69) Deng, Y.; Luo, Z.; Conrad, N. J.; Liu, H.; Gong, Y.; Najmaei, S.; Ajayan, P. M.; Lou, J.; Xu, X.; Ye, P. D. Black Phosphorus-Monolayer MoS₂ Van der Waals Heterojunction p-n Diode. *ACS Nano* **2014**, *8*, 8292.
- 70) Late, D. J. Liquid Exfoliation of Black Phosphorus Nanosheets and its Application as Humidity Sensor. *MicroporousMesoporous Mater.* **2016**, *225*, 494-503.

Chapter 5: High-Performance Sensing Behavior Using Electronic Ink of 2D SnSe₂ Nanosheets

The paper based on this chapter is published in ChemistrySelect

M. Pawar et al. *ChemistrySelect* **2017**, *2*, 4068.

5.1 Introduction

The detection of poisonous or dangerous gases is become most important for the environment monitoring, comprising our personal safety and manufacturing products and monitoring. To date gas sensors of various metal oxide nanostructures materials have been widely investigated and shown excellent sensing performance towards hazardous gases such as NO_2 , NH_3 and H_2S .¹⁻⁴ The gas sensors fabricated on semiconductor oxides materials displays superior performance in terms of sensitivity and selectivity, but they works at high temperature, which generate several questions related to high power consumption and safety related issues. Considering these restrictions researchers are still in the phase of developing highly sensitive gas sensors with few atom thin in nature and more importantly which can functions at room temperature. The carbon nanotubes⁵⁻⁷ and graphene⁸⁻¹⁰ have shown quick response and maximum sensitivity towards detection of single molecule of poisonous gases. The reports on graphene interaction with gas molecules clearly depicts that it can be suitable candidate for sensor device.⁸⁻⁹ The increase in charge carrier concentration induced by gas molecules adsorbed on the graphene can be used to fabricate highly sensitive gas sensors.⁸⁻⁹ As graphene is a semi metallic in nature, due to which there is limitation on removal of the physisorbed gas molecules from the nanosheet surface. Considering this fact it require longer time to recover the original resistance.¹⁰ Further, the theoretical and experimental investigations suggest that the gas molecules adsorb on the two-dimensional (2D) inorganic transition-metal dichalcogenides (TMDCs) nanosheets such as MoS_2 ,¹¹⁻¹³ WS_2 ,¹⁴ MoSe_2 ,¹⁵ BP¹⁶⁻¹⁸ etc. have ability to improve the response / recovery time and sensitivity. In contrast to graphene, TMDCs have recently been received a considerable attention because of semiconducting in nature and tunable bandgap¹⁹⁻²⁰ The 2D materials such as MoS_2 ,¹¹⁻¹³ WS_2 ,¹⁴ MoSe_2 ,¹⁵ Black Phosphorous¹⁶⁻¹⁸ possess remarkable properties at the mono or few-layer level and have been integrated into gas sensing devices. The atomically thin layered SnSe_2 is a sandwich of Se and

Sn atoms where Sn atom is sandwiched between two Se atoms via covalent bonds in the upright direction creating Se-Sn-Se layer structure.²¹⁻²⁴ In monolayer SnSe₂, the Sn-Se distance is 2.793 Å and the Se-Se distance is 3.293 Å and the lattice constant $|a| = 3.321$ Å. The monolayer SnSe₂ has a larger atomic radius of the Se atoms compared to monolayer MoS₂ and WS₂ hence it possesses larger atomic structure. Like other TMDCs, SnSe₂ also holds indirect band gap 1.0 eV, whereas monolayer SnSe₂ possess direct band gap of 1.4 eV, which facilitate the fabrication of switchable transistors²⁴ and extremely responsive photodetector devices.²⁵⁻²⁶ Recent experimental reports shows that the SnSe₂ nanosheets have a potential candidate to be used in new generation vdW vertical heterojunctions devices.²⁷ In the view of growing attention of atomically thin layer SnSe₂ for possible gas sensor device applications, it is essential to examine the gas sensing performance of this layered material. The electronic and optical properties of other layered materials such as MoS₂,²⁸⁻³¹ WS₂,³²⁻³³ MoSe₂,³⁴⁻³⁵ WSe₂,³⁶⁻³⁸ GaS,³⁹ GaSe,³⁹ Black Phosphorus⁴⁰ have been widely studied but the sensing investigations of 2D SnSe₂ layered crystals has not yet been reported. In this work, we report liquid exfoliation of few layer SnSe₂ nanosheets using ultrasonication and explore for gas sensing applications. Considering atomically thin nature and good mechanical sturdiness, our results open up exploratory paths for use of 2D SnSe₂ nanosheets ink as appropriate contender for humidity and toxic gas sensor applications.

5.2 Experimental section

Liquid Exfoliation of 2D SnSe₂ Nanosheets

The bulk single crystal SnSe₂ sample was purchased from 2D Semiconductors CA USA (purity 99.998%). The SnSe₂ nanosheets were synthesized by facile liquid exfoliation method through ultrasonication bath in NMP solvent. For the exfoliation we have taken SnSe₂ bulk crystal dispersed in NMP using ultrasonication further continued for 10h. The temperature of sonicator

bath was controlled by circulating continuous flow of water through pump. Followed by exfoliation, the SnSe₂ nanosheets of different thickness and lateral dimension were collected after centrifuging the sample at different rpm such as 1000 rpm, 3000 rpm and 5000 rpm. After 10 h the exfoliated dispersion of nanosheets were centrifuged (REMI R-8C BL centrifuge) at 1000 rpm for 10 min and the supernatant was subjected for the centrifugation at 3000 rpm. Thereafter, supernatant remained in the centrifuge tube was again centrifuged at 5000 rpm for 10 min and settled product is then collected. The samples obtained from centrifugation were allowed to dry in vacuum oven for 6 h at 90°C. Further, SnSe₂ nanosheets were dispersed in ethanol via sonication for 10 min to obtain appropriate dispersal of the nanosheets ink. The resultant dispersion of 2D SnSe₂ nanosheets ink samples were then used for characterization and device fabrications.

Material Characterizations details

For the structural investigations, Horiba JY Lab Raman HR 800 Micro Raman Spectrometer was used having wavelength 632.8 nm and power ~ 30mW. The AFM was carried out using the instrument Nanosurf Easyscan2. HR-TEM images were acquired using JEOL JEM-2200FS Transmission Electron Microscope operating at 200 kV instrument.

5.3 Results and Discussion

5.3.1 Material characterization

The Figure 5.1(a) shows the typical SnSe₂ nanosheets exfoliation process using N-Methyl-2-pyrrolidone (NMP) via ultrasonication bath for 10 h. The optical photograph of SnSe₂ nanosheet ink sample synthesized with ultrasonication and after various centrifugation rate was also recorded. Figure 5.1(b) shows the typical schematic and optical photograph of SnSe₂ sample after 10 h of ultrasonication without any centrifuge. The typical optical photograph of

SnSe₂ sample centrifuged for 10 min at 1000 rpm, 3000 rpm and 5000 rpm respectively can also be seen in Figure 5.1(b).

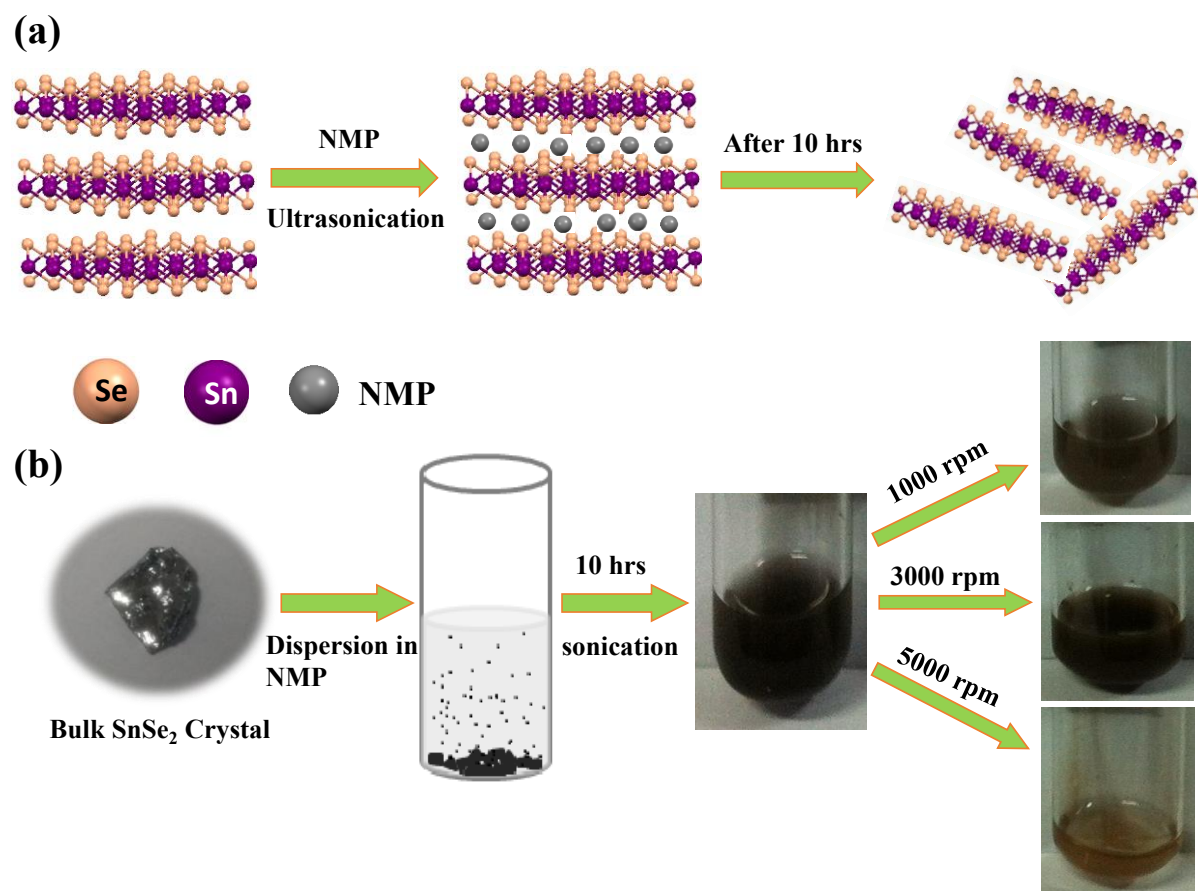


Figure 5.1: (a) SnSe₂ nanosheets exfoliation using NMP via ultrasonication bath for 10 h. (b) schematic and optical photograph of SnSe₂ nanosheets without centrifuge and centrifuge at 1000 rpm, 3000 rpm and 5000 rpm respectively.

The change in color clearly reflects the reduction in the size and thickness of SnSe₂ nanosheet. It is important to note that all the nanosheets samples were well dispersed in NMP. The dispersed sample can be used like ink to transfer on any desired substrate for various nanoelectronic device applications. Figure 5.2(a) shows the side view of SnSe₂ crystal structure and (b) shows the top view of single-layer SnSe₂. The Raman spectroscopy was used to investigate the structural information of the SnSe₂ nanosheets. The Figure 5.2(c) shows the Raman spectras for SnSe₂ bulk crystal and nanosheet samples centrifuged at different rpm. The two main peaks were observed at 109 cm⁻¹ and 180 cm⁻¹ are characteristic of the SnSe₂ phase.

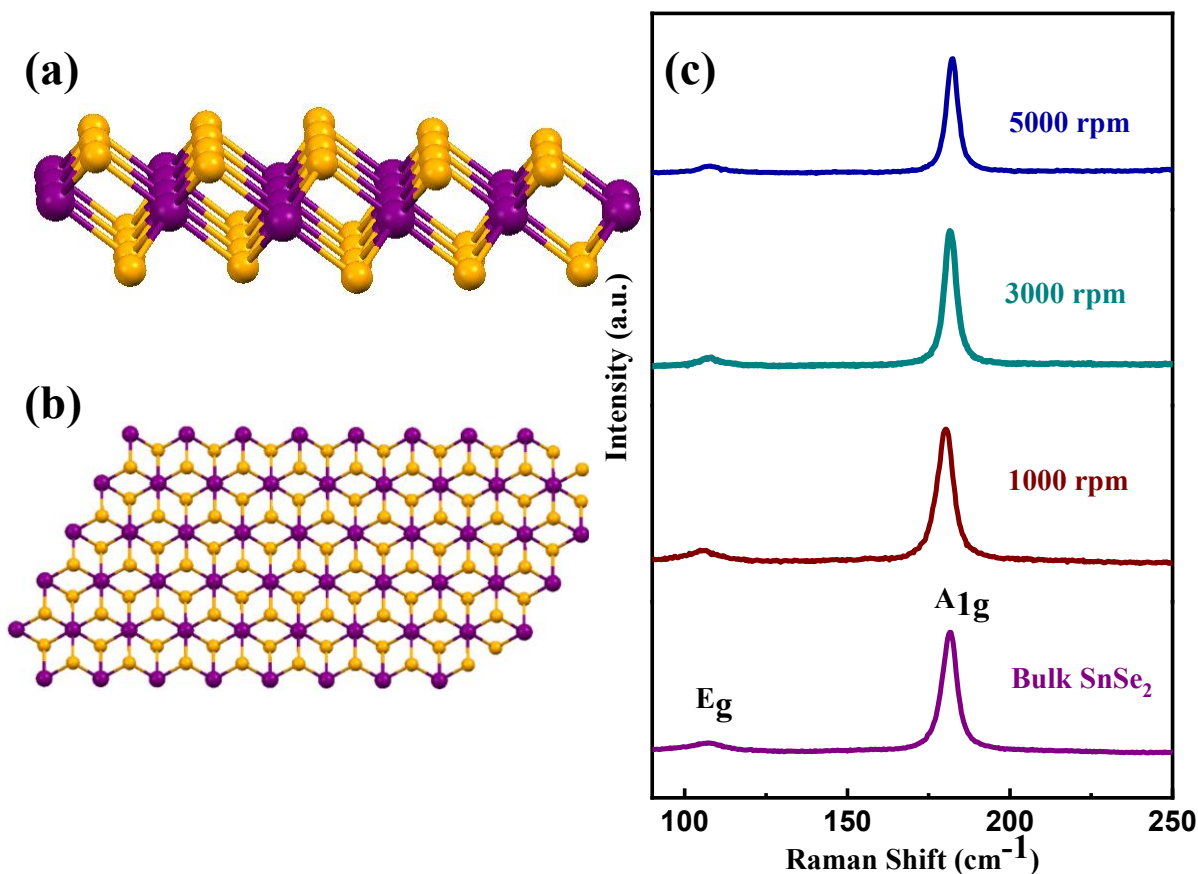


Figure 5.2: (a) Typical SnSe₂ crystal structure side view, (b) Top view and (c) Comparative Raman spectra of SnSe₂ bulk crystal and nanosheets samples prepared at different rpm.

The first peak refers to the E_g mode and the second peak refer to the A_{1g} mode. The typical Raman spectra of nanosheet sample depicts the change in intensity, shift in peak position and slight increase in FWHM as compared with that of bulk SnSe₂ crystal. Further, the TEM analysis was carried out on SnSe₂ samples centrifuged at 1000 rpm, 3000 rpm and 5000 rpm respectively. The sample collected at 1000 rpm has been analyzed by TEM and results were depicted in the Figure 5.3(a,b). The TEM analysis clearly shows the sheet like morphology seen in Figure 5.3(a). The typical TEM image also confirms the thick and bulky nature of the SnSe₂ nanosheets. The morphology and average size of the sample were analyzed from the TEM measurements and which shows sheet like morphology with average lateral dimensions ~2 μm. Figure 5.3(b) presents the HRTEM image captured on the side of the nanosheets, which gives precise structural information and highly crystalline nature of the sample.

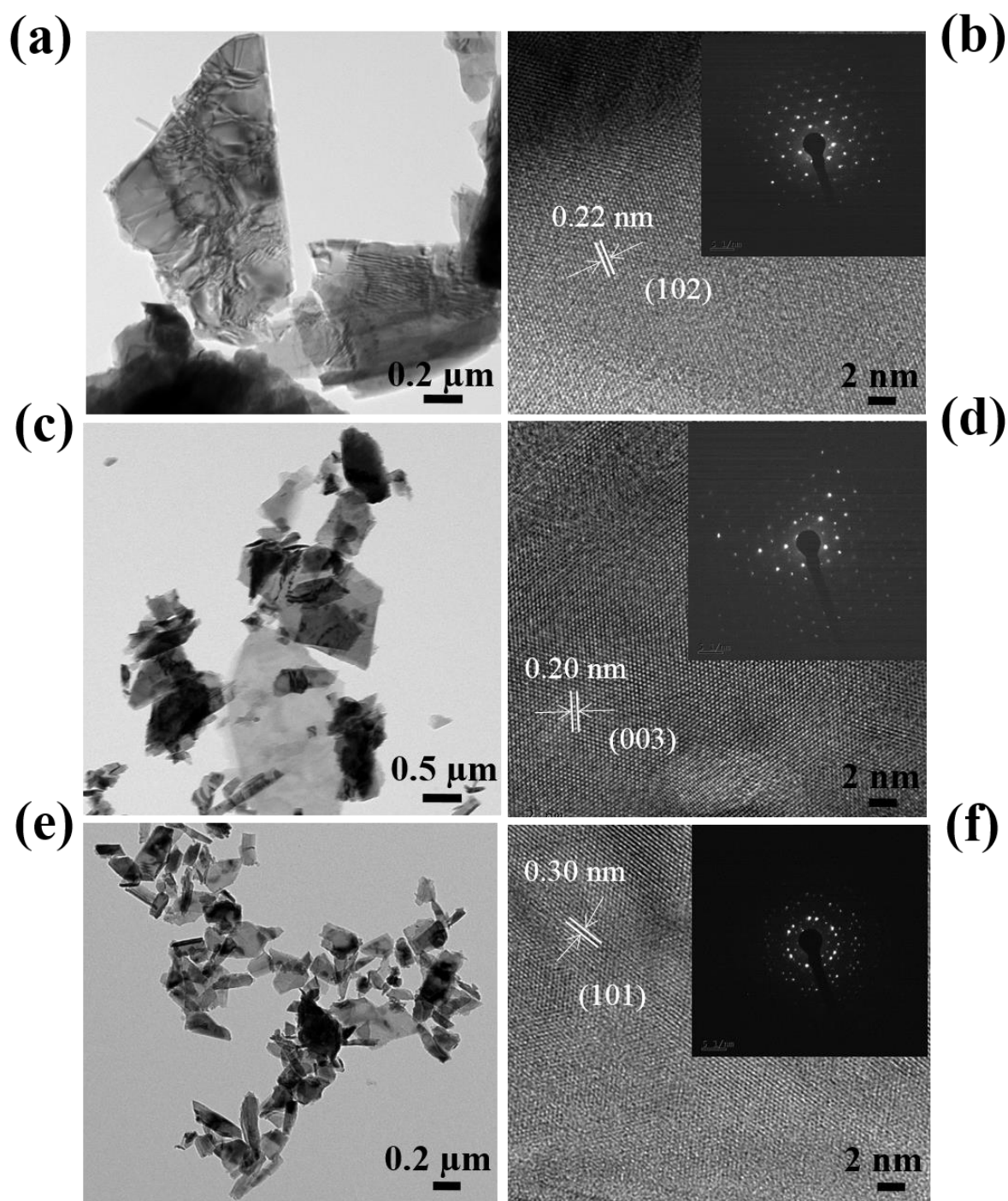


Figure 5.3: TEM characterization of exfoliated SnSe_2 nanosheets (a, c and e) typical low-magnification TEM image and (b, d and f) HRTEM images and inset of (b, d and f) SAED pattern for 1000 rpm, 3000 rpm, and 5000 rpm sample respectively.

The lattice spacing were found to be ~ 0.224 nm which matches well with (102) plane. The inset of figure 5.3(b) shows the typical SAED pattern of sample which depicts highly crystalline nature of the SnSe_2 sample. TEM images taken for the sample collected at 3000 rpm

are shown in Figure 5.3(c). The TEM shows the sheet like morphology with typical sheet dimension of 1-2 μm . The Figure 5.3(d) shows the HRTEM image of the sample confirming highly crystalline nature of sample. The lattice spacing of ~ 0.2 nm corresponding to (003) plane was recorded from the HRTEM image. The inset of Figure 5.3(d) shows the SAED pattern which clearly shows the highly crystalline nature of the SnSe_2 nanosheet sample. Figure 5.3(e) shows the typical TEM image of the sample collected at 5000 rpm showing the sheet like morphology with typical sheet dimension of 200-500 nm.

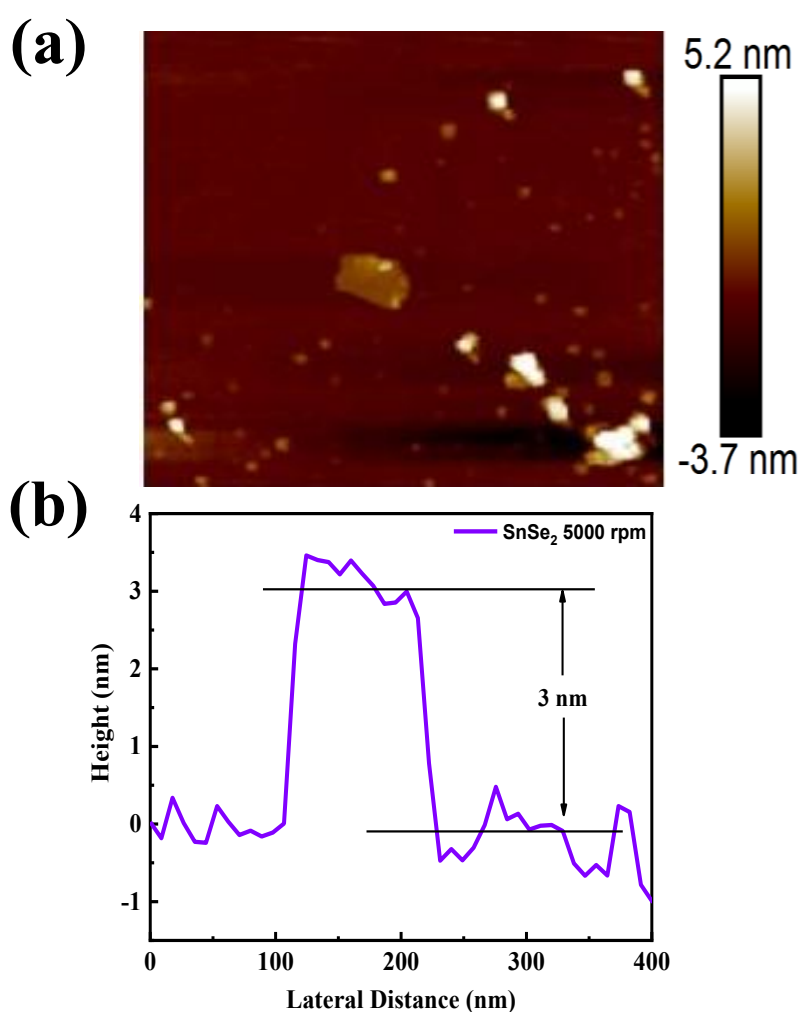


Figure 5.4: (a) AFM image and (b) corresponding height profile plot for the SnSe_2 nanosheets (5000 rpm sample).

The Figure 5.3(f) shows the typical HRTEM image of the sample confirming the highly crystalline nature of the sample collected at 5000 rpm. The lattice spacing was also measured

from the HRTEM image showing ~ 0.3 nm which corresponds to the (101) plane. The inset of Figure 5.3(f) shows the typical SAED pattern of sample which depicts the crystalline nature of the SnSe₂ sample collected at 5000 rpm.

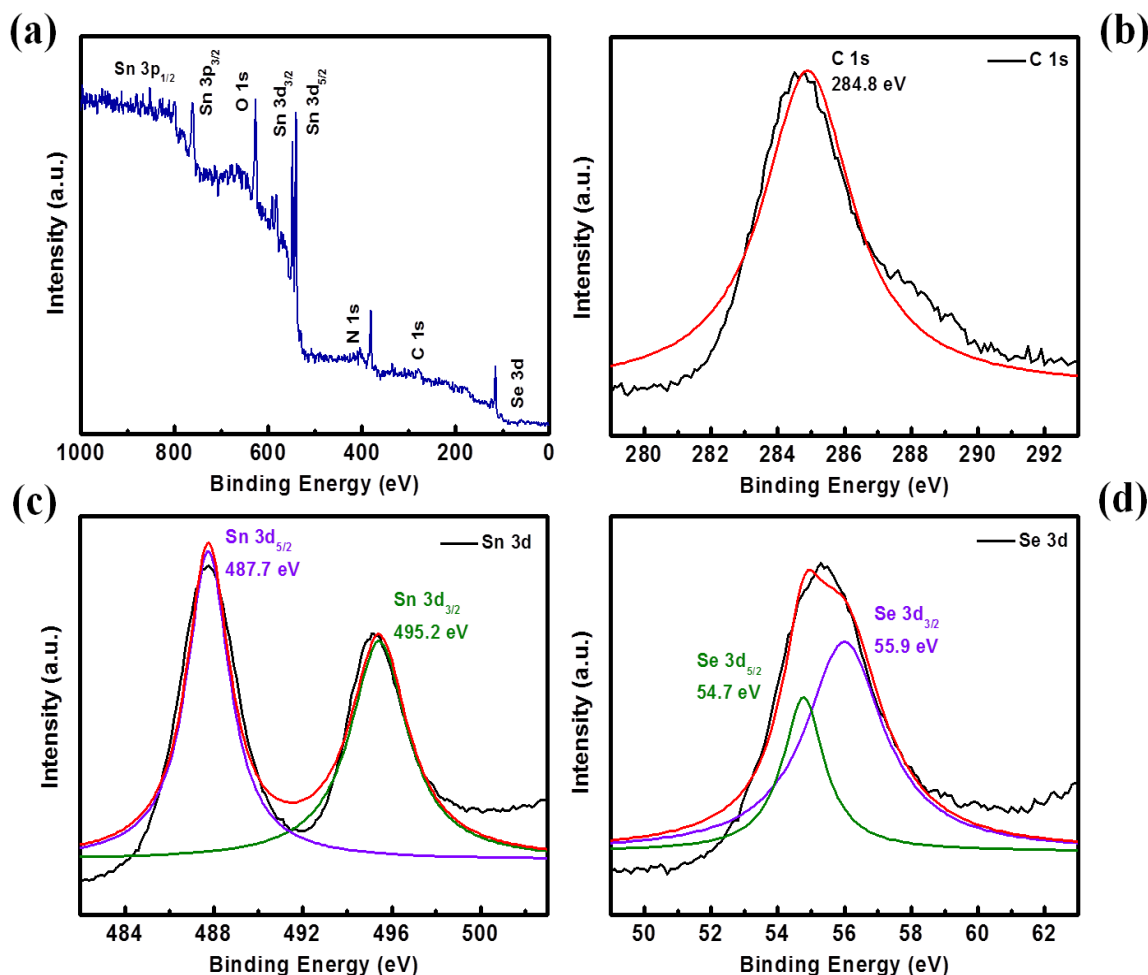


Figure 5.5: XPS spectra of SnSe₂ nanosheets sample centrifuged at 1000 rpm (a) survey spectrum, core level XPS spectra for (b) C 1s, (c) Sn 3d and (d) Se 3d.

From the TEM analysis it is clear that there is presence of transparent sheet possessing less thickness in 3000 rpm and 5000 rpm sample than that of 1000 rpm sample. Further the AFM analysis was used to find out the thickness of the as synthesized sample. The Figure 5.4 shows the typical AFM images and corresponding height profile for the three different samples. The AFM images shows sheet like morphology along with typical thickness for 1000 rpm sample was found to be ~ 170 nm, for 3000 rpm thickness was found to be ~ 8 nm and for the sample prepared at 5000 rpm the average thickness of nanosheets sample was found to be 2.5 nm.

The elemental analysis of the 1000 rpm SnSe₂ nanosheet sample was investigated by using XPS. Figure 5.5(a) show the survey spectra for SnSe₂ nanosheets, (b) shows the C 1s Spectra, (c) and (d) shows deconvoluted XPS spectras for Sn and Se elements.

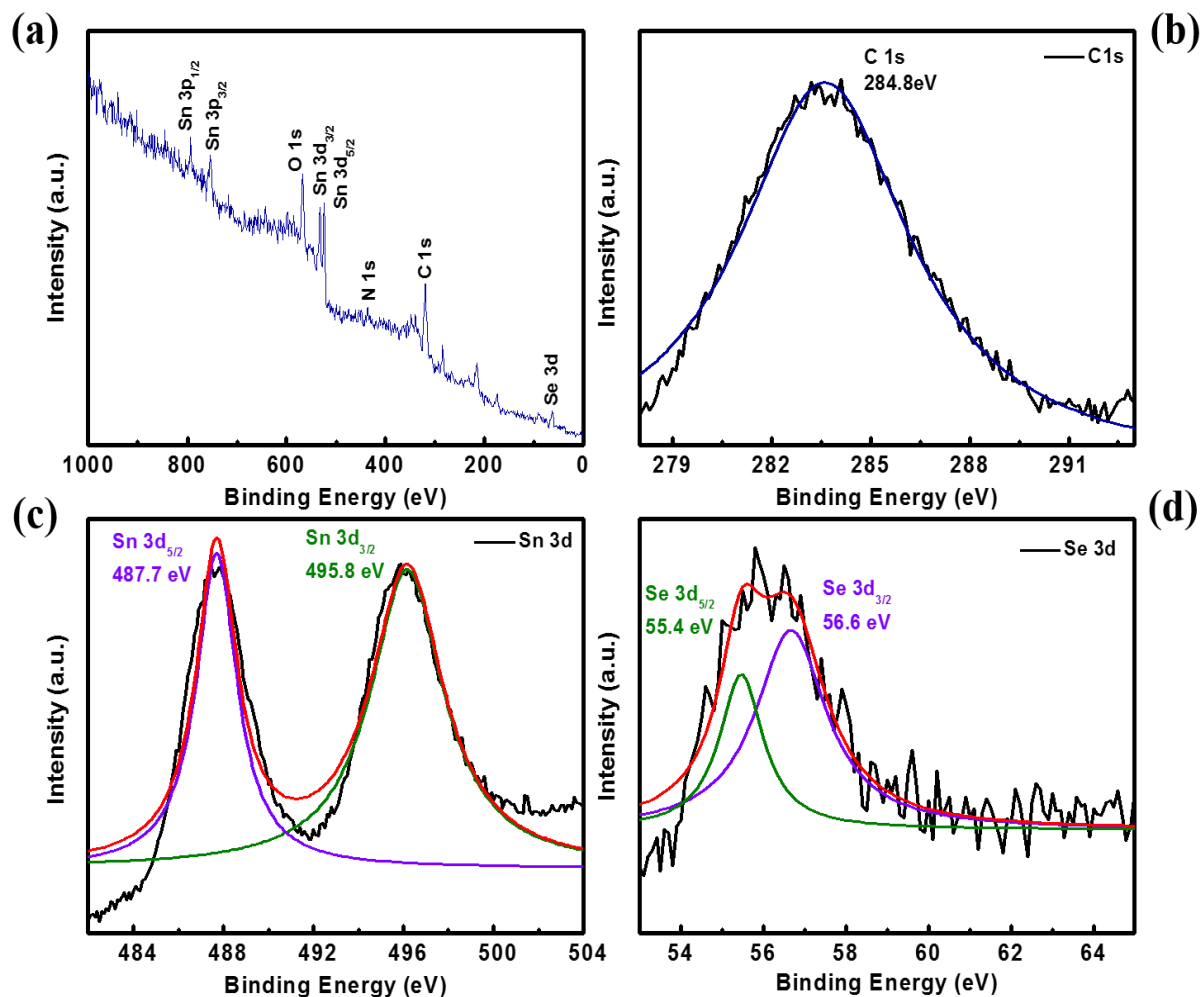


Figure 5.6: XPS spectra of SnSe₂ bulk crystal (a) survey spectrum, core level XPS spectra for (b) C 1s, (c) Sn 3d and (d) Se 3d.

The Sn 3d_{5/2} and Sn 3d_{3/2} peaks for nanosheet sample observed at 487.7 eV, 495.2 eV individually confirms an indication of the existence of (+2) oxidation state of Sn. Also, the peak of 487.7 eV was observed for Sn which indicates the Sn in (+4) oxidation state⁴¹⁻⁴³. Figure 5.5(d) shows the Se 3d_{5/2} and Se 3d_{3/2} peaks appeared at 54.7 eV and 55.9 eV respectively, which further confirms the formation of SnSe₂ stoichiometry.⁴⁴⁻⁴⁶ The Figure 5.6 shows the XPS spectra for the bulk SnSe₂ sample. It consists of (a) survey spectra for bulk SnSe₂ (b) C

1s spectra and (c, d) represents core level XPS spectra of Sn and Se, the Sn 3d_{5/2} and Sn 3d_{3/2} peaks appeared at 487.7 eV and 495.8 eV respectively. The figure 5.6(d) shows the Se 3d_{5/2} and Se 3d_{3/2} peaks appeared at 55.4 eV and 56.6 eV respectively. The binding energies of SnSe₂nanosheet sample were observed to be slightly lower than that of bulk SnSe₂ sample. This slight change in binding energy is due to the alteration in the chemical bonding of respective element (For detail comparison see the Table 1).

Sample	B.E. (eV)	Sn 3d		Se 3d	
		3d _{5/2}	3d _{3/2}	3d _{5/2}	3d _{3/2}
SnSe ₂ Bulk		487.7	495.8	55.4	56.6
SnSe ₂ Nanosheets (1000 rpm)		487.7	495.2	54.7	55.9

Table 1: The comparative B.E. values calculated from XPS spectrum for Sn 3d and Se 3d for bulk and nanosheet SnSe₂ sample. The table also shows the detailed binding energies of Sn (3d_{5/2} and 3d_{3/2}) and Se (3d_{5/2} and 3d_{3/2}) for SnSe₂.

5.3.2 Humidity sensor

For the humidity and gas sensing measurements, the nanosheets ink were drop casted onto the electrode. The change in resistance of the device with various RH levels was recorded and analyzed. Figure 5.7(a) shows the resistance Vs RH plot for 1000 rpm sample and from the plot it is clear that there is remarkable decrease in the resistance from 18.99 GΩ to 1.56 MΩ. The sensitivity Vs RH plot was displayed in figure 5.7(b). Inset of 5.7(b) shows the typical two-probe sensor device. The sensitivity for SnSe₂ nanosheets based humidity sensor device

were defined as $S = (R_{11} - R_{\Delta RH}) / R_{\Delta RH}$, where R_{11} is the resistance of the sensor device in 11% RH, and $R_{\Delta RH}$ is the resistance of the sensor device in various relative humidity.

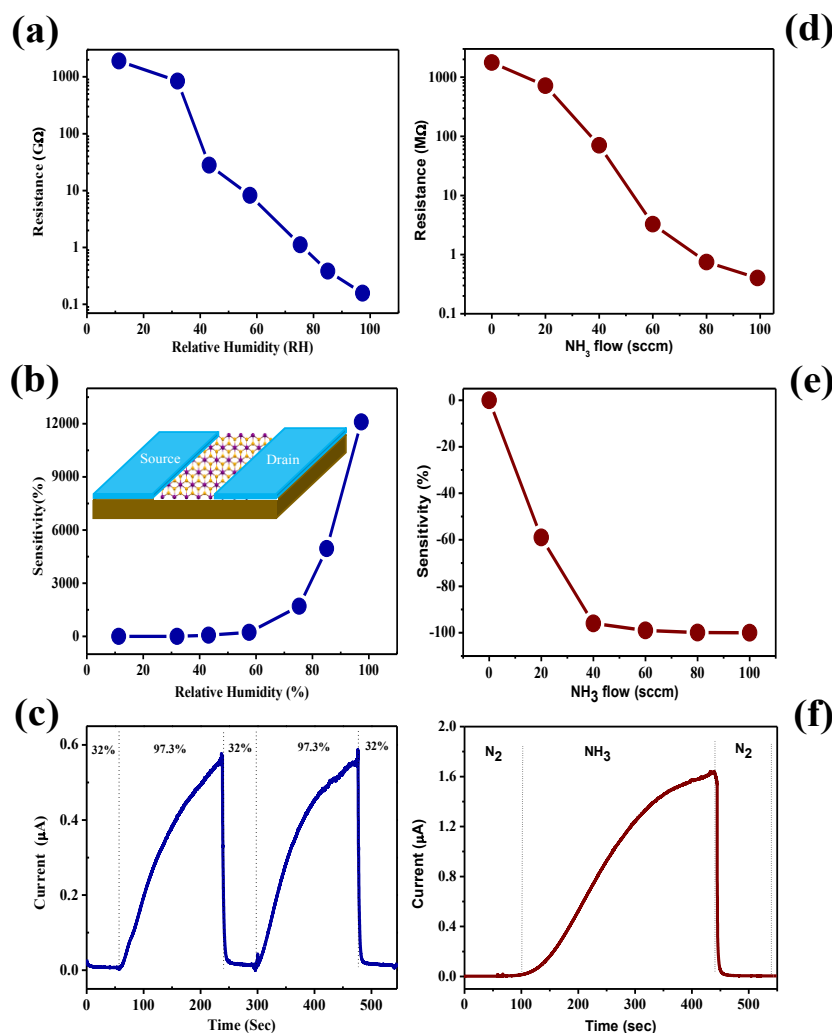


Figure 5.7: Humidity and NH_3 gas sensors based on SnSe_2 nanosheet ink sample synthesized at 1000 rpm (a) Resistance vs RH plot (b) Sensitivity vs RH plot and (c) (I-t) plot for two cycles for lower and higher humidity levels. The inset of (b) shows typical humidity sensor device. NH_3 gas sensor based on 2D SnSe_2 nanosheets ink sample synthesized at 1000 rpm (d) typical resistance vs NH_3 gas flow rate, (e) Sensitivity vs NH_3 gas concentrations and (f) typical I-t plot for NH_3 gas sensor device.

We have observed maximum sensitivity of $\sim 12,103\%$ for the RH of 97% for the sample synthesized at 1000 rpm. The figure 5.7(c) shows the typical I-t plot where the cycles of 32.78%

and 97.3% RH levels were used to calculate the response and recovery time. The response and recovery time for the SnSe₂ nanosheets based sensor device were found to be 167 sec and 12 sec respectively. The high response time is might be due to the rate of adsorption of water molecules on the surface of SnSe₂ nanosheets based sensor is less.

5.3.3 NH₃ gas sensor

The SnSe₂ nanosheets sample centrifuged at 1000 rpm was also tested for NH₃ gas sensing application. Figure 5.7(d) shows the typical resistance of the sensor device Vs NH₃ gas flow (sccm) plot.

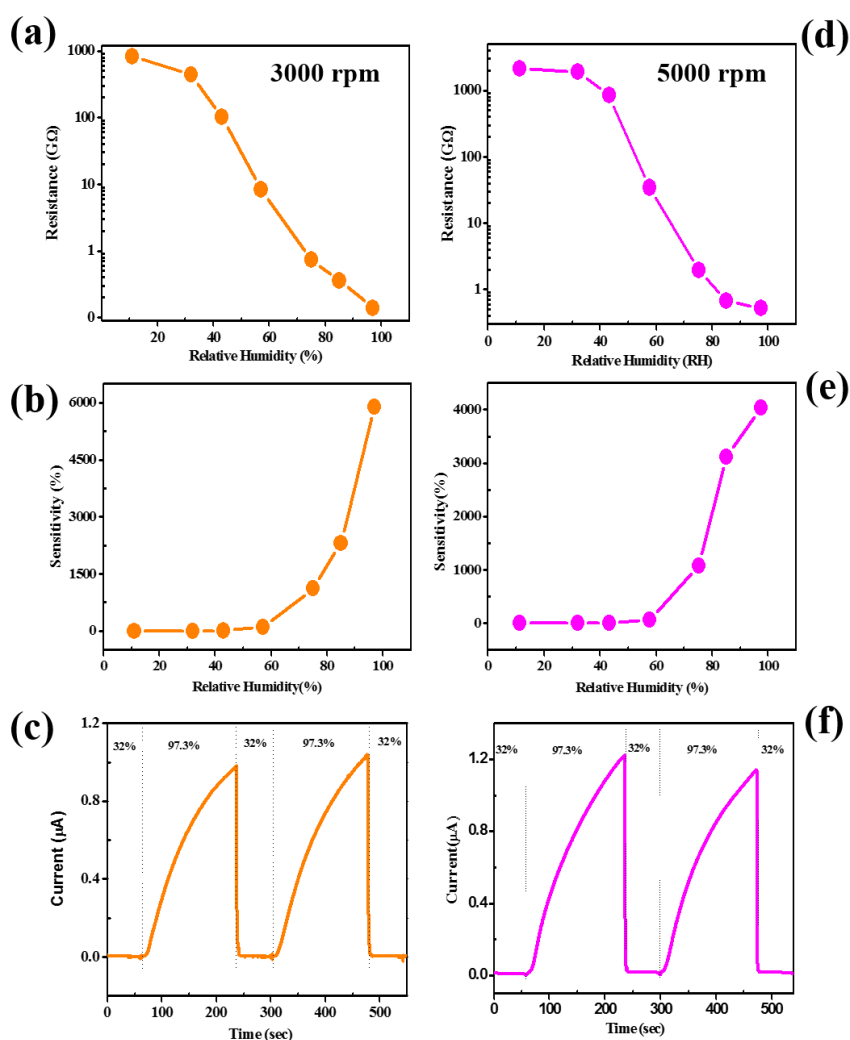


Figure 5.8: Humidity sensor based on SnSe₂ nanosheets synthesized at 3000 rpm and 5000 rpm (a,d) Resistance Vs RH plot (b,c) Sensitivity Vs RH plot and (c,f) (I-t) plot for two cycles of humidity respectively.

The sensing result clearly indicates the resistance decreases with respect to increasing gas flow. The sensitivity varies as the function of gas flow as shown in Figure 5.7(e). The maximum sensitivity of -99.97% were observed for NH_3 gas flow of 100 sccm. Figure 5.7(f) shows the typical I-t plot for NH_3 gas sensor based on SnSe_2 nanosheets. The typical response time of ~ 264 sec and recovery time of ~ 26 sec were noted. The typical resistance Vs relative humidity plot for the humidity sensor based on SnSe_2 nanosheets sample synthesized at 3000 rpm were shown in Figure 5.8(a). From the plot it is clear that there is remarkable decrease in the resistance from $8.21 \text{ G}\Omega$ to $1.39 \text{ M}\Omega$. The Figure 5.8(b) shows the plot of sensitivity Vs RH. The sensitivity factor was calculated to be $\sim 5894\%$ for SnSe_2 nanosheets sample collected at 3000 rpm. The (I-t) plot has been recorded to investigate the response and recovery time as shown in Figure 5.8(c). The response and recovery time for the SnSe_2 nanosheets based humidity sensor device were found to be 163 sec and 7 sec respectively. The Figure 5.8(d) shows the typical resistance Vs RH plot for 5000 rpm sample and from the plot it is clear that there is remarkable decrease in the resistance from $21.15 \text{ G}\Omega$ to $5.24 \text{ M}\Omega$. The typical plot of sensitivity Vs RH shown in Figure 5.8(e). The sensitivity factor was calculated to be $\sim 4034\%$ for SnSe_2 nanosheets sample collected at 5000 rpm. The response and recovery time values were calculated from the I-t plot shown in figure 5.8(f). The response and recovery time for the SnSe_2 nanosheets based humidity sensor device were found to be 160 sec and 4 sec respectively. The response of the SnSe_2 sensors device is restricted by strong adsorption of gas molecules. The thermodynamic process may not be much superior for adsorption of gas molecules on SnSe_2 nanosheet surface due which we noted prolonged response time. In other hand the gas molecules easily get desorbs during the recovery time due to little absorption energy. The response of sensor device can be tuned by keeping the device at higher temperature or by light irradiation.

The 2D SnSe₂ nanosheets shows superior performance as compared with other 2D nanomaterials such as MoS₂,¹³ WS₂,⁴⁷ MoSe₂,¹⁷ BP,⁴⁸ VS₂⁴⁹ and Graphene Oxide⁵⁰ (see the below Table 2).

Sr. No	Name of 2D nanomaterial	Response Time (sec)	Recovery Time (sec)	Sensitivity (%)	References
1	MoS ₂	600	Few sec	800	13
2	WS ₂	Few sec	<600	400	47
3	MoSe ₂	150	540	1100	15
4	Black Phosphorus	60	30	150	48
5	VS ₂	30-40	12-50	3000	49
6	Graphene Oxide	10.5	41	350	50
7	SnSe ₂				
	1000 rpm	168	12	12103	Present work
		163	7	5894	
	3000 rpm	160	4	4034	
	5000 rpm				

Table 2: Comparative data for sensitivity, response and recovery time of the various 2D nanomaterials.

The sensitivity value depends on the number of water molecules adsorbing on the surface of SnSe₂ nanosheets based sensor. The humidity sensing is the adsorption of water molecules on the surface of material and then transfer of charge from one water molecule to its next neighboring molecule. In brief when water molecules get adsorbed on the surface of SnSe₂ nanosheets, proton starts hopping from one water molecule to its next neighboring water molecule. This hopping of proton will give rise to increase in the electrical conductivity. The

sensitivity of the humidity sensor device based on 1000 rpm sample was found to be ~ 12103% highest amongst the sample exfoliated at 3000 rpm and 5000 rpm. This is because of the fact that, in case of 1000 rpm sample, large number of bulky sheets were seen which acts as perspective sites for adsorption of water molecules. In the same sample (1000 rpm) due to bulky sheet nature, it takes more time to recover the original resistance. In contrast with 1000 rpm and 3000 rpm sample, in case of 5000 rpm sample we observed the fast response and recovery time for the SnSe₂ nanosheets sample because of drastic reduction in thickness of SnSe₂ nanosheets. The existence of Se- vacancies created during the liquid exfoliation using ultrasonication might plays an important role in the high sensitivity values. Further, it is also possible that, the liquid exfoliation method results into a large number of defect sites in SnSe₂ nanosheet sample, the main defects being Se-vacancies with the absence of either one or two Se atoms per SnSe₂. The response and recovery time depends on the thickness of the material i.e. thinner the material rate of adsorption and desorption of water molecules will be high due to large surface area. The thickness of the nanosheets plays key role in the high performance humidity sensor. The sensing mechanism for NH₃ gas sensing can be explained as below. When the SnSe₂ sensor device exposed with NH₃ gas, a charge transfer between the NH₃ gas molecules and SnSe₂ nanosheets occur. This further result in the decrease in resistance of the sensor device as a function of increase of NH₃ gas flow. The interactions among the NH₃ gas molecules (electron donor) and SnSe₂ nanosheets (n-type) results into the significant increase in the conductivity of SnSe₂ sensor device as observed for MoS₂.⁵¹ The future scope for this material is to carry out the extensive theoretical work on atomically thin sheet of SnSe₂ in particularly the calculations of scattering rates on phonon and charge impurities were needed for the complete understanding. It is important to investigate the detail analysis of role of vacancy sites, anti-sites, grain boundaries and defects present in the sample for complete understanding of materials which might be responsible for high performance of the sensing

device. The liquid / chemically exfoliated nanosheets involves randomly oriented crystalline domains which might be interconnected by definite grain boundary region as evidenced from AFM imaging for other 2D layered materials.⁵² The SnSe₂ is one of the promising 2D layered semiconducting materials. The synthesis process is highly important for good quality nanosheets of this material, as the properties are highly dependent on quality and structure of the SnSe₂ nanosheets which may provide profound information of this material on the performances of the sensor devices, as it might lead to design superior future nanoelectronics devices⁵³⁻⁵⁷ and other applications.⁵⁸ Further, improvement in the device performance can be achieved by synthesizing high quality SnSe₂ nanosheets along with control thickness and suitable engineering of materials such as doping, surface functionalization and heterojunctions architecture with other 2D materials.

5.4 Conclusions

We successfully investigated sensing behavior of 2D SnSe₂ nanosheets synthesized using simple liquid exfoliation method which provides further opportunities to improve the sensing behavior and make 2D SnSe₂ nanosheets useful for the detection of humidities and toxic gases. The fast recovery time of 4 sec was observed for the humidity sensor device based on 2D SnSe₂ nanosheet synthesized at 5000 rpm. The maximum sensitivity of 12103% were observed for SnSe₂ nanosheet ink sample synthesized at 1000 rpm. Even though the precise sensing mechanisms of SnSe₂ behavior is uncertain, still it has demonstrated superior sensing properties, makes it worthy of further investigations.

5.5 References

- 1) Arnold, S. P.; Prokes, S. M.; Perkins, F. K.; Zaghloul, M. E. Design and performance of a simple, room-temperature Ga₂O₃ nanowire gas sensor. *Appl. Phys. Lett.* **2009**, *95*, 103102.
- 2) Tian, S.; Yang, F.; Zeng, D.; Xie, C. Solution-Processed Gas Sensors Based on ZnO Nanorods Array with an Exposed (0001) Facet for Enhanced Gas-Sensing Properties. *J. Phys. Chem. C* **2012**, *116*, 10586.
- 3) Zhang, J.; Liu, J.; Peng, Q.; Wang, X.; Li, Y. Nearly Monodisperse Cu₂O and CuO Nanospheres: Preparation and Applications for Sensitive Gas Sensors. *Chem. Mater.* **2006**, *18*, 867.
- 4) Zhao, X.; Cao, M.; Hu, C. Thermal oxidation synthesis hollow MoO₃ microspheres and their applications in lithium storage and gas-sensing. *Mater. Res. Bull.* **2013**, *48*, 2289.
- 5) Kong, J.; Franklin, N. R.; Zhou, C.; Chapline, M. G.; Peng, S.; Cho, K.; Dai, H. Nanotube molecular wires as chemical sensors. *Science* **2000**, *287*, 622-625.
- 6) Chopra, S.; McGuire, K.; Gothard, N.; Rao, A.M.; Pham, A. Selective gas detection using a carbon nanotube sensor. *Appl. Phys. Lett.* **2003**, *83*, 2280-2282.
- 7) Li, J.; Ye, Y.; Ye, Q.; Cinke, M.; Han, J.; Meyyaoan, M. Carbon Nanotube Sensors for Gas and Organic Vapor Detection. *Nano Lett.* **2003**, *3*, 929.
- 8) Schedin, F.; Geim, A. K.; Morozov, S. V.; Hill, E. W.; Blake, P.; Katsnelson, M. I.; Novoselov, K. S. Detection of individual gas molecules adsorbed on graphene. *Nat. Mater.* **2007**, *6*, 652.
- 9) Arjmandi-Tash, H.; Belyaeva, L.A.; Schneider, G. F. Single molecule detection with graphene and other two-dimensional materials: nanopores and beyond. *Chem. Soc. Rev.* **2016**, *45*, 476.

- 10) Ghosh, A.; Late, D. J.; Panchakarla, L. S.; Govindaraj, A.; Rao, C.N. R. NO₂ and humidity sensing characteristics of few-layer graphenes. *J. Exp. Nanosci.* **2009**, *4*, 313.
- 11) Late, D. J.; Huang, Y. K.; Liu, B.; Acharya, J.; Shirodkar, S. N.; Luo, J.; Yan, A.; Charles, D.; Waghmare, U. V.; Dravid, V.P.; Rao, C.N. R. Sensing behavior of atomically thin-layered MoS₂ transistors. *ACS Nano* **2013**, *7*, 4879.
- 12) Lee, K.; Gatensby, R.; McEvoy, N.; Hallam, T.; Duesberg, G. S. High-performance sensors based on molybdenum disulfide thin films. *Adv. Mater.* **2013**, *25*, 6699.
- 13) Li, H.; Yin, Z.; He, Q.; Li, H.; Huang, X.; Lu, G.; Fam, D. W. H.; Tok, A. I. Y.; Zhang, Q.; Zhang, H. Fabrication of single-and multilayer MoS₂ film-based field-effect transistors for sensing NO at room temperature. *Small* **2012**, *8*, 63.
- 14) Huo, N.; Yang, S.; Wei, Z.; Li, S. S.; Xia, J. B.; Li, J. Photoresponsive and gas sensing field-effect transistors based on multilayer WS₂ nanoflakes. *Sci. Rep.* **2014**, *4*, 5209.
- 15) Late, D. J.; Doneux, T.; Bougouma, M. Single-layer MoSe₂ based NH₃ gas sensor. *Appl. Phys. Lett.* **2014**, *105*, 233103.
- 16) Abbas, A. N.; Liu, B.; Chen, L.; Ma, Y.; Cong, S.; Aroonyadet, N.; Köpf, M.; Nilges, T.; Zhou, C. Black phosphorus gas sensors. *ACS Nano* **2015**, *9*, 5618.
- 17) Yan, S.; Wang, B.; Wang, Z.; Hu, D.; Xu, X.; Wang, J.; Shi, Y. Supercritical carbon dioxide-assisted rapid synthesis of few-layer black phosphorus for hydrogen peroxide sensing. *Biosens. Bioelectron.* **2016**, *80*, 34.
- 18) Li, P.; Zhang, D.; Liu, J.; Chang, H.; Sun, Y. E.; Yin, N. Air-stable black phosphorus devices for ion sensing. *ACS App. Mater. Interfaces*, **2015**, *7*, 24396.

- 19) Wang, Q. H.; Kalantar-Zadeh, K.; Kis, A.; Coleman, J. N.; Strano, M. S. Electronics and optoelectronics of two-dimensional transition metal dichalcogenides. *Nat. Nanotechnol.* **2012**, *7*, 699.
- 20) Kannan, P. K.; Late, D. J.; Morgan, H.; Rout, C. S. Recent developments in 2D layered inorganic nanomaterials for sensing. *Nanoscale* **2015**, *7*, 13293.
- 21) Taube, A.; Łapińska, A.; Judek, J.; Zdrojek, M. Temperature dependence of Raman shifts in layered ReSe₂ and SnSe₂ semiconductor nanosheets. *Appl. Phys. Lett.* **2015**, *107*, 013105.
- 22) Huang, L.; Yu, Y.; Li, C.; Cao, L. Substrate mediation in vapor deposition growth of layered chalcogenides nanoplates: a case study of SnSe₂. *J. Phys. Chem. C* **2013**, *117*, 6469.
- 23) Kim, S. I.; Hwang, S.; Kim, S. Y.; Lee, W. J.; Jung, D. W.; Moon, K. S.; Park, H. J.; Cho, Y. J.; Cho, Y. H.; Kim, J. H.; Yun, D. J. Metallic conduction induced by direct anion site doping in layered SnSe₂. *Sci. Rep.* **2016**, *6*, 19733.
- 24) Pei, T.; Bao, L.; Wang, G.; Ma, R.; Yang, H.; Li, J.; Gu, C.; Pantelides, S.; Du, S.; Gao, H. J. Few-layer SnSe₂ transistors with high on/off ratios. *Appl. Phys. Lett.* **2016**, *108*, 053506.
- 25) Zhou, X.; Gan, L.; Tian, W.; Zhang, Q.; Jin, S.; Li, H.; Bando, Y.; Golberg, D.; Zhai, T. Ultrathin SnSe₂ Flakes Grown by Chemical Vapor Deposition for High-Performance Photodetectors. *Adv. Mater.* **2015**, *27*, 8035-8041.
- 26) Ma, Y. Ultrathin SnSe₂ flakes: a new member in two-dimensional materials for high-performance photodetector. *Sci. Bull.* **2015**, *60*, 1789.
- 27)(a) Zhou, X.; Zhou, N.; Li, C.; Song, H.; Zhang, Q.; Hu, X.; Gan, L.; Li, H.; Lü, J.; Luo, J.; Xiong, J. Vertical heterostructures based on SnSe₂/MoS₂ for high performance photodetectors. *2D Mater.* **2017**, *4*, 025048. (b) Roy, T.; Tosun, M.;

- Hettick, M.; Ahn, G. H.; Hu, C.; Javey, A. 2D-2D tunneling field-effect transistors using WSe₂/SnSe₂ heterostructures. *Appl. Phys. Lett.* **2016**, *108*, 083111.
- 28) Radisavljevic, B.; Radenovic, A.; Brivio, J.; Giacometti, V.; Kis, A. Single-layer MoS₂ transistors. *Nat. Nanotechnol.* **2011**, *6*, 147.
- 29) Yin, Z.; Li, H.; Li, H.; Jiang, L.; Shi, Y.; Sun, Y.; Lu, G.; Zhang, Q.; Chen, X.; Zhang, H. Single-layer MoS₂ phototransistors. *ACS Nano* **2012**, *6*, 74-80.
- 30) Late, D. J.; Liu, B.; Matte, H. R.; Dravid, V. P.; Rao, C. N. R. Hysteresis in single-layer MoS₂ field effect transistors. *ACS Nano* **2012**, *6*, 5635.
- 31) Sundaram, R. S.; Engel, M.; Lombardo, A.; Krupke, R.; Ferrari, A. C.; Avouris, P.; Steiner, M. Electroluminescence in single layer MoS₂. *Nano Lett.* **2013**, *13*, 1416.
- 32) Ovchinnikov, D.; Allain, A.; Huang, Y. S.; Dumcenco, D.; Kis, A. Electrical transport properties of single-layer WS₂. *ACS Nano* **2014**, *8*, 8174.
- 33) Perea-López, N.; Elías, A. L.; Berkdemir, A.; Castro-Beltrán, A.; Gutiérrez, H. R.; Feng, S.; Lv, R.; Hayashi, T.; López-Urías, F.; Ghosh, S.; Muchharla, B. Photosensor device based on few-layered WS₂ films. *Adv. Funct. Mater.* **2013**, *23*, 5511.
- 34) Chang, Y. H.; Zhang, W.; Zhu, Y.; Han, Y.; Pu, J.; Chang, J. K.; Hsu, W. T.; Huang, J. K.; Hsu, C. L.; Chiu, M. H.; Takenobu, T. Monolayer MoSe₂ grown by chemical vapor deposition for fast photodetection. *ACS Nano* **2014**, *8*, 8582.
- 35) Larentis, S.; Fallahazad, B.; Tutuc, E. Field-effect transistors and intrinsic mobility in ultra-thin MoSe₂ layers. *Appl. Phys. Lett.* **2012**, *101*, 223104.
- 36) Das, S.; Appenzeller, J. WSe₂ field effect transistors with enhanced ambipolar characteristics. *Appl. Phys. Lett.* **2013**, *103*, 103501.
- 37) Allain, A.; Kis, A. Electron and hole mobilities in single-layer WSe₂. *ACS Nano* **2014**, *8*, 7180.

- 38)Huang, J. K.; Pu, J.; Hsu, C. L.; Chiu, M. H.; Juang, Z. Y.; Chang, Y. H.; Chang, W. H.; Iwasa, Y.; Takenobu, T.; Li, L. J. Large-area synthesis of highly crystalline WSe₂ monolayers and device applications. *ACS Nano* **2014**, *8*, 923.
- 39)Late, D. J.; Liu, B.; Luo, J.; Yan, A.; Matte, H. R.; Grayson, M.; Rao, C. N. R.; Dravid, V.P. GaS and GaSe ultrathin layer transistors. *Adv. Mater.* **2012**, *24*, 3549.
- 40)Buscema, M.; Groenendijk, D. J.; Blanter, S. I.; Steele, G. A.; Van Der Zant, H. S.; Castellanos-Gomez, A. Fast and broadband photoresponse of few-layer black phosphorus field-effect transistors. *Nano Lett.* **2014**, *14*, 3347.
- 41)Boscher, N. D.; Carmalt, C. J.; Palgrave, R.G.; Parkin, I. P. Atmospheric pressure chemical vapour deposition of SnSe and SnSe₂ thin films on glass. *Thin Solid Films*, **2008**, *516*, 4750.
- 42)Ranmohotti, K. G.; Djieutedjeu, H.; Poudeu, P. F. Chemical Manipulation of Magnetic Ordering in Mn_{1-x}Sn_xBi₂Se₄ Solid-Solutions. *J. Am. Chem. Soc.* **2012**, *134*, 14033.
- 43)Djieutedjeu, H.; Zhou, X.; Chi, H.; Haldolaarachchige, N.; Ranmohotti, K. G.; Uher, C.; Young, D.; Poudeu, P. F. Donor and acceptor impurity-driven switching of magnetic ordering in MnSb_{2-x}Sn_xSe₄. *J. Mater. Chem. C* **2014**, *2*, 6199.
- 44)Li, L.; Chen, Z.; Hu, Y.; Wang, X.; Zhang, T.; Chen, W.; Wang, Q. Single-layer single-crystalline SnSe nanosheets. *J. Am. Chem. Soc.* **2013**, *135*, 1213.
- 45)Zhang, W.; Yang, Z.; Liu, J.; Zhang, L.; Hui, Z.; Yu, W.; Qian, Y.; Chen, L.; Liu, X. Room temperature growth of nanocrystalline tin (II) selenide from aqueous solution. *J. Cryst. Growth* **2007**, *217*, 157.
- 46)Harbec, J. Y.; Powell, B. M.; Jandl, S. Lattice dynamics of SnSe₂. *Phys. Rev. B* **1983**, *28*, 7009.

- 47) O'Brien, M.; Lee, K.; Morrish, R.; Berner, N. C.; McEvoy, N.; Wolden, C. A.; Duesberg, G. S. Plasma assisted synthesis of WS₂ for gas sensing applications. *Chem. Phys. Lett.* **2014**, *615*, 6.
- 48) Yasaei, P.; Behranginia, A.; Foroozan, T.; Asadi, M.; Kim, K.; Khalili-Araghi, F.; Salehi-Khojin, A. Stable and selective humidity sensing using stacked black phosphorus flakes. *ACS Nano* **2015**, *9*, 9898.
- 49) Feng, J.; Peng, L.; Wu, C.; Sun, X.; Hu, S.; Lin, C.; Dai, J.; Yang, J.; Xie, Y. Giant moisture responsiveness of VS₂ ultrathin nanosheets for novel touchless positioning interface. *Adv. Mater.* **2012**, *24*, 1969.
- 50) Bi, H.; Yin, K.; Xie, X.; Ji, J.; Wan, S.; Sun, L.; Terrones, M.; Dresselhaus, M. S. Ultrahigh humidity sensitivity of graphene oxide. *Sci. Rep.* **2013**, *3*, 2714.
- 51) SoóáKang, B.; YongáSong, J. Sensor based on chemical vapour deposition-grown molybdenum disulphide for gas sensing application. *RSC Adv.* **2016**, *6*, 75839.
- 52) Mongillo, M.; Chiappe, D.; Arutchelvan, G.; Asselberghs, I.; Perucchini, M.; Manfrini, M.; Lin, D.; Huyghebaert, C.; Radu, I. Transport properties of chemically synthesized MoS₂-Dielectric effects and defects scattering. *Appl. Phys. Lett.* **2016**, *109*, 233102.
- 53) Xue, D. J.; Tan, J.; Hu, J. S.; Hu, W.; Guo, Y.G.; Wan, L. J. Anisotropic photoresponse properties of single micrometer-sized GeSe nanosheet. *Adv. Mater.* **2012**, *24*, 4528.
- 54) Bharatula, L. D.; Erande, M. B.; Mulla, I. S.; Rout, C. S. Late, D. J. SnS₂ nanoflakes for efficient humidity and alcohol sensing at room temperature. *RSC Adv.* **2016**, *6*, 105421.

- 55) Pawbake, A. S.; Date, A.; Jadkar, S. R.; Late, D. J. Temperature dependent raman spectroscopy and sensing behavior of few layer SnSe₂ nanosheets. *ChemistrySelect* **2016**, *1*, 5380.
- 56) Late, D. J. Liquid exfoliation of black phosphorus nanosheets and its application as humidity sensor. *Microporous Mesoporous Mater.* **2016**, *225*, 494.
- 57) Erande, M. B.; Pawar, M. S.; Late, D. J. Humidity sensing and photodetection behavior of electrochemically exfoliated atomically thin-layered black phosphorus nanosheets. *ACS App. Mater. Interfaces* **2016**, *8*, 11548.
- 58) Saha, S.; Banik, A.; Biswas, K. Few-Layer Nanosheets of n-Type SnSe₂. *Chem. Euro. J.* **2016**, *22*, 15634.

Chapter 6

Temperature dependent Raman Spectroscopy investigations of PtSe₂ Nanosheets synthesized by wet Chemistry and its Sensor application

The paper based on this chapter is published in Beilstein Journal of Nanotechnology

M. Pawar et al. *Beilstein J. Nanotechnol.* **2019**, 10, 467.

6.1 Introduction

Graphene was the most celebrated example of 2D aromatic compounds and which is the building block of all forms of carbon allotropes¹. In the recent years, it has been studied widely due to its extraordinary optical, electrical, mechanical, magnetic and chemical properties²⁻⁵. Like graphene and its organic analogues⁶ inorganic 2D metal dichalcogenides also shows an outstanding performance in many applications like transistor, sensors, photodetector, solar cells, field emitters, battery materials, light harvesting and energy storage devices, catalysts for H₂ generation and drug delivery application⁷⁻¹². The most of the TMDCs are semiconducting in nature with MX₂ type in which M is metal (W, Mo, Sn, Nb, V and so on) from group (IV-V) and X represent chalcogenides family (S, Se, Te). The metal atom M is sandwiched between layers of chalcogenides (X) atoms as (X-M-X). The TMDC shows diverse functional properties at monolayer compare to bulk due to quantum confinement effect. Apart from bulk to monolayer these TMDCs for example MoS₂ and MoSe₂ show an indirect to direct band gap transition¹³⁻¹⁷.

The 2D Platinum diselenide (PtSe₂) has recently joined the growing class of stable TMDCs due its promising applications. The 2D PtSe₂ has not been explored much due to difficulty in synthesis. It is well known that the bulk PtSe₂ is a semimetal in nature with nearly zero band gap^{18,19}. With the help of theoretical calculations such as Density functional theory (DFT) and Local-density approximations (LDA) it was observed that the bulk PtSe₂ shows semi-metallic nature and the single layer PtSe₂ has a semiconducting nature with bandgap of 1.2 eV. Bilayer of PtSe₂ is also a semiconducting but with slightly smaller band gap then monolayer.¹⁹ This layer dependent conversion of semimetal-to-semiconductor transition has potential for electronic device applications²⁰⁻²². The bulk PtSe₂ was first prepared by minozzi from elements in 1909²³. The PtSe₂ nanosheets has been recently prepared by heating thin foils of platinum in selenium vapors at 400°C^{19,24}. In this paper we have synthesized few layer thick

PtSe₂ nanosheets by wet-chemical method²⁵ at 90°C using chloroplatinic acid (H₂PtCl₆) precursor and Se powder as a precursors followed by thermal annealing at 500°C and investigated its temperature dependent Raman spectroscopic characterizations.

6.2 Experimental Section

Materials

All the chemicals such as Chloroplatinic acid, Se powder, Hexamethylenetetramine, NaBH₄ were purchased from Sigma-Aldrich for the synthesis of PtSe₂ nanosheets.

Synthesis Method

The PtSe₂ Nano-sheets were synthesized using solvothermal method followed by annealing at 500°C using earlier method of PtSe₂ synthesis²⁵. The PtSe₂ were prepared in two steps. First step is the formation of PtSe complex on a wall of a container by wet-chemical method and second step is the phase transformation of PtSe₂ by thermal annealing. The 0.5 ml of 0.015M solution of chloroplatinic acid (H₂PtCl₆) was mixed with 0.5 ml of 0.5M hexamethylenetetramine (C₆H₁₂N₄). In order to get homogeneous solution the above mixture was carefully stirred for 15-20 s till the colour of solution becomes slightly yellow called as Pt precursor. In another beaker 0.8 mg of Se powder was added into 10 ml ice-cold solution of 0.1M NaBH₄ which act as a strong reducing agent for the reduction of Se powder. The solution of Se was then heated in oil bath at 90°C for ~20 min in order to reduce Se completely. After complete reduction colour of solution becomes dark brown called as Se precursor. The Pt precursor was then slowly added into the Se precursor. The colour of the solution was found to be suddenly changes to greenish brown. The mixture was then kept undisturbed for ~20 min. After 20 min the complex of Pt and Se was formed on a wall of beaker. The complex was then washed several times using DI water. First complex was transferred on to Si substrate and heated at 100°C on hot plate. After complete evaporation substrate was annealed in chemical

vapour deposition system at 500°C in argon gas atmosphere for 5h. Figure 6.1 shows the schematic of PtSe₂ nanosheet synthesis steps.

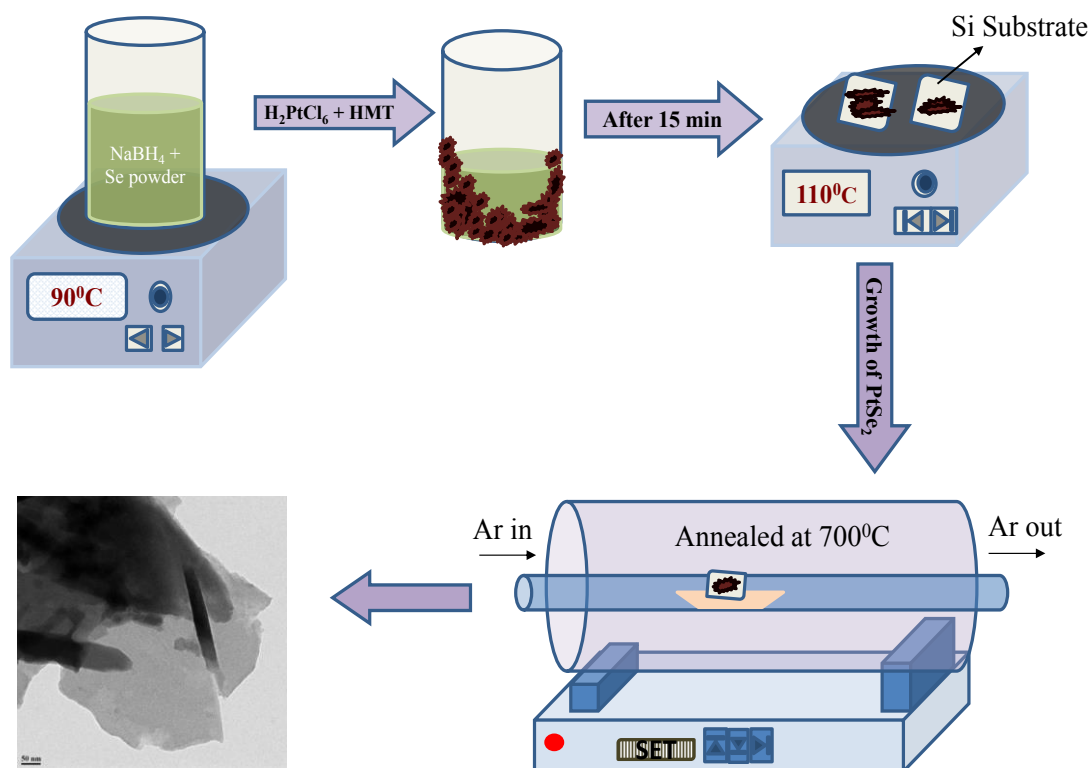


Figure 6.1: Schematic of the experimental set up used for the synthesis of PtSe₂ nanosheets.

6.3 Results and Discussion

6.3.1 Material Characterization

The structural characterization was carried out by using powder XRD and Raman spectroscopy. Figure 6.2(a) shows the typical XRD pattern of the as-prepared sample deposited on Si substrate. The XRD was performed on PANalytical X'pert pro dual goniometer diffractometer using Cu-K_α radiation. The sample were mounted flat and scanned between 10 to 60°. The XRD pattern of the as-prepared sample shows the strong characteristic peaks around 2θ=17.41° and 33.17° belongs to (001) and (011) planes of the PtSe₂ and these values matches well with the JCPDS data card number (88-2281) and earlier report²⁷. The Figure 6.2(b) shows Raman

spectra of as-prepared few layer PtSe₂ nanosheet. The Raman spectra were recorded using Renishaw microscope at a wavelength of 532 nm with laser power ~25 mW and laser spot diameter ~1 μm. The typical Raman spectra recorded at room temperature consist of two distinguish peak ~176 cm⁻¹ corresponds to E_g mode and another slightly less intense peak ~205 cm⁻¹ corresponds to A_{1g} mode. The E_g mode in Raman spectra corresponds to in-plane vibration due to the opposite motion of upper and lower Se atom. The A_{1g} mode in Raman spectra corresponds to out-of-plane vibration of Se atom^{22,28}. The morphological investigations were carried out using SEM.

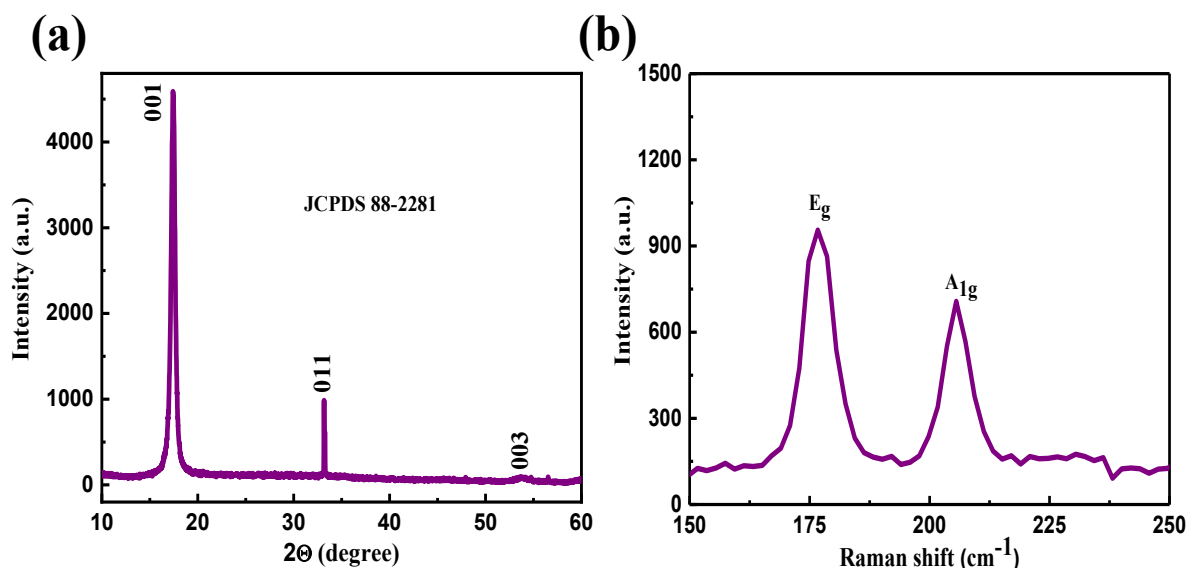


Figure 6.2: PtSe₂ nanosheets. (a) Typical XRD pattern and (b) Raman spectra recorded at room temperature.

Figure 6.3(a-c) shows SEM images of few layer PtSe₂ with typical overlapping of multiple sheets on each other. The Figure 6.3(d) shows a SEM image indicating more transparent thin layer of PtSe₂ stack on each other showing the few layer nature of the as synthesized PtSe₂ sample. Figure 6.4(a-c) shows the low resolution TEM images of the as synthesized PtSe₂ sample clearly shows the sheet like morphology with lateral dimension ~700 nm. Figure 3d shows the HRTEM image of PtSe₂ nanosheets. The inset of Figure 6.4(d) shows SAED which depicts the crystalline nature of the as synthesized PtSe₂ sample. The XPS spectra of the Pt 4f

and Se 3d region, acquired on a PtSe₂ nanosheet sample were carried out on the Si substrate. The Figure 6.5(a) represents the Pt fitted spectrum for 4f_{7/2} and 4f_{5/2} with binding energy 72.55eV and 75.83eV respectively.

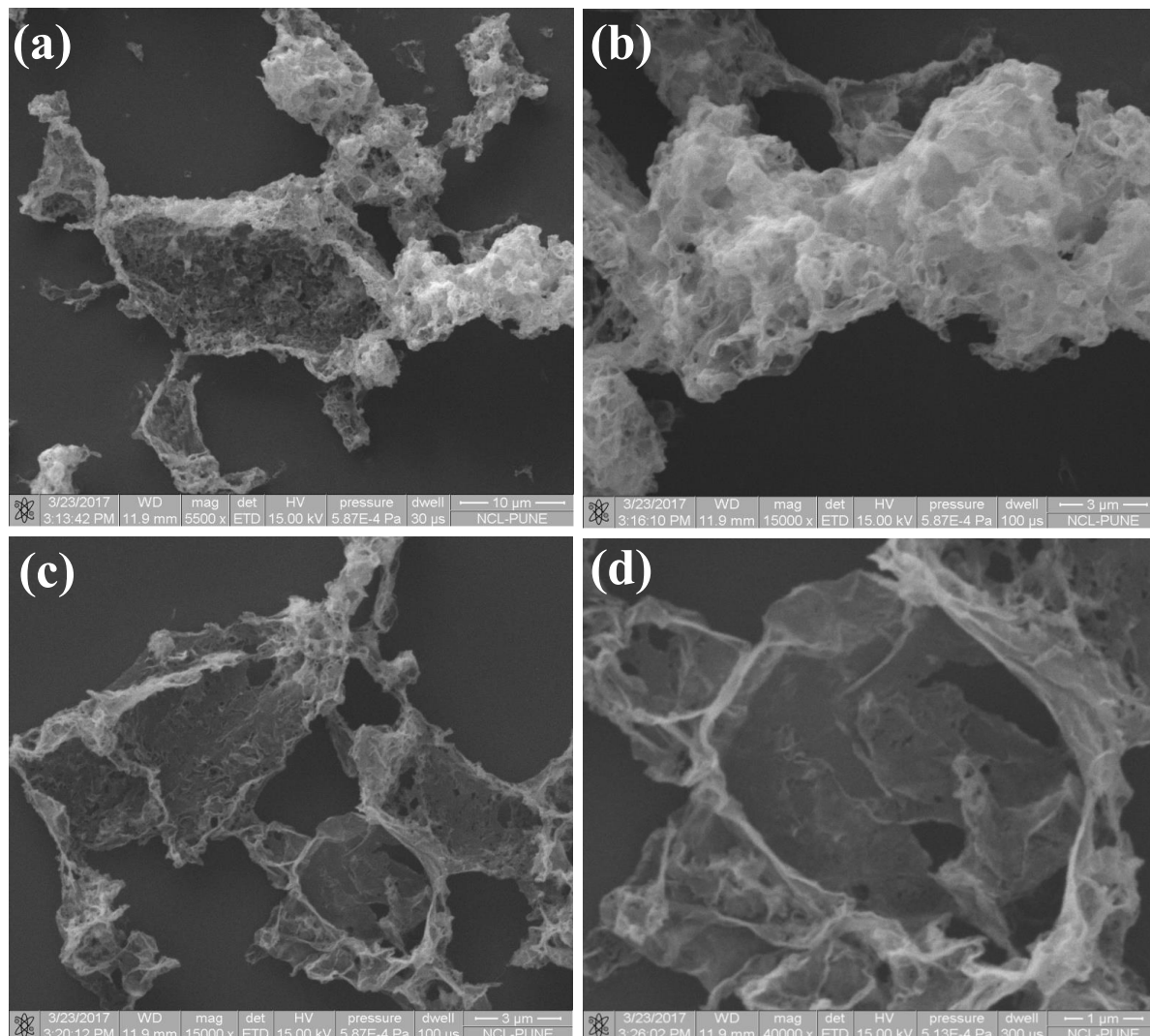


Figure 6.3: (a-d) Typical SEM images for PtSe₂ nanosheets synthesized using the wet chemistry method.

Similarly, for Se the binding energy spectrum can be fitted by Gaussian-Lorentzian curves shown in Figure 6.5(b). The two peaks with binding energy 54.8eV and 55.6eV are observed for the 3d_{5/2} and 3d_{3/2} states respectively. There is one more peak observed in the Se fitting with low intensity at 55.8eV which corresponds to Pt 5d_{3/2} state²⁴.

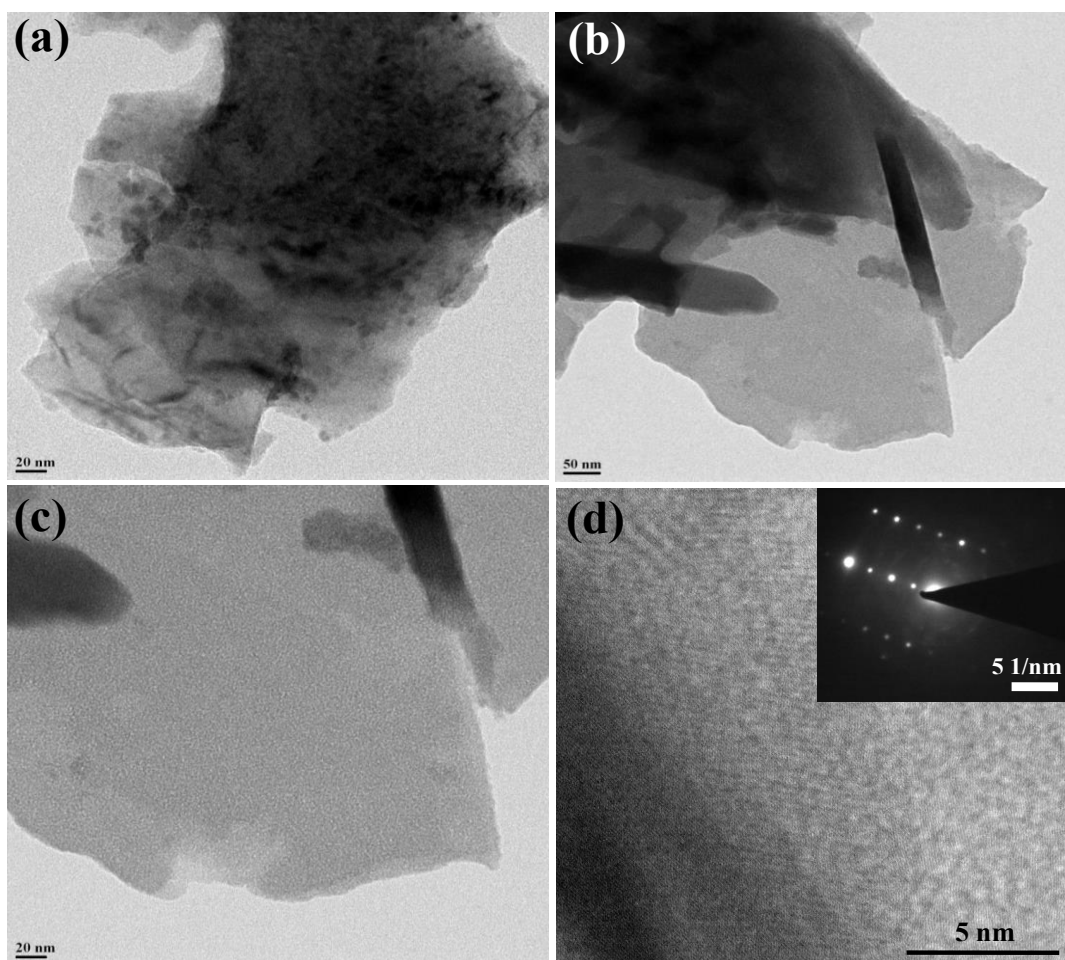


Figure 6.4: (a-c) Low-magnification TEM images and (d) a HRTEM image, where the inset shows the SAED pattern for the as-synthesized PtSe₂ nanosheets.

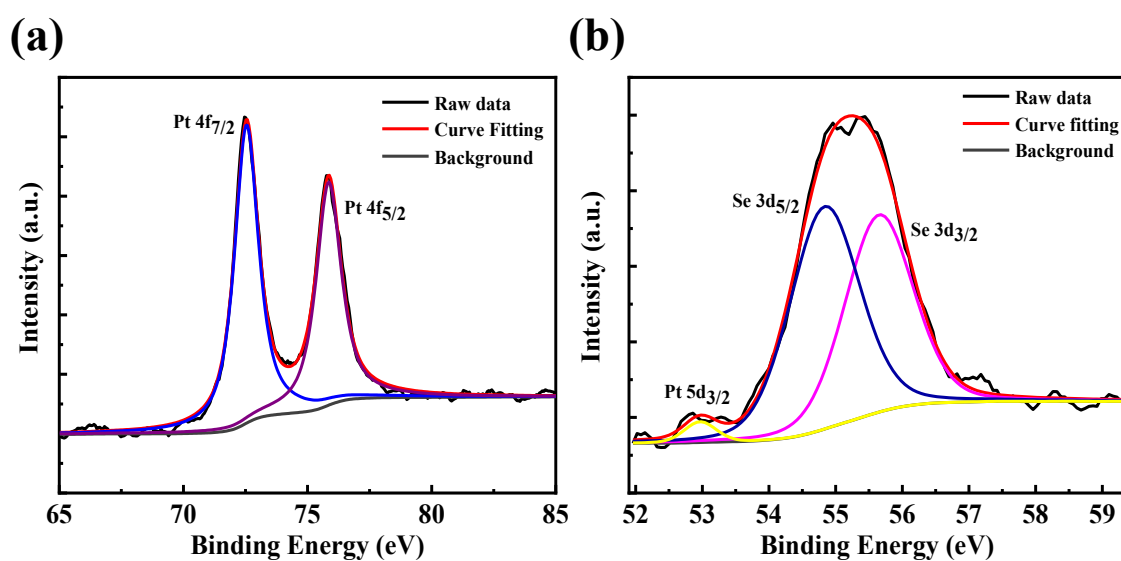


Figure 6.5: (a) Deconvoluted XPS spectra for Pt and (b) Se elements.

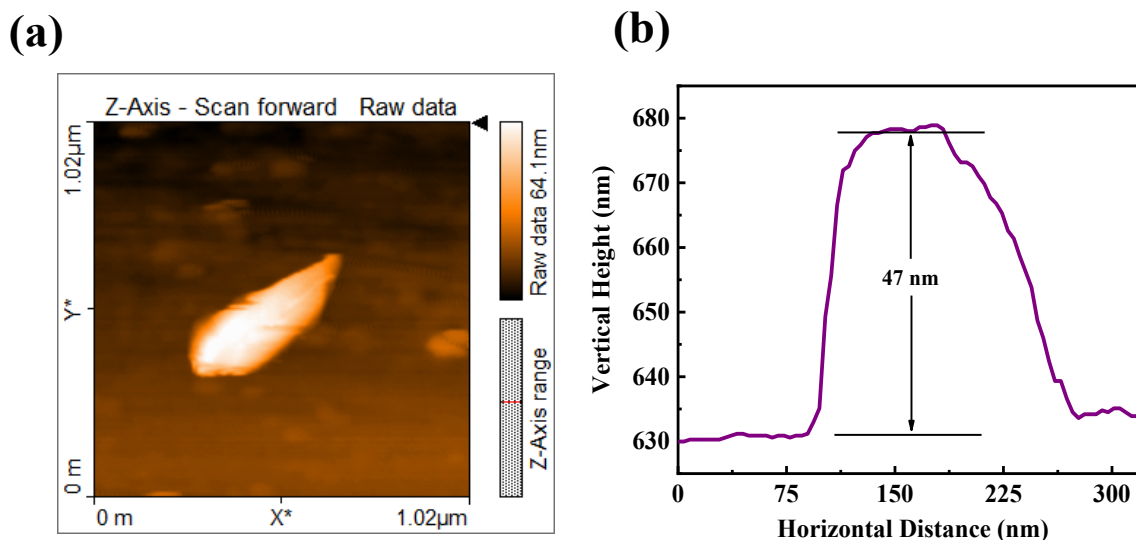


Figure 6.6: (a) AFM image and (b) AFM height profile plot for a PtSe₂ nanosheet.

The thickness of the as prepared PtSe₂ nanosheets was calculated using AFM shown in Figure 6.6. From the AFM image figure 6.6(a) which clearly shows the lateral dimensions of nanosheets are ~700 nm and Figure 6.6(b) represents the corresponding height profile plot for the PtSe₂ nanosheet with thickness found to be ~ 47 nm.

6.3.2 Temperature dependent Raman spectroscopic investigations

The temperature dependent Raman spectroscopy investigations of few layer PtSe₂ nanosheets were carried out between 100K to 506K. The Raman mode E_g and A_{1g} as a function of temperature has shown in Figure 6.7(a) and 6.7(b). It is clearly seen that, the position of peak A_{1g} and E_g modes shifts to lower wave number as temperature increases from 100K to 506K. The Raman modes E_g and A_{1g} for PtSe₂ behave linearly with temperature ranges from 100K to 506K. Further, it was observed that FWHM increases with increase in temperature. The peak position in Raman spectra were calculated by fitting the Lorentzian function for A_{1g} and E_g modes. The temperature coefficient can be calculated by equation (1)²⁹.

$$\omega(T) = \omega_0 + \chi T \quad \dots (1)$$

Where, ω_0 is the peak position of A_{1g} and E_g mode at zero Kelvin temperature and χ is the temperature coefficient of the A_{1g} and E_g modes and ω is a Raman phonon frequency. The

slope of the plot Raman modes vs temperature directly gives the value of temperature coefficient as given in table 1.

Material	Raman modes	Temperature Coefficient (χ)	$\Delta\omega$ (cm^{-1})
PtSe ₂ Nanosheets	E _g	-0.014	6.11
	A _{1g}	-0.008	3.14

Table 1: Temperature coefficient values for the A_{1g} and E_g modes in PtSe₂ nanosheet sample.

Further, it was clearly seen that the Raman peak position and peak broadening was affected by temperature.

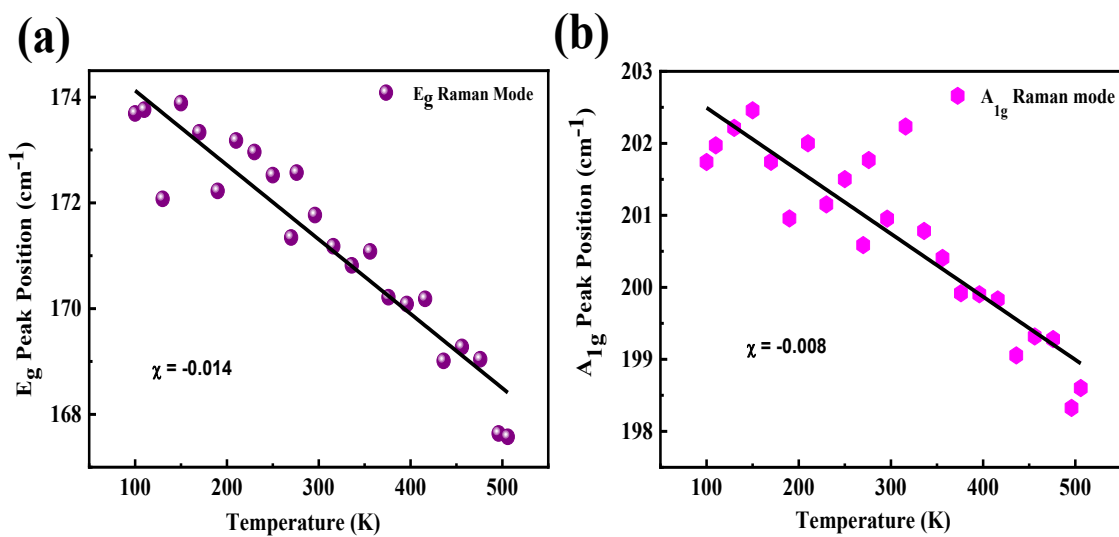


Figure 6.7: Temperature-dependent Raman spectra analysis for PtSe₂ nanosheets for the (a) E_g mode and the (b) A_{1g} mode as a function of temperature.

This change in Raman modes is mainly due to contribution from the thermal Anharmonicity. The phonon frequency variation with volume and temperature is given in following equation (2) and (3)³⁰.

$$\left(\frac{\partial \ln \omega}{\partial T}\right)_P = \left(\frac{\partial \ln V}{\partial T}\right)_P \left(\frac{\partial \ln \omega}{\partial \ln V}\right)_T + \left(\frac{\partial \ln \omega}{\partial T}\right)_V \dots \dots (2)$$

$$\left(\frac{\partial \ln \omega}{\partial T}\right) P = -\frac{\gamma}{K} \left(\frac{\partial \ln \omega}{\partial P}\right) T + \left(\frac{\partial \ln \omega}{\partial T}\right) V \quad \dots\dots (3)$$

Where γ is the volume thermal coefficient and k represent the isothermal volume compressibility. The term $-\gamma/K (\partial \ln \omega / \partial P)_T$ represent volume contribution at a constant temperature and second term i.e. $(\partial \ln \omega / \partial T)_V$ represent the temperature contribution at constant volume. In single layer TMDCs due to direct band gap; double resonance phenomenon is very useful to explain the effect of temperature on the FWHM, intensity and shift in the Raman modes. A double resonance phenomenon consist of several process which include absorption of an incident photon, creation of hole pair, double scattering of created hole pair by phonon and recombination of electron-hole pair with emission of phonon. The temperature coefficient for both E_g and A_{1g} modes were found to be -0.014 and -0.008 respectively. The comparative values of temperature coefficient corresponding to various 2D materials were shown in Table 2.

TMDCs	Raman modes	Temperature coefficient (χ)	$\Delta\omega$ (cm ⁻¹)	Reference
MoSe ₂	A _{1g}	-0.0096	4.75	29
WSe ₂	A _{1g}	-0.0071	3.81	29
MoS ₂	E _g	-0.0136	8	29
	A _{1g}	-0.0113	6.11	
WS ₂	E _g	-0.0098	4.51	29
	A _{1g}	-0.014	6.43	

Black Phosphorus	A _{1g}	-0.008	4.39	31
	B _{2g}	-0.013	8.14	
	A _{2g}	-0.014	8.63	
TiS ₃	A _{1g}	-0.022,-0.025, -0.024,-0.017	-	32
Single layer graphene	G	-0.0162	-	33
	G	-0.0154	-	
Bi-layer graphene				
MoTe ₂ (bilayer)	E' _{2g}	-0.0116	-	34
	B' _{2g}	-0.0181	-	
PtSe ₂	E _g	-0.014	6.11	Present work
	A _{1g}	-0.008	3.14	

Table 2: The comparative values of temperature coefficient for various 2D materials.

The values of $\Delta\omega$ for both E_g and A_{1g} modes were found to be 6.11 and 3.14 respectively. Evidently, the nature of temperature dependence of Raman spectra of PtSe₂ nanosheet is found to be similar in nature as that of graphene and other 2D materials such as MoS₂, WS₂, MoSe₂, WSe₂, BP, TiS₃, multilayer graphene, MoTe₂^{29, 31-34}.

6.3.3 Humidity Sensor and Photodetector

Figure 6.8(a) shows the typical resistance of the sensor device Vs RH plot and from the plot it is clear that there is remarkable decrease in the resistance from 3.75 G Ω to 0.83 M Ω .

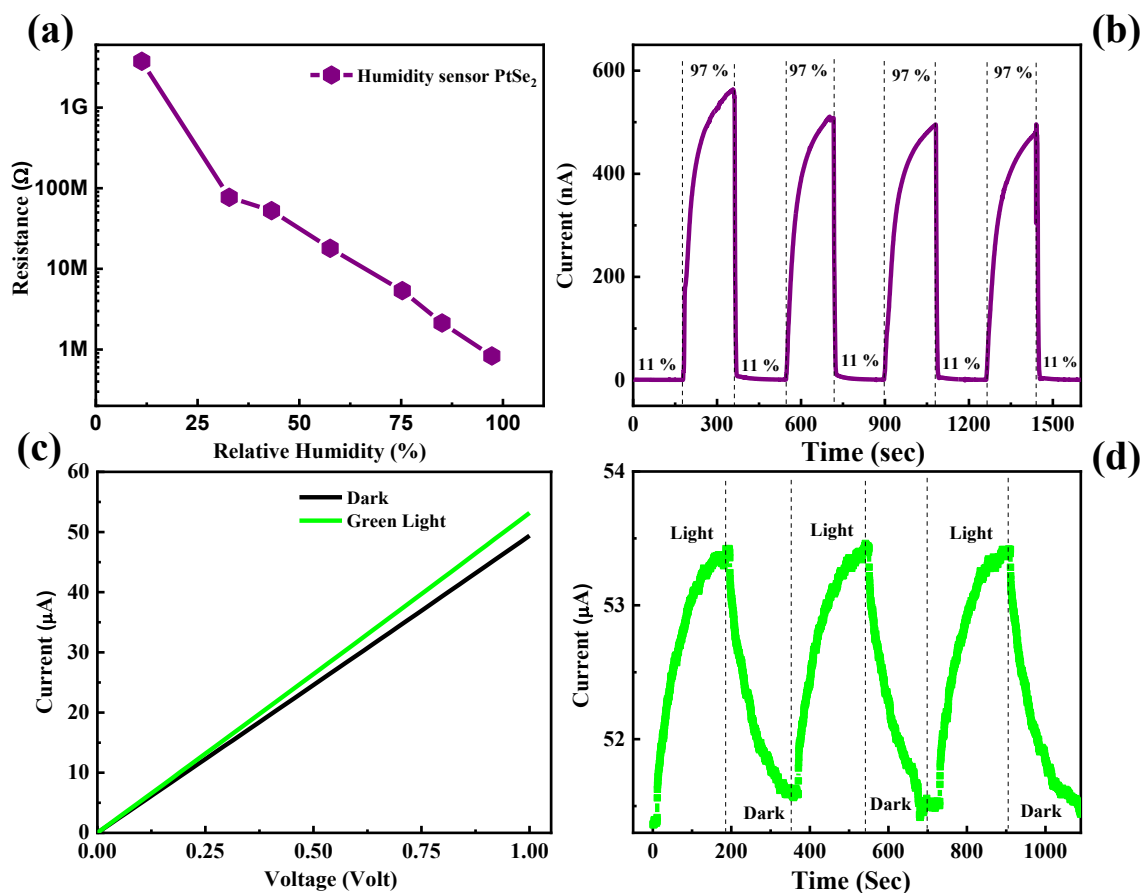


Figure 6.8: PtSe₂ nanosheet based humidity sensor: (a) Typical resistance versus RH plot and (b) I-t plot taken after switching 11% RH and 97% RH. The photodetector application of PtSe₂ nanosheets: (c) I-V in dark conditions and with green LED light and (d) typical I-t cycle when the LED is on and off, showing a favourable response.

The humidity sensing mechanism for the PtSe₂ sensor can be explained as below. When the PtSe₂ nanosheet sensor device were exposed with water molecules/vapors, a charge transfer between the water molecules and PtSe₂ nanosheets will occur. This further resulted in the decrease in resistance of the PtSe₂ nanosheet sensor device as a function of increase relative humidity. The interactions among the water molecules (electron donor) and PtSe₂ nanosheets results into the considerable enhancement in the conductivity of sensor device as observed for other 2D materials like SnSe₂³⁵, MoS₂³⁶, BP²⁶, and MoSe₂³⁷. The Figure 6.8(b) shows the

typical current-time (I-t) plot where cycles of 11.3% and 97.3% RH levels were used to calculate the response and recovery time. The response and recovery time for the PtSe₂ based humidity sensor device were found to be 118 sec and 5 sec respectively.

The significant advantage of PtSe₂ based humidity sensor device is rapid recovery and its functions at room temperature. Figure 6.8(c) shows the typical I-V plot in dark and under green light illumination. Figure 6.8(d) shows the I-t plot for the photodetector based on PtSe₂ nanosheets. The typical response time of ~110 s and recovery time of ~129 s were noted.

6.4 Conclusions

In conclusion, we report wet chemistry method to grow PtSe₂ nanosheets. The morphological investigations were carried out using microscopy techniques on PtSe₂ sample. Further, the crystal structure and phase formation of PtSe₂ were validated from the XRD, Raman and SAED pattern. The temperature dependent Raman spectroscopy experiments were performed for 100 K to 506 K temperature on PtSe₂ nanosheet film. The temperature coefficient for both E_g and A_{1g} Raman modes were observed to be -0.014 and -0.008 respectively. The room temperature sensor device exhibited superior recovery time of ~5 sec indicates its potential for future nanoelectronics and sensor devices.

6.5 References

- 1) Geim, A. K.; Novoselov, K. S. The rise of graphene. *Nat. Mater.* **2007**, *6*, 183-191.
- 2) Grigorenko, A. N.; Polini, M.; Novoselov, K. S. Graphene plasmonics. *Nat. Photonics* **2012**, *6*, 749-758.
- 3) Stankovich, S.; Dikin, D. A. Dommett, G. H. B.; Kohlhaas, K. M.; Zimney, E. J.; Stach, E. A.; Piner, R. D.; Nguyen, S. T.; Ruoff, R. S. Graphene-based composite materials. *Nature*, **2006**, *442*, 282-286.
- 4) Zhao, X.; Zhang, Q.; Chen, D.; Lu, P. Enhanced mechanical properties of graphene-based poly (vinyl alcohol) composites. *Macromolecules* **2010**, *43*, 2357-2363.
- 5) Pawbake, A. S.; Mishra, K. K.; L. Machuno, G. B.; Gelamo, R. V.; Ravindran, T. R.; Rout, C. S.; Late, D. J. Temperature and pressure dependent Raman spectroscopy of plasma treated multilayer graphene nanosheets. *Diamond Relat. Mater.* **2018**, *84*, 146-156.
- 6) Liu, W.; Luo, X.; Bao, Y.; Liu, Y.; Ning, G.; Abdelwahab, I.; Li, L.; Nai, C.; Hu, Z. G.; Zhao, D.; Liu, B.; Quek, S.; Loh, K. A two-dimensional conjugated aromatic polymer via C-C coupling reaction. *Nat. Chem.* **2017**, *9*, 563-570.
- 7) Wang, H. Q.; Kalantar-Zadeh, K.; Kis, A.; Coleman, J. N.; Strano, M. S. Electronics and optoelectronics of two-dimensional transition metal dichalcogenides. *Nat. Nanotechnol.* **2012**, *7*, 699-712.
- 8) Peng, B.; Ang, P. K.; Loh, K. P. Two-dimensional dichalcogenides for light-harvesting applications. *Nano Today* **2015**, *10*, 128-137.
- 9) Li, H.; Shi, Y.; Chiu, M. H.; Li, L. J. Emerging energy applications of two-dimensional layered transition metal dichalcogenides. *Nano Energy* **2015**, *18*, 293-305.

- 10) Jariwala, D.; Sangwan, V. K.; Lauhon, L. J.; Marks, T. J.; Hersam, M. C. Emerging Device Applications for Semiconducting Two-Dimensional Transition Metal Dichalcogenides *ACS Nano* **2014**, *8*, 1102-1120.
- 11) Shi, J.; Ma, D.; Han, G. F.; Zhang, Y.; Ji, Q.; Gao, T.; Sun, J.; Song, X.; Li, C.; Zhang, Y.; Lang, X. Y. Controllable growth and transfer of monolayer MoS₂ on Au foils and its potential application in hydrogen evolution reaction. *ACS Nano* **2014**, *8*, 10196-10204.
- 12) Voiry, D.; Salehi, M.; Silva, R.; Fujita, T.; Chen, M.; Asefa, T.; Shenoy, V. B.; Eda, G.; Chhowalla, M. Conducting MoS₂ nanosheets as catalysts for hydrogen evolution reaction. *Nano Lett.* **2013**, *13*, 6222-6227.
- 13) Splendiani, A.; Sun, L.; Zhang, Y.; Li, T.; Kim, J.; Chim, C. Y.; Galli, G.; Wang, F. Emerging photoluminescence in monolayer MoS₂. *Nano Lett.* **2010**, *10*, 1271-1275.
- 14) Tongay, S.; Zhou, J.; Ataca, C.; Lo, K.; Matthews, T. S.; Li, J.; Grossman, J. C.; Wu, J. Thermally driven crossover from indirect toward direct bandgap in 2D semiconductors: MoSe₂ versus MoS₂. *Nano Lett.* **2012**, *12*, 5576-5580.
- 15) Zhang, Y.; Chang, T. R.; Zhou, B.; Cui, Y. T.; Yan, H.; Liu, Z.; Schmitt, F.; Lee, J.; Moore, R.; Chen, Y.; Lin, H.; Jeng, H. T.; Mo, S. K.; Hussain, Z.; Bansil, A.; Shen, Z. X. Direct observation of the transition from indirect to direct bandgap in atomically thin epitaxial MoSe₂. *Nat. Nanotechnol.* **2014**, *9*, 111-115.
- 16) Mak, K. F.; Lee, C.; Hone, J.; Shan, J.; Heinz, T. F. Atomically thin MoS₂ a new direct-gap semiconductor. *Phys. Rev. Lett.* **2010**, *105*, 136805-136808.
- 17) Sundaram, R. S.; Engel, M.; Lombardo, A.; Krupke, R.; Ferrari, A. C. Avouris, Ph.; Steiner, M. Electroluminescence in single layer MoS₂. *Nano Lett.* **2013**, *13*, 1416-1421.

- 18) Guo, G. Y.; Liang, W. Y. The electronic structures of platinum dichalcogenides: PtS₂, PtSe₂ and PtTe₂. *J. Phys. C: Solid State Phys.* **1986**, *19*, 995.
- 19) Wang, Y.; Li, L.; Yao, W.; Song, S.; Sun, J. T.; Pan, J.; Ren, X.; Li, C.; Okunishi, E.; Wang, Y. Q.; Wang, E. Monolayer PtSe₂, a new semiconducting transition-metal-dichalcogenide, epitaxially grown by direct selenization of Pt. *Nano Lett.* **2015**, *15*, 4013-4018.
- 20) Zhao, Y.; Qiao, J.; Yu, Z.; Yu, P.; Xu, K.; Lau, S. P.; Zhou, W.; Liu, Z.; Wang, X.; Ji, W.; Chai, Y. High-electron-mobility and air-stable 2D layered PtSe₂ FETs. *Adv. Mater.* **2017**, *29*, 1604230.
- 21) Sattar, S.; chwingenschlög, U. S. Electronic properties of graphene–PtSe₂ contacts. *ACS Appl. Mater. Interfaces* **2017**, *9*, 15809-15813.
- 22) O'Brien, M.; McEvoy, N.; Motta, C.; Zheng, J. Y.; Berner, N. C.; Kotakoski, J.; Elibol, K.; Pennycook, T. J.; Meyer, J. C.; Yim, C.; Abid, M.; Hallam, T.; Donegan, J. F.; Sanvito, S.; Duesberg, G. S. Raman characterization of platinum diselenide thin films. *2D Mater.* **2016**, *3*, 21004.
- 23) Gronvold, F.; Haraldsen, H.; Kjekshus, A. On the sulfides, selenides and tellurides of platinum. *Acta Chem. Scand.* **1960**, *14*, 1879-1893.
- 24) Yim, C.; Lee, K.; McEvoy, N.; O'Brien, M.; Riazimehr, S.; Berner, N. C.; Cullen, C. P.; Kotakoski, J.; Meyer, J. C.; Lemme, M. C.; Duesberg, G. S. High-performance hybrid electronic devices from layered PtSe₂ films grown at low temperature. *ACS Nano* **2016**, *10*, 9550-9558.
- 25) Umar, A.; Saad, S.; Salleh, M. Scalable mesoporous platinum diselenide nanosheet synthesis in water. *ACS Omega* **2017**, *2*, 3325-3332.

- 26) Erande, M. B.; Pawar, M. S.; Late, D. J. Humidity sensing and photodetection behavior of electrochemically exfoliated atomically thin-layered black phosphorus nanosheets. *ACS Appl. Mater. Interfaces* **2016**, *8*, 11548-11556.
- 27) Yu, X.; Yu, P.; Wu, D.; Singh, B.; Zeng, Q.; Lin, H.; Zhou, W.; Lin, J.; Suenaga, K.; Liu, Z.; Wang, Q. J. Atomically thin noble metal dichalcogenide: a broadband mid-infrared semiconductor. *Nat. Commun.* **2018**, *9*, 1-9.
- 28) Zhang, K.; Yan, M.; Zhang, H.; Huang, H.; Arita, M.; Sun, Z.; Duan, W.; Wu, Y.; Zhou, S. Experimental evidence for type-II Dirac semimetal in PtSe₂. *Phys. Rev. B* **2017**, *96*, 125102.
- 29) Pawbake, A. S.; Pawar, M. S.; Jadkar, S. R.; Late, D. J. Large area chemical vapor deposition of monolayer transition metal dichalcogenides and their temperature dependent Raman spectroscopy studies. *Nanoscale*, **2016**, *8*, 3008-3018.
- 30) Late, D. J.; Maitra, U.; Panchakarla, L. S.; Waghmare, U. V.; Rao, C. N. R. Temperature effects on the Raman spectra of graphenes: dependence on the number of layers and doping. *J. Phys.: Condens. Matter* **2011**, *23*, 055303.
- 31) Late, D. J. Temperature dependent phonon shifts in few-layer black phosphorus. *ACS Appl. Mater. Interfaces* **2015**, *7*, 5857-5862.
- 32) Pawbake, A. S.; Island, J. O.; Flores, E.; Ares, J. R.; Sanchez, C.; Ferrer, I. J.; Jadkar, S. R.; Van der Zant, H. S.; Castellanos-Gomez, A.; Late, D. J. Temperature-dependent Raman spectroscopy of titanium trisulfide (TiS₃) nanoribbons and nanosheets. *ACS Appl. Mater. Interfaces* **2015**, *7*, 24185-24190.
- 33) Calizo, I.; Balandin, A. A.; Bao, W.; Miao, F.; Lau, C. N. Temperature dependence of the Raman spectra of graphene and graphene multilayers. *Nano Lett.* **2007**, *7*, 2645-2649.

- 34) Late, D. J. Temperature-dependent phonon shifts in atomically thin MoTe₂ nanosheets. *Appl. Mater. Today*, **2016**, *5*, 98-102.
- 35) Pawar, M.; Kadam, S.; Late, D. J. High-Performance Sensing Behavior Using Electronic Ink of 2D SnSe₂ Nanosheets. *ChemistrySelect* **2017**, *2*, 4068-4075.
- 36) Late, D. J.; Huang, Y. K.; Liu, B.; Acharya, J.; Shirodkar, S. N.; Luo, J.; Yan, A.; Charles, D.; Waghmare, U. V.; Dravid, V. P.; Rao, C. N. R. Sensing behavior of atomically thin-layered MoS₂ transistors. *ACS Nano* **2013**, *7*, 4879-4891.
- 37) Late, D. J.; Doneux, T.; Bougouma, M. Single-layer MoSe₂ based NH₃ gas sensor. *Appl. Phys. Lett.* **2014**, *105*, 233103.

Chapter 7

MoS₂ and CdMoS₄ nanostructure based UV light Photodetectors

The paper based on this chapter published in Nanoscale Advances

M. Pawar et al. *Nanoscale Adv.* **2021**, *3*, 4799.

7.1 Introduction

The Photodetectors based on nanostructured materials are the significant component in nanoelectronic and optoelectronic devices.¹⁻⁴ The photodetector with quick photoresponse and high photoresponsivity are much on demand for real-world applications such as optical imaging and communication.^{2,5} To date, photodetectors from various nanomaterials (0D, 1D, and 2D) with remarkable response time, high responsivity were reported for the excitation wavelengths ranging from ultraviolet to near-infrared.⁶⁻¹² For the development of high performance photodetector, the semiconducting materials with appropriate bandgap and nanostructured morphology are highly desirable and important. Although the 2D graphene has attracted much interest in various nanoelectronic systems due to its outstanding electronic, thermal, and mechanical properties, the further development has been restricted in the optoelectronic devices due to zero bandgap or semimetallic nature.¹³ In previous reports, where researchers have developed a strategy to create bandgap in graphene and utilized it for broadband photodetector application.¹⁴ In contrast, the presence of favourable bandgap in other 2D inorganic layered materials such as MoS₂, WS₂, MoS₂, SnSe₂ and BP suggests great promise in the fabrication of large scale photodetector devices.¹⁵⁻²³ These 2D materials also possesses layer dependent tunable bandgap i.e. direct bandgap in monolayer and indirect bandgap in bulk form. It makes these materials a potential candidate in various applications such as FET, solar cells, gas sensor and energy storage etc.²⁴⁻²⁸ Due to the strong light absorption in the visible to near-infrared region, MoS₂ is widely used in optoelectronic systems. In 2012, Zhang et al. has reported single layer MoS₂ phototransistor for the first time and obtained maximum photoresponsivity ~ 7.5 mA/W at applied gate voltage (V_g , 50V).¹² Jason et al. reported near-infrared photodetection using bilayer MoS₂, where they have injected hot electrons into MoS₂ in order to originate sub-bandgap photocurrent results into photogain of the order of $\sim 10^5$. This photogain leads to photoreponsivity of 5.2 A/W at 1070 nm, which is

much higher than the Si based photodetector.²⁹ Also in another report from Zhai et al. on monolayer MoS₂ coupled with organic molecule, showed fast reponse time of 8 ms and maximum photoresponsivity of ~430 A/W after Al₂O₃ passivation.³⁰ Further, reports on MoS₂ based photodetector shows the addition of transport material reduces the recombination rate of charge carriers alongwith it acts as a photoabsorber thus leads to increase in the photocurrent.³¹⁻
³³ Here, we report the fabrication of 2D MoS₂ nanosheets and 3D CdMoS₄ nanoflowers based UV light photodetector. The solvothermal route was implied for the synthesis of these structures followed by structural and morphological investigations. We also demonstrate, the device performance of these samples under UV light illumination and their cyclic response.

7.2 Experimental Section

Synthesis Method

The details about the synthesis of MoS₂ nanosheets and CdMoS₄ nanoflowers were reported previously.³⁴ We have used hydrothermal method and the details are as follows:

For the synthesis of MoS₂ nanosheets: Initially, we have dissolved 2 mmol of ammonium molybdate in (40-50 ml) methanol with the help of stirrer. To this mixture, we have added dissolved thiourea in methanol drop wise followed by stirring for 15 min. The whole solution is then transferred into teflon lined stainless steel autoclave at 150°C for 48 h. The precipitate was obtained using Whatman filter paper followed by washing with ethanol several times and then heated in oven at 80°C for 4 h. The MoS₂ powder sample was then annealed at 400°C for 4 h in N₂ atmosphere.

For the CdMoS₄ nanoflowers synthesis: We have taken 2 mmol of cadmium nitrate (Cd(NO₃)₂) and dissolved it in 40-50 ml methanol also we prepared 20 ml solution by dissolving (NH₄)₆Mo₇O₂₄ precursor in CH₃OH with the help of stirrer which continued for 10

min. To this solution, we have added dissolved cadmium nitrate solution dropwise and continuously stirred for 10 min. Thereafter, dropwise addition of dissolved $\text{CH}_4\text{N}_2\text{S}$ was carried out to it and the solution was stirred for 15 more min. The solution is then transferred into autoclave which then heated at 150°C for 48 h. The precipitate was collected from the Whatman filter paper followed by washing with ethanol few times and then heated in oven at 80°C for 4 h. The CdMoS_4 powder sample was then annealed at 400°C for 4 h in N_2 atmosphere.

Characterization Details

The structural investigations were carried out with the help of X-Ray powder diffraction technique (XRD-D8, Advance, Bruker-AXS) and Raman spectrometer HR-800, Horiba JobinYvon, France with an excitation laser wavelength 632.8 nm. The surface morphologies of the as prepared samples were obtained from FESEM (FESEM, Hitachi, S-4800) and TEM (TEM, JEOL, 2010F Instrument).

7.3 Results and Discussion

7.3.1 Material Characterization

The phase formation of the as synthesized MoS_2 and CdMoS_4 samples are confirmed by XRD and depicted in Figure 7.1(a-b). The XRD of MoS_2 sample synthesized at 400°C for 4h was shown in Figure 7.1(a), matches with the JCPDS data card no. 00-009-0312 which confirms the formation pure hexagonal phase of layered MoS_2 and matches well with the earlier report.³⁵ Figure 7.1(b) shows the XRD pattern for CdMoS_4 sample annealed at 400°C for 4h. Indexing of the annealed CdMoS_4 sample is carried out with the help of Powder 4-DICVOLE software which validates the development of monoclinic structure of CdMoS_4 . The Figure 7.1(c) and 7.1(d) presents the Raman spectras for the MoS_2 and CdMoS_4 samples annealed at 400°C for

4h. The two Raman peaks are assigned for MoS₂ sample corresponds to E¹_{2g} (in-plane) and A_{1g} (out-of plane) vibration mode shown in Figure 7.1(c). These two Raman modes E¹_{2g} and A_{1g} appears at 382.5 and 406 cm⁻¹ respectively. The peak difference between two peaks is found to be 27.56 cm⁻¹ specifies the few layer formation of MoS₂ using simple solvothermal method. The intense Raman peak at 125, 150, 182, 238, 285, 307, 398, 664, 754, 819, 860 and 890 cm⁻¹ are observed for annealed CdMoS₄ sample shown in Figure 7.1(d).

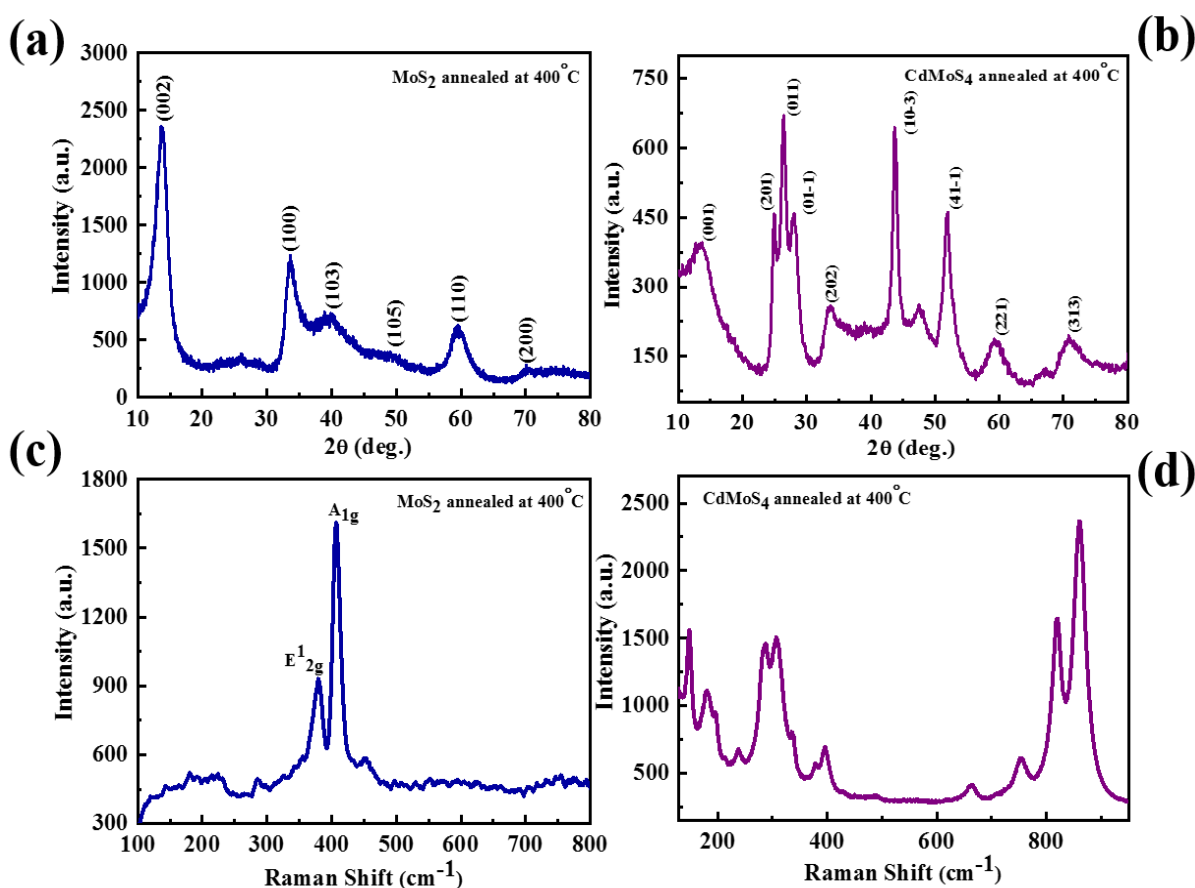


Figure 7.1: XRD pattern of (a) MoS₂ and (b) CdMoS₄ samples annealed at 400°C, Raman Spectra of (c) MoS₂ and (d) CdMoS₄ samples annealed at 400°C.

In order to investigate the surface morphology of the synthesized MoS₂ and CdMoS₄ Sample FESEM analysis has been carried out and results are depicted in the Figure 7.2 and 7.3 respectively. We observed some brake petals of MoS₂ Sheets with different size located on the long sheet shown in Figure 7.2(a-b). The long honeycomb like sheets up to 10 μm and thickness

found to be ~ 200 nm Figure 7.2(a-b). The pore size of the honeycomb sheet is 40-50 nm and thickness of the single cell is ~ 10 nm.

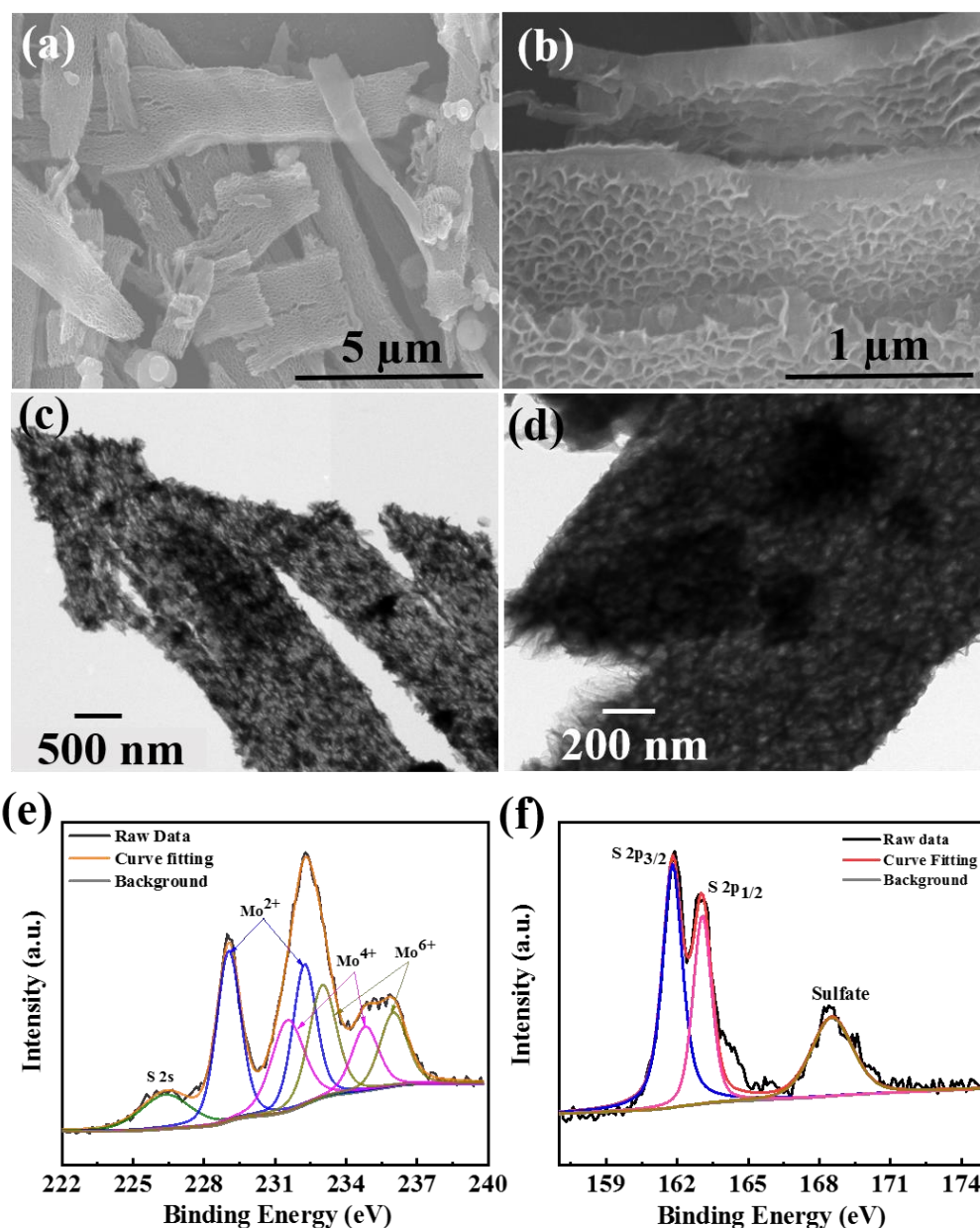


Figure 7.2: (a,b) FESEM images, (c,d) TEM images and (e,f) deconvoluted XPS spectras for Mo 3d and S 2p elements of the MoS₂ samples annealed at 400°C.

In the TEM image depicted in Figure 7.2(c-d) represents the sheet like structure of MoS₂ also matches well with the FESEM results. The MoS₂ samples were entirely honeycomb like sheets without aggregation. The XPS were carried out for MoS₂ sheets and core level XPS spectra's

for Mo 3d and S 2p were acquired shown in Figure 7.2(e-f). Figure 7.2(e) displays few characteristic peaks corresponding to the orbital of Mo^{2+} , Mo^{4+} and Mo^{6+} are observed at 232.29/229.05, 234.86/231.57 and 236.07/233.03 eV respectively.

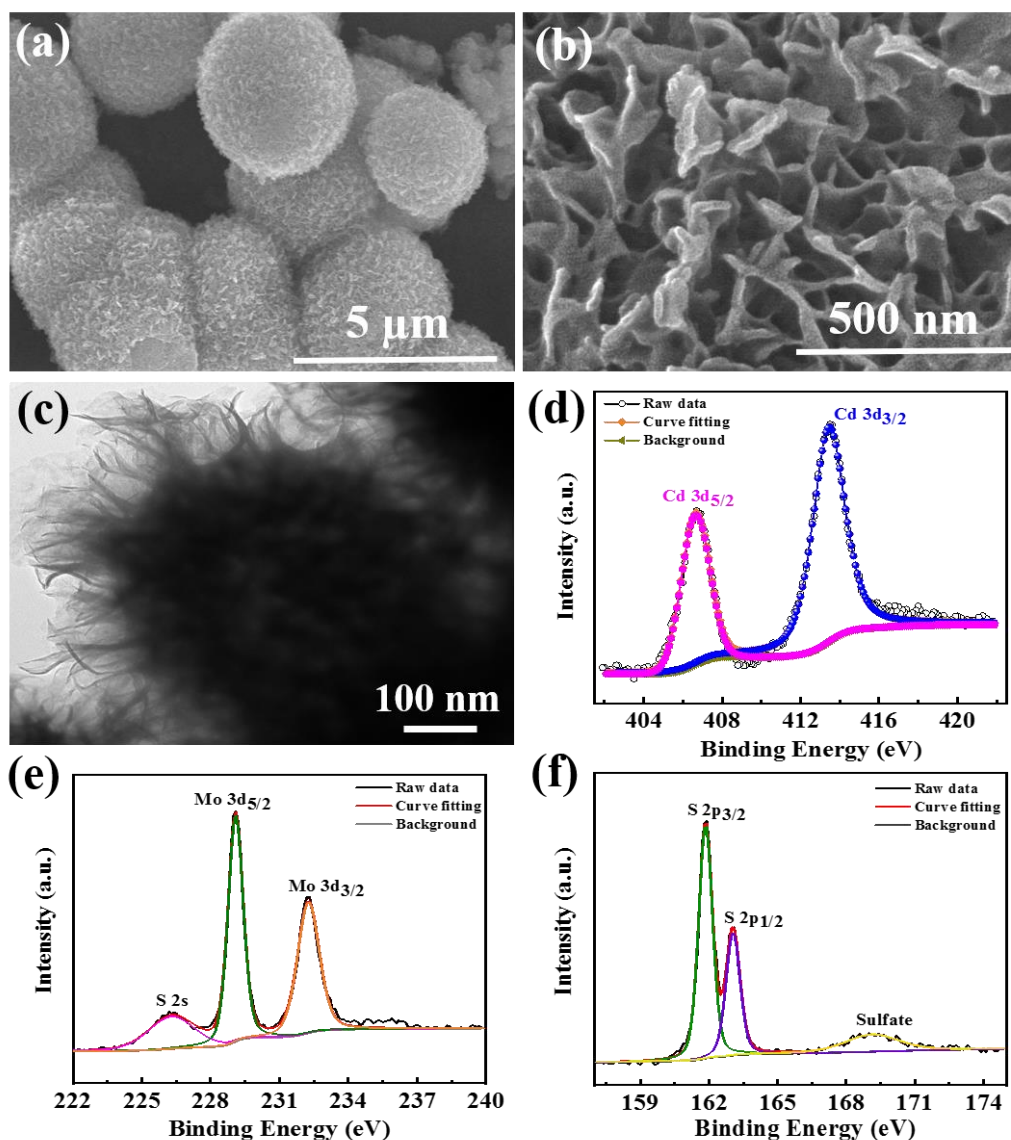


Figure 7.3: (a-b) FESEM images and (c) TEM image and (d-f) deconvoluted XPS spectras for Cd 3d, Mo 3d, S 2p of the CdMoS_4 nanoflowers annealed at 400°C .

In addition to this one peak for S 2s is observed at 226.4 eV which specifies the presence of bridging S^{2-} .³⁶ The two peaks at binding energies of 163 and 161.8 eV are detected for S 2p which can be attributed to S 2p_{3/2} and 2_{1/2} respectively shown in Figure 7.2(f). One minor peak

for S at higher binding energy of 168.52 eV was appeared i.e. due to surface oxidation of MoS_2 sheets.³⁷ The Figure 7.3(a-c) presents the surface morphology of the CdMoS_4 samples annealed at 400°C . Figure 7.3(a-b) are the FESEM images clearly shows the formation of porous nano flower like surface morphology of CdMoS_4 sample. The average size of the nano flower was observed to be $\sim 3 \mu\text{m}$ and thickness $\sim 50 \text{ nm}$. This kind of porous nano flower like structure of CdMoS_4 provides a fairly more surface area, which make easy transport of generated electron-hole to the surface and enhance the photo detector activity. Figure 7.3(c) shows TEM images for the as prepared CdMoS_4 sample. An original CdMoS_4 nanoflowers in Figure 7.3(c) shows marigold flower micro-structure of $\sim 2 \mu\text{m}$. The uniform hierarchical nanostructures consist of well-organized independent nano petals with a length of 20-30 nm Figure 7.3(c). Figure 7.3(d-f) presents the XPS spectra for Cd 3d, Mo 3d and S 2p elements of the CdMoS_4 annealed at 400°C .

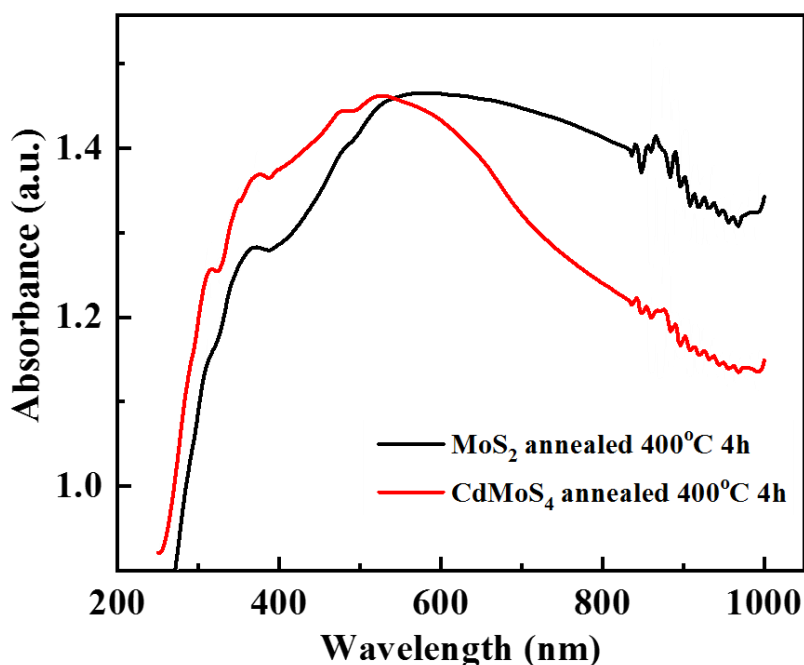


Figure 7.4: UV-Visible spectra for MoS_2 (Black color) and CdMoS_4 (Red color) samples annealed at 400°C .

The Cd 3d doublet peaks at 413.4 eV and 406.6 eV are observed for Cd 3d_{3/2} and 3d_{5/2} respectively shown in Figure 7.3(d). The Figure 7.3(e) displays two prominent peaks at 232.24 eV and 229.1 eV for Mo 3d indicates the presence of +4 oxidation state for Mo. The S 2p spectra (Figure 7.3(f)) also shows two peaks at 163.1 eV and 161.8 eV assigned to S 2p_{1/2} and S 2p_{3/2} respectively. Our XPS results matches well with the earlier reports and further confirms that existence of Cd, Mo and S in CdMoS₄ nanoflowers. It is apparent that the surface of the CdMoS₄ is made up of sheets which is quite smooth. The UV-Vis spectroscopy has been carried out for MoS₂ and CdMoS₄ annealed samples to investigate the optical properties presented in Figure 7.4. The red plot shows the broad absorption for CdMoS₄ nanoflowers in the UV region compared to MoS₂ (black color).

7.3.2 MoS₂ nanosheets based Photodetector

The as synthesized MoS₂ and CdMoS₄ samples further used for UV light photodetection. Figure 7.5(a) presents the I-V curves of the MoS₂ nanosheets under various power densities of UV light ranging from 0 mW/cm² upto 200 mW/cm². We observed that the current increases with the increasing power density of UV light. Photocurrents as a function of power density plot were shown in Figure 7.5(b) which indicates that the Photocurrent increases with the increasing power density. Photocurrent is calculated using the formula shown in equation 1.

$$I_p = I_{illumination} - I_{dark} \quad \dots\dots (1)$$

Figure 7.5(c) shows the photoresponsivity vs power density plot. The photoresponsivity is defined as the ratio of photocurrent to power density. We observed that the photoresponsivity increases with the increasing power density. The photocurrent response of the MoS₂ nanosheets photodetector is shown in Figure 7.5(d), which is measured with light illumination and dark conditions at an applied bias voltage of 0.5V. The Response and recovery time with the MoS₂ nanosheets based sensor is ~118 sec and ~123 sec respectively.

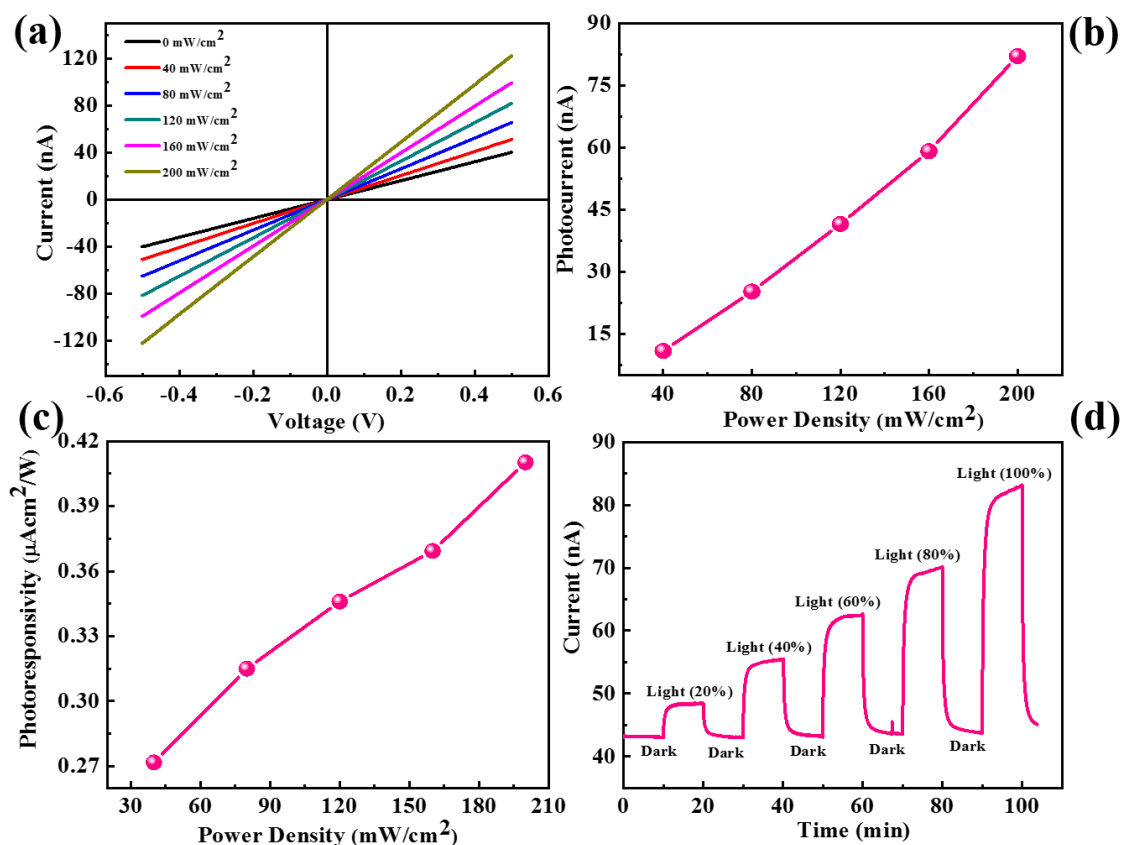


Figure 7.5: (a) *I-V* characteristics, (b) Photocurrent as a function of Power Density, (c) Photoresponsivity vs. Power Density, and (d) *I-t* plot to represent response and recovery time for MoS₂ nanosheets based device.

7.3.3 CdMoS₄ nanoflowers based Photodetector

Similarly, we have performed the UV light photodetector measurements for the CdMoS₄ device shown in figure 7.6. Figure 7.6(a) displays the *I-V* plots of the CdMoS₄ nanosheets upon illumination to various power densities of UV light ranging from 0 mW/cm² upto 200 mW/cm². We observed the increment in the current value with the increase in power density. The photocurrent as a function of power density shown in figure 7.6(b). Upon increasing the power density, photocurrent also increases. The photoresponsivity vs. power density plot depicted in figure 7.6(c). The obtained maximum photoresponsivity ~325 μAcm²/W for power density of 200 mW/cm², which is much higher than the MoS₂ based device.

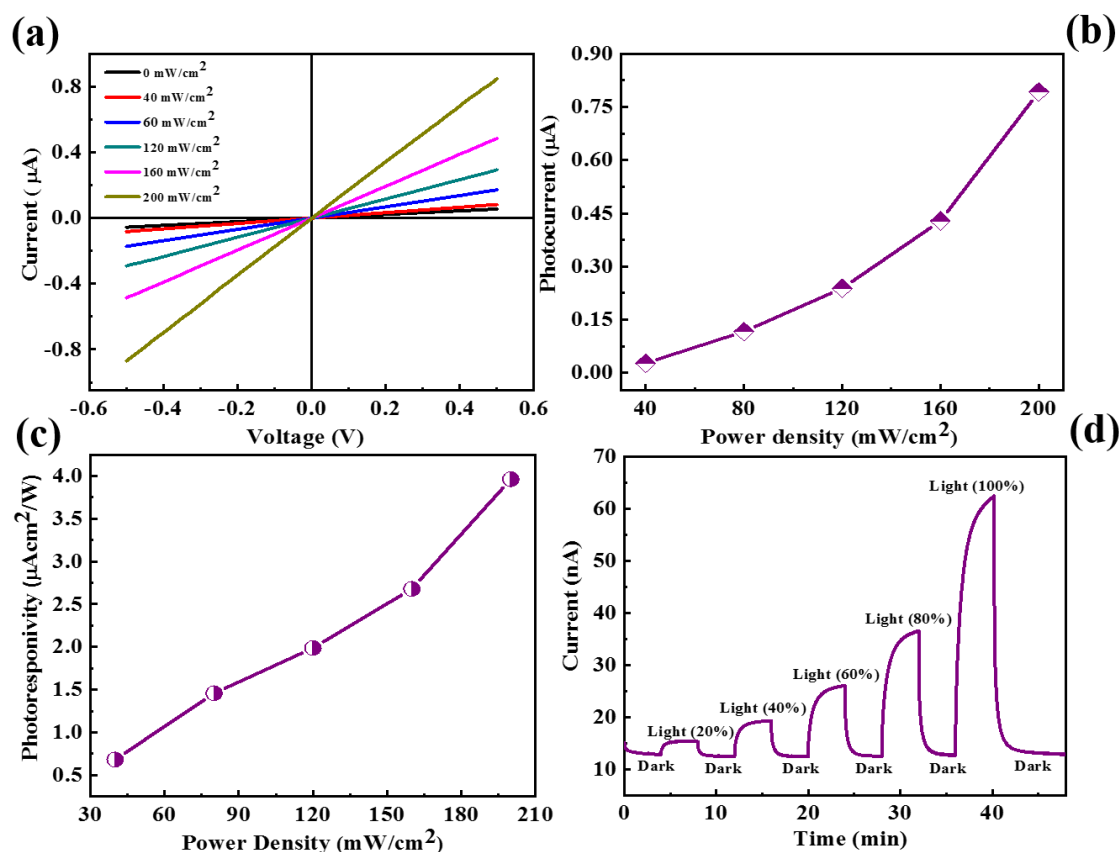


Figure 7.6: (a) *I-V* characteristics, (b) Photocurrent as a function of Power Density, (c) Photoresponsivity vs. Power Density, and (d) *I-t* plot to represent response and recovery time for CdMoS₄ nanoflowers based device.

The response time and recovery time for the CdMoS₄ based device were calculated from *I-t* plot shown in figure 7.6(d). The values are found to be ~74 sec and ~94 sec respectively which are lower than the device fabricated for MoS₂ nanosheets sample. The introduction of Cd into semiconducting MoS₂ not only increases the light absorption but also it improves the performance parameters. The role of Cd is to produce impurity energy levels into the material which shifts the absorption edges toward longer wavelength results into the enhancement in the properties of photodetector. Due to the enhanced photo excited carrier density of the CdMoS₄ sample suppresses the electron-hole recombination helps in improving the performance of the photodetector. In addition, the self-assembled nanoflowers from thin

petals, and high surface area required for the absorption of light results in higher number of charge carriers.

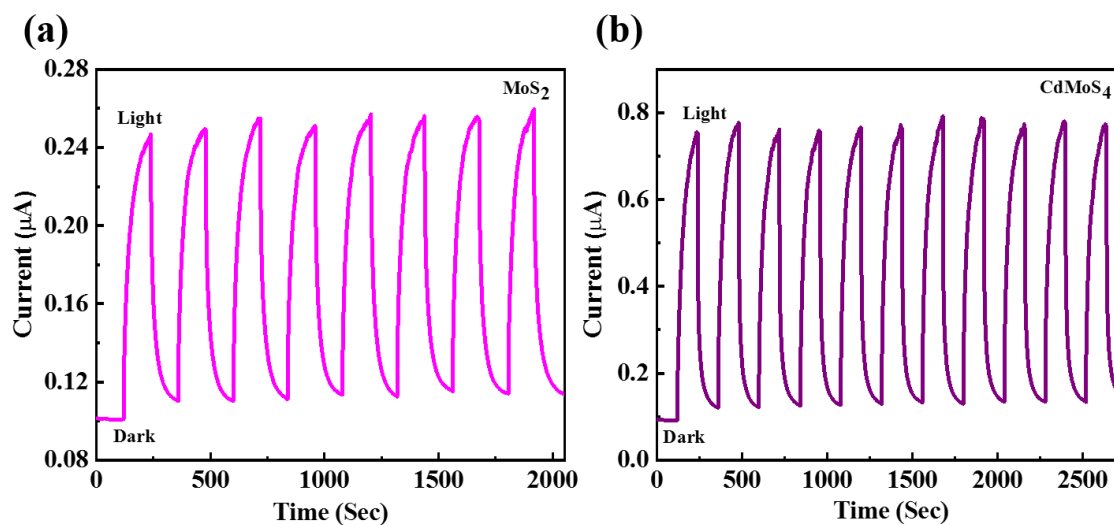


Figure 7.7: Cyclic photo response study on (a) MoS₂ and (b) CdMoS₄ samples annealed at 400°C.

The electron transfer becomes faster because of the thin petal like morphology of the CdMoS₄ sample which also inhibits charge recombination. The cyclic photoresponse study for the annealed MoS₂ and CdMoS₄ samples were carried out for more than 3h and the various cycles have been recorded in the light and dark conditions. The current-time (I-t) plot for the MoS₂ and CdMoS₄ based devices shown in Figure 7.7. Both the devices displays good photoresponse stability and reproducibility under UV light illumination. The results reveals that CdMoS₄ device shows good cyclic stability without showing any change in the photocurrent value compared to MoS₂ device for a long period of time.

7.4 Conclusions

In conclusion, the structural and morphological investigations of as synthesized MoS₂ nanosheets and CdMoS₄ nanoflowers were studied using spectroscopic and microscopic tools. The UV photodetector device were fabricated on ITO coated glass substrates with electrode

separation of ~ 0.5 mm. The CdMoS₄ nanoflower device showed better response to UV light compared to MoS₂ nanosheets in terms of Photoresponsivity, response time (74 sec) and recovery time (94 sec). Our results reveals that the device performance of CdMoS₄ materials can be improved by making composite or heterostructure using other 2D materials or by functionalization.

7.5 References

- 1) Konstantatos, G.; Sargent, E. H. Nanostructured materials for photon detection. *Nat. Nanotechnol.* **2010**, *5*, 391-400.
- 2) Pospischil, A.; Humer, M.; Furchi, M. M.; Bachmann, D.; Guider, R.; Fromherz, T.; Mueller, T. CMOS-compatible graphene photodetector covering all optical communication bands. *Nat. Photonics* **2013**, *7*, 892-896.
- 3) Tang, L.; Kocabas, S. E.; Latif, S.; Okyay, A. K.; Ly-Gagnon, D. S.; Saraswat, K. C.; Miller, D. A. Nanometre-scale germanium photodetector enhanced by a near-infrared dipole antenna. *Nat. Photonics* **2008**, *2*, 226-229.
- 4) Jie, J. S.; Zhang, W. J.; Jiang, Y.; Meng, X. M.; Li, Y. Q.; Lee, S. T. Photoconductive characteristics of single-crystal CdS nanoribbons. *Nano Lett.* **2006**, *6*, 1887-1892.
- 5) Mueller, T.; Xia, F.; Avouris, P. Graphene photodetectors for high-speed optical communications. *Nat. Photonics* **2010**, *4*, 297-301.
- 6) Oertel, D. C.; Bawendi, M. G.; Arango, A. C.; Bulović, V. Photodetectors based on treated CdSe quantum-dot films. *Appl. Phys. Lett.* **2005**, *87*, 213505.
- 7) McDonald, S. A.; Konstantatos, G.; Zhang, S.; Cyr, P. W.; Klem, E. J.; Levina, L.; Sargent, E.H. Solution-processed PbS quantum dot infrared photodetectors and photovoltaics. *Nat. Mater.* **2005**, *4*, 138-142.
- 8) Hu, L.; Yan, J.; Liao, M.; Wu, L.; Fang, X. Ultrahigh external quantum efficiency from thin SnO₂ nanowire ultraviolet photodetectors. *Small* **2011**, *7*, 1012-1017.
- 9) Lan, C.; Li, C.; Yin, Y.; Guo, H.; Wang, S. Synthesis of single-crystalline GeS nanoribbons for high sensitivity visible-light photodetectors. *J. Mater. Chem. C* **2015**, *3*, 8074-8079.

- 10) Pawar, M. S.; Bankar, P. K.; More, M. A.; Late, D. J. Ultra-thin V_2O_5 nanosheet based humidity sensor, photodetector and its enhanced field emission properties. *RSC Adv.* **2015**, *5*, 88796-88804.
- 11) Hu, P.; Wen, Z.; Wang, L.; Tan, P. Xiao, K. Synthesis of few-layer GaSe nanosheets for high performance photodetectors. *ACS Nano* **2012**, *6*, 5988-5994.
- 12) Yin, Z.; Li, H.; Li, H.; Jiang, L.; Shi, Y.; Sun, Y.; Lu, G.; Zhang, Q.; Chen, X.; Zhang, H., Single-layer MoS_2 phototransistors. *ACS Nano* **2012**, *6*, 74-80.
- 13) Meric, I.; Han, M. Y.; Young, A. F.; Ozyilmaz, B.; Kim, P.; Shepard, K. L. Current saturation in zero-bandgap, top-gated graphene field-effect transistors. *Nat. Nanotechnol.* **2008**, *3*, 654-659.
- 14) Shi, Y.; Fang, W.; Zhang, K.; Zhang, W.; Li, L. J. Photoelectrical response in single-layer graphene transistors. *Small* **2009**, *5*, 2005-2011.
- 15) Wu, J. Y.; Chun, Y. T.; Li, S.; Zhang, T.; Wang, J.; Shrestha, P. K.; Chu, D. Broadband MoS_2 Field-Effect Phototransistors: Ultrasensitive Visible-Light Photoresponse and Negative Infrared Photoresponse. *Adv. Mater.* **2018**, *30*, 1705880.
- 16) Yu, S. H.; Lee, Y.; Jang, S. K.; Kang, J.; Jeon, J.; Lee, C.; Lee, J. Y.; Kim, H.; Hwang, E.; Lee, S.; Cho, J. H. Dye-sensitized MoS_2 photodetector with enhanced spectral photoresponse. *ACS Nano* **2014**, *8*, 8285-8291.
- 17) Tan, H.; Fan, Y.; Zhou, Y.; Chen, Q.; Xu, W.; Warner, J. H. Ultrathin 2D photodetectors utilizing chemical vapor deposition grown WS_2 with graphene electrodes. *ACS Nano* **2016**, *10*, 7866-7873.
- 18) Perea-López, N.; Elías, A. L.; Berkdemir, A.; Castro-Beltran, A.; Gutiérrez, H. R.; Feng, S.; Lv, R.; Hayashi, T.; López-Urías, F.; Ghosh, S.; Muchharla, B. Photosensor device based on few-layered WS_2 films. *Adv. Funct. Mater.* **2013**, *23*, 5511-5517.

- 19) Chang, Y. H.; Zhang, W.; Zhu, Y.; Han, Y.; Pu, J.; Chang, J. K.; Hsu, W. T.; Huang, J. K.; Hsu, C. L.; Chiu, M. H.; Takenobu, T. Monolayer MoSe₂ grown by chemical vapor deposition for fast photodetection. *ACS Nano* **2014**, *8*, 8582-8590.
- 20) Zhang, W.; Chiu, M. H.; Chen, C. H.; Chen, W.; Li, L. J.; Wee, A. T. S. Role of metal contacts in high-performance phototransistors based on WSe₂ monolayers. *ACS Nano* **2014**, *8*, 8653-8661.
- 21) Zhou, X.; Gan, L.; Tian, W.; Zhang, Q.; Jin, S.; Li, H.; Bando, Y.; Golberg, D.; Zhai, T. Ultrathin SnSe₂ Flakes Grown by Chemical Vapor Deposition for High-Performance Photodetectors. *Adv. Mater.* **2015**, *27*, 8035-8041.
- 22) Buscema, M.; Groenendijk, D. J.; Blanter, S. I.; Steele, G. A.; Van Der Zant, H. S.; Castellanos-Gomez, A. Fast and broadband photoresponse of few-layer black phosphorus field-effect transistors. *Nano Lett.* **2014**, *14*, 3347-3352.
- 23) Ye, L.; Li, H.; Chen, Z.; Xu, J. 2016. Near-infrared photodetector based on MoS₂/black phosphorus heterojunction. *ACS Photonics* **2016**, *3*, 692-699.
- 24) Guo, C.; Tian, Z.; Xiao, Y.; Mi, Q.; Xue, J. Field-effect transistors of high-mobility few-layer SnSe₂. *Appl. Phys. Lett.* **2016**, *109*, 203104.
- 25) Tsai, M. L.; Su, S. H.; Chang, J. K.; Tsai, D. S.; Chen, C. H.; Wu, C. I.; Li, L. J.; Chen, L. J.; He, J. H. Monolayer MoS₂ heterojunction solar cells. *ACS Nano* **2014**, *8*, 8317-8322.
- 26) Late, D. J.; Huang, Y. K.; Liu, B.; Acharya, J.; Shirodkar, S. N.; Luo, J.; Yan, A.; Charles, D.; Waghmare, U. V.; Dravid, V. P.; Rao, C. N. R. Sensing behavior of atomically thin-layered MoS₂ transistors. *ACS Nano* **2013**, *7*, 4879-4891.
- 27) Hao, C.; Yang, B.; Wen, F.; Xiang, J.; Li, L.; Wang, W.; Zeng, Z.; Xu, B.; Zhao, Z.; Liu, Z.; Tian, Y. Flexible all-solid-state supercapacitors based on liquid-exfoliated black-phosphorus nanoflakes. *Adv. Mater.* **2016**, *28*, 3194-3201.

- 28) Bhandavat, R.; David, L.; Singh, G. Synthesis of surface-functionalized WS₂ nanosheets and performance as Li-ion battery anodes. *J. Phys. Chem. Lett.* **2012**, *3*, 1523-1530.
- 29) Wang, W.; Klots, A.; Prasai, D.; Yang, Y.; Bolotin, K. I.; Valentine, J. Hot electron-based near-infrared photodetection using bilayer MoS₂. *Nano Lett.* **2015**, *15*, 7440-7444.
- 30) Huang, Y.; Zhuge, F.; Hou, J.; Lv, L.; Luo, P.; Zhou, N.; Gan, L.; Zhai, T. Van der Waals coupled organic molecules with monolayer MoS₂ for fast response photodetectors with gate-tunable responsivity. *ACS Nano*, **2018**, *12*, 4062-4073.
- 31) Fang, C.; Wang, H.; Shen, Z.; Shen, H.; Wang, S.; Ma, J.; Wang, J.; Luo, H.; Li, D. High-performance photodetectors based on lead-free 2D Ruddlesden–Popper perovskite/MoS₂ heterostructures. *ACS Appl. Mater. Interfaces* **2019**, *11*, 8419-8427.
- 32) Wang, L.; Jie, J.; Shao, Z.; Zhang, Q.; Zhang, X.; Wang, Y.; Sun, Z.; Lee, S. T. MoS₂/Si heterojunction with vertically standing layered structure for ultrafast, high-detectivity, self-driven visible–near infrared photodetectors. *Adv. Funct. Mater.* **2015**, *25*, 2910-2919.
- 33) Zhang, W.; Chuu, C. P.; Huang, J. K.; Chen, C. H.; Tsai, M. L.; Chang, Y. H.; Liang, C. T.; Chen, Y. Z.; Chueh, Y. L.; He, J. H.; Chou, M. Y. Ultrahigh-gain photodetectors based on atomically thin graphene-MoS₂ heterostructures. *Sci. Rep.* **2014**, *4*, 3826.
- 34) Kadam, S. R.; Late, D. J.; Panmand, R. P.; Kulkarni, M. V.; Nikam, L. K.; Gosavi, S. W.; Park, C.J.; Kale, B. B. Nanostructured 2D MoS₂ honeycomb and hierarchical 3D CdMoS₄ marigold nanoflowers for hydrogen production under solar light. *J. Mater. Chem. A* **2015**, *3*, 21233-21243.
- 35) Zhang, X.; Tang, H.; Xue, M.; Li, C. Facile synthesis and characterization of ultrathin MoS₂ nanosheets. *Mater. Lett.* **2014**, *130*, 83-86.

- 36) Wu, C.; Liu, D.; Li, H.; Li, J. Molybdenum Carbide-Decorated Metallic Cobalt@ Nitrogen-Doped Carbon Polyhedrons for Enhanced Electrocatalytic Hydrogen Evolution. *Small* **2018**, 14, 1704227.
- 37) Karikalan, N.; Karthik, R.; Chen, S. M.; Karuppiah, C.; Elangovan, A. Sonochemical synthesis of sulfur doped reduced graphene oxide supported CuS nanoparticles for the non-enzymatic glucose sensor applications. *Sci. Rep.* **2017**, 7, 1-10

Chapter 8

Summary and Future Perspectives

8.1 Summary

The events reflected in this dissertation are presented in the five working chapters aligned with growth of 2D materials and their use in various nanoelectronic devices. In the introductory chapter of this thesis (*Chapter 1*), the background about nanomaterials and the importance of 2D materials are stated with special emphasis on device applications FET, Field Emitter, Humidity Sensor and photodetector. The importance of TMDCs and their ease of synthesis over graphene has been thoroughly discussed. The utilization of these 2D materials based on their properties for different applications are also covered in detail. The (*Chapter 2*), where various synthesis approaches (i.e. top down and bottom up) of 2D materials are briefly described also their advantages/disadvantages has been mentioned. In the second part of chapter 2, the working principle and some aspects of various characterization tools are described in brief. The major success of this thesis as they emerge in different working chapters are listed below:

Ultra-thin V₂O₅ Nanosheet based Humidity Sensor, Photodetector and its Enhanced Field Emission Properties (*Chapter 3*)

In this chapter, we present the preparation of V₂O₅ nanosheets and their characterization using few microscopy and spectroscopic techniques. We have investigated device performance for V₂O₅ nanosheets in the presence of water vapors having RH ranging from 11-97%. The maximum sensitivity of ~45.3% and response time of ~4 min. and recovery time ~5 min. were observed for the fabricated sensor device. Further, the as synthesized V₂O₅ nanosheet showed good performance towards UV photodetector with response time of ~65 s and maximum

photoresponsivity of $\sim 6.2 \mu\text{Acm}^2/\text{W}$. The FE properties were studied in planar diode assembly at base pressure of $\sim 1 \times 10^{-8}$ mbar. The turn on field required to draw an emission current density of $1 \mu\text{A}/\text{cm}^2$ and $10 \mu\text{A}/\text{cm}^2$ is found to be 1.15 and 1.72 V/ μm respectively which is very less as compared to previous reports for different V_2O_5 nanostructures. We achieved emission current density of $1532 \mu\text{A}/\text{cm}^2$ at 3.2 V/ μm and also high β value of 8580 and 3538 for low field and high field region. Our results open up several avenues and key success towards the utilization of other oxide nanosheet materials with layered structure for various energy harvesting, optoelectronics and nanoelectronics device applications.

Humidity Sensing and Photodetection Behavior of Electrochemically Exfoliated Atomically Thin-Layered Black Phosphorus Nanosheets (Chapter 4)

The first report where we have demonstrated electrochemical exfoliation of an atomically thin layer of BP nanosheets. We also present our investigation on few layer nanosheet thick film based BP photo detector, humidity sensor, and field effect transistor. The FET characteristics showed *p-type* behavior and the field effect mobility of $\sim 7.3 \text{ cm}^2/\text{Vs}$ and current ON/OFF ratio of $\sim 10^4$ were achieved. The BP nanosheets based thick film sensor devices are more sensitive to water vapors and UV light. The maximum photoresponsivity of $\sim 1.51 \text{ mA}/\text{W}$ were noted for power density of $200 \text{ mW}/\text{cm}^2$ with response time and recovery time were found to be $\sim 15\text{s}$ and 30s , respectively. Our results reveals that BP based thick film devices possess great potential to improve the sensing performance and allow selective response to certain kinds of gases and humidities.

High-Performance Sensing Behavior Using Electronic Ink of 2D SnSe₂ Nanosheets (Chapter 5)

We have successfully investigated sensing behavior of 2D SnSe₂ nanosheets synthesized using simple liquid exfoliation method. The N-Methyl-2-Pyrrolidone solvent was used for the

efficient exfoliation process to occur and the sonication was continued upto 10 h. Further, the centrifugation was carried out at different rpm in order to distinguish SnSe₂ layers. The fast recovery time of 4 sec was observed for the humidity sensor device based on 2D SnSe₂ nanosheet synthesized at 5000 rpm. The maximum sensitivity of 12103% were observed for SnSe₂ nanosheet ink sample synthesized at 1000 rpm. Even though the precise sensing mechanisms of SnSe₂ behavior is uncertain, still it has demonstrated superior sensing properties, makes it worthy of further investigations.

Temperature dependent Raman Spectroscopy investigations of PtSe₂ Nanosheets synthesized by wet Chemistry and its Sensor application (*Chapter 6*)

Here, we report wet chemistry method to grow PtSe₂ nanosheets. The synthesis process consists of two steps: Initially we have prepared PtSe complex and in the second step the obtained PtSe complex was heated at 700°C for 4 h in Ar atmosphere for the growth of PtSe₂ nanosheets. Further, the crystal structure and phase formation of PtSe₂ were validated from the XRD, Raman and SAED pattern. The temperature dependent Raman spectroscopy experiments were performed for 100 K to 506 K temperature on PtSe₂ nanosheet film. The temperature coefficient for both E_g and A_{1g} Raman modes were observed to be -0.014 and -0.008 respectively. The room temperature sensor device exhibited superior recovery time of ~5 sec indicates its potential for future nanoelectronics and sensor devices.

MoS₂ and CdMoS₄ nanostructure based UV light Photodetectors (*Chapter 7*)

The MoS₂ and CdMoS₄ nanostructures were synthesized using solvothermal method. The structural and morphological investigations of as synthesized MoS₂ nanosheets and CdMoS₄ nanoflowers were studied using spectroscopic and microscopic tools. The UV photodetector device were fabricated on ITO coated glass substrates with electrode separation of ~0.5 mm. The CdMoS₄ nanoflower device showed better response to UV light compared to MoS₂ nanosheets in terms of Photoresponsivity (~325 μAcm²/W), response time (74 sec) and

recovery time (94 sec). The response and recovery time of the MoS₂ nanosheets based sensor was observed to be ~118 sec and ~123 sec individually. Our results reveals that the device performance of CdMoS₄ materials can be improved by making composite or heterostructure using other 2D materials or by functionalization.

8.2 Future Perspectives

The present thesis discusses about the growth of 2D materials beyond graphene for the nanoelectronic device applications. The research work on V₂O₅, BP, SnSe₂, PtSe₂ and MoS₂ and CdMoS₄ described in five working chapters of this thesis is likely to have wide-ranging attention in the field of 2D materials and devices. Although, we have demonstrated electronic devices based on these materials in the context of this thesis, the prospect of using these materials for energy storage applications such as H₂ production, Li-ion battery and supercapacitor can be explored. The main advantage of these 2D materials is few of them possess similar lattice parameter hence heterostructures can be formed and various devices can be fabricated for electronic and optoelectronic applications. The heterostructures such as graphene-BP, MoS₂-BP, graphene-SnSe₂ can be formed using chemical vapor deposition technique. The devices can be fabricated with the help of electron beam lithography followed by metallization using thermal evaporator. The device performance can be analyzed with Keithley sourcemeter and plotted for further interpretation.

Recently, perovskite have attracted a great deal of attention in optoelectronic device applications. The unique properties such as high absorption coefficient (10^5 cm^{-1}) over a broad range of wavelengths, band gap tenability and high diffusion length ($> 1 \mu\text{m}$) makes them highly promising candidate for next generation devices. Some of them suffer from variability concerns such as moisture, temperature and UV illumination which limits their use when we look for particular application. Among all these perovskite cubic phase of $\alpha\text{-CsPbI}_3$ possess

precise band gap (1.73 eV) with high thermal stability over 300°C can be used with our 2D materials for further enhancing the device performance. These Cesium based perovskite can be synthesized using chemical route and monolayer TMDCs by CVD method followed by formation of α -CsPbI₃ - monolayer TMDCs hybrids with the help of dry transfer process. These formed hybrids could be used for the investigation of optoelectronic devices and we expect the performance parameter will enhance and it will open several windows for the researchers towards its utilization in optoelectronic device applications such as photodetector, solar cells and LED's.

ABSTRACT

Name of the Student: Mahendra S. Pawar

Registration No.: 10PP17A26044

Faculty of Study: Physical Sciences

Year of Submission: 2021

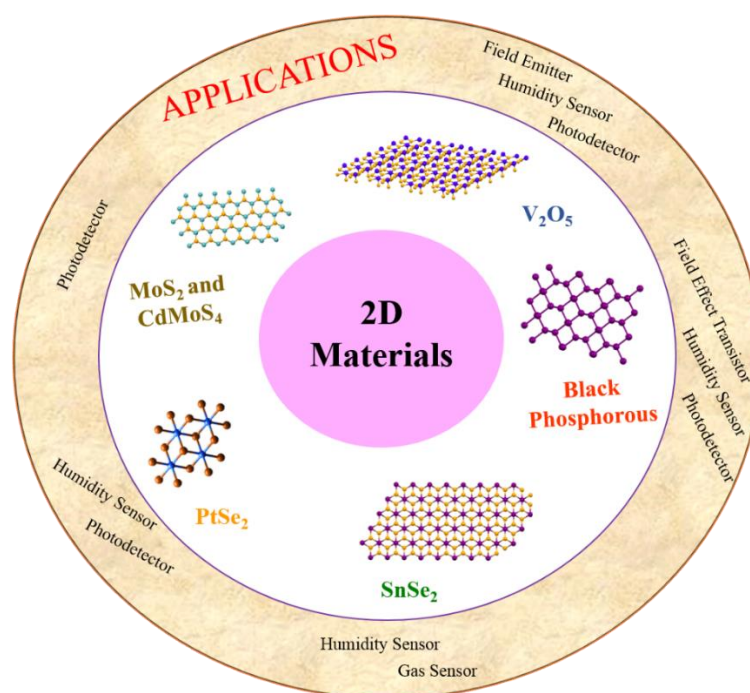
AcSIR academic centre/CSIR Lab: CSIR-NCL, Pune

Name of the Supervisor: Dr. T. G. Ajithkumar

Name of the Co-supervisor: Dr. Dattatray J. Late

Title of the thesis: Growth of Two Dimensional (2D) Materials and its Applications in Nanoelectronic Devices

The 2D materials like Graphene and MoS₂ are widely studied over the last decade due to their unique structural, mechanical, electrical and optical properties for nanoelectronics device applications. There are many other materials from 2D family possess similar properties as that of MoS₂ but are less explored by the researchers. In the present thesis, various 2D materials such as V₂O₅, Black Phosphorous, SnSe₂, PtSe₂ and CdMoS₄ are synthesized using top down and bottom up approaches. The structural, morphological and optical investigations were carried out using microscopic and spectroscopic techniques. Based on the characterization analysis these materials are utilized for fabricating nanoelectronic devices including FET, photodetector, humidity sensor and gas sensor. Our results reveals that these 2D materials can be potential candidate in next generation nanoelectronic devices.



Details of publications emanating from the thesis work

A) List of Research publications

- 1) Pawar, M. S.; Kadam S. R.; Kale, B. B.; Late, D. J. MoS₂ and CdMoS₄ nanostructure-based UV light photodetectors. *Nanoscale Adv.* **2021**, 3, 4799.
- 2) Pawar, M. S.; Late, D. J. Temperature-dependent Raman spectroscopy and sensor applications of PtSe₂ nanosheets synthesized by wet chemistry. *Beilstein J. Nanotechnol.* **2019**, 10, 467.
- 3) Pawar, M. S.; Sunil R. Kadam, Late, D. J. High-Performance Sensing Behavior Using Electronic Inks of 2D SnSe₂ Nanosheets. *ChemistrySelect* **2017**, 2, 4068.
- 4) Erande, M. B.; Pawar, M. S.; Late, D. J. Humidity Sensing and Photodetector Behavior of Atomically Thin-Layered Black Phosphorus Nanosheets Synthesized Using Electrochemical Exfoliation. *ACS Appl. Mater. Interfaces.* **2016**, 8, 11548. (Contributed equally)
- 5) Pawar, M. S.; Bankar, P. K.; More, M. A.; Late, D. J. Ultra-thin V₂O₅ Nanosheets based Humidity Sensor, Photodetector and its Enhanced Field Emission Properties. *RSC Adv.* **2015**, 5, 88796.

B) List of Papers with abstract presented poster at national/international conferences/seminars

- 1) Delivered oral talk at International Conference on Nanotechnology: Ideas, Innovations & Initiatives (ICN:3I 2017) at IIT, Roorkee (India)

Title: “High-Performance Sensing Behavior of Two Dimensional (2D) SnSe₂ Nanosheets”

Abstract: We have synthesized few layer thick SnSe₂ nanosheets using liquid exfoliation method. The structural, morphological, thickness / layering and elemental analysis of the nanosheets were characterized by using Raman spectroscopy, Transmission Electron Microscopy, Atomic Force Microscopy and X-Ray Photoelectron Spectroscopy. Further, these 2D SnSe₂ nanosheets with varying thickness were used for sensor device applications such as humidity and gas sensing. The sensor device has been tested for various relative humidity ranging from 11% to 97% at room temperature. The sensing results for few layers SnSe₂ based device exhibit excellent sensitivity, response and recovery time as compared with the bulk / thicker counterpart and it has ability to tune the sensing performance with thickness. The

atomically thin nature and good mechanical sturdiness open up new avenues for use of 2D SnSe₂ nanosheets as a suitable candidate for high-performance humidity / gas sensor applications.

- 2) Presented poster at International Conference on Nanoscience and Technology (**ICONSAT 2016**) at IISER, Pune (India)

Title: “Humidity Sensing and Photodetector Behavior of Atomically Thin-Layered Black Phosphorus Nanosheets Synthesized Using Electrochemical Exfoliation”

Abstract: The recent research on black phosphorous layered materials becomes hot topic and the one atomic layer of black phosphorous nanosheets is ideal structure for the enhanced gas-solid interactions due to large surface area. In the present investigations, we have synthesized few atomic layer thick nanosheets of black phosphorous using electrochemical exfoliation method. As synthesized nanosheets of black phosphorous then characterized by using optical microscopy, AFM, TEM, and further confirmed by Raman spectroscopy. The humidity sensor behavior then studied in the range of 11-97 % of relative humidity (RH) levels at room temperature. The response time of ~ 116 sec and recovery time of ~ 26 sec were observed for the Black Phosphorous nanosheets based humidity sensor. The UV light irradiation on black phosphorous nanosheets shows good response of ~ 15 sec and recovery time of ~ 30 sec respectively. Our results show that few layer black phosphorous nanosheets sample exhibits excellent sensitivity, recovery and can be utilized for nanoelectronics device applications.

C) List of Research publications (Out of Thesis)

- 1) Pawar, M. S.; Bankar, P. K.; More, M. A.; Late, D. J. PbS Nanostar-Like Structures as Field Emitters. *ChemistrySelect* **2017**, 2, 5175.
- 2) Pawbake, A. S.; Pawar, M. S.; Jadkar, S. R.; Late, D. J. Large area chemical vapor deposition of monolayer transition metal dichalcogenides and their temperature dependent Raman spectroscopy studies. *Nanoscale* **2016**, 8, 3008.
- 3) Bankar, P. K.; Pawar, M. S.; Pawbake, A. S.; Warule, S. S.; Late, D. J.; More, M. A. Spatially Branched CdS-Bi₂S₃ Heteroarchitecture: Single Step Hydrothermal Synthesis Approach with Enhanced Field Emission Performance and Highly Responsive Broadband Photodetection. *RSC Adv.* **2016**, 6, 95092. (Contributed equally)

- 4) Suryawanshi, S. R.; Pawbake, A. S.; **Pawar, M. S.**; Jadkar, S. R.; More, M. A.; Late, D. J. Enhanced Field Emission from Single-Layer MoSe₂. *Mater. Res. Express.* **2016**, 3, 035003.

D) List of Research Awards

Senior Research Fellow (Physical Sciences) by Council of Scientific and Industrial Research (CSIR), India (2019).

Erratum

CrossMark
click for updatesCite this: *RSC Adv.*, 2015, 5, 88796

Ultra-thin V₂O₅ nanosheet based humidity sensor, photodetector and its enhanced field emission properties

Mahendra S. Pawar,^a Prashant K. Bankar,^b Mahendra A. More^{*b} and Dattatray J. Late^{*a}

We report the synthesis of V₂O₅ nanosheets by a simple hydrothermal method. The as synthesized V₂O₅ nanosheets were characterized by Raman spectroscopy, Field Emission Scanning Electron Microscopy (FESEM), Transmission Electron Microscopy (TEM) and UV-Vis spectroscopy. The humidity sensing behaviors were investigated in the range of 11–97% relative humidity (RH) at room temperature. The maximum sensitivity of 45.3%, response time of ~4 min and recovery time of ~5 min were observed for the V₂O₅ nanosheet based sensor. We also demonstrated the V₂O₅ nanosheets as an ultra-violet photodetector with a sensing response time of ~65 s and recovery time of ~75 s with a maximum photoresponsivity of ~6.2%. Further, we have also carried out field emission (FE) investigations of V₂O₅ nanosheets under a planar "Diode" assembly in an ultrahigh vacuum (UHV) chamber at a base pressure of $\sim 1 \times 10^{-8}$ mbar. The turn on fields required to draw field emission current densities of $1 \mu\text{A cm}^{-2}$ and $10 \mu\text{A cm}^{-2}$ are found to be $1.15 \text{ V } \mu\text{m}^{-1}$ and $1.72 \text{ V } \mu\text{m}^{-1}$, respectively. We achieved a maximum field emission current density of 1.532 mA cm^{-2} at an applied electric field of $3.2 \text{ V } \mu\text{m}^{-1}$. The field enhancement factors calculated from the slope of the Fowler–Nordheim (F–N) plot are found to be 8530 and 3530 at low field and high field regions, respectively. Our results open up several avenues towards the successful utilization of V₂O₅ nanosheets and other metal oxide nanosheets for various nanoelectronics device applications including sensors, photodetector and flat panel displays.

Received 26th August 2015
Accepted 12th October 2015

DOI: 10.1039/c5ra17253e

www.rsc.org/advances

Introduction

Since the invention of graphene, atomically thin two dimensional (2D) materials have attracted enormous attention due to their potential applications in next generation nano-electronics and optoelectronics devices.^{1,2} The first 2D layered materials isolated were graphene followed by several inorganic layered such as MoS₂, WS₂, MoSe₂, WSe₂, black phosphorous³⁸ *etc.* and metal oxides materials such as MoO₃, WO₃, MnO₂ were invented for various applications including humidity sensor,^{3–8} photodetector,^{9–23} transistor,²⁴ gas sensor,^{25,26} solar cell,^{43–46} supercapacitor,^{47–50} catalyst for water splitting^{51,52} *etc.* Humidity sensors have been developed to measure and monitor the environmental humidity that plays an important role in agriculture, food as well as the medical industry along with human activities.²⁷ The layered V₂O₅ is most stable oxide as compared with other oxides of vanadium. The 2D form of V₂O₅ has high surface to volume ratio and high oxidation state at nanoscale geometry. Recently nanostructure V₂O₅ has been used in

various application including field emission,^{29,30,59–63} supercapacitor,^{31–34} Li ion battery,³⁵ transistor,³⁶ photodetector³⁷ *etc.* A variety of methods of synthesis of V₂O₅ nanostructures have been reported till date including hydrothermal,^{28,53,54} electrospinning,^{55,56} polycondensation method.⁵⁷ Among them, hydrothermal method is widely used for the synthesis of V₂O₅ nanostructures due to low cost, fast reaction time, well controlled morphology and highly pure product. In hydrothermal method, the morphology of the materials can be tuned by the hydrothermal temperatures which can be kept slightly below the melting point of the reactants and also by varying the concentration of solvents used. The nanostructure V₂O₅ possesses direct bandgap of 2.2 eV to 2.7 eV in the visible light region which inspires to investigate the optoelectronic properties such as photodetection,³⁷ optical waveguide³⁹ and high speed photoelectric switches.³⁸

In this paper, we report V₂O₅ nanosheets based humidity sensor with superior performance with fast response and recovery time along with the high sensitivity. We also demonstrated the photodetector based on V₂O₅ nanosheet with fast response time ~65 s and recovery time of ~75 s to UV light. We have also done the field emission measurement for V₂O₅ nanosheets. We achieved turn on field to be $1.15 \text{ V } \mu\text{m}^{-1}$ and maximum current density of $\sim 1.532 \text{ mA cm}^{-2}$ at an applied

^aPhysical and Material Chemistry Division, CSIR – National Chemical Laboratory, Pune, 411008, Maharashtra, India. E-mail: datta099@gmail.com; dj.late@ncl.res.in

^bCentre for Advanced Studies in Material Science and Condensed Matter Physics, Department of Physics, SavitribaiPhule Pune University, Pune 411007, India. E-mail: mam@physics.unipune.ac.in

field of $3.2 \text{ V } \mu\text{m}^{-1}$ with high field enhancement factor of ~ 8580 shows applications in flat panel displays, electron emitter *etc.*

Experimental

Materials

Commercially available vanadium(v) oxide (Sigma-Aldrich, 99.99%) and dodecylamine (Sigma-Aldrich, $\geq 99\%$) were used for the synthesis of V_2O_5 nanosheets. The required salts for humidity sensing were purchased from the Thomas Baker chemicals Pvt. Ltd. Mumbai (India).

Synthesis method

The V_2O_5 nanosheets were synthesized using simple hydrothermal method for that V_2O_5 (15 mM) and dodecylamine (7.5 mM) were mixed with 5 ml of ethanol stirred for 2 h. To this mixture 15 ml of DI water was added and stirring was continued for further 48 h, then the mixture was transferred into the 50 ml Teflon lined stainless steel autoclave and placed in muffle furnace at 180°C for 7 days. The obtained black precipitate was finally washed with ethanol for several times followed by centrifugation and the precipitate was then dried in a vacuum furnace at 80°C for 12 h.

Material characterizations

The samples were characterized by using Raman Spectroscopy with Horiba JY Lab HR 800 instrument using Ar laser with wavelength of 632.5 nm operated in the back scattering geometry with synapse CCD detector. The surface morphology were investigated by using FESEM with HITACHI S-4800 instrument and the TEM images were captured using FEI TECNAI G2-20 (TWIN, The Netherlands) instrument operating at 200 kV. A UV-Vis spectrum was recorded using Shimadzu (UV-3600) Plus UV-Vis-NIR Spectrophotometer in the wavelength range 200–1300 nm.

Sensor device fabrication

The humidity sensor as well as photodetector devices were fabricated on an ITO (tin doped indium oxide) substrate by making scratch at the centre on the conducting surface with the help of glass cutter with separation between source and drain was $\sim 100 \mu\text{m}$. The contacts were then made using silver paint. For device preparation the as synthesized V_2O_5 nanosheets powder were dispersed into the ethanol and then ultrasonicated for 10 min, and subsequently drop casted between the source and drain. The devices were subsequently annealed in vacuum furnace at 200°C to improve the contact resistance.

Humidity sensing

All the electrical measurements were carried out using Keithley 2612A system source meter which was attached to a computer through GPIB 488A interface. The response of the device as a function of RH was performed by introducing the device inside the closed RH levels. The relative humidity levels were obtained by keeping the saturated salts of LiCl, MgCl_2 , K_2CO_3 , NaBr, KI, NaCl, KCl and K_2SO_4 in a closed vessel.

Photodetector

To investigate the photo detection property we used HAMA-MATSU (Model name: L9566-01A-02) UV light source. All the measurements were carried out at room temperature and in identical conditions.

Field emission

All the field emission (FE) measurements were carried out at room temperature in the planer “Diode” assembly in an all metal ultrahigh vacuum (UHV) chamber at a base pressure of $\sim 1 \times 10^{-8}$ mbar. A typical ‘diode’ configuration consists of a phosphor coated semitransparent screen as an anode. In order to investigate the FE properties, V_2O_5 nanosheets were sprinkled onto a piece of carbon tape ($0.3 \text{ cm} \times 0.3 \text{ cm}$). Such V_2O_5 sprinkled carbon tape was pasted onto a copper rod holder (diameter $\sim 50 \text{ mm}$), which acted as a cathode. The FE measurements were carried out at fixed cathode–anode separation of $\sim 2 \text{ mm}$. The emission current density – applied field and current–time measurements were carried out using Keithley (6514) electrometer by sweeping DC voltage applied to cathode with a step of 40 V (0–40 kV, Spellman, U.S.). The field emission current stability was recorded at preset current value of $1 \mu\text{A}$ using computer controlled data acquisition system.

Results and discussion

Characterization analysis

Fig. 1(a) shows the typical side view of the single-layer V_2O_5 nanosheet and Fig. 1(b) shows the top view. In Fig. 1(c) we show the typical experimental set-up used for the UV photo detection. The Raman spectrum for V_2O_5 nanosheets as well as for the bulk V_2O_5 material were shown in Fig. 2. The observed Raman spectra for V_2O_5 nanosheets matches well with that reported previously in the literature.^{28,40–42} The Raman shift corresponds to different modes of vibrations are 143, 194, 286, 408, 525, 693 and 993 cm^{-1} . The Raman spectra are found to be slightly down shifted for V_2O_5 nanosheets as compared to the V_2O_5 bulk material due to decrease in interlayer bonding. The Raman mode 993 cm^{-1} corresponds to the stretching modes of $\text{V}=\text{O}$ terminal oxygen and V_2-O *i.e.* doubly coordinated oxygen bonds respectively which is triply coordinated oxygen bonds. The Raman mode observed at 525 cm^{-1} corresponds to the stretching mode of V_3-O *i.e.* triply coordinated oxygen bonds. The bending vibration of the $\text{V}=\text{O}$ bonds arises for the 408 and 286 cm^{-1} modes. The Raman mode frequency 143 and 194 cm^{-1} corresponds to the external VO_5-VO_5 modes. Fig. 3(a–d) shows the typical FESEM images of the as synthesized V_2O_5 nanosheets which indicates that the high yield of nanosheets synthesized by using hydrothermal method. Typical FESEM images show V_2O_5 nanosheets with lateral dimensions in few tens of micrometers. Fig. 4(a–d) shows the TEM images of V_2O_5 nanosheets and Fig. 4(e) shows the HRTEM image taken from the V_2O_5 nanosheet which depicts the interplanar distance between the two plane is $\sim 0.35 \text{ nm}$, which corresponds to (202) plane of the V_2O_5 . Fig. 4(f) shows the corresponding selected area electron diffraction pattern which shows crystalline nature of the V_2O_5 nanosheets.

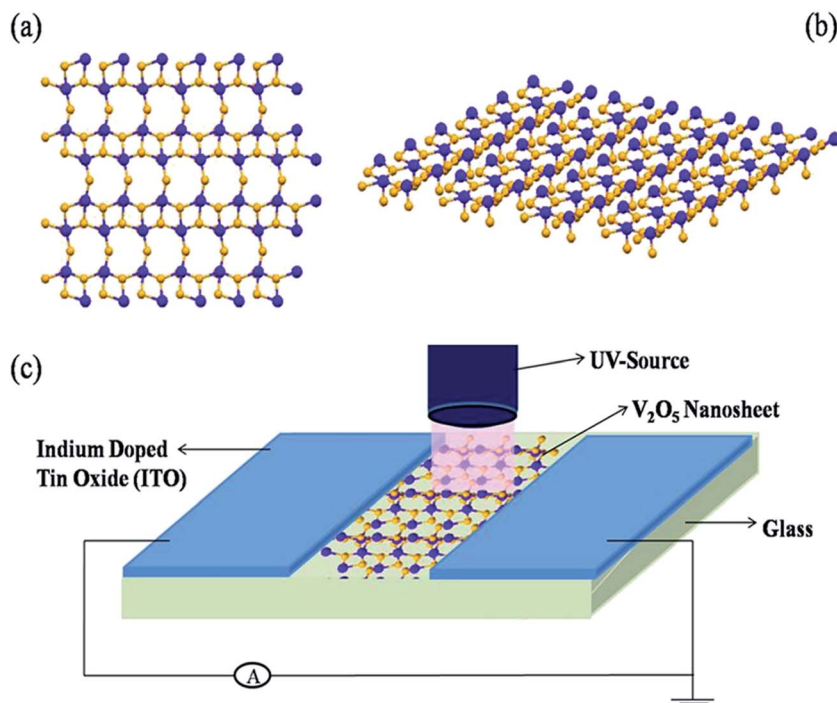


Fig. 1 Schematics for V_2O_5 nanosheets (a) side view, (b) top view and (c) photo detection experimental set up.

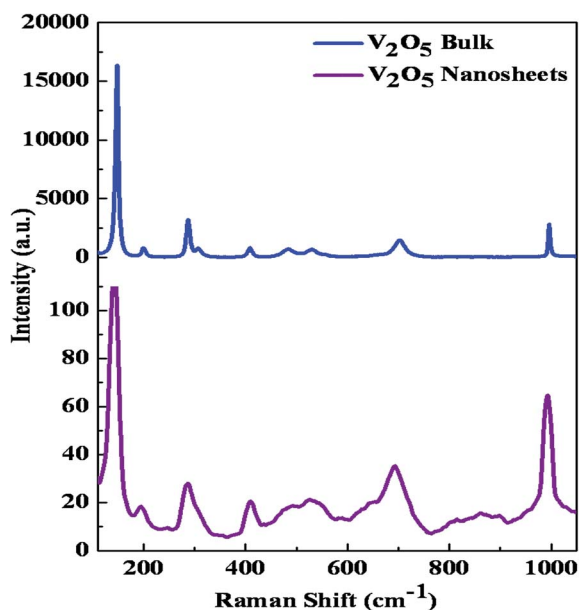


Fig. 2 Raman spectrum for as obtained V_2O_5 nanosheets and V_2O_5 bulk powder.

Optical properties

To investigate the optical properties of the V_2O_5 nanosheets, we recorded the UV-Vis spectrum as shown in Fig. 5. The spectrum represents the major absorption bands for V_2O_5 nanosheets ~ 410 nm. Our UV-Vis spectrum matches well with the reported spectrum of V_2O_5 nanosheets in the literature.⁶⁴

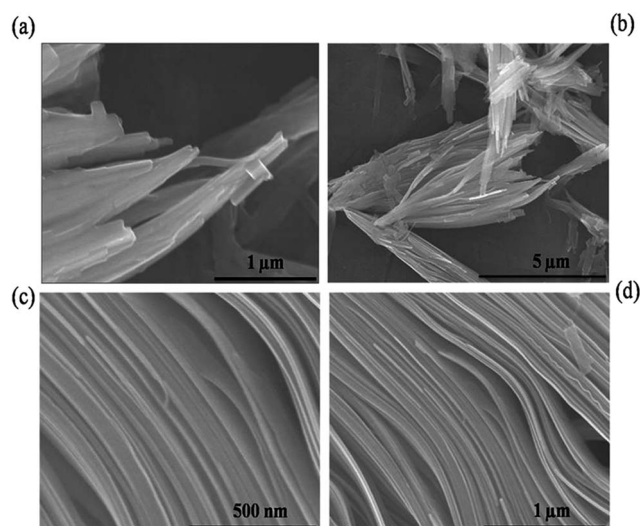


Fig. 3 (a–d) FESEM images of as synthesized V_2O_5 nanosheets by using hydrothermal method.

Humidity sensor

The V_2O_5 nanosheets synthesized by using hydrothermal method were used to further investigate the humidity sensing performance. The humidity sensing properties were investigated by fabricating the two probe device and then introducing to different relative humidity (RH) conditions, which were attained by using saturated salt solutions. It is noted that all the humidity measurements were carried out at room temperature. Fig. 6(a) shows the current–voltage (I – V) characteristics of V_2O_5

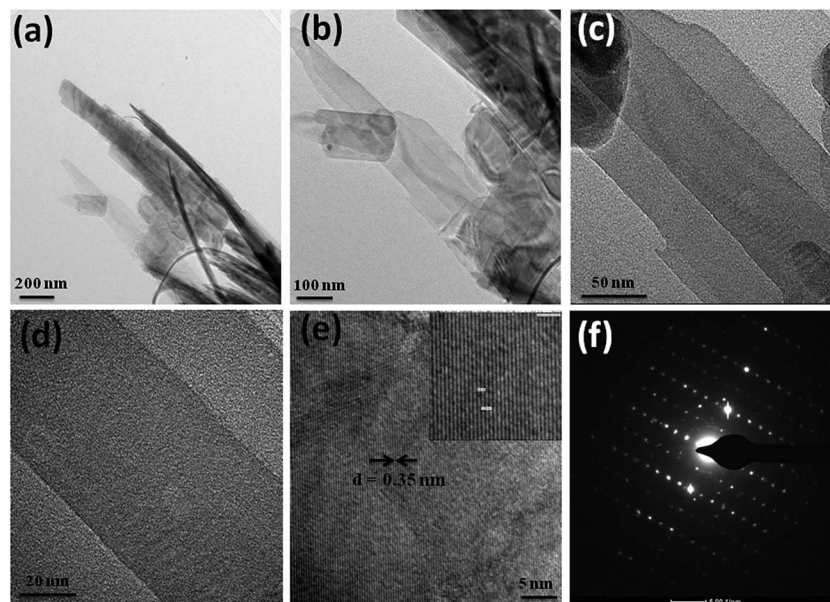


Fig. 4 Typical low magnification TEM images (a) 200 nm, (b) 100 nm, (c) 50 nm, (d) 20 nm and high resolution TEM (HRTEM) image (e) 5 nm. (f) shows the corresponding selected area electron diffraction pattern showing crystalline nature of as synthesized V_2O_5 nanosheets.

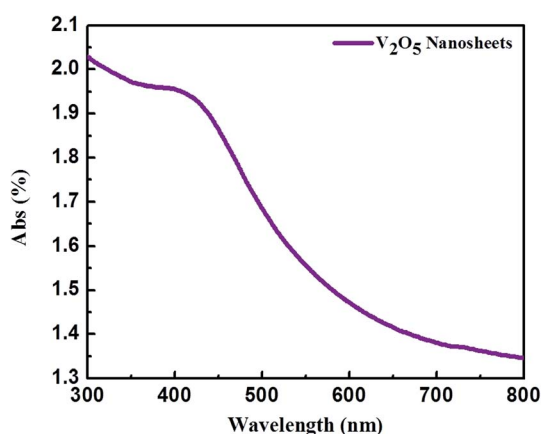


Fig. 5 UV-Vis spectra of V_2O_5 nanosheets.

sensor device in different RH levels. It is clear from the (I - V) that the current decreases with the increase in relative humidity value. Fig. 6(b) shows the resistance *vs.* relative humidity plot for the V_2O_5 nanosheets based sensor device. The obtained (I - V) curve represents that the resistance increases with the increasing relative humidity (RH) levels. The sensitivity as a function of relative humidity plot was also shown in Fig. 6(c). The sensitivity of the device depends on the number of H_2O molecules adsorbed on the V_2O_5 nanosheets. We observed the positive sensitivity for the presented V_2O_5 nanosheets based sensor with increased RH levels. The sensitivity for V_2O_5 nanosheets sensor is defined as $S = \frac{R_H}{R_A} - 1$, where R_H and R_A is the resistances of the device to the humidity and in air respectively. The positive sensitivity implies that the H_2O

molecules present in the saturated salts acts as an electron acceptor which results in the p-type doping. The water molecules present in the saturated salts adsorbed on the surface of V_2O_5 nanosheets which shifts the Fermi level closer to the valence band edge. The maximum sensitivity for the presented V_2O_5 nanosheets sensor device was calculated to be 45.3%. The response and recovery time for the V_2O_5 nanosheets based sensor device were shown in Fig. 6(d). The cycles of 11.3% and 97.3% RH were used to record the response and recovery time. The current-time (I - t) measurements were carried out for several cycles to check the reproducibility in the response and recovery time. The response and recovery time for the V_2O_5 nanosheets sensor were found to be 4 min and 5 min respectively. The long recovery time may be due to slow desorption process of H_2O molecules from the V_2O_5 nanosheets and the faster response is due to hydrophilic surface of the V_2O_5 nanosheets results into immediate adsorption of H_2O molecules on the surface of nanosheets.⁶⁵ Another reason is due to the thickness of V_2O_5 nanosheets layer, thicker the sheet recovery will be more because desorption of H_2O molecules is difficult in the thick sheets so recovery time will be less in case of thin sheets. The response of the sensors device is based on strong adsorption/desorption of analyte molecules at room temperature along with traps or impurities at V_2O_5 and underlying substrate interface. The slow response is related to the activation energy of binding gas molecules to the V_2O_5 nanosheets. The response can be faster with light irradiation, manifested by the slope change during response.²⁶ The response rate can be improved by applying light irradiation, or increasing operating temperature. The traps at V_2O_5 /substrate interface are also possibly responsible for the slow recovery. However, we suspect that if this is the dominate factor, we should see recovery/response much slower in thick layer sample as

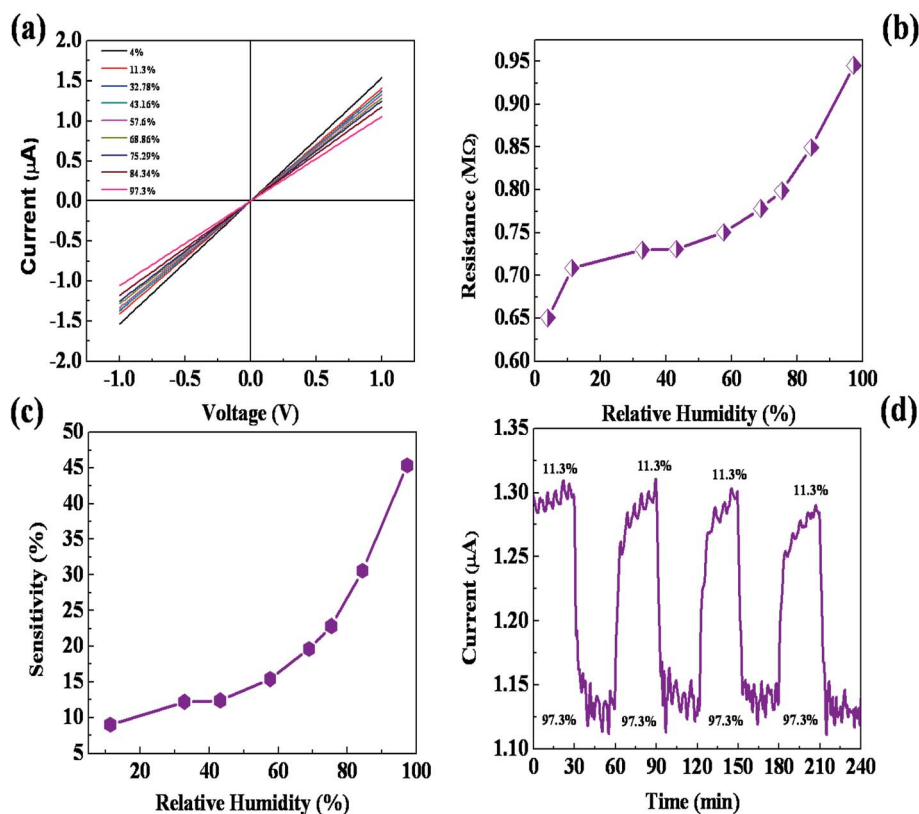


Fig. 6 (a) Current–voltage (I – V) characteristics, (b) resistance vs. relative humidity, (c) sensitivity vs. relative humidity and (d) current vs. time for as obtained V_2O_5 nanosheets based sensor device.

compared with thin layer sample, since our device requires longer time for the gas molecules to diffuse into interface.

UV photodetector

The V_2O_5 nanosheets synthesized by using hydrothermal method were also used for UV light photo detection. Fig. 7(a) shows the (I – V) characteristics of the V_2O_5 nanosheets sensor device with power density of UV light used upto 200 mW cm^{-2} . We observed that the current increases with the increasing power density of UV light. Photocurrent as a function of power density plot was shown in Fig. 7(b) which indicates that the photocurrent increases with the increasing power density. Photocurrent is the difference in the current recorded in the light illumination condition and the current recorded in the dark condition. Fig. 7(c) shows the photoresponsivity vs. power density plot. The photoresponsivity is defined as the ratio of photocurrent to power density. We observed that the photoresponsivity increases with the increasing power density. We observed the maximum photoresponsivity of $\sim 6.2 \mu\text{A cm}^2 \text{ W}^{-1}$ for 200 mW cm^{-2} power density. The photocurrent response of the V_2O_5 nanosheets photodetector is shown in Fig. 7(d), which is measured under the 365 nm light illumination with on and off cycles at applied bias voltage of 1 V. The response and recovery time with the V_2O_5 nanosheets based sensor is found to be $\sim 65 \text{ s}$ and $\sim 75 \text{ s}$ respectively.

Field emission

As synthesized V_2O_5 nanosheets were further used to investigate the field emission properties. Fig. 8(a) depicts the field emission current density versus an applied electric field (J – E) characteristics of V_2O_5 nanosheets. It is noted that the current density exponentially increases with an elevated applied electric field, indicating that the emission is as per the Fowler–Nordheim (F–N) theory.⁶³ It demonstrate a turn-on and threshold field defined as, field require to draw an emission current density of $\sim 1 \mu\text{A cm}^{-2}$ and $\sim 10 \mu\text{A cm}^{-2}$, respectively is found to be 1.15 and $1.72 \text{ V } \mu\text{m}^{-1}$. Interestingly, an emission current density of 1.532 mA cm^{-2} is achieved at an applied field of $3.2 \text{ V } \mu\text{m}^{-1}$. The results suggest that the observed value of turn-on and threshold field is much lower than the earlier reported values for different V_2O_5 nanostructures. The comparison of FE properties between the as-synthesized product and various V_2O_5 nanostructures is shown in Table 1. As noticed from the SEM image, most of the V_2O_5 nanosheets are randomly oriented, it could be expected that some of them will protrude outside the substrate surface, which act as potential emitting sites. The dependence of field electron emission current density over applied field (J – E) is further characterized by modified Fowler–Nordheim (F–N) theory⁶³ using the following equation,

$$J = \lambda_{\text{MA}} a \phi^{-1} E^2 \beta^2 \exp\left(-\frac{b \phi^2}{\beta E} v_{\text{F}}\right) \quad (1)$$

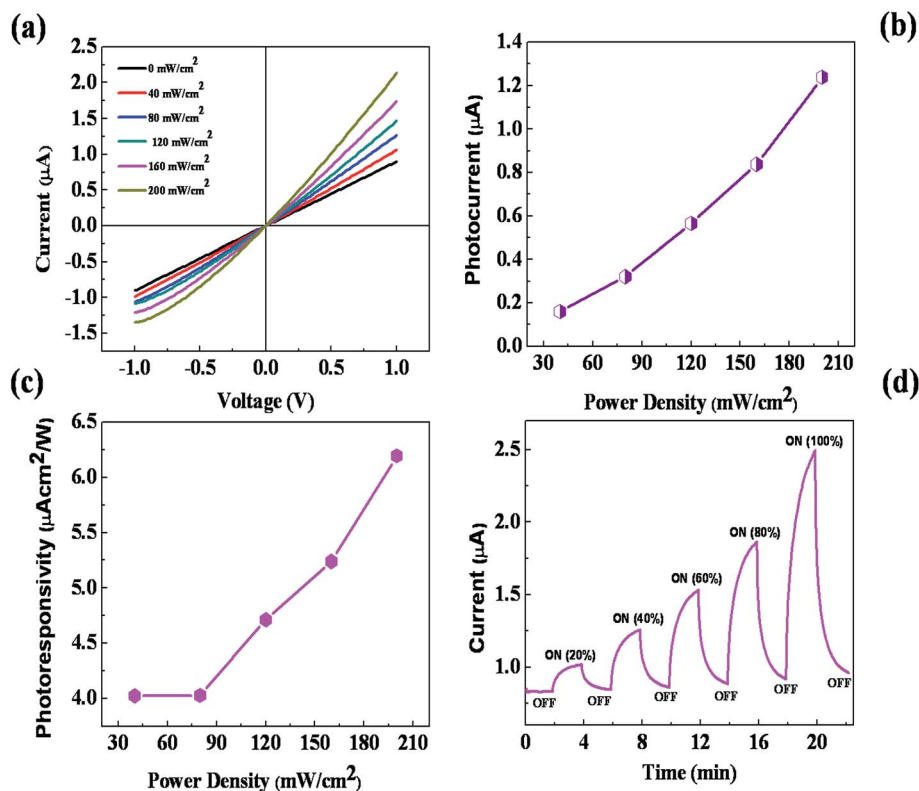


Fig. 7 (a) Current–voltage (I – V) characteristics, (b) photocurrent vs. power density, (c) photo responsivity vs. power density and (d) current vs. time under the illumination of light from 0 mW cm^{-2} to 200 mW cm^{-2} .

where, J is the emission current density, E is the applied average electric field, a and b are constants, typically $1.54 \times 10^{-6} \text{ A eV V}^{-2}$ and $6.83 \text{ eV}^{-3/2} \text{ V nm}^{-1}$, respectively, ϕ is the work function of the emitter material, λ_M be the macroscopic pre-exponential correction factor, ν_F is value of the principal Schottky–Nordheim barrier function (a correction factor), and β is the field enhancement factor. In the present investigations, the applied electric field (E) is defined as $E = V/d$, where V is the applied voltage, and d is the separation between anode and cathode ($\sim 2 \text{ mm}$). Furthermore, the emission current density (J) is estimated as $J = I/A$, where, I is the emission current and A is the total area of the emitter. The J – E characteristic is further analyzed by plotting a graph of $\ln(J/E^2)$ versus $(1/E)$, known as a Fowler–Nordheim (F–N) plot. The corresponding F–N plot is shown in Fig. 8(b). In the present study, the F–N plot is found to be nonlinear and such F–N plots have been reported for many semiconducting nanomaterials. The nonlinearity in the F–N plot can be resolved into two linear sections with distinct slopes in the high-field and low-field regions (see Fig. 8(b)). The field enhancement factors (β) are calculated from the slope of the low-field and the high-field regions of the F–N plot, using the following eqn (2),

$$\beta = -\frac{6.8 \times 10^3 \times \phi^3}{\text{slope}} \quad (2)$$

The field enhancement factor for low field and high field regions are found to be 8580 and 3538 respectively. These calculated values of may be overestimates due to the limitation of the F–N equation. For the application purpose in field emission based devices, emission current stability receives an important parameter. The emission current and time (I – t) plot recorded at a base pressure of $\sim 1 \times 10^{-8} \text{ mbar}$ is shown in Fig. 8(c). The average emission current is seen to remain stable at pre-set value of $\sim 1 \mu\text{A}$ over three and half hour. The emission current is seen to be stable over the duration of measurement and characterized by fluctuation in the form of “spike”. The appearance of the “spikes” in the emission current is attributed to the adsorption, desorption, and migration of the residual gas molecules on the emitter surface. The striking feature of the observed field emission behavior is that the average emission current remains nearly constant over the entire duration and shows no signs of degradation. This is very important feature particularly from the practical application of the emitter material as an electron source. Typical FE image, captured at emission current of $\sim 50 \mu\text{A cm}^{-2}$, is shown in Fig. 8(d). The image show a number of tiny spots, corresponding to the emission from the most protruding edges of V_2O_5 nanosheets. The temporal changes in the intensity of these spots are observed to be commensurate with the emission current fluctuation, depicted in the I – t plot.

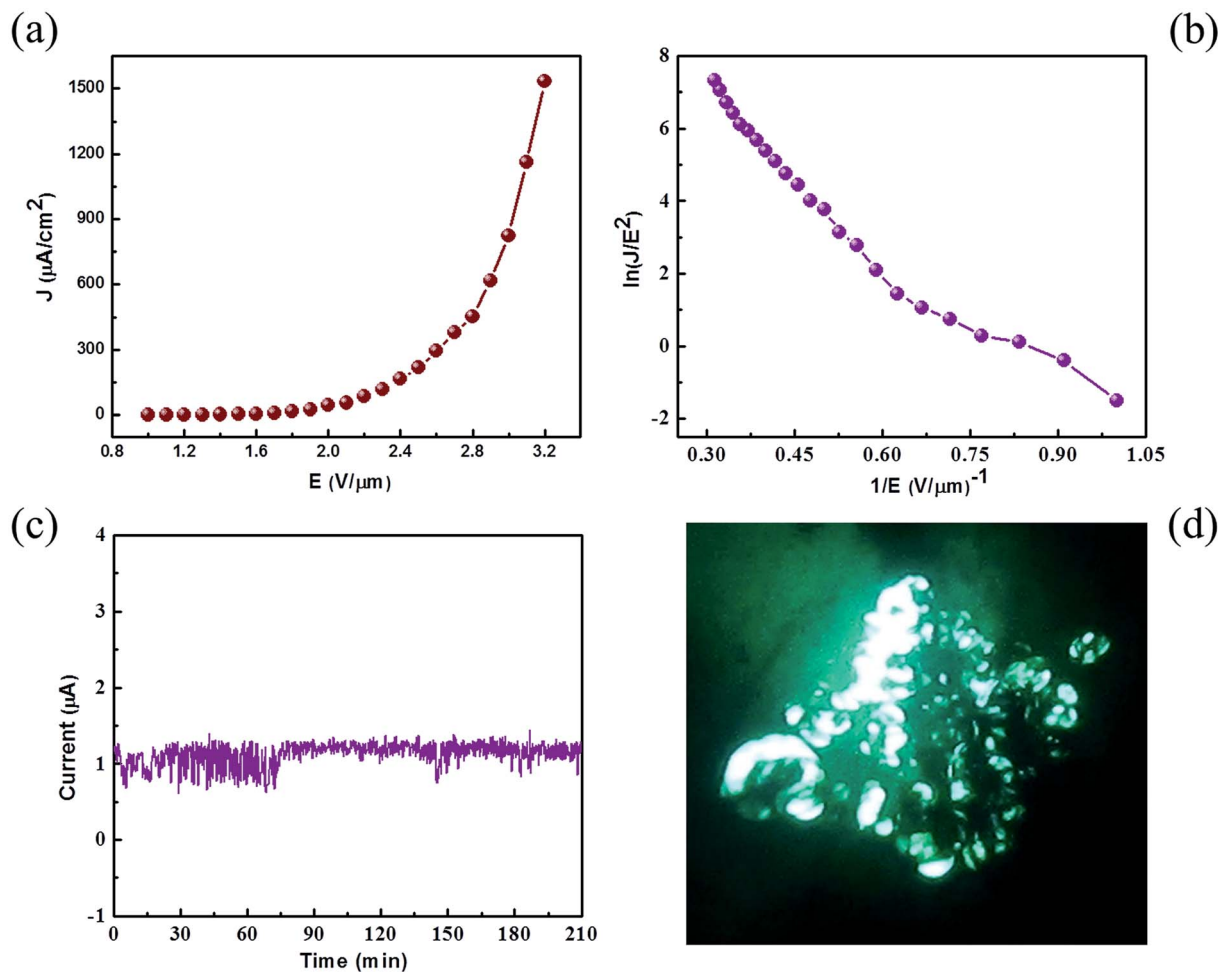


Fig. 8 Field emission properties of V_2O_5 nanosheets, (a) emission current density vs. applied electric field (J - E plot), (b) Fowler-Nordheim plot showing nonlinear behavior indicating field electron emission from semiconducting material, (c) field emission long term current stability (I - t plot), (d) field emission pattern recorded at current density of $50 \mu A cm^{-2}$.

Table 1 Comparison of field emission properties of various nanomaterials

Sr. no.	Morphology	Turn-on field (at $10 \mu A cm^{-2}$)	Max. current density at applied field	References
1	Nanofiber-bundles	$\sim 1.84 V \mu m^{-1}$	$213 \mu A cm^{-2}$ at $3.3 V \mu m^{-1}$	60
2	Centimeter long nanowires	$\sim 2.82 V \mu m^{-1}$	$14 mA cm^{-2}$ at $4.42 V \mu m^{-1}$	61
3	Vertically aligned nanowires	$\sim 8.30 V \mu m^{-1}$	$1.8 mA cm^{-2}$ at $18 V \mu m^{-1}$	29
4	Nanotubes array	$\sim 6.35 V \mu m^{-1}$	$2.1 mA cm^{-2}$ at $9.20 V \mu m^{-1}$	62
5	Nanorod array	$\sim 6.3 V \mu m^{-1}$	$2.31 mA cm^{-2}$ at $10 V \mu m^{-1}$	30
6	Nanosheets	$\sim 1.72 V \mu m^{-1}$	$1.53 mA cm^{-2}$ at $3.2 V \mu m^{-1}$	Present

Conclusion

In conclusion, we report the simple synthesis of V_2O_5 nanosheets by one step hydrothermal method. The as synthesized V_2O_5 nanosheets were characterized using Raman spectroscopy, FESEM, TEM and UV-Vis spectroscopy. The humidity sensing performances were carried out over a range of 11–97% relative humidity at room temperature. The maximum sensitivity of $\sim 45.3\%$ and response time of ~ 4 min and recovery time ~ 5 min

were observed for the V_2O_5 nanosheets sensor. Further, the as synthesized V_2O_5 nanosheets also shows good performance towards UV photodetector with response time of ~ 65 s and recovery time of ~ 75 s with maximum photoresponsivity of $\sim 6.2\%$. The field emission properties were studied in planer “Diode” assembly at base pressure of $\sim 1 \times 10^{-8}$ mbar. The turn on field required to draw an emission current density of $1 \mu A cm^{-2}$ and $10 \mu A cm^{-2}$ is found to be 1.15 and $1.72 V \mu m^{-1}$ respectively which is very less as compared to previous reports

for different V₂O₅ nanostructures. We achieved emission current density of 1.532 mA cm⁻² at an applied field of 3.2 V μm⁻¹ and also high field enhancement factor 8580 and 3538 for low field and high field region. Our results open up several avenues and key success towards the utilization of other oxide nanosheet materials with layered structure for various energy harvesting, optoelectronics and nanoelectronics device applications including sensors, photodetector, flat panel displays, electron source and transistor.

Acknowledgements

Dr D. J. Late would like to thank Prof. C. N. R. Rao (FRS), JNCASR and ICMS Bangalore (India) for encouragement, support and the experimental facilities. The research work was supported by Department of Science and Technology (Government of India) under Ramanujan Fellowship to Dr D. J. Late (Grant No. SR/S2/RJN-130/2012), NCL-MLP project grant 028626, DST-SERB Fast-track Young scientist project Grant No. SB/FT/CS-116/2013, Broad of Research in Nuclear Sciences (BRNS) Grant No. 34/14/20/2015 (Government of India) and the partial support by INUP IITB project sponsored by DeitY, MCIT, Government of India.

Notes and references

- Q. H. Wang, K. Kalantar-Zadeh, A. Kis, J. N. Coleman and M. S. Strano, *Nat. Nanotechnol.*, 2012, 7, 699–712.
- (a) M. Buscema, J. O. Island, D. J. Groenendijk, S. I. Blanter, G. A. Steele, H. S. J. van der Zant and A. Castellanos-Gomez, *Chem. Soc. Rev.*, 2015, 44, 3691–3718; (b) D. J. Late, *Advanced Device Materials*, 2015, 1, 52–58.
- Z. Li, H. Zhang, W. Zheng, W. Wang, H. Huang, C. Wang, A. G. MacDiarmid and Y. Wei, *J. Am. Chem. Soc.*, 2008, 130, 5036–5037.
- H. Bi, K. Yin, X. Xie, J. Ji, S. Wan, L. Sun, M. Terrones and M. S. Dresselhaus, *Sci. Rep.*, 2013, 3, 2714–2720.
- J. Chu, X. Peng, P. Feng, Y. Sheng and J. Zhang, *Sens. Actuators, B*, 2013, 178, 508–513.
- M. V. Kulkarni, S. K. Apte, S. D. Naik, J. D. Ambekar and B. B. Kale, *Sens. Actuators, B*, 2013, 178, 140–143.
- P. G. Su and Z.-M. Lu, *Sens. Actuators, B*, 2015, 211, 157–163.
- Q. Y. Tang, Y. C. Chan and K. Zhang, *Sens. Actuators, B*, 2011, 152, 99–106.
- F. Xia, T. Mueller, Y.-M. Lin, A. Valdes-Garcia and P. Avouris, *Nat. Nanotechnol.*, 2009, 4, 839–843.
- S. H. Yu, Y. Lee, S. K. Jang, J. Kang, J. Jeon, C. Lee, J. Y. Lee, H. Kim, E. Hwang, S. Lee and J. H. Cho, *ACS Nano*, 2014, 8, 8285–8291.
- Y. Chang, O. W. Zhang, O. Y. Zhu, Y. Han, J. Pu, J. Chang and W. Hsu, *ACS Nano*, 2014, 8, 8582–8590.
- N. Huo, S. Yang, Z. Wei, S.-S. Li, J.-B. Xia and J. Li, *Sci. Rep.*, 2014, 4, 5209–5217.
- (a) D. J. Late, P. A. Shaikh, R. Khare, R. V. Kashid, M. Chaudhary, M. A. More and S. B. Ogale, *ACS Appl. Mater. Interfaces*, 2014, 6, 15881–15888; (b) D. J. Late, B. Liu, H. S. S. R. Matte, V. P. Dravid and C. N. R. Rao, *ACS Nano*, 2012, 6, 5635–5641; (c) D. J. Late, B. Liu, H. S. S. Matte, C. N. R. Rao and V. P. Dravid, *Adv. Funct. Mater.*, 2012, 22, 1894–1905; (d) M. Thripuranthaka and D. J. Late, *ACS Appl. Mater. Interfaces*, 2014, 6, 1158–1163; (e) D. J. Late, S. N. Shirodkar, U. V. Waghmare, V. P. Dravid and C. N. R. Rao, *ChemPhysChem*, 2014, 15, 1592–1598; (f) M. Thripuranthaka, R. V. Kashid, C. S. Rout and D. J. Late, *Appl. Phys. Lett.*, 2014, 104, 081911; (g) D. Chakravarty and D. J. Late, *Eur. J. Inorg. Chem.*, 2015, (11), 1973–1980.
- S. Lei, L. Ge, Z. Liu, S. Najmaei, G. Shi, G. You, J. Lou, R. Vajtai and P. M. Ajayan, *Nano Lett.*, 2013, 13, 2777–2781.
- S. Lei, A. Sobhani, F. Wen, A. George, Q. Wang, Y. Huang, P. Dong, B. Li, S. Najmaei, J. Bellah, G. Gupta, A. D. Mohite, L. Ge, J. Lou, N. J. Halas, R. Vajtai and P. Ajayan, *Adv. Mater.*, 2014, 26, 7666–7672.
- O. Lopez-Sanchez, D. Lembke, M. Kayci, A. Radenovic and A. Kis, *Nat. Nanotechnol.*, 2013, 8, 497–501.
- J. Wang, M. S. Gudiksen, X. Duan, Y. Cui and C. M. Lieber, *Science*, 2001, 293, 1455–1457.
- J. Xia, X. Huang, L.-Z. Liu, M. Wang, L. Wang, B. Huang, D.-D. Zhu, J.-J. Li, C.-Z. Gu and X.-M. Meng, *Nanoscale*, 2014, 6, 8949–8955.
- C. Zhang, S. Wang, L. Yang, Y. Liu, T. Xu, Z. Ning, A. Zak, Z. Zhang, R. Tenne and Q. Chen, *Appl. Phys. Lett.*, 2012, 100, 243101–243105.
- K. Liu, M. Sakurai and M. Aono, *Sensors*, 2010, 10, 8604–8634.
- L. Hu, J. Yan, M. Liao, L. Wu and X. Fang, *Small*, 2011, 7, 1012–1017.
- D.-Y. Guo, C.-X. Shan, S.-N. Qu and D.-Z. Shen, *Sci. Rep.*, 2014, 4, 7469–7474.
- K. Deng, H. Lu, Z. Shi, Q. Liu and L. Li, *ACS Appl. Mater. Interfaces*, 2013, 5, 7845–7851.
- D. J. Late, B. Liu, J. Luo, A. Yan, H. S. S. R. Matte, M. Grayson, C. N. R. Rao and V. P. Dravid, *Adv. Mater.*, 2012, 24, 3549–3554.
- V. Galstyan, E. Comini, G. Faglia and G. Sberveglieri, *Sensors*, 2013, 13, 14813–14838.
- (a) D. J. Late, Y. K. Huang, B. Liu, J. Acharya, S. N. Shirodkar, J. Luo, A. Yan, D. Charles, U. V. Waghmare, V. P. Dravid and C. N. R. Rao, *ACS Nano*, 2013, 7, 4879–4891; (b) D. J. Late, T. Doneux and M. Bougouma, *Appl. Phys. Lett.*, 2014, 105, 233103; (c) P. K. Kannan, D. J. Late, H. Morgan and C. S. Rout, *Nanoscale*, 2015, 7, 13293–13312; (d) D. J. Late, C. S. Rout, D. Chakravarty and S. Ratha, *Can. Chem. Trans.*, 2015, 3, 118–157.
- G. Li, S. Pang, L. Jiang, Z. Guo and Z. Zhang, *J. Phys. Chem. B*, 2006, 110, 9383–9386.
- M. Niederberger, H. J. Muhr, F. Krumeich, F. Bieri, D. Günther and R. Nesper, *Chem. Mater.*, 2000, 12, 1995–2000.
- M. C. Wu and C. S. Lee, *J. Solid State Chem.*, 2009, 182, 2285–2289.
- W. Chen, C. Zhou, L. Mai, Y. Liu, Y. Qi and Y. Dai, *J. Phys. Chem. C*, 2008, 112, 2262–2265.
- L. Cao, J. Zhu, Y. Li, P. Xiao, Y. Zhang, S. Zhang and S. Yang, *J. Mater. Chem. A*, 2014, 2, 13136–13142.

- 32 D. Kim, J. Yun, G. Lee and J. S. Ha, *Nanoscale*, 2014, **6**, 12034–12041.
- 33 S. Myung, M. Lee, G. T. Kim, J. S. Ha and S. Hong, *Adv. Mater.*, 2005, **17**, 2361–2364.
- 34 Y. Wang and G. Cao, *Chem. Mater.*, 2006, **18**, 2787–2804.
- 35 L. Mai, F. Dong, X. Xu, Y. Luo, Q. An, Y. Zhao, J. Pan and J. Yang, *Nano Lett.*, 2013, **13**, 740–745.
- 36 G. T. Kim, J. Muster, V. Krstic, J. G. Park, Y. W. Park, S. Roth and M. Burghard, *Appl. Phys. Lett.*, 2000, **76**, 1875–1877.
- 37 R. S. Chen, W.-C. Wang, C.-H. Chan, H.-P. Hsu, L.-C. Tien and Y.-J. Chen, *Nanoscale Res. Lett.*, 2013, **8**, 443–450.
- 38 J. Lu, M. Hu, Y. Tian, C. Guo, C. Wang, S. Guo and Q. Liu, *Opt. Express*, 2012, **20**, 6974–6979.
- 39 B. Yan, L. Liao, Y. You, X. Xu, Z. Zheng, Z. Shen, J. Ma, L. Jong and T. Yu, *Adv. Mater.*, 2009, **21**, 2436–2440.
- 40 M. R. Parida, C. Vijayan, C. S. Rout, C. S. S. Sandeep, R. Philip and P. C. Deshmukh, *J. Phys. Chem. C*, 2011, **115**, 112–117.
- 41 E. Das, H. Eckert, H. Hu, I. E. Wachs, J. F. Walzer and F. J. Feher, *J. Phys. Chem.*, 1993, **97**, 8240–8243.
- 42 R. Baddour-Hadjean, J. P. Pereira-Ramos, C. Navone and M. Smirnov, *Chem. Mater.*, 2008, **20**, 1916–1923.
- 43 X. Miao, S. Tongay, M. K. Petterson, K. Berke, A. G. Rinzler, B. R. Appleton and A. F. Hebard, *Nano Lett.*, 2012, **12**, 2745–2750.
- 44 U. Bach, D. Lupo, P. Comte, J. E. Moser, F. Weissörtel, J. Salbeck, H. Spreitzer and M. Grätzel, *Nature*, 1998, **395**, 583–585.
- 45 J. Hu and R. G. Gordon, *Sol. Cells*, 1991, **30**, 437–450.
- 46 S.-Y. Tai, C.-J. Liu, S.-W. Chou, F. S.-S. Chien, J.-Y. Lin and T.-W. Lin, *J. Mater. Chem.*, 2012, **22**, 24753–24759.
- 47 S. Chen, J. Zhu, X. Wu, Q. Han and X. Wang, *ACS Nano*, 2010, **4**, 2822–2830.
- 48 L. Cao, S. Yang, W. Gao, Z. Liu, Y. Gong, L. Ma, G. Shi, S. Lei, Y. Zhang, S. Zhang, R. Vajtai and P. M. Ajayan, *Small*, 2013, **9**, 2905–2910.
- 49 S. Yoon, E. Kang, J. K. Kim, C. W. Lee and J. Lee, *Chem. Commun.*, 2011, **47**, 1021–1023.
- 50 C. Liu, Z. Yu, D. Neff, A. Zhamu and B. Z. Jang, *Nano Lett.*, 2010, **10**, 4863–4868.
- 51 K. Maeda and K. Domen, *Chem. Mater.*, 2010, **22**, 612–623.
- 52 Z. Chen, D. Cummins, B. N. Reinecke, E. Clark, M. K. Sunkara and T. F. Jaramillo, *Nano Lett.*, 2011, **11**, 4168–4175.
- 53 J. Livage, *Materials*, 2010, **3**, 4175–4195.
- 54 J. Liu, X. Wang, Q. Peng and Y. Li, *Adv. Mater.*, 2005, **17**, 764–767.
- 55 D. Yu, C. Chen, S. Xie, Y. Liu, K. Park, X. Zhou, Q. Zhang, J. Li and G. Cao, *Energy Environ. Sci.*, 2011, **4**, 858–861.
- 56 L. Mai, L. Xu, C. Han, X. Xu, Y. Luo, S. Zhao and Y. Zhao, *Nano Lett.*, 2010, **10**, 4750–4755.
- 57 H. Y. Yu, B. H. Kang, U. H. Pi, C. W. Park, S. Y. Choi and G. T. Kim, *Appl. Phys. Lett.*, 2005, **86**, 253102–253104.
- 58 D. J. Late, *ACS Appl. Mater. Interfaces*, 2015, **7**, 5857–5862.
- 59 (a) C. S. Rout, P. D. Joshi, R. V. Kashid, D. S. Joag, M. A. More, A. J. Simbeck, M. Washington, S. K. Nayak and D. J. Late, *Sci. Rep.*, 2013, **3**, 3282; (b) R. V. Kashid, D. J. Late, S. S. Chou, Y. K. Huang, M. De, D. S. Joag, M. A. More and V. P. Dravid, *Small*, 2013, **9**, 2730–2734; (c) S. R. Suryawanshi, P. S. Kolhe, C. S. Rout, D. J. Late and M. A. More, *Ultramicroscopy*, 2015, **149**, 51–57.
- 60 K. Dewangan, N. N. Sinha, P. G. Chavan, P. K. Sharma, A. C. Pandey, M. A. More, D. S. Joag, N. Munichandraiah and N. S. Gajbhiye, *Nanoscale*, 2012, **4**, 645–651.
- 61 T. Zhai, H. Liu, H. Li, X. Fang, M. Liao, L. Li, H. Zhou, Y. Koide, Y. Bando and D. Golberg, *Adv. Mater.*, 2010, **22**, 2547–2552.
- 62 C. Zhou, L. Mai, Y. Liu, Y. Qi, Y. Dai and W. Chen, *J. Phys. Chem. C*, 2007, **111**, 8202–8205.
- 63 R. G. Forbes, *Elev. Int. Vac. Microelectron. Conf. IVMC'98 (Cat. No. 98TH8382)*, 1998, p. 534.
- 64 M. B. Shreedhara, K. Vasu and C. N. R. Rao, *Z. Anorg. Allg. Chem.*, 2014, **640**, 2737.
- 65 Z. Zhang, C. Hu, Y. Xiong, R. Yang and Z. L. Wang, *Nanotechnology*, 2007, **18**, 465504–465508.

Humidity Sensing and Photodetection Behavior of Electrochemically Exfoliated Atomically Thin-Layered Black Phosphorus Nanosheets

Manisha B. Erande,[†] Mahendra S. Pawar,[†] and Dattatray J. Late^{*,†,‡}

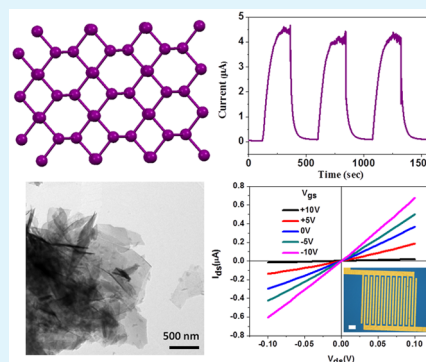
[†]Physical & Materials Chemistry Division, CSIR-National Chemical Laboratory, Dr. Homi Bhabha Road, Pune 411008, India

[‡]Academy of Scientific and Innovative Research, Anusandhan Bhawan, Rafi Marg, New Delhi 110001, India

Supporting Information

ABSTRACT: Recent investigations on two-dimensional black phosphorus material mainly highlight work on few atomic layers and multilayers. It is still unknown if the black phosphorus atomically thin sheet is an ideal structure for the enhanced gas–solid interactions due to its large surface area. To further investigate this concern, we have synthesized few atomic layer thick nanosheets of black phosphorus using an electrochemical exfoliation method. The surface morphology and thickness of the nanosheet were identified using AFM, TEM, and Raman spectroscopy. The black phosphorus nanosheet thick film device was used for the gas sensing application with exposure to different humidities. Further, the few layer black phosphorus nanosheet based transistor shows good mobility and on/off ratio. The UV light irradiation on the black phosphorus nanosheet shows good response time. The overall results show that the few layer thick film of black phosphorus nanosheets sample exhibits credible sensitivity and better recovery time to be used in humidity sensor and photodetector applications.

KEYWORDS: electrochemical exfoliation, black phosphorus, humidity sensor, photodetector



INTRODUCTION

Two-dimensional (2D) graphene has attracted much attention because of its potential for use in next generation devices such as field effect transistors,^{1–5} supercapacitors,^{6–8} solar cells,^{9–12} and gas sensors.^{13–15} In the case of gas sensors, the previous reports of conventional semiconducting metal oxide nanostructures indicates an amplified sensing concert due to the enhancement in the surface-to-volume ratio.^{16,17} Indeed, earlier papers on graphene nanosheets show exceptional sensing behavior with single molecule detection.^{13–15} However, in addition to better surface-to-volume ratio and high sensitivity, other important parameters needed for a superior gas sensor are the semiconducting nature^{17,18} and the easy accessibility of reactive sites for the redox reactions. The semiconductors are particularly fascinating due to their ability to manipulate the enhancement in sensing performance by tuning the optical and electronic properties.^{19,20} The zero band gap in graphene restricts its widespread applications in various nanoelectronics devices due to low on/off ratio. There is an emerging interest to search graphene-like other 2-D layered materials with semiconducting properties. Recently, there are a number of ultrathin layered 2D materials investigated by researchers, such as molybdenum disulfide (MoS₂),^{21–28} tungsten–disulfide (WS₂),^{22,29–31} molybdenum–diselenide (MoSe₂),^{32–34} tungsten–diselenide (WSe₂),^{33,35} gallium sulfide (GaS),^{23,36} gallium selenide (GaSe),^{23,36} and black phosphorus,^{37–50} among others.

Among these materials, black phosphorus is found to be more thermodynamically stable under ambient environment. The black phosphorus is known to be a p-type semiconductor

and has been widely investigated recently for various nanoelectronics applications.^{40–45,47} Although the bulk black phosphorus material is the most thermodynamically stable phosphorus allotrope,⁵¹ and it can undergo electrochemical and ambient oxidation.^{52,53} More significantly, the bulk black phosphorus material possesses a direct bandgap (0.3 eV). Surprisingly, for the 2D single-layer black phosphorus, the bandgap remains direct and becomes wider (2.2 eV).^{40,41} These excellent semiconducting properties of black phosphorus materials attracted the possibility to use this atomically thin-layered nanosheet in various nanoelectronics and photonics applications which cover the entire range of spectrum.^{40–45,47} There are recent reports in the literature on black phosphorus as a potentially viable and effective application in field effect transistors,^{40,42,43} photodetectors,^{44,45} field emissions,⁴¹ and so forth. Further, the literature reports do not emphasize on easy and one step synthesis and subtleties of humidity sensing performance of atomically thin black phosphorus layered materials.

Herein, we have synthesized atomically thin nanosheets of black phosphorus using electrochemical exfoliation and show its excellent performance toward humidity sensor, photo detector, and field effect transistor. The sensing performance of black phosphorus nanosheets toward humidity has been studied to

Received: October 26, 2015

Accepted: April 20, 2016

Published: April 20, 2016



reveal the role of black phosphorus nanosheets in the interactions between solid and gas vapors.

RESULTS AND DISCUSSION

Figure 1(a) and (b) shows the typical structure of black phosphorus nanosheets with one layer. The few layer

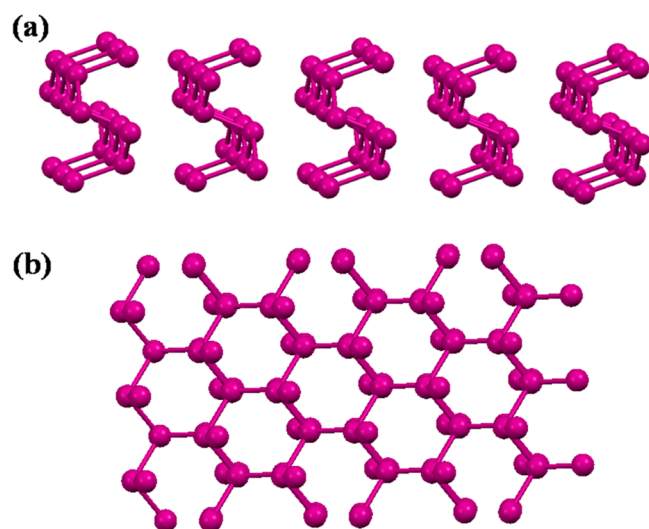


Figure 1. Schematic representation of single-layer black phosphorus nanosheet, (a) side view and (b) top view.

atomically thin black phosphorus nanosheet samples were synthesized by a simple electrochemical exfoliation method. The typical setup used for the experiment is shown in Figure 2.

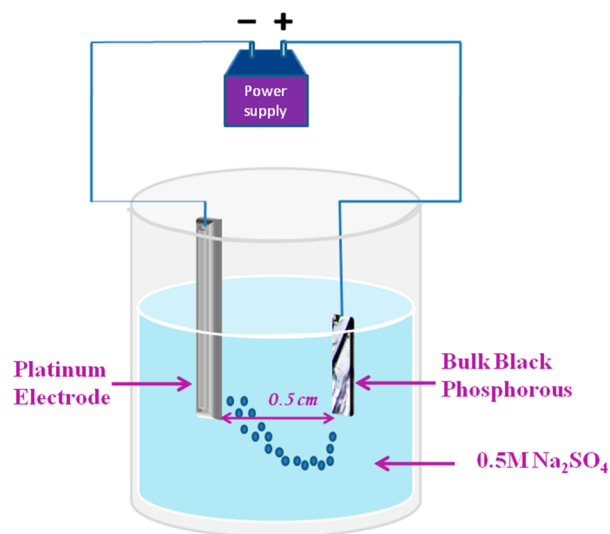
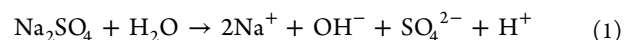


Figure 2. Experimental setup used for electrochemical exfoliation of black phosphorus nanosheets.

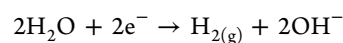
The obtained yield is in excess of 80 wt % which confirms that the method can be used on bulky scale for the synthesis of black phosphorus nanosheets. The major advantages of the electrochemical synthesis method involve the high product yield, high crystalline quality of the sample, fast synthesis process, it does not require any additional catalyst, and importantly it is an inexpensive method to synthesize materials in large quantity.

The typical reactions occurring during electrochemical exfoliation are as follows:

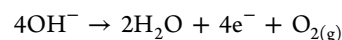
Overall Reaction:



Cathode (Reduction):



Anode (Oxidation):



The optical images of few layer black phosphorus nanosheet deposited on Si substrate by drop casting method are shown in Figure 3(a,b). Figure 3(c) shows the AFM image of the thinnest black phosphorus nanosheet which we found in our experiment and Figure 3(d) shows the AFM height profile data of the black phosphorus nanosheet sample. A statistical analysis based on AFM measurements was carried out to find the precise average heights of black phosphorus nanosheet samples, which indicates that the flakes have different thicknesses, with the majority lying in the range of 1.4 to 10 nm which indicates that the 3 to 15 layer nature of the nanosheets sample. Further, the lateral dimension of flakes were found to be 0.5 to 30 μm . Figure 4(a,b) shows the low magnification TEM images of few layer black phosphorus nanosheet samples transferred onto the Quanta Foil TEM grid. Figure 4(c) shows the SAED pattern of few layers black phosphorus nanosheets sample confirming the hexagonal structure.⁴¹ Figure 4(d) shows the high resolution TEM image depicting the inter atomic spacing to be ~ 0.25 nm. We have also noticed the amorphization of the black phosphorus nanosheets sample during TEM measurements.

The Raman spectroscopy is a very powerful and accurate characterization technique for giving exact information about the various properties of the materials. The Raman spectroscopy is quite sensitive to the number of layers in the layered material systems, and our Raman spectroscopy results of black phosphorus nanosheet agree with the reported data in the literature.^{48,49} Figure 5 shows the comparative Raman spectra for the bulk black phosphorus single crystal and electrochemically exfoliated black phosphorus nanosheets sample.⁴¹ The Raman peaks A_1^g , B_{2g} and A_2^g were observed at 362, 437, and 466 cm^{-1} for the electrochemically exfoliated black phosphorus nanosheets sample.⁴¹ For the bulk samples the Raman peaks corresponds to A_1^g , B_{2g} and A_2^g mode were observed at 364, 440, and 468 cm^{-1} respectively. Interestingly, for both the bulk and nanosheets sample the characteristic peaks which corresponds to the A_1^g , B_{2g} and A_2^g phonon modes of vibration originating from the in-plane (B_{2g} and A_2^g) and out-of-plane (A_1^g) vibrational mode were observed.⁴¹ This clearly indicates the good crystalline quality of the sample after the electrochemical exfoliation. Furthermore, the change in the peak shift, broadening clearly indicates the reduction in the size of black phosphorus sample.

The field effect transistor device was fabricated by using standard optical lithography technique with electrodes patterned on 300 nm SiO_2/Si substrate with channel length ~ 150 μm and channel width ~ 5 μm . The as synthesized black phosphorus nanosheets sample were then dispersed into the ethanol solvent and then drop casted on the electrode geometry followed by the annealing of the device in Argon

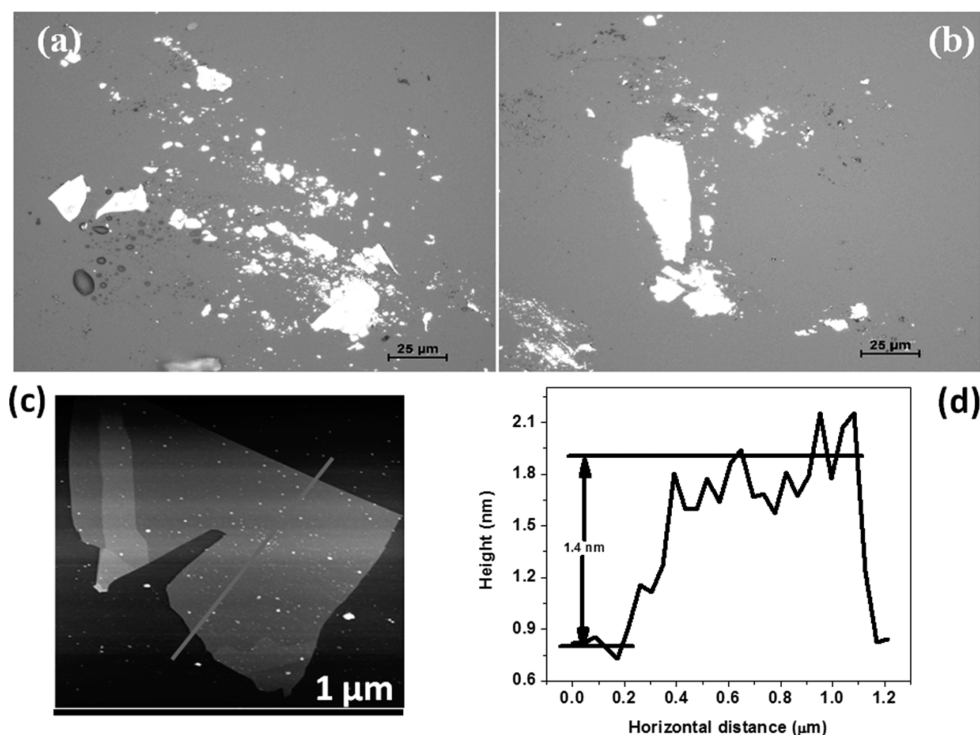


Figure 3. Electrochemically exfoliated of black phosphorus nanosheets, (a, b) optical images of nanosheets deposited on Si substrate, (c) typical AFM image of nanosheet, and (d) corresponding AFM height profile.

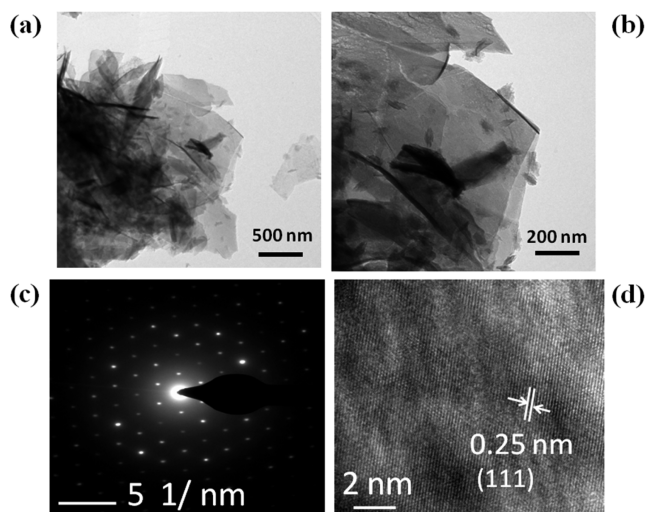


Figure 4. (a,b) Low resolution TEM images of electrochemically exfoliated of black phosphorus nanosheets. (c) SAED pattern of black phosphorus nanosheets and (d) high resolution TEM image of electrochemically exfoliated black phosphorus nanosheet.

(Ar) for 2 h at 200 °C. The typical schematic diagram of the black phosphorus field effect transistor device is shown in Figure 6(a). Figure 6(b) shows the typical optical photograph of the lithographically fabricated transistor device based on few layer black phosphorus nanosheets. The transistor characterization of the device was carried out in ambient conditions immediately after the annealing of the device using Keithley 4200 semiconductor analyzer. Figure 6(c) shows the representative linear output characteristics I_{ds} vs V_{ds} . The semilog transfer curves shown in Figure 6(d) of atomically thin black phosphorus nanosheets based field effect transistor shows p -type behavior. The transfer curves were acquired at a bias

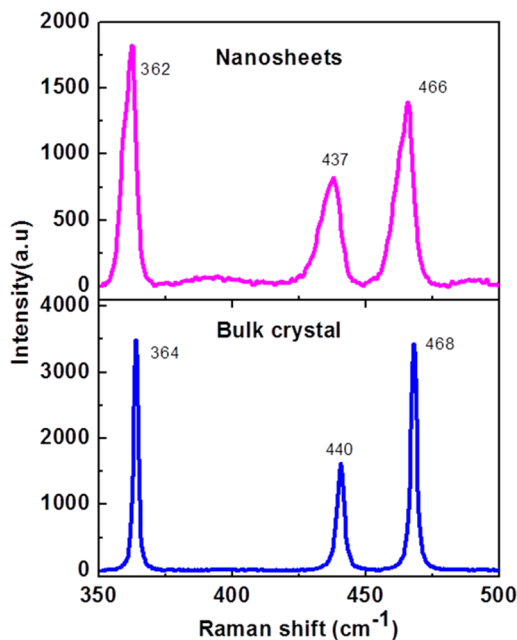


Figure 5. Comparative Raman spectra of bulk and electrochemically exfoliated black phosphorus nanosheets.

ramp rate of 10 V/s in steps of 1 V. The field-effect mobility (μ) is calculated using this curve according to the following equation:^{54,55}

$$\mu_{FE} = \frac{dI_D}{dV_G} \left[\frac{L}{WC_1V_D} \right] \quad (3)$$

where, dI_D/dV_G is the transconductance, C_1 is capacitance of 300 nm thick SiO_2 (11 nF/cm²), V_D is the drain voltage, and L (150 μm) and W (5 μm) are the length and width of the

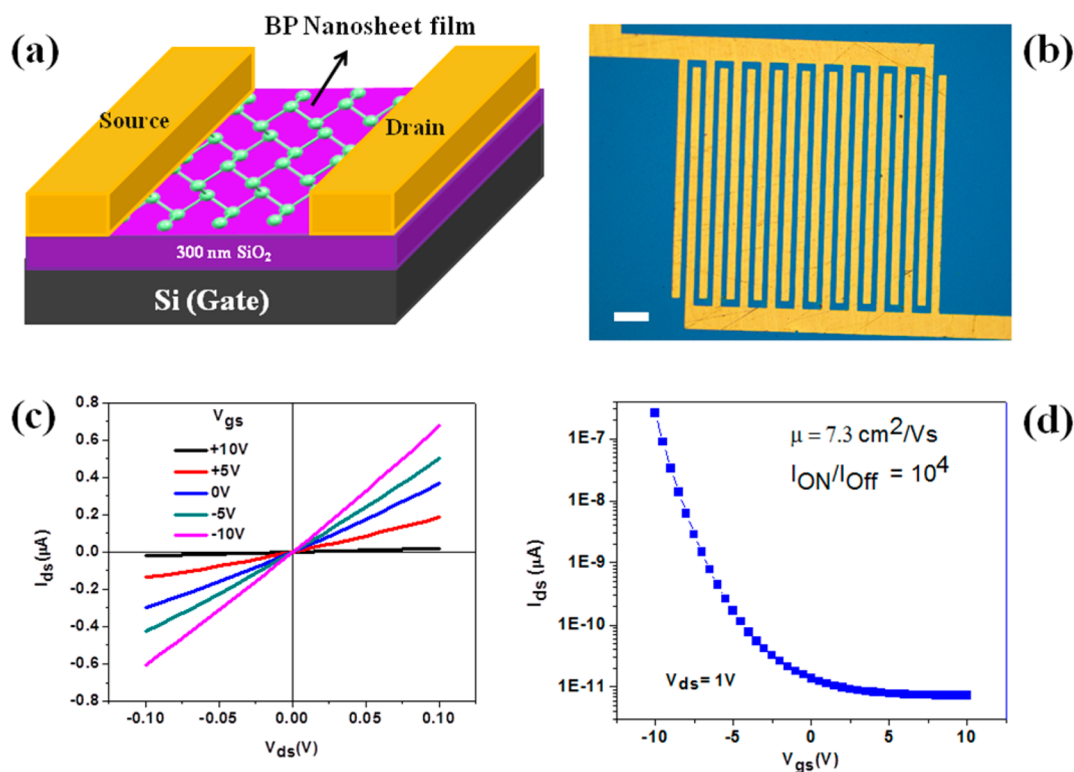


Figure 6. Field effect transistor based on electrochemically exfoliated Black phosphorus nanosheets: (a) schematic diagram of the transistor device, (b) optical photograph of the photolithography prepared typical transistor device, (c) output characteristics of the transistor device, and (d) transfer characteristics of the transistor devices. Inset of (b) scale bar is 20 μm .

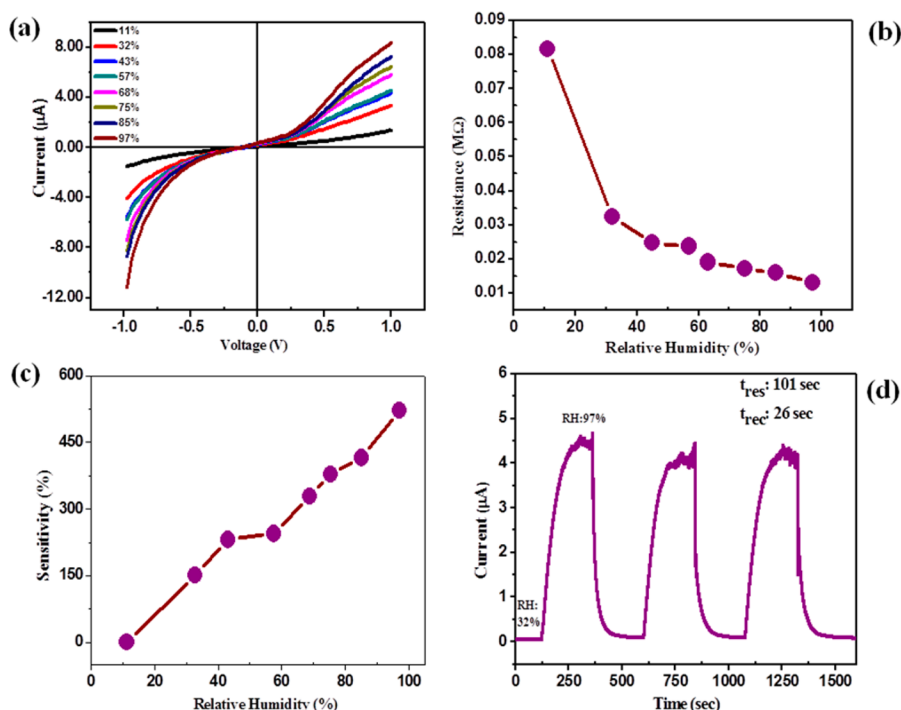


Figure 7. Black phosphorus nanosheets (a) Current–voltage (I – V) characteristics at different RH, (b) resistance vs RH plot, (c) sensitivity vs RH plot, and (d) typical I – t plot for three cycles of humidity switching between 32% and 97%.

channel, respectively, for the data shown in Figure 6(b). The field-effect mobility for this device was found to be $\sim 7.3 \text{ cm}^2/(\text{V s})$ with an $I_{\text{on/off}}$ ratio of 10^4 . The subthreshold swing extracted from Figure 6(d) has a value of $\sim 2 \text{ V/decade}$. The values reported here for the field-effect mobility are an

underestimate since we do not exclude the contact resistances in our two-probe measurements. As a result, the actual mobility value is likely to be higher as per the recent reports in the literature.^{40,42–45,47} It is noted that the black phosphorus

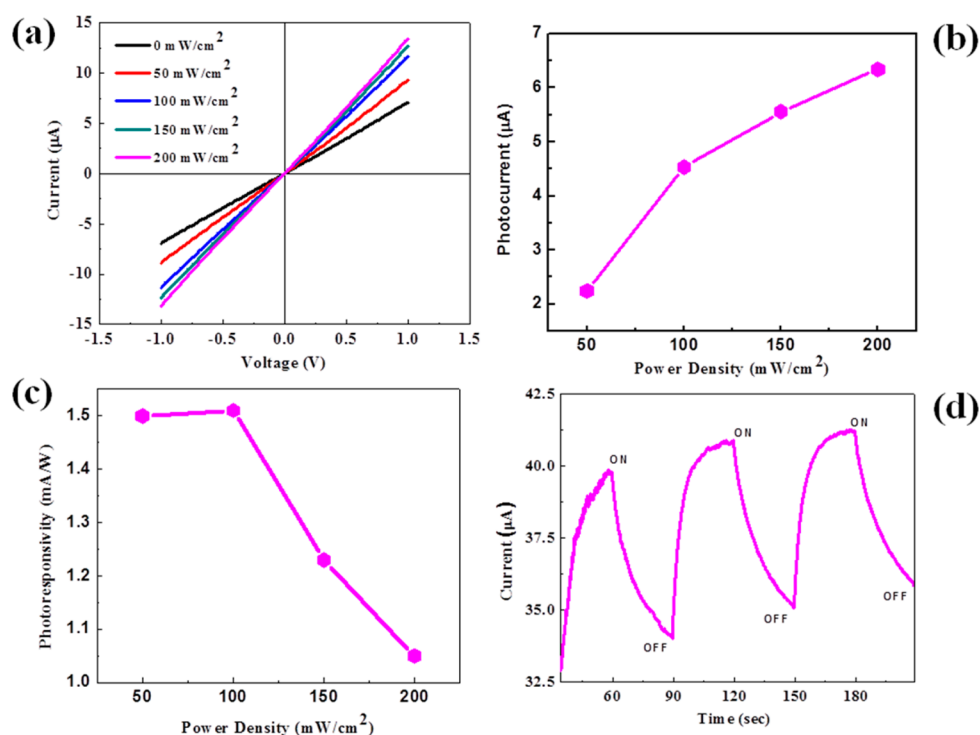


Figure 8. Black phosphorus nanosheets (a) Current–voltage (I – V) characteristics at different UV light intensities. (b) Photocurrent Vs power density, (c) photoresponsivity Vs power density, and (d) I – t cycles on illumination of UV light of 150 mW/cm^2 and with applied bias of 2 V.

transistor device kept in ambient, shows degradation in their performance with time.^{51,52}

Further, the humidity sensing performance of an atomically thin few layer black phosphorus nanosheets thick film sensor device were investigated. In this investigation, we have prepared the thick film sensor device of few layer black phosphorus nanosheets sample and measured its I – V characteristics as a function of varying RH. It is found that the slope of I – V increases with increasing humidity from 11% to 97%, as shown in Figure 7 (a). The water is e^- donor molecule, the resistance of the few layer thick black phosphorus nanosheets sample was found to decrease with the increasing RH as depicted in Figure 7(b). The results show that the charge transfer from water molecules to the black phosphorus nanosheets plays a key role in the sensing mechanism. The sensitivity vs RH shown in Figure 7(c) for a few layer black phosphorus nanosheets thick film sensor device. The sensitivity is calculated using the equation,

$$S = (R_{11} - R_{\Delta RH})/R_{\Delta RH} \quad (4)$$

where R_{11} and $R_{\Delta RH}$ are the resistances of the device in the 11% RH and change in relative humidity, respectively. The highest sensitivity value was found to be $\sim 521\%$. Figure 7(d) shows current–time (I – t) curve for the sensor device when the RH changes from 32% to 97%. From the I – t curve, it is clear that the response time of the thick film humidity sensor was found to be ~ 101 s, and the recovery time was found to be ~ 26 s which is comparable to other 2D inorganic layered materials such as MoS_2 ²⁶ and MoSe_2 .³⁴ To see the repeatability in response and recovery time, we have carried out the I – t measurements for more than hundreds of cycles and three represented cycles were shown for the brevity.

Moreover, the vibrant experimental results shown in Figure 7(d) indicate the good cyclic stability of the device depicting

well-defined response to water molecules. It is expected that the atomically thin nature of the sample shows quick response and fast recovery time which are the key important parameters for the advanced miniaturized next generation humidity sensor device. Remarkably, the bulk sample of black phosphorus is insensible toward the change of relative humidity; in that case, no noticeable change in the I – t plot could be observed under the alternating on/off cycle of the moisture due to the instability of the device as observed for the VS_2 based humidity sensor.⁵⁶ It is important to note that our black phosphorus nanosheets film humidity sensor device is quite thick, its properties are remarkably different from those of the bulk black phosphorus single crystal. For example, the resistance of our nanosheets film with few μm thicknesses in a low-humidity environment is on the order of a 0.081 $\text{M}\Omega$ at 11% RH, and in a high humidity environment, it is on the order of 0.013 $\text{M}\Omega$ at 97% RH. In the case of the bulk black phosphorus sample, the resistance is on the order of a few hundred ohms. This large difference is mainly attributed to the randomly stacked nanosheets in our thick film sensor device compared to a bulk single crystalline sample. The large channel resistance is a huge advantage for the sensing application purpose due to the ionic conduction through the absorbed water molecule layer can be measurable. This is not the case in bulk black phosphorus crystal due to its high conductance and instability at high current.⁵⁷ (See the Supporting Information for the comparative humidity sensing performance of bulk crystal and black phosphorus nanosheets thick film sensor).

Briefly, the humidity sensing mechanism can be explained as follows. The sensitivity of the moisture is based on the top surface and side exposed P atoms. The electrons might move on the surface of the sheet along with side exposed atoms. In humidity sensing, water molecules get adsorbed on the surface of the nanosheet as well as on the side exposed atom. After

Table 1. Comparative Humidity and Gas Sensing Performance of Various Nanomaterials

nanomaterial-based sensors	response time (sec)	recovery time (sec)	sensitivity (%)	reference
graphene oxide	10.5	41	350	60
	20–30 (ms)	90–30 (ms)		61
MoS ₂	300	600	800	26
	90	110		62
WS ₂	5–10	<600	400	64
MoSe ₂	150	540	1100	34
black phosphorus	60	30	150	67
	255	10	–99.17	70
VS ₂	30–40	12–50	3000	56
V ₂ O ₅	240	300	45.3	65
SnO ₂	120–170	20–60	3500	66
black phosphorus	101	26	521	Present work

water molecules adsorb on the surface of the nanosheet, an auto ionization reaction occurs, and the water molecule starts losing (H⁺) protons and forms hydroxide ion (OH⁻). This released proton starts hopping from one water molecule to another water molecule to form hydronium ion (H₃O⁺). At low humidity (11%), the surface of the nanosheets gets slightly covered by the water molecules so hopping of proton between neighboring sites of the water molecules results into slow charge transfer compared to higher humidity levels (97%). As it is expected that at higher humidity level the surface of the nanosheets gets fully covered by the water molecules which increases the magnitude of charge transfer.⁵⁸ Interestingly, this results in an increase in the conductivity values, increasing the relative humidity levels. Therefore, proton acts as an effective carrier for the electrical conductivity. The suggested mechanism might also be influenced by the thickness of the sample and the operating conditions such as temperature, composition of gas phase, and hydroxylation of the nanosheet surface.

Figure 8(a) shows the typical *I*–*V* characteristics for the black phosphorus nanosheets device under illumination of various intensities of UV light. The power densities were varied in the range from 0 to 200 mW/cm². It has been observed that for the few-layer black phosphorus nanosheets based photo detector, as the UV light intensity increases, the current of the device is found to increase. Figure 8(b) shows the photocurrent *V*s power density plot, and the equation to calculate photocurrent is $I_{ph} = I_{light} - I_{dark}$. The maximum photocurrent of ~6.3451 μA was observed for the power density of ~200 mW/cm². Figure 8(c) depicts the typical photoresponsivity *V*s power density plot. The photoresponsivity can be calculated by using the following relation:⁵⁹

$$R = \frac{I_{ph}}{P_{light}} \quad (5)$$

where, *I*_{ph} is the photocurrent and $P_{light} = W \times l \times L_{intensity}$, *W* is the width of the channel (1 cm), *l* is the channel length (300 μm), and *L*_{intensity} is the light intensity. We observed that the decrease in photoresponsivity with the increasing power density. The maximum photoresponsivity of ~1.51 mA/W were noted for power density of 100 mW/cm². Figure 8(d) shows the typical *I*–*t* cure for the illumination of UV light with 150 mW/cm². To see the repeatability in the *I*–*t* cycle, we have carried out several hundred cycles, and the three representative cycles are shown for clarity. From the *I*–*t* plot response time and recovery time were found to be ~15 and 30 s, respectively.

The reported photo detector is more stable and reproducible under ambient conditions for more than a hundred cycles.

The observed response and recovery times for the humidity sensor device were larger due to the charge trapping at the semiconductor interface. It is also important to observe that the recovery of the device is not complete in all cycles, which is also found earlier in the graphene sensors^{13,60,61} and MoS₂,^{26,62,63} WS₂,⁶⁴ MoSe₂,³⁴ VS₂,⁵⁶ and other oxide-based sensors.^{65,66} Table 1 shows the comparative sensing data with the existing literature based on various nanomaterials. Interestingly, we also notice that thin layer black phosphorus sample has better sensitivity, which seems counterintuitive. Our humidity sensor devices show better performance compared with the very recent report on the 55 nm thick black phosphorus nanosheet device toward NO₂ sensing⁶⁷ and black phosphorus thick film sensor.⁵⁷ It has been shown recently that the black phosphorus nanosheets are quite sensitive to the number of layers, metal contacts, and ambient conditions for field effect transistor characteristics,⁶⁸ and p–n junction diode.⁶⁹ The specific sensing mechanism is still under study and therefore complicated to understand right now, which requires further, more detailed investigation. The engineering of black phosphorus nanosheets with metal contacts, a controlled number of layers, and an oxygen-free environment might solve the issues related to better sensitivity, high mobility, and high ON/OFF ratio.

CONCLUSIONS

We report comprehensive suite electrochemical exfoliation of an atomically thin layer of black phosphorus nanosheets. We also present our investigation on few layer nanosheet thick film based black phosphorus photo detector, humidity sensor, and field effect transistor. In the case of the field effect transistor, it shows p-type behavior and the field effect mobility of ~7.3 cm²/(V s) and current ON/OFF ratio of ~10⁴. The black phosphorus nanosheets based thick film sensor devices are more sensitive to water vapors and UV light. Further, black phosphorus based thick film devices open several avenues to improve the sensing performance and allow selective response to certain kinds of gases and humidities.

EXPERIMENTAL SECTION

Synthesis of Black Phosphorus Nanosheets. Bulk black phosphorus crystal was Purchased from Smart Elements GmbH Ferrogasse 4/I A-U80 Wien GERMANY (purity 99.998%). Electrochemical synthesis of black phosphorus nanosheets was carried out using the highly crystalline black phosphorus bulk crystal which acts as

a working electrode. The bulk black phosphorus crystal was then fixed using a highly conductive metal electrode, and special care has been taken so as only the crystal will be submerged into the ionic solution (0.5 M Na₂SO₄). The platinum wire was used as a counter electrode. The voltage applied between the two electrodes was +7 V and the corresponding current was ~1 mA. The electrochemical process was carried out by applying a positive bias on the working electrode (bulk crystal), the oxidation of water molecule produces the •OH and •O radicals which were gathered around the bulk black phosphorus crystal. The van der Waals interaction between the bulk black phosphorus layered crystal becomes weakened because the produced radical was inserted between the consecutive layers of bulk black phosphorus. Thereafter, O₂ gas was produced due to the oxidation of the radical which can cause the black phosphorus interlayer to separate out. The separated nanosheets of black phosphorus were dispersed into the electrolyte solution. The distance between the counter electrode and the working electrode was kept at 0.5 cm, and both electrodes were held parallel to each other. The obtained yield from the exfoliated black phosphorus nanosheets was directly related to the oxidized bulk black phosphorus material. At the beginning of the reaction, the solution was colorless, it turned faint yellow after ~25 min, and the reaction was continued for 90 min. The exfoliated black phosphorus nanosheets were collected in a glass beaker and kept stable to develop the black color precipitate overnight. The solution was then washed with DI water by using ultrasonic for 15 min followed by centrifugation process. Further, the samples were repeatedly washed by using ethanol for 20 min at room temperature. The precipitate was then collected in a glass tube and annealed in the vacuum oven which kept at 60 °C for ~3 h to remove the solvent.

Optical Microscopy. The optical images were captured with the help of optical microscopy (Nikon Eclipse LV150NL). The imaging modes and objective used are bright field and 20X.

Atomic Force Microscopy. The AFM images and height profile were studied using an ICON system (Bruker, Santa Barbara Ca.) in tapping mode.

Raman Spectroscopy and Raman Imaging. The Raman spectra were recorded at room temperature, with a (LabRAM HR) using Ar laser (514.5 nm) in the back scattering geometry with laser power ~1 mW.

Transistor Device Fabrication. For device fabrication, the optical lithography technique was employed to fabricate a black phosphorus FET device,⁵³ on which titanium/gold (3 nm/70 nm) metals was deposited on the patterned electrodes by thermal evaporator. The black phosphorus nanosheet samples were then drop casted onto the electrode. The devices were then subsequently annealed in Ar atmosphere at 200 °C for 2 h to improve the contact resistance.

Sensor and Photodetector Device Fabrication. The humidity sensor device was fabricated on highly conductive indium doped tin oxide coated glass by making a scratch in the middle with the help of a glass cutter on the conducting surface with channel length ~300 μm and channel width ~1 cm. For the humidity sensing purpose, the as-synthesized black phosphorus nanosheet samples were then drop casted onto the electrode as a thick film with an average thickness of a few μm.

Humidity Test. For the humidity test, the saturated solutions of LiCl, MgCl₂, K₂CO₃, NaBr, KI, NaCl, KCl, and K₂SO₄ were taken in a closed vessel which gives approximate relative humidities of 11%, 32%, 43%, 57%, 69%, 75%, 85%, and 97%, respectively. All the tests were carried out at 25 °C.

UV Light Illumination. For the UV light sensing properties detection, a Hamamatsu L9566 LC8 Lightning cure UV lamp with 100% UV intensity of 200 mW/cm² at 365 nm were used.

Electrical Characterization. The Keithley 4200 semiconductor characterization system was used for field effect transistor properties measurements. For the humidity sensor and photo detector, the electrical measurement was conducted using a Keithley 2612A system source meter.

■ ASSOCIATED CONTENT

📄 Supporting Information

The Supporting Information is available free of charge on the ACS Publications website at DOI: 10.1021/acsami.5b10247.

The Comparative Raman spectra details and humidity sensing of bulk sample (PDF)

■ AUTHOR INFORMATION

Corresponding Author

*E-mail: datta099@gmail.com; dj.late@ncl.res.in (D.J.L.).

Author Contributions

M.B.E. and M.S.P. contributed equally to the work. The manuscript was written through contributions of all authors. All authors have given approval to the final version of the manuscript.

Notes

The authors declare no competing financial interest.

■ ACKNOWLEDGMENTS

D.J.L. would like to thank Prof. C. N. R. Rao (FRS), JNCASR, and ICMS Bangalore (India) for encouragement and support. The research work was supported by Department of Science and Technology (Government of India) under Ramanujan Fellowship to D.J.L. (Grant No. SR/S2/RJN-130/2012), CSIR-NCL-MLP project grant 028626, DST-SERB Fast-track Young scientist project Grant No. SB/FT/CS-116/2013, Broad of Research in Nuclear Sciences (BRNS) (Government of India) grant no. 34/14/20/2015 and the partial support by INUP IITB project sponsored by DeitY, MCIT, Government of India.

■ REFERENCES

- (1) Novoselov, K. S.; Jiang, D.; Schedin, F.; Booth, T. J.; Khotkevich, V. V.; Morozov, S. V.; Geim, A. K. Two-dimensional Atomic Crystals. *Proc. Natl. Acad. Sci. U. S. A.* **2005**, *102*, 10451–10453.
- (2) Novoselov, K. S.; Geim, A. K.; Morozov, S. V.; Jiang, D.; Zhang, Y.; Dubonos, S. V.; Grigorieva, I. V.; Firsov, A. A. Electric Field Effect in Atomically Thin Carbon Films. *Science* **2004**, *306*, 666–669.
- (3) Novoselov, K. S.; Geim, A. K.; Morozov, S. V.; Jiang, D.; Katsnelson, M. I.; Grigorieva, I. V.; Dubonos, S. V.; Firsov, A. A. Two-Dimensional Gas of Massless Dirac Fermions in Graphene. *Nature* **2005**, *438*, 197–200.
- (4) Schwierz, F. Graphene Transistors. *Nat. Nanotechnol.* **2010**, *5*, 487–496.
- (5) Liao, L.; Bai, J.; Cheng, R.; Lin, Y.; Jiang, S.; Qu, Y.; Huang, Y.; Duan, X. F. Sub-100 nm Channel Length Graphene Transistors. *Nano Lett.* **2010**, *10*, 3952–3956.
- (6) Wang, Y.; Shi, Z. Q.; Huang, Y.; Ma, Y. F.; Wang, C. Y.; Chen, M. M.; Chen, Y. S. Supercapacitor Devices Based on Graphene Materials. *J. Phys. Chem. C* **2009**, *113*, 13103–13107.
- (7) Vivekchand, S. R. C.; Rout, C. S.; Subrahmanyam, K. S.; Govindaraj, A.; Rao, C. N. R. Graphene-Based Electrochemical Supercapacitors. *Proc. - Indian Acad. Sci., Chem. Sci.* **2008**, *120*, 9–13.
- (8) Stoller, M. D.; Park, S.; Zhu, Y.; An, J.; Ruoff, R. S. Graphene-Based Ultracapacitors. *Nano Lett.* **2008**, *8*, 3498–3502.
- (9) Arco, L. G.; Zhang, Y.; Schlenker, C. W.; Ryu, K.; Thompson, M. E.; Zhou, C. Continuous, Highly Flexible and Transparent Graphene Films by Chemical Vapor Deposition for Organic Photovoltaics. *ACS Nano* **2010**, *4*, 2865–2873.
- (10) Yang, N.; Zhai, J.; Wang, D.; Chen, Y.; Jiang, L. Two-Dimensional Graphene Bridges Enhanced Photoinduced Charge Transport in Dye-Sensitized Solar Cells. *ACS Nano* **2010**, *4*, 887–894.
- (11) Jang, Y. H.; Xin, X.; Byun, M.; Jang, Y. J.; Lin, Z.; Kim, D. H. An Unconventional Route to High-Efficiency Dye-Sensitized Solar Cells

via Embedding Graphitic Thin Films into TiO₂ Nanoparticle Photoanode. *Nano Lett.* **2012**, *12*, 479–485.

(12) Li, X.; Zhu, H.; Wang, K.; Cao, A.; Wei, J.; Li, C.; Jia, Y.; Li, Z.; Li, X.; Wu, D. Graphene-On-Silicon Schottky Junction Solar Cells. *Adv. Mater.* **2010**, *22*, 2743–2748.

(13) Ghosh, A.; Late, D. J.; Panchakarla, L. S.; Govindaraj, A.; Rao, C. N. R. NO₂ and Humidity Sensing Characteristics of Few-Layer Graphene. *J. Exp. Nanosci.* **2009**, *4*, 313–322.

(14) Schedin, F.; Geim, A. K.; Morozov, S. V.; Hill, E. W.; Blake, P.; Katsnelson, M. I.; Novoselov, K. S. Detection of Individual Gas Molecules Adsorbed On Graphene. *Nat. Mater.* **2007**, *6*, 652–655.

(15) Dan, Y. P.; Lu, Y.; Kybert, N. J.; Luo, Z.; Johnson, A. T. C. Intrinsic Response of Graphene Vapor Sensors. *Nano Lett.* **2009**, *9*, 1472–1475.

(16) Fan, S.; Srivastava, A.; Dravid, V. P. Nanopatterned Polycrystalline ZnO for Room Temperature Gas Sensing. *Sens. Actuators, B* **2010**, *144*, 159–163.

(17) Korotcenkov, G. Metal Oxides for Solid-State Gas Sensors: What Determines Our Choice? *Mater. Sci. Eng., B* **2007**, *139*, 1–23.

(18) Doll, T.; Lechner, J.; Eisele, I.; Schierbaum, K.; Gopel, W. Ozone Detection in the ppb Range with Work Function Sensors Operating at Room Temperature. *Sens. Actuators, B* **1996**, *34*, 506–510.

(19) Fan, S.; Srivastava, A.; Dravid, V. P. UV-Activated Room-Temperature Gas Sensing Mechanism of Polycrystalline ZnO. *Appl. Phys. Lett.* **2009**, *95*, 142106.

(20) Peng, N.; Zhang, Q.; Lee, Y.; Tan, O.; Marzari, N. Gate Modulation in Carbon Nanotube Field Effect Transistors-Based NH₃ Gas Sensors. *Sens. Actuators, B* **2008**, *132*, 191–195.

(21) Jariwala, D.; Sangwan, V. K.; Late, D. J.; Johns, J. E.; Dravid, V. P.; Marks, T. J.; Lauhon, L. J.; Hersam, M. C. Band-Like Transport in High Mobility Unencapsulated Single-Layer MoS₂ Transistors. *Appl. Phys. Lett.* **2013**, *102*, 173107.

(22) Matte, H. S. S. R.; Gomathi, A.; Manna, A. K.; Late, D. J.; Datta, R.; Pati, S. K.; Rao, C. N. R. MoS₂ and WS₂ Analogues of Graphene. *Angew. Chem., Int. Ed.* **2010**, *49*, 4059–4062.

(23) Late, D. J.; Liu, B.; Matte, H. S. S. R.; Rao, C. N. R.; Dravid, V. P. Rapid Characterization of Ultrathin Layers of Chalcogenides on SiO₂/Si Substrates. *Adv. Funct. Mater.* **2012**, *22*, 1894–1905.

(24) Ghatak, S.; Pal, A. N.; Ghosh, A. Nature of Electronic States in Atomically Thin MoS₂ Field-Effect Transistors. *ACS Nano* **2011**, *5*, 7707–7712.

(25) Late, D. J.; Liu, B.; Matte, H. S. S. R.; Dravid, V. P.; Rao, C. N. R. Hysteresis in Single-Layer MoS₂ Field Effect Transistors. *ACS Nano* **2012**, *6*, 5635–5641.

(26) Late, D. J.; Huang, Y.; Liu, B.; Luo, J.; Acharya, J.; Shirodkar, S. N.; Luo, J.; Yan, A.; Charles, D.; Waghmare, U. V.; Dravid, V. P.; Rao, C. N. R. Sensing Behavior of Atomically Thin-Layered MoS₂ Transistors. *ACS Nano* **2013**, *7*, 4879–4891.

(27) Kashid, R. V.; Late, D. J.; Chou, S. S.; Huang, Y.; De, M.; Joag, D. S.; More, M. A.; Dravid, V. P. Enhanced Field-Emission Behavior of Layered MoS₂ Sheets. *Small* **2013**, *9*, 2730–2734.

(28) Late, D. J.; Shaikh, P. A.; Khare, R.; Kashid, R. V.; Chaudhary, M.; More, M. A.; Ogale, S. B. Pulsed Laser Deposited MoS₂ Thin Films on W and Si: Field Emission and Photoresponse Studies. *ACS Appl. Mater. Interfaces* **2014**, *6*, 15881–15888.

(29) Rout, C. S.; Joshi, P. D.; Kashid, R. V.; Joag, D. S.; More, M. A.; Simbeck, A. J.; Washington, M.; Nayak, S. K.; Late, D. J. Superior Field Emission Properties of Layered WS₂-RGO Nanocomposites. *Sci. Rep.* **2013**, *3*, 3282.

(30) Braga, D.; Lezama, I. G.; Berger, H.; Morpurgo, A. F. Quantitative Determination of the Band Gap of WS₂ with Ambipolar Ionic Liquid Gated Transistors. *Nano Lett.* **2012**, *12*, 5218–5223.

(31) Georgiou, T.; Jalil, R.; Belle, B. D.; Britnell, L.; Gorbachev, R. V.; Morozov, S. V.; Kim, Y. J.; Gholinia, A.; Haigh, S. J.; Makarovskiy, O.; Eaves, L.; Ponomarenko, L. A.; Geim, A. K.; Novoselov, K. S.; Mishchenko, A. Vertical Field Effect Transistor Based on Graphene–WS₂ Heterostructures for Flexible and Transparent Electronics. *Nat. Nanotechnol.* **2012**, *8*, 100–103.

(32) Larentis, S.; Fallahzad, B.; Tutuc, E. Field Effect Transistors and Intrinsic Mobility in Ultra Thin MoSe₂ Layers. *Appl. Phys. Lett.* **2012**, *101*, 223104.

(33) Late, D. J.; Shirodkar, S. N.; Waghmare, U. V.; Dravid, V. P.; Rao, C. N. R. Thermal Expansion, Anharmonicity and Temperature-Dependent Raman Spectra of Single- and Few-Layer MoSe₂ and WSe₂. *ChemPhysChem* **2014**, *15*, 1592–1598.

(34) Late, D. J.; Doneux, T.; Bougouma, M. Single Layer MoSe₂ Based NH₃ Sensor. *Appl. Phys. Lett.* **2014**, *105*, 233103.

(35) Allain, A.; Kis, A. Electron and Hole Mobilities in Single-Layer WSe₂. *ACS Nano* **2014**, *8*, 7180–7185.

(36) Late, D. J.; Liu, B.; Luo, J.; Yan, A.; Matte, H. S. S. R.; Grayson, M.; Rao, C. N. R.; Dravid, V. P. GaS and GaSe Ultrathin Layer Transistors. *Adv. Mater.* **2012**, *24*, 3549–3554.

(37) Warschauer, D. Electrical and Optical Properties of Crystalline Black Phosphorus. *J. Appl. Phys.* **1963**, *34*, 1853.

(38) Nishii, T.; Maruyama, Y.; Inabe, T.; Shirotani, I. Synthesis and Characterization of Black Phosphorus Intercalation Compounds. *Synth. Met.* **1987**, *18*, 559–564.

(39) Bridgman, P. M. Two New Modifications of Phosphorus. *J. Am. Chem. Soc.* **1914**, *36*, 1344–1363.

(40) Li, L.; Yu, Y.; Ye, G. J.; Ge, Q.; Ou, X.; Wu, H.; Feng, D.; Chen, X. H.; Zhang, Y. Black Phosphorus Field Effect Transistors. *Nat. Nanotechnol.* **2014**, *9*, 372–377.

(41) Erande, M. B.; Suryawanshi, S. R.; More, M. A.; Late, D. J. Electrochemically Exfoliated Black Phosphorus Nanosheets—Prospective Field Emitters. *Eur. J. Inorg. Chem.* **2015**, *19*, 3102–3107.

(42) Liu, H.; Neal, A. T.; Zhu, Z.; Luo, Z.; Xu, X.; Tomanek, D.; Ye, P. D. Phosphorene: An Unexplored 2D Semiconductor with a High Hole Mobility. *ACS Nano* **2014**, *8*, 4033–4041.

(43) Na, J.; Lee, Y. T.; Lim, J. A.; Hwang, D. K.; Kim, G.; Choi, W. K.; Song, Y. Few Layer Black Phosphorus Field-Effect Transistors with Reduced Current Fluctuation. *ACS Nano* **2014**, *8*, 11753–11765.

(44) Buscema, M.; Groenendijk, D. J.; Steele, G. A.; van der Zant, H. S. J.; Castellanos-Gomez, A. Photovoltaic Effect in Few Layer Black Phosphorus P-N Junctions Defined by Local Electrostatic Gating. *Nat. Commun.* **2014**, *5*, 4651–4658.

(45) Buscema, M.; Groenendijk, D. J.; Blanter, S. I.; Steele, G. A.; van der Zant, H. S. J.; Castellanos-Gomez, A. Fast and Broadband Photoresponse of Few-Layer Black Phosphorus Field-Effect Transistors. *Nano Lett.* **2014**, *14*, 3347–3352.

(46) Du, Y.; Ouyang, C.; Shi, S.; Lei, M. Abinitio Studies on Atomic and Electronic Structures of Black Phosphorus. *J. Appl. Phys.* **2010**, *107*, 093718.

(47) Qiao, J.; Kong, X.; Hu, Z.; Yang, F.; Ji, W. High Mobility Transport Anisotropy and Linear Dichroism in Few Layer Black Phosphorus. *Nat. Commun.* **2014**, *5*, 4475.

(48) Zhang, S.; Yang, J.; Xu, R.; Wang, F.; Li, W.; Ghufri, M.; Zhang, Y.; Yu, Z.; Zhang, G.; Qin, Q.; Lu, Y. Extraordinary Photoluminescence and Strong Temperature/Angle-Dependent Raman Responses in Few-Layer Phosphorene. *ACS Nano* **2014**, *8*, 9590–9596.

(49) Late, D. J. Temperature Dependent Phonon Shifts in Few-Layer Black Phosphorus. *ACS Appl. Mater. Interfaces* **2015**, *7*, 5857–5862.

(50) Threlfall, R. E. *100 Years of Phosphorus Making*; Albright and Wilson Ltd.: Oldbury, 1951; pp 1851–1951.

(51) Ling, X.; Liang, L.; Huang, S.; Puzetzy, A. A.; Geoghegan, D. B.; Sumpter, B. G.; Kong, J.; Meunier, V.; Dresselhaus, M. S. Low Frequency Interlayer Breathing Modes in Few-Layer Black Phosphorus. *Nano Lett.* **2015**, *15*, 4080–4088.

(52) Wood, J. D.; Wells, S. A.; Jariwala, D.; Chen, K.; Cho, E.; Sangwan, V. K.; Liu, X.; Lauhon, L. J.; Marks, T. J.; Hersam, M. C. Effective Passivation of Exfoliated Black Phosphorus Transistors against Ambient Degradation. *Nano Lett.* **2014**, *14*, 6964–6970.

(53) Kim, J.; Liu, Y.; Zhu, W.; Kim, S.; Wu, D.; Tao, L.; Dodabalapur, A.; Lai, K.; Akinwande, D. Toward Air Stable Multilayer Phosphorene Thin Films and Transistors. *Sci. Rep.* **2015**, *5*, 8989.

(54) Late, D. J.; Ghosh, A.; Subrahmanyam, K. S.; Panchakarla, L. S.; Krupanidhi, S. B.; Rao, C. N. R. Characteristics of Field Effect

Transistors Based on Undoped and B-and N Doped Few-Layer Graphenes. *Solid State Commun.* **2010**, *150*, 734–738.

(55) Li, L.; Ye, G. J.; Tran, V.; Fei, R.; Chen, G.; Wang, H.; Wang, J.; Watanabe, K.; Taniguchi, T.; Yang, L.; Chen, X. H.; Zhang, Y. Quantum Oscillations in a Two Dimensional Electron gas in Black Phosphorus Thin Films. *Nat. Nanotechnol.* **2015**, *10*, 608–613.

(56) Feng, J.; Peng, L.; Wu, C.; Sun, X.; Hu, S.; Lin, C.; Dai, J.; Yang, Y.; Xie, Y. Giant Moisture Responsiveness of VS₂ Ultrathin Nanosheets for Novel Touchless Positioning Interface. *Adv. Mater.* **2012**, *24*, 1969–1974.

(57) Yasaei, P.; Behranginia, A.; Foroozan, T.; Asadi, A.; Kim, K.; Khalili-Araghi, F.; Salehi-Khojin, A. Stable and Selective Humidity Sensing Using Stacked Black Phosphorus Flakes. *ACS Nano* **2015**, *9*, 9898–9905.

(58) Farahani, H.; Wagiran, R.; Hamidon, M. N. Humidity Sensors Principle, Mechanism, and Fabrication Technologies: A Comprehensive Review. *Sensors* **2014**, *14*, 7881–7939.

(59) Cao, Y.; Cai, K.; Hu, P.; Zhao, L.; Yan, T.; Zhang, X.; Wu, X.; Wang, K.; Zheng, H. Strong Enhancement of Photoresponsivity with Shrinking the Electrodes Spacing in few Layer GaSe Photodetectors. *Sci. Rep.* **2015**, *5*, 8130.

(60) Bi, H.; Yin, K.; Xie, X.; Ji, J.; Wan, S.; Sun, L.; Terrones, M.; Dresselhaus, M. S. Ultrahigh Humidity Sensitivity of Graphene Oxide. *Sci. Rep.* **2013**, *3*, 2714.

(61) Borini, S.; White, R.; Wei, D.; Astley, M.; Haque, S.; Spigone, E.; Harris, N.; Kivioja, J.; Ryhanen, T. Ultrafast Graphene Oxide Humidity Sensors. *ACS Nano* **2013**, *7*, 11166–11173.

(62) Tan, Y.; Yu, K.; Yang, T.; Zhang, Q.; Cong, W.; Yin, H.; Zhang, Z.; Chen, Y.; Zhu, Z. The Combinations of Hollow MoS₂ Micro@ nano-spheres: One-step Synthesis, Excellent Photocatalytic and Humidity Sensing Properties. *J. Mater. Chem. C* **2014**, *2*, 5422–5430.

(63) Kannan, P. K.; Late, D. J.; Morgan, H.; Rout, C. S. Recent Developments in 2D Layered Inorganic Nanomaterials for Sensing. *Nanoscale* **2015**, *7*, 13293.

(64) O'Brien, M.; Lee, K.; Morrish, R.; Berner, N. C.; McEvoy, N.; Wolden, C. A.; Duesberg, G. S. Plasma Assisted Synthesis of WS₂ For Gas Sensing Application. *Chem. Phys. Lett.* **2014**, *615*, 6–10.

(65) Pawar, M. S.; Bankar, P. K.; More, M. A.; Late, D. J. Ultra-thin V₂O₅ Nanosheets Based Humidity Sensor, Photodetector and Its Enhanced Field Emission Properties. *RSC Adv.* **2015**, *5*, 88796–88804.

(66) Kuang, Q.; Lao, C.; Wang, Z. L.; Xie, Z.; Zheng, L. High Sensitivity Humidity Sensor Based on a Single SnO₂ Nanowire. *J. Am. Chem. Soc.* **2007**, *129*, 6070–6071.

(67) Abbas, A. N.; Liu, B.; Chen, L.; Ma, Y.; Cong, S.; Aroonyadet, N.; Kopf, M.; Nilges, T.; Zhou, C. Black Phosphorus Gas Sensors. *ACS Nano* **2015**, *9*, 5618–5624.

(68) Perello, D. J.; Chae, S. H.; Song, S.; Lee, Y. H. High Performance n-Type Black Phosphorus Transistors with Type Control via Thickness and Contact Metal Engineering. *Nat. Commun.* **2015**, *6*, 7809.

(69) Deng, Y.; Luo, Z.; Conrad, N. J.; Liu, H.; Gong, Y.; Najmaei, S.; Ajayan, P. M.; Lou, J.; Xu, X.; Ye, P. D. Black Phosphorus–Monolayer MoS₂ Van der Waals Heterojunction p–n Diode. *ACS Nano* **2014**, *8*, 8292.

(70) Late, D. J. Liquid Exfoliation of Black Phosphorus Nanosheets and its Application as Humidity Sensor. *Microporous Mesoporous Mater.* **2016**, *225*, 494–503.

■ Material Science inc. Nanomaterials & Polymers

High-Performance Sensing Behavior Using Electronic Ink of 2D SnSe₂ Nanosheets

Mahendra Pawar, Sunil Kadam, and Dattatray J. Late*^[a]

Most of the recent research work on layered chalcogenides is understandably focused on single atomic layers. However, it is uncertain if the single layer units are most ideal structures for enhanced gas-solid interactions. To probe this concern, we have synthesized few layer thick SnSe₂ nanosheets ink using liquid exfoliation method. The morphology, thickness / layering and elemental analysis of the sheets were characterized by using SEM, TEM, AFM, Raman spectroscopy and by XPS. The

two dimensional (2D) SnSe₂ nanosheets sensor device with different thicknesses was assessed for the humidity and gas sensing performances with exposure to humidity in different conditions. The results show that compared to the bulk / thicker counterpart, sensor device of few SnSe₂ layers exhibit excellent sensitivity, recovery and ability to be tune the sensing performance with thickness and can be used in lab on chip devices.

1. Introduction

The detection of toxic or harmful gases is become most essential for the environment monitoring including our own safety and industrial products manufacturing/monitoring. To date gas sensors of various metal oxide nanostructures materials have been widely investigated and shown good sensing performance for hazardous gases such as NO₂, NH₃ and H₂S.^[1-4] The gas sensors based on semiconductor oxides materials show excellent performance in terms of sensitivity and selectivity, but they usually operate only at high temperatures, which generate several questions related to high power consumption and safety related issues.

Considering these restrictions researchers are still in the phase of developing highly sensitive gas sensors with few atom thin in nature and more importantly which can functions at room temperature. The carbon nanotubes^[5-7] and graphene^[8-10] have shown very fast response and high sensitivity towards detection of single molecule of toxic gases. The reports on graphene interaction with gas molecules clearly depicts that it can be act as a good sensor.^[8-9] The increase in charge carrier concentration induced by gas molecules adsorbed on the graphene can be used to fabricate highly sensitive gas sensors.^[8-9] As graphene is a semi metallic in nature, due to which there is limitation on removal of the physisorbed gas molecules from the nanosheet surface. Considering this fact it require longer time to recover the original resistance.^[10] Further, the theoretical and experimental investigations suggest that the gas molecules adsorb on the two-dimensional (2D)

inorganic transition-metal dichalcogenides (TMDCs) nanosheets such as MoS₂,^[11-13] WS₂,^[14] MoSe₂,^[15] Black Phosphorous^[16-18] etc. have ability to improve the response / recovery time and sensitivity. In contrast to graphene, TMDCs have recently been received a considerable attention because of semiconducting in nature and tunable bandgap^[19-20] The 2D materials such as MoS₂,^[11-13] WS₂,^[14] MoSe₂,^[15] Black Phosphorous^[16-18] possess remarkable electrical, optical and magnetic properties at the single-or few-layer level and have been integrated into gas sensing devices.

The atomically thin layered SnSe₂ is a sandwich of Se and Sn atoms where Sn atom is sandwiched between two Se atoms through covalent bonds in the vertical direction forming Se–Sn–Se layer structure.^[21-24] In single layer SnSe₂, the Sn–Se distance is 2.793 Å and the Se–Se distance is 3.293 Å and the lattice constant $|a| = 3.321$ Å. The single-layer SnSe₂ has a larger atomic structure due to the larger atomic radius of the Se atoms in contrast with the single layer MoS₂ and WS₂. The bulk SnSe₂ is a layered semiconductor with a direct band gap 1.0 eV, the mono-layer SnSe₂ has a direct band gap of 1.4 eV, which facilitate the fabrication of switchable transistors^[24] and extremely responsive photodetector devices.^[25-26] Recent experimental reports shows that the SnSe₂ nanosheets have a potential candidate to be used in new generation van der Waals vertical heterojunction devices.^[27] In the view of growing attention of atomically thin layer SnSe₂ for possible gas sensor device applications, it is essential to examine the gas sensing performance of this layered material. The electronic and optical properties of other layered materials such as MoS₂,^[28-31] WS₂,^[32-33] MoSe₂,^[34-35] WSe₂,^[36-38] GaS,^[39] GaSe,^[39] Black Phosphorous^[40] etc. have been extensively studied to date but gas sensing behaviors of 2D SnSe₂ layered crystals has not yet been reported.

In this work, we report liquid exfoliation of few layer SnSe₂ nanosheets using ultrasonication and explore for gas sensing applications. Considering atomically thin nature and good mechanical sturdiness, our investigations open up ground-

[a] M. Pawar, S. Kadam, Dr. D. J. Late
Physical and Materials Chemistry Division
CSIR-National Chemical Laboratory
Dr. Homi Bhabha Road, Pashan, Pune- 411008, Maharashtra, India
E-mail: datta099@gmail.com
dj.late@ncl.res.in

Supporting information for this article is available on the WWW under <https://doi.org/10.1002/slct.201700261>

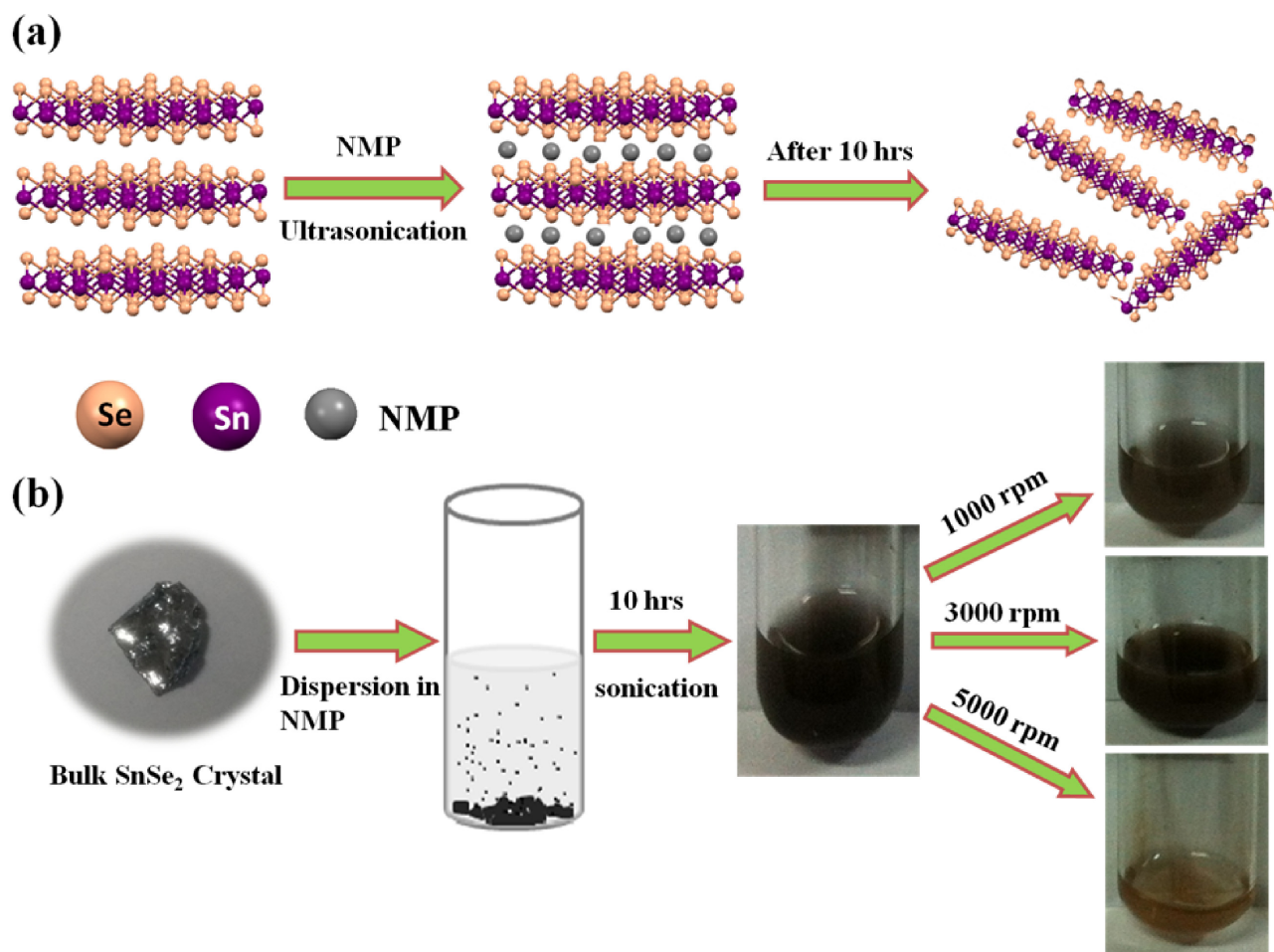


Figure 1. (a) SnSe₂ nanosheets exfoliation using NMP via ultrasonication bath for 10 hours. (b) schematic and optical Photograph of SnSe₂ nanosheets without centrifuge and centrifuge at 1000 rpm, 3000 rpm and 5000 rpm respectively.

breaking avenues for use of 2D SnSe₂ nanosheets ink as a suitable candidate for high-performance humidity and toxic gas sensor applications.

2. Results and Discussion

Raman Spectroscopy:

The Figure 1 (a) shows the typical SnSe₂ nanosheets exfoliation process using N-Methyl-2-pyrrolidone (NMP) via ultrasonication bath for 10 hours. The optical photograph of SnSe₂ nanosheet ink sample synthesized with ultrasonication and after various centrifugation rate was also recorded. Figure 1 (b) shows the typical schematic and optical photograph of SnSe₂ sample after 10 hours of ultrasonication without any centrifuge. The typical optical photograph of SnSe₂ sample centrifuged for 10 min at 1000 rpm, 3000 rpm and 5000 rpm respectively can also be seen in figure 1(b).

The change in color clearly reflects the reduction in the size and thickness of SnSe₂ nanosheet. It is important to note that all the nanosheets samples were well dispersed in NMP. The dispersed sample can be used like ink to transfer on any

desired substrate for various nanoelectronic device applications.

Figure 2 (a) shows the side view of SnSe₂ crystal structure and (b) shows the top view of single-layer SnSe₂. The as synthesized samples were well characterized using Raman spectroscopy. The Raman spectroscopy is a very powerful and non-destructive technique; it gives very precise and accurate information about the changes in bond distance and mechanical properties such as strain, stress, phase transition etc. The as synthesized and bulk SnSe₂ samples were analyzed using Raman spectroscopy as shown in Figure 2c. The two main peaks were observed at 109 cm⁻¹ and 180 cm⁻¹ are characteristic of the SnSe₂ phase. The first peak refers to the E_g mode and the second peak refer to the A_{1g} mode. The typical Raman spectra of nanosheet sample depicts the change in intensity, shift in peak position and slight increase in FWHM as compared with that of bulk SnSe₂ crystal.

Transmission Electron Microscopy:

The morphological and crystalline natures of the samples were further characterized by transmission electron microscopy

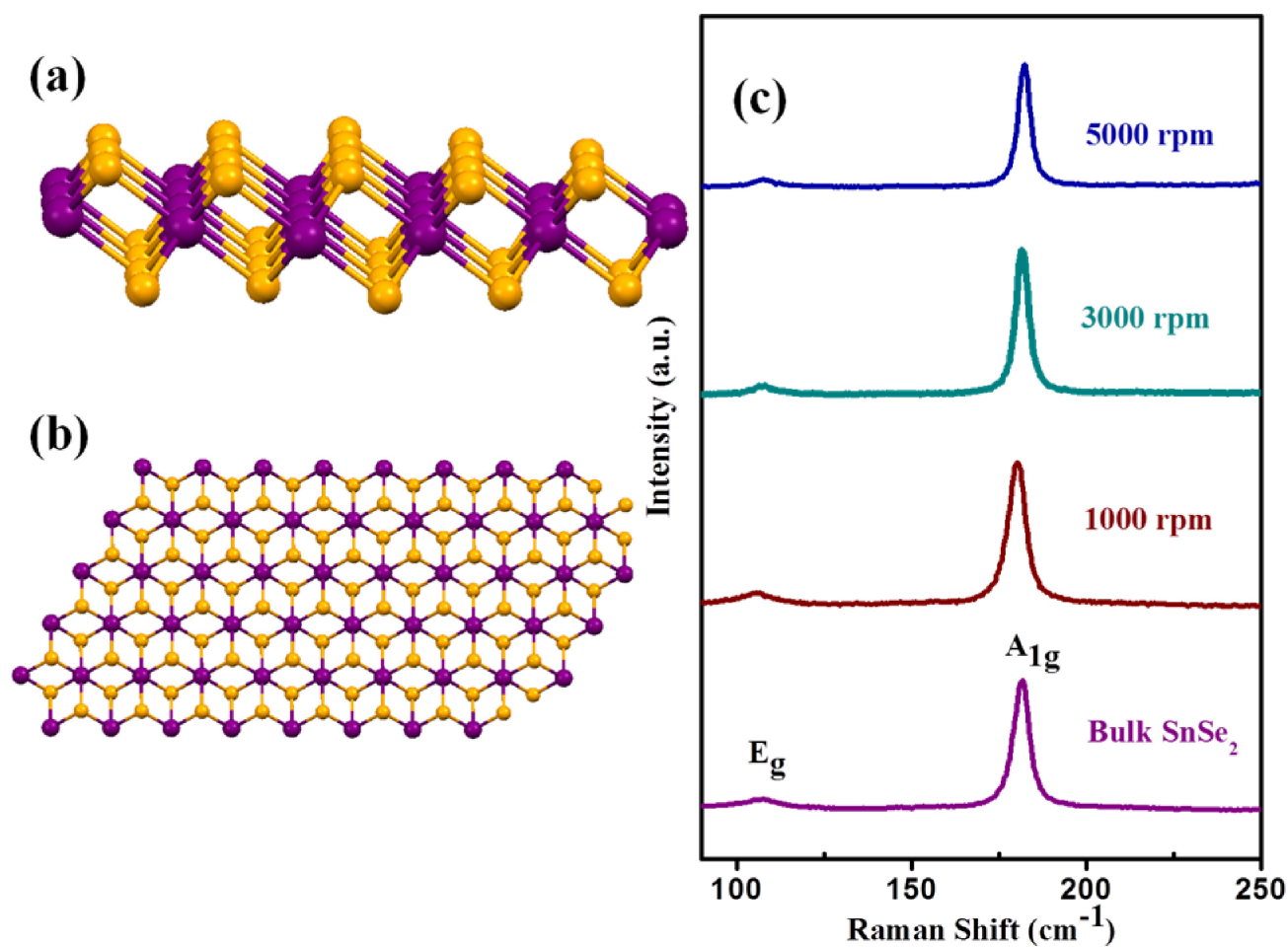


Figure 2. (a) Typical SnSe₂ crystal structure side view, (b) Top view and (c) Comparative Raman spectra of SnSe₂ bulk crystal and nanosheets samples prepared at different rpm.

(TEM). The sample collected at 1000 rpm has been analyzed by TEM and results were depicted in the Figure 3 (a,b). The TEM analysis clearly shows the sheet like morphology seen in Figure 3(a). The typical TEM image also confirms the thick and bulky nature of the SnSe₂ nanosheets. The morphology and average size of the sample were analyzed from the TEM measurements and which shows sheet like morphology with average lateral dimensions $\sim 2 \mu\text{m}$. Figure 3(b) shows the high resolution HRTEM image taken from the edge of the nanosheets, which provides more detailed structural information and highly crystalline nature of the sample. The lattice spacing were found to be $\sim 0.224 \text{ nm}$ which matches well with (102) plane. The inset of figure 3 (b) shows the typical selected area electron diffraction (SAED) pattern of sample which depicts highly crystalline nature of the SnSe₂ sample. TEM images taken for the sample collected at 3000 rpm are shown in Figure 3(c). The TEM shows the sheet like morphology with typical sheet dimension of 1–2 μm .

The Figure 3(d) shows the HRTEM image of the sample confirming highly crystalline nature of sample. The lattice spacing of $\sim 0.200 \text{ nm}$ corresponding to (003) plane was recorded from the HRTEM image. The inset of Figure 3(d)

shows the SAED pattern which clearly shows the highly crystalline nature of the SnSe₂ nanosheet sample. Figure 3(e) shows the typical TEM image of the sample collected at 5000 rpm showing the sheet like morphology with typical sheet dimension of 200–500 nm. The Figure 3(f) shows the typical HRTEM image of the sample confirming the highly crystalline nature of the sample collected at 5000 rpm. The lattice spacing was also measured from the HRTEM image showing $\sim 0.30 \text{ nm}$ which corresponds to the (101) plane. The inset of Figure 3(f) shows the typical SAED pattern of sample which depicts the crystalline nature of the SnSe₂ sample collected at 5000 rpm. From the TEM analysis it is clear that there is presence of transparent sheet possessing less thickness in 3000rpm and 5000 rpm sample than that of 1000 rpm sample.

Atomic Force Microscopy:

Further the AFM analysis was used to find out the thickness of the as synthesized sample. The Figure S3 shows the typical AFM images and corresponding height profile for the three different samples. The AFM images shows sheet like morphology along with typical thickness for 1000 rpm sample was

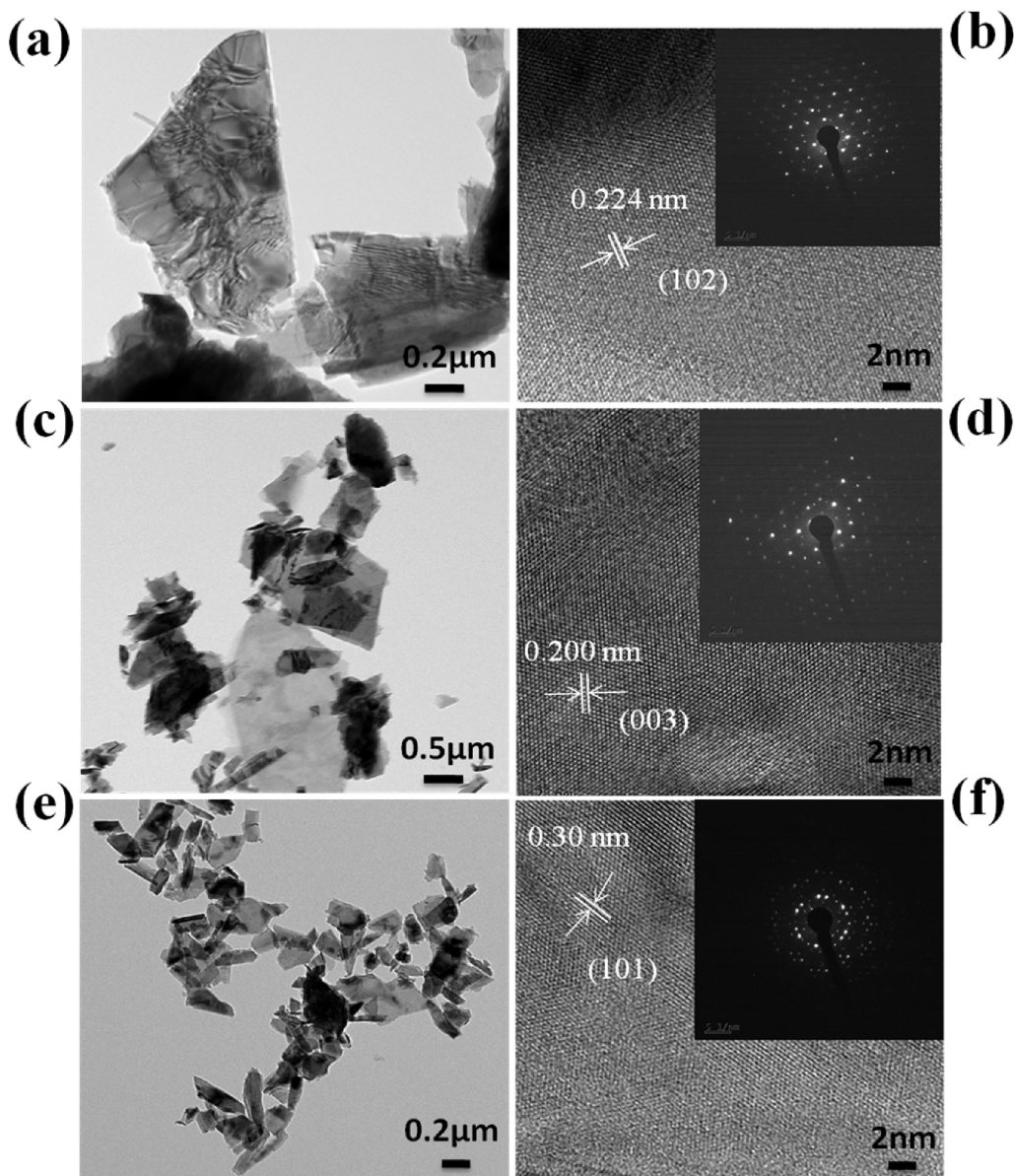


Figure 3. TEM characterization of exfoliated SnSe₂ nanosheets (a, c and e) typical low-magnification TEM image and (b, d and f) HRTEM images and inset of (b, d and f) SAED pattern for 1000 rpm, 3000 rpm, and 5000 rpm sample respectively.

found to be ~ 170 nm, for 3000 rpm thickness was found to be ~ 8 nm and for the sample prepared at 5000 rpm the average thickness of nanosheets sample was found to be 2.5 nm.

X-Ray Photoelectron Spectroscopy:

The elemental analysis of the 1000 rpm SnSe₂ nanosheet sample was investigated by using X-ray photoelectron spectroscopy (XPS). Figure 4(a) show the survey spectra for SnSe₂ nanosheets, (b) shows the C 1 s Spectra, (c) and (d) represents the core level XPS spectra of Sn and Se elements. The Sn 3d_{5/2} and Sn 3d_{3/2} peaks for nanosheet sample appeared at 487.7 eV and 495.2 eV respectively which is an evidence of the presence of (+2) oxidation state of Sn in the nanosheets. Moreover, a little higher binding energy of 487.7 eV were observed for Sn which indicates the Sn in (+4) oxidation state^[41–43].

Figure 4(d) shows the Se 3d_{5/2} and Se 3d_{3/2} peaks appeared at 54.7 eV and 55.9 eV respectively, which further confirms the formation of SnSe₂ stoichiometry.^[44–46] The Figure S2 shows the XPS spectra for the bulk SnSe₂ sample. It consists of (a) survey spectra for bulk SnSe₂ (b) C 1 s spectra and (c, d) represents core level XPS spectra of Sn and Se, the Sn 3d_{5/2} and Sn 3d_{3/2} peaks appeared at 487.7 eV and 495.8 eV respectively. The figure S2 (d) shows the Se 3d_{5/2} and Se 3d_{3/2} peaks appeared at 55.4 eV and 56.6 eV respectively. The binding energies of SnSe₂ nanosheet sample were observed to be slightly lower than that of bulk SnSe₂ sample. This slight change in binding energy is due to the alteration in the chemical bonding of respective element (For detail comparison see the supporting information Table S1).

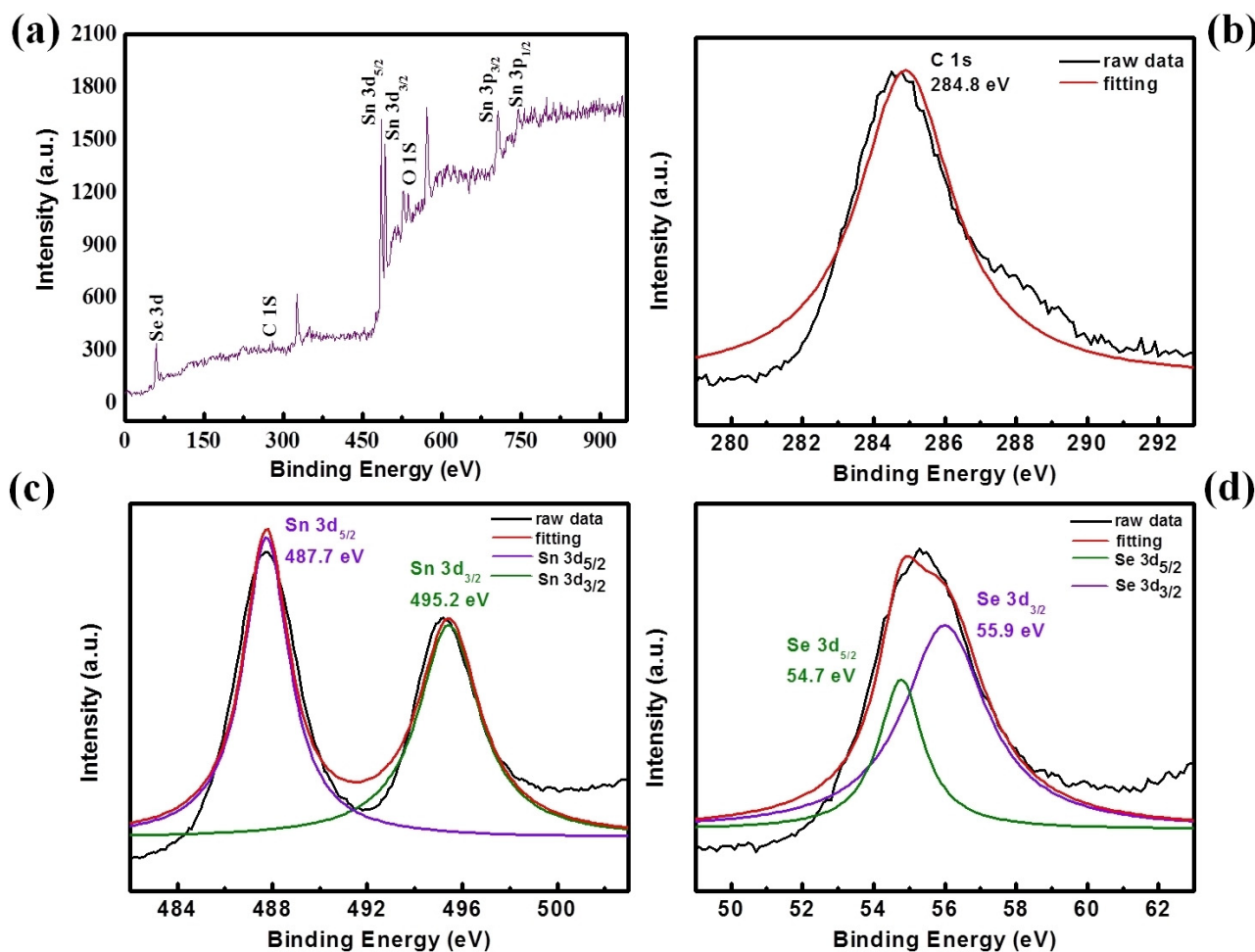


Figure 4. XPS spectra of SnSe₂ nanosheets sample centrifuged at 1000 rpm (a) survey spectrum, (b) C 1 s, (c) Sn 3d and (d) Se 3d.

Humidity and gas Sensing:

For the humidity and gas sensing measurements, the nanoflakes ink were dropcasted onto the electrode. The change in resistance of the device with various humidity levels was recorded and analyzed. Figure 5(a) shows the resistance Vs relative humidity plot for 1000 rpm sample and from the plot it is clear that there is remarkable decrease in the resistance from 18.99 GΩ to 1.56 MΩ. The sensitivity as a function of relative humidity plot was also shown in figure 5(b). Inset of 5(b) shows the typical two-probe sensor device.

The sensitivity for SnSe₂ nanosheets based humidity sensor device were defined as $S = (R_{11} - R_{\Delta RH}) / R_{\Delta RH}$, where R_{11} is the resistance of the sensor device in 11% RH, and $R_{\Delta RH}$ is the resistance of the sensor device in various relative humidity. We have observed maximum sensitivity of ~12,103 for the relative humidity of 97% for the sample synthesized at 1000 rpm. The figure 5(c) shows the typical current-time (I-t) plot where the cycles of 32.78% and 97.3% RH levels were used to calculate the response and recovery time. The response and recovery time for the SnSe₂ nanosheets based sensor device were found to be 167 sec and 12 sec respectively. The high response time is

might be due to the rate of adsorption of water molecules on the surface of SnSe₂ nanosheets based sensor is less. The advantage of sensor is fast recovery and it works at room temperature. The SnSe₂ nanosheets sample centrifuged at 1000 rpm was also tested for NH₃ gas sensing application. Figure 5(d) shows the typical resistance of the sensor device Vs NH₃ gas flow (sccm) plot. The sensing result clearly indicates the resistance decreases with respect to increasing gas flow. The sensitivity varies as the function of gas flow as shown in figure 5(e). The maximum sensitivity of -99.97% were observed for NH₃ gas flow of 100 sccm. Figure 5(f) shows the typical I-t plot for NH₃ gas sensor based on SnSe₂ nanosheets. The typical response time of ~264 sec and recovery time of ~26 sec were noted. The typical resistance Vs relative humidity plot for the humidity sensor based on SnSe₂ nanosheets sample synthesized at 3000 rpm were shown in Figure S4 (a). From the plot it is clear that there is remarkable decrease in the resistance from 8.21 GΩ to 1.39 MΩ. The Figure S4 (b) shows the plot of sensitivity Vs RH. The sensitivity factor was calculated to be ~5894 for SnSe₂ nanosheets sample collected at 3000 rpm. The I-t plot has been recorded to investigate the response and recovery time as shown in Figure S4 (c). The response and

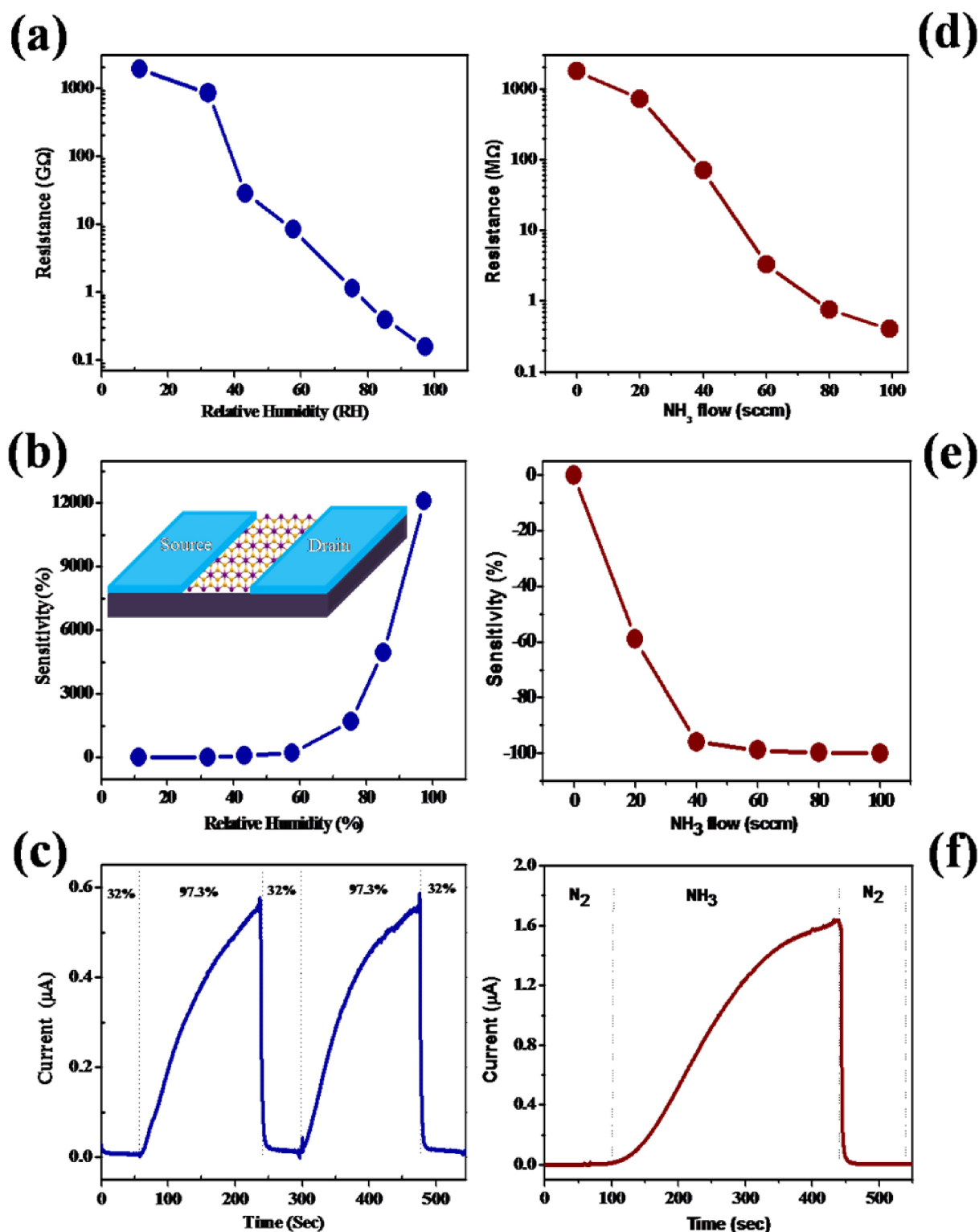


Figure 5. Humidity and NH₃ gas sensors based on SnSe₂ nanosheet ink sample synthesized at 1000 rpm (a) Resistance Vs RH plot (b) Sensitivity Vs RH plot and (c) Typical I-t plot for two cycles for lower and higher humidity levels. The inset of (b) shows typical humidity sensor device. NH₃ gas sensor based on 2D SnSe₂ nanosheets ink sample synthesized at 1000 rpm (d) typical resistance Vs NH₃ gas flow rate, (e) Sensitivity Vs NH₃ gas concentrations and (f) typical I-t plot for NH₃ gas sensor device.

recovery time for the SnSe₂ nanosheets based humidity sensor device were found to be 163 sec and 7 sec respectively. The

Figure S5 (a) shows the typical resistance Vs relative humidity plot for 5000 rpm sample and from the plot it is clear that there

is remarkable decrease in the resistance from 21.15 G Ω to 5.24 M Ω . The typical plot of sensitivity Vs RH shown in Figure S5 (b). The sensitivity factor was calculated to be ~ 4034 for SnSe₂ nanosheets sample collected at 5000 rpm. The typical I-t plot has been recorded in order to find out the response and recovery time as shown in figure S5 (c). The response and recovery time for the SnSe₂ nanosheets based humidity sensor device were found to be 160 sec and 4 sec respectively. The 2D SnSe₂ nanosheets shows superior performance as compared with other 2D nanomaterials such as MoS₂,^[13] WS₂,^[47] MoSe₂,^[17] Black Phosphorous,^[48] VS₂^[49] and Graphene Oxide^[50] (see supporting information Table S2).

The response of the SnSe₂ sensors device is restricted by strong adsorption of gas molecules. The thermodynamic process may not be much superior for adsorption of gas molecules on SnSe₂ nanosheet surface due which we noted prolonged response time. In other hand the gas molecules easily get desorbs during the recovery time due to little absorption energy. The response of sensor device can be tuned by keeping the device at higher temperature or by light irradiation. The sensitivity value depends on the number of water molecules adsorbing on the surface of SnSe₂ nanosheets based sensor. The humidity sensing is the adsorption of water molecules on the surface of material and then transfer of charge from one water molecule to its next neighboring molecule. In brief when water molecules get adsorbed on the surface of SnSe₂ nanosheets, proton starts hopping from one water molecule to its next neighboring water molecule. This hopping of proton will give rise to increase in the electrical conductivity. The sensitivity of the humidity sensor device based on 1000 rpm sample was found to be ~ 12103 highest amongst the sample exfoliated at 3000 rpm and 5000 rpm. This is because of the fact that, in case of 1000 rpm sample, large number of bulky sheets were seen which acts as perspective sites for adsorption of water molecules. In the same sample (1000 rpm) due to bulky sheet nature, it takes more time to recover the original resistance. In contrast with 1000 rpm and 3000 rpm sample, in case of 5000 rpm sample we observed the fast response and recovery time for the SnSe₂ nanosheets sample because of drastic reduction in thickness of SnSe₂ nanosheets. The existence of Se- vacancies created during the liquid exfoliation using ultrasonication might plays an important role in the high sensitivity values. Further, it is also possible that, the liquid exfoliation method results into a large number of defect sites in SnSe₂ nanosheet sample, the main defects being Se- vacancies with the absence of either one or two Se-atoms per SnSe₂. The response and recovery time depends on the thickness of the material i.e. thinner the material rate of adsorption and desorption of water molecules will be high due to large surface area. The thickness of the nanosheets plays key role in the high performance humidity sensor. The sensing mechanism for NH₃ gas sensing can be explained as below. When the SnSe₂ sensor device exposed with NH₃ gas, a charge transfer between the NH₃ gas molecules and SnSe₂ nanosheets occur. This further result in the decrease in resistance of the sensor device as a function of increase of NH₃ gas flow. The interactions among the NH₃ gas molecules (electron donor)

and SnSe₂ nanosheets (n-type) results into the significant increase in the conductivity of SnSe₂ sensor device as observed for MoS₂.^[51]

The future scope for this material is to carry out the extensive theoretical work on atomically thin sheet of SnSe₂ in particularly the calculations of scattering rates on phonon and charge impurities were needed for the complete understanding. It is also interesting to estimate the amount of charge transferred between SnSe₂ and H₂O in presence and in the absence of external electric field. It is important to investigate the detail analysis of role of vacancy sites, anti-sites, grain boundaries and defects present in the sample for complete understanding of materials which might be responsible for high performance of the sensing device. The liquid / chemically exfoliated nanosheets involves randomly oriented crystalline domains which might be interconnected by definite grain boundary region as evidenced from AFM imaging for other 2D layered materials.^[52] The SnSe₂ is one of the promising 2D layered semiconducting materials. The synthesis process is highly important for good quality nanosheets of this material, as the properties are highly dependent on quality and structure of the SnSe₂ nanosheets which may provide profound information of this material on the performances of the sensor devices, as it might lead to design superior future nano-electronics devices^[53-57] and other applications.^[58] Further, improvement in the device performance can be achieved by synthesizing high quality SnSe₂ nanosheets along with control thickness and suitable engineering of materials such as doping, surface functionalization and heterojunction architecture with other 2D materials.

3. Conclusions

We successfully investigated sensing behavior of 2D SnSe₂ nanosheets synthesized using simple liquid exfoliation method which provides further opportunities to improve the sensing behavior and make 2D SnSe₂ nanosheets ink to selectively respond to certain kinds of humidities and toxic gases. The fast recovery time of 4 sec was observed for the humidity sensor device based on 2D SnSe₂ nanosheet synthesized at 5000 rpm. The maximum sensitivity of 12103 were observed for SnSe₂ nanosheet ink sample synthesized at 1000 rpm. Although the exact sensing mechanisms of SnSe₂ behavior is unclear and clearly has subtleties and nuances, it shows excellent sensing properties, worthy of further investigations.

Acknowledgements

The research work was supported by Department of Science and Technology (Government of India) under Ramanujan Fellowship to Dr. D. J. Late (Grant No. SR/S2/RJN-130/2012), NCL-MLP project grant 028626, DST-SERB Fast-track Young scientist project Grant No. SB/FT/CS-116/2013, Broad of Research in Nuclear Sciences (BRNS) (Government of India), Grant No. 34/14/20/2015 and partial support by INUP IITB project sponsored by DeitY, MCIT, Government of India.

Conflict of Interest

The authors declare no conflict of interest.

Keywords: Liquid Exfoliation · SnSe₂ · sensor · Nanosheets

- [1] S. P. Arnold, S. M. Prokes, F. K. Perkins, M. E. Zaghoul, *Appl. Phys. Lett.* **2009**, *95*, 103102.
- [2] S. Tian, F. Yang, D. Zeng, C. Xie, *J. Phys. Chem. C* **2012**, *116*, 10586.
- [3] J. Zhang, J. Liu, Q. Peng, X. Wang, Y. Li, *Chem. Mater.* **2006**, *18*, 867.
- [4] X. Zhao, M. Cao, C. Hu, *Mater. Res. Bull.* **2013**, *48*, 2289.
- [5] J. Kong, N. R. Franklin, C. Zhou, M. G. Chapline, S. Peng, K. Cho, H. Dai, *Science* **2000**, *287*, 622.
- [6] S. Chopra, K. McGuire, N. Gothard, A. M. Rao, A. Pham, *Appl. Phys. Lett.* **2003**, *83*, 2280.
- [7] J. Li, Y. Lu, Q. Ye, M. Cinke, J. Han, M. Meyyappan, *Nano Lett.* **2003**, *3*, 929.
- [8] F. Schedin, A. K. Geim, S. V. Morozov, E. W. Hill, P. Blake, M. I. Katsnelson, K. S. Novoselov, *Nat. Mater.* **2007**, *6*, 652.
- [9] H. Arjmandi-Tash, L. A. S. Belyaeva, G. F. Chneider, *Chem. Soc. Rev.* **2016**, *45*, 476.
- [10] A. Ghosh, D. J. Late, L. S. Panchakarla, A. Govindraj, C. N. R. Rao, *J. Exp. Nanosci.* **2009**, *4*, 313.
- [11] D. J. Late, Y. K. Huang, B. Liu, J. Acharya, S. N. Shirodkar, J. Luo, A. Yan, D. Charles, U. V. Waghmare, V. P. Dravid, C. N. R. Rao, *ACS Nano* **2013**, *7*, 4879.
- [12] K. Lee, R. Gatensby, N. McEvoy, T. Hallam, G. S. Duesberg, *Adv. Mater.* **2013**, *25*, 6699.
- [13] H. Li, Z. Yin, Q. He, H. Li, X. Huang, G. Lu, D. W. H. Fam, A. I. Y. Tok, Q. Zhang, H. Zhang, *Small* **2012**, *8*, 63.
- [14] N. Huo, S. Yang, Z. Wei, S. S. Li, J.-B. Xia, J. Li, *Sci. Rep.* **2014**, *4*, 5209.
- [15] D. J. Late, T. Doneux, M. Bougouma, *Appl. Phys. Lett.* **2014**, *105*, 233103.
- [16] A. N. Abbas, B. Liu, L. Chen, Y. Ma, S. Cong, N. Aroonyadet, M. Kopf, T. Nilges, C. Zhou, *ACS Nano* **2015**, *9*, 5618.
- [17] S. Yan, B. Wang, Z. Wang, D. Hu, X. Xu, J. Wang, Y. Shi, *Biosens. Bioelectron.* **2016**, *80*, 34.
- [18] P. Li, D. Zhang, J. Liu, H. Chang, Y. E. Sun, N. Yin, *ACS App. Mater. Interfaces* **2015**, *7*, 24396.
- [19] Q. H. Wang, K. Kalantar-Zadeh, A. Kis, J. N. Coleman, M. S. Strano, *Nat. Nanotechnol.* **2012**, *7*, 699.
- [20] P. K. Kannan, D. J. Late, H. Morgan, C. S. Rout, *Nanoscale* **2015**, *7*, 13293.
- [21] A. Taube, A. Łapińska, J. Judek, M. Zdrojek, *Appl. Phys. Lett.* **2015**, *107*, 013105.
- [22] L. Huang, Y. Yu, C. Li, L. Cao, *J. Phys. Chem. C* **2013**, *117*, 6469.
- [23] S. I. Kim, S. Hwang, S. Y. Kim, W. J. Lee, D. W. Jung, K. S. Moon, D. J. Yun, *Sci. Rep.* **2016**, *6*, 19733.
- [24] T. Pei, L. Bao, G. Wang, R. Ma, H. Yang, J. Li, C. Gu, S. Pantelides, S. Du, H. Gao, *Appl. Phys. Lett.* **2016**, *108*, 053506.
- [25] X. Zhou, L. Gan, W. Tian, Q. Zhang, S. Jin, H. Li, T. Zhai, *Adv. Mater.* **2015**, *27*, 8035–8041.
- [26] Y. Ma, *Sci. Bull.* **2015**, *60*, 1789.
- [27] a) X. Zhou, N. Zhou, C. Li, H. Song, Q. Zhang, X. Hu, L. Gan, H. Li, J. Lü, J. Luo, J. Xiong, T. Zhai, *2D Mater.* **2017**, *4*, 025048; b) T. Roy, M. Tosun, M. Hettick, G. H. Ahn, C. Hu, A. Javey, *Appl. Phys. Lett.* **2016**, *108*, 083111.
- [28] B. Radisavljevic, A. Radenovic, J. Brivio, V. Giacometti, A. Kis, *Nat. Nanotechnol.* **2011**, *6*, 147.
- [29] Z. Yin, H. Li, L. Jiang, Y. Shi, Y. Sun, G. Lu, Q. Zhang, X. Chen, H. Zhang, *ACS Nano* **2012**, *6*, 74–80.
- [30] D. J. Late, B. Liu, H. S. S. R. Matte, V. P. Dravid, C. N. R. Rao, *ACS Nano* **2012**, *6*, 5635.
- [31] R. S. Sundaram, M. Engel, A. Lombardo, R. Krupke, A. C. Ferrari, P. Avouris, M. Steiner, *Nano Lett.* **2013**, *13*, 1416.
- [32] D. Ovchinnikov, A. Allain, Y. Huang, D. Dumcenco, A. Kis, *ACS Nano* **2014**, *8*, 8174.
- [33] N. P. Lopez, A. L. Eliaz, A. Berkdemir, A. C. Beltran, H. R. Gutierrez, S. Feng, R. Lv, T. Hayashi, F. L. Uria, S. Ghosh, B. Muchharla, S. Talapatra, H. Terrones, M. Terones, *Adv. Funct. Mater.* **2013**, *23*, 5511.
- [34] Y.-H. Chang, W. Zhang, Y. Zhu, Y. Han, J. Pu, J.-K. Chang, W.-T. Hsu, J.-K. Huang, C.-L. Hsu, M.-H. Chiu, T. Takenobu, H. Li, C.-I. Wu, W.-H. Chang, A. T. S. Wee, L.-J. Li, *ACS Nano* **2014**, *8*, 8582.
- [35] S. Larentis, B. Fallahzad, E. Tutuc, *Appl. Phys. Lett.* **2012**, *101*, 223104.
- [36] S. Das, J. Appenzeller, *Appl. Phys. Lett.* **2013**, *103*, 103501.
- [37] A. Allain, A. Kis, *ACS Nano* **2014**, *8*, 7180.
- [38] J. Huang, J. Pu, C.-L. Hsu, M. Chiu, Z. Juang, Y.-H. Chang, W.-H. Chang, Y. Iwasa, T. Takenobu, L.-J. Li, *ACS Nano* **2014**, *8*, 923.
- [39] D. J. Late, B. Liu, J. Luo, A. Yan, H. S. S. R. Matte, M. Grayson, C. N. R. Rao, V. P. Dravid, *Adv. Mater.* **2012**, *24*, 3549.
- [40] M. Buscema, D. J. Groenendijk, S. I. Blanter, G. A. Steele, H. S. van der Zant, A. Castellanos-Gomez, *Nano Lett.* **2014**, *14*, 3347.
- [41] N. D. Boscher, C. J. Carmalt, R. G. Palgrave, I. D. Parkin, *Thin Solid Films* **2008**, *516*, 4750.
- [42] K. G. S. Ranmohotti, H. Djieutedjeu, P. F. P. Poudeu, *J. Am. Chem. Soc.* **2012**, *134*, 14033.
- [43] H. Djieutedjeu, X. Zhou, H. Chi, N. Haldolaarachchige, K. G. S. Ranmohotti, C. Uher, D. Young, P. F. P. Poudeu, *J. Mater. Chem. C* **2014**, *2*, 6199.
- [44] L. Li, Z. Chen, Y. Hu, X. Wang, T. Zhang, W. Chen, Q. Wang, *J. Am. Chem. Soc.* **2013**, *135*, 1213.
- [45] W. Zhang, Z. Yang, J. Liu, L. Zhang, Z. Hui, W. Yu, Y. Qian, L. Chen, X. Liu, *J. Cryst. Growth* **2007**, *217*, 157.
- [46] J. Harbec, B. M. Powell, S. Jandl, *Phys. Rev. B* **1983**, *28*, 7009.
- [47] M. O'Brien, K. Lee, R. Morrish, N. C. Berner, N. McEvoy, C. A. Wolden, G. S. Duesberg, *Chem. Phys. Lett.* **2014**, *615*, 6.
- [48] P. Yasaei, A. Behranginia, T. Foroozan, M. Asadi, K. Kim, F. Khalili-Araghi, A. Salehi-Khojin, *ACS Nano* **2015**, *9*, 9898.
- [49] J. Feng, L. Peng, C. Wu, X. Sun, S. Hu, C. Lin, J. Dai, Y. Yang, Y. Xie, *Adv. Mater.* **2012**, *24*, 1969.
- [50] B. Bi, K. Yin, X. Xie, J. Ji, S. Wan, L. Sun, M. Terrones, M. S. Dresselhaus, *Sci. Rep.* **2013**, *3*, 2714.
- [51] H. Hassan, J. Mun, B. S. Kang, J. Y. Song, T. Kim, S. Kang, *RSC Adv.* **2016**, *6*, 75839.
- [52] M. Mongillo, D. Chiappe, G. Arutchev, I. Asselberghs, M. Perucchini, M. Manfrini, D. Lin, C. Huyghebaert, I. Radu, *Appl. Phys. Lett.* **2016**, *109*, 233102.
- [53] D. Xue, J. Tan, J. Hu, W. Hu, Y. Guo, L. Wan, *Adv. Mater.* **2012**, *24*, 4528.
- [54] D. Bharatula, M. B. Erande, I. S. Mulla, C. S. Rout, D. J. Late, *RSC Adv.* **2016**, *6*, 105421.
- [55] A. S. Pawbake, S. R. Jadkar, D. J. Late, *Chemistry Select* **2016**, *1*, 5380.
- [56] D. J. Late, *Microporous and Mesoporous Materials* **2016**, *225*, 494.
- [57] M. B. Erande, M. Pawar, D. J. Late, *ACS App. Mater. Interfaces* **2016**, *8*, 11548.
- [58] S. Saha, A. Banik, K. Biswas, *Chem. Euro. J.* **2016**, *22*, 15634.

Submitted: February 8, 2017

Accepted: May 5, 2017



Temperature-dependent Raman spectroscopy and sensor applications of PtSe₂ nanosheets synthesized by wet chemistry

Mahendra S. Pawar^{1,2} and Dattatray J. Late^{*1,2}

Full Research Paper

Open Access

Address:

¹Physical and Materials Chemistry Division, CSIR-National Chemical Laboratory, Dr. Homi Bhabha Road, Pune 411008, India and

²Academy of Scientific and Innovative Research (AcSIR), Ghaziabad 201002, India

Email:

Dattatray J. Late* - dj.late@ncl.res.in

* Corresponding author

Keywords:

nanosheets; PtSe₂; Raman spectroscopy; sensor; thermal effect

Beilstein J. Nanotechnol. **2019**, *10*, 467–474.

doi:10.3762/bjnano.10.46

Received: 01 November 2018

Accepted: 16 January 2019

Published: 13 February 2019

This article is part of the thematic issue "Low-dimensional materials and systems".

Guest Editor: S. Walia

© 2019 Pawar and Late; licensee Beilstein-Institut.

License and terms: see end of document.

Abstract

We report on a wet chemistry method used to grow PtSe₂ nanosheets followed by thermal annealing. The SEM and TEM analysis confirms the formation of PtSe₂ nanosheets. Furthermore, XRD, Raman, XPS and SAED patterns were used to analyze the crystal structure and to confirm the formation of the PtSe₂ phase. The temperature-dependent Raman spectroscopy investigations were carried out on PtSe₂ nanosheets deposited on Si substrates in the temperature range 100–506 K. The shifts in Raman active E_g and A_{1g} modes as a function of temperature were monitored. The temperature coefficient for both modes was calculated and was found to match well with the reported 2D transition metal dichalcogenides. A PtSe₂ nanosheet-based sensor device was tested for its applicability as a humidity sensor and photodetector. The humidity sensor based on PtSe₂ nanosheets showed an excellent recovery time of ≈5 s, indicating the great potential of PtSe₂ for future sensor devices.

Introduction

Graphene, the most well-studied example of the two-dimensional (2D) aromatic compounds, is the building block of all forms of carbon allotropes [1]. In recent years, it has been widely studied due to its extraordinary optical, electrical, mechanical, magnetic and chemical properties [2–5]. Like graphene and its organic analogues [6], inorganic 2D metal dichalcogenides also exhibit outstanding performance in many applications including transistors, sensors, photodetectors, solar

cells, field emitters, battery materials, light harvesting and energy storage devices, catalyst for H₂ generation, and drug delivery applications [7–12]. Most of the transition metal dichalcogenides (TMDCs) are semiconducting in nature with MX₂ type – where M is a metal, M = W, Mo, Sn, Nb, V, etc. from group IV–V and X represents the chalcogenides family, X = S, Se, Te, etc. The metal atom M is sandwiched between layers of chalcogenide (X) atoms in the structure X–M–X. The

TMDCs show diverse functional properties at the monolayer level in contrast to bulk due to the quantum confinement effect. Apart from this, these TMDCs, for example MoS₂ and MoSe₂, show an indirect to direct band gap transition [13–17].

A 2D platinum diselenide (PtSe₂) material has recently joined the growing class of stable TMDCs due its promising applications. The 2D PtSe₂ has not been explored much to date due to difficulties in synthesis. It is well known that bulk PtSe₂ is a semimetal in nature with a nearly zero band gap [18,19]. With the help of theoretical calculations such as density functional theory (DFT) and local-density approximations (LDAs), it has been observed that bulk PtSe₂ shows a semimetallic nature and single-layer PtSe₂ has a semiconducting nature with a bandgap of 1.2 eV. Bilayer PtSe₂ is also a semiconducting material but with a slightly smaller band gap than the monolayer material [19]. This layer-dependent conversion of semimetal-to-semiconductor transition has potential for electronic device applications [20–22]. Bulk PtSe₂ was first prepared in 1909 by Minozzi from elements [23]. PtSe₂ nanosheets have been recently prepared by heating thin foils of platinum in selenium vapors at 400 °C [19,24]. In this paper we have synthesized few-layer-thick PtSe₂ nanosheets by a wet chemical method [25] at 90 °C using chloroplatinic acid (H₂PtCl₆) and Se powder as precursors followed by thermal annealing at 500 °C. Temperature-dependent Raman spectroscopic characterization was carried out on the materials.

Materials and Methods

All the chemicals such as chloroplatinic acid, Se powder, hexamethylenetetramine, and NaBH₄ were purchased from Sigma-Aldrich for the synthesis of PtSe₂ nanosheets.

Synthesis method

The PtSe₂ nanosheets were synthesized using a solvothermal method followed by annealing at 500 °C using a previously described method for PtSe₂ synthesis [25]. The PtSe₂ material was prepared in two steps. The first step is the formation of the PtSe complex on the wall of a container by a wet chemical method; the second step is the phase transformation of PtSe₂ by thermal annealing. 0.5 mL of a 0.015 M solution of H₂PtCl₆ was mixed with 0.5 mL of 0.5 M hexamethylenetetramine. In order to get a homogeneous solution, the mixture was carefully stirred for 15–20 s until the colour of the solution became slightly yellow; this is referred to as the Pt precursor. In another beaker 0.8 mg of Se powder was added into a 10 mL ice-cold solution of 0.1 M NaBH₄ which acts as a strong reducing agent for the reduction of Se powder. The solution of Se was then heated in an oil bath at 90 °C for ≈20 min in order to completely reduce the Se. After complete reduction, the colour of the solution became dark brown and is referred to as the Se precursor. The Pt

precursor was then slowly added into the Se precursor. The colour of the solution was found to suddenly change to greenish brown. The mixture was then kept undisturbed for ≈20 min. After 20 min the complex of Pt and Se was formed on the wall of the beaker. The complex was then washed several times using deionized water. First complex was transferred onto a Si substrate and heated at 100 °C on a hot plate. After complete evaporation, the substrate was annealed in a chemical vapour deposition system at 500 °C in argon gas atmosphere for 5 h. Supporting Information File 1, Figure S1 shows the schematic of the PtSe₂ nanosheet synthesis steps.

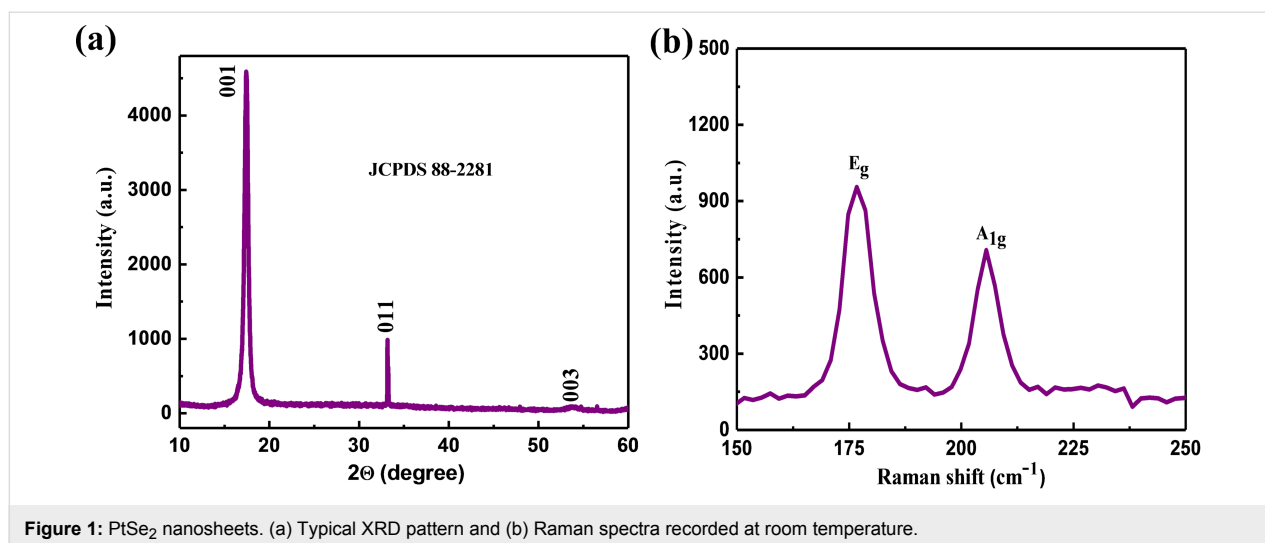
Sensor device fabrication and testing

Sensor devices were fabricated on a tin-doped indium oxide (ITO) substrate with a channel length of ≈300 μm and width ≈5 mm. The PtSe₂ nanosheet powder was dispersed in *N*-methyl-2-pyrrolidone (NMP) solvent and then drop casted between the channels. The devices were further annealed in a vacuum furnace at 170 °C to improve the contact resistance and adhesion of the nanosheets with the substrate. The humidity sensing performance was investigated by exposing the sensor device to various relative humidity (RH) levels ranging from 11.3–97.3% as described in detail previously [26]. All of the electrical tests such as current–voltage (*I*–*V*) and current–time (*I*–*t*) measurements were carried out using a Keithley 2612A system source meter which was attached to a computer through a GPIB 488A interface. For the photodetection study, a green LED was used. All sensor experiments were carried out at ambient pressure and room temperature.

Results and Discussion

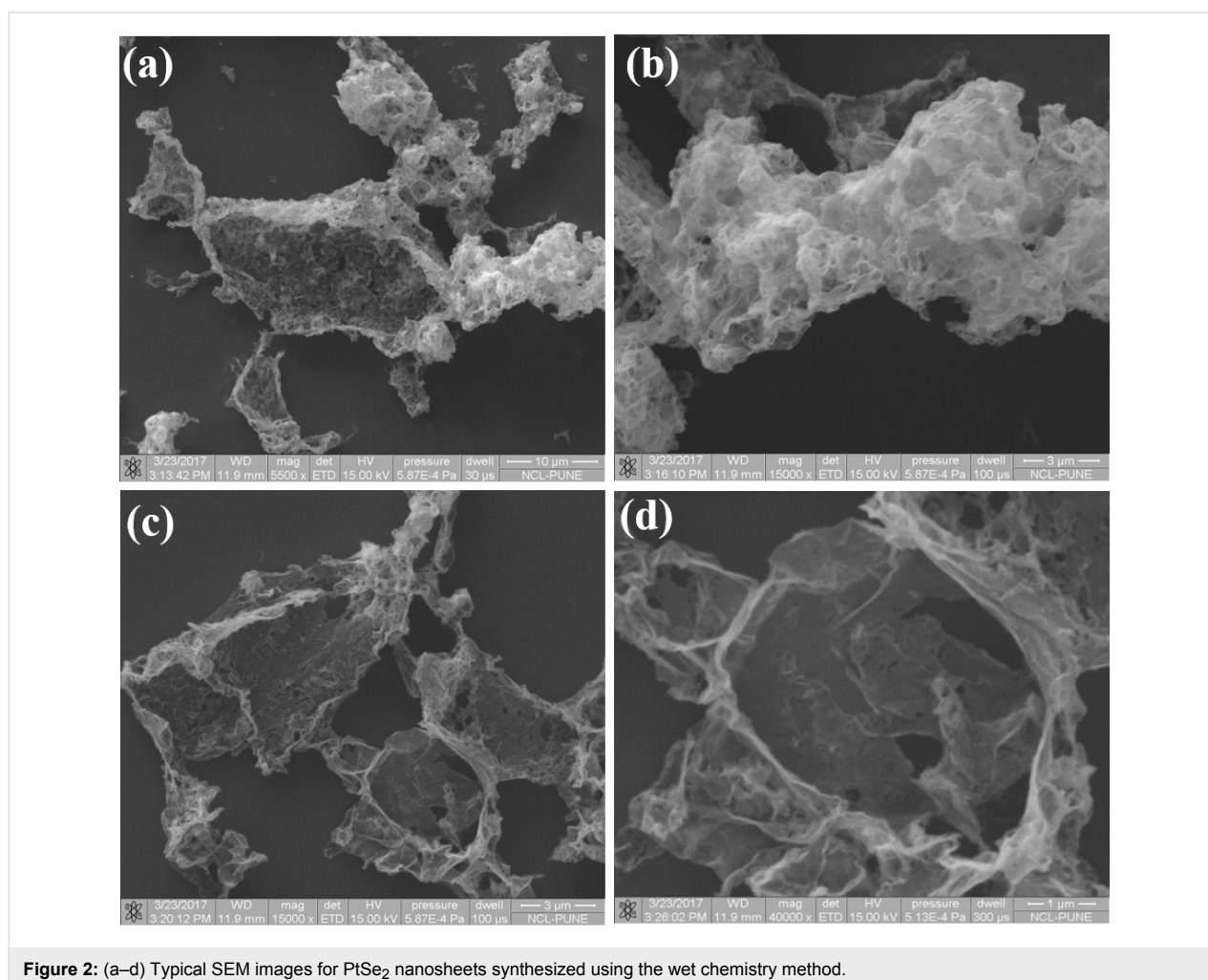
Structural characterization

The structural characterization was carried out using X-ray diffraction (XRD) and Raman spectroscopy. Figure 1a shows the typical XRD pattern of the as-prepared sample deposited on a Si substrate. XRD was performed on a PANalytical X'pert pro dual goniometer diffractometer using Cu Kα radiation. The samples were mounted flat and scanned between 10 to 60°. The XRD pattern of the as-prepared sample shows the strong characteristic peaks around 2θ = 17.41° and 33.17° belonging to the (001) and (011) planes of PtSe₂. These values match well with the JCPDS data card number (88-2281) and as observed in a previous report [27]. Figure 1b shows the Raman spectra of the as-prepared few-layer PtSe₂ nanosheets. The Raman spectra were recorded using a Renishaw microscope at a wavelength of 532 nm with laser power ≈25 mW and laser spot diameter ≈1 μm. The typical Raman spectra recorded at room temperature consist of two distinct peaks, one at ≈176 cm⁻¹ corresponding to the E_g mode and another slightly less intense peak at ≈205 cm⁻¹ corresponding to the A_{1g} mode. The E_g mode in the Raman spectra corresponds to in-plane vibration due to the



opposite motion of the upper and lower Se atoms. The A_{1g} mode in the Raman spectra corresponds to the out-of-plane vibration of Se atoms [22,28].

Morphological investigations were carried out using scanning electron microscopy (SEM). Figure 2a–c shows SEM images of few-layer PtSe₂ with typical overlapping of multiple sheets on



each other. Figure 2d shows an SEM image indicating a more transparent thin layer of PtSe₂ stacked on each other, exhibiting the few-layer nature of the as-synthesized PtSe₂ sample. Figure 3a–c shows the low-resolution TEM images of the as-synthesized PtSe₂ sample clearly showing the sheet-like morphology with lateral dimension of ≈ 700 nm. Figure 3d shows a high-resolution TEM image of the PtSe₂ nanosheets. The inset of Figure 3d shows the selected area electron diffraction pattern (SAED) which depicts the crystalline nature of the as-synthesized PtSe₂ sample. The X-ray photoelectron spectroscopy (XPS) spectra of the Pt 4f and Se 3d regions acquired on a PtSe₂ nanosheet sample were carried out on a film deposited on the Si substrate. The Figure 4a represents the fitted spectrum for Pt 4f_{7/2} and Pt 4f_{5/2} with binding energy 72.55 eV and 75.83 eV, respectively. Similarly, for Se, the binding energy spectrum can be fitted by Gaussian–Lorentzian curves shown in Figure 4b. The two peaks with binding energy 54.8 eV and 55.6 eV are observed for the 3d_{5/2} and 3d_{3/2} states, respectively.

There is one more peak observed in the Se region with low intensity at 52.9 eV which corresponds to Pt 5d_{3/2} [24]. The thickness of the as-prepared PtSe₂ nanosheets was calculated using atomic force microscopy (AFM). Figure 5a shows the AFM image which clearly shows that the lateral dimensions of the nanosheets are ≈ 700 nm. Figure 5b represents the corresponding height profile plot for the PtSe₂ nanosheet with thickness found to be ≈ 47 nm.

Temperature-dependent Raman spectroscopy of few-layer PtSe₂ nanosheets

The temperature-dependent Raman spectroscopy investigations of few-layer PtSe₂ nanosheets were carried out between 100–506 K. The Raman spectra of the PtSe₂ nanosheets at different temperatures are provided in Supporting Information File 1, Figures S2 and S3. The Raman mode E_g and A_{1g} as a function of temperature is shown in Figure 6a,b. It can be clearly seen that the position of the A_{1g} and E_g modes shifts to

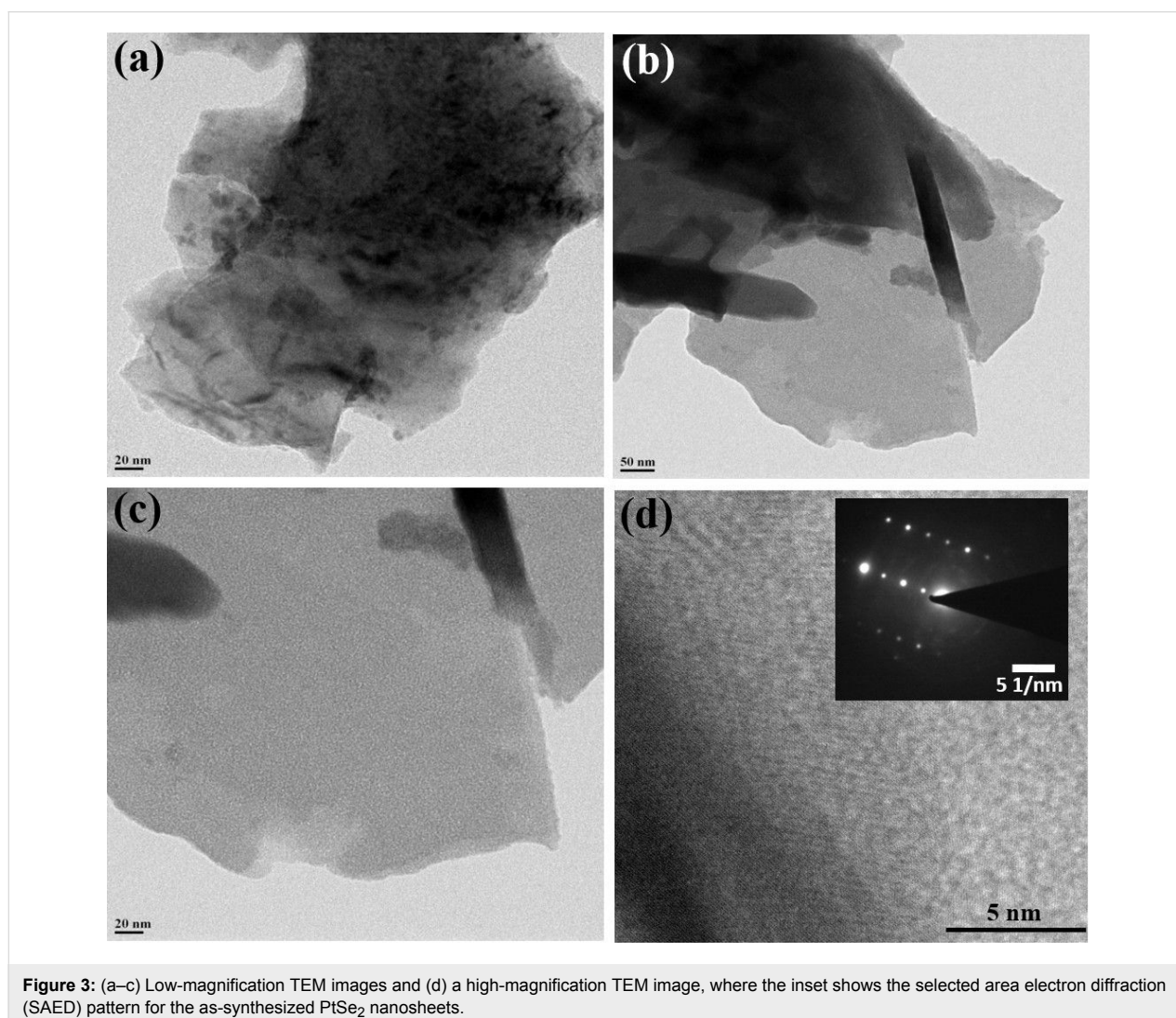
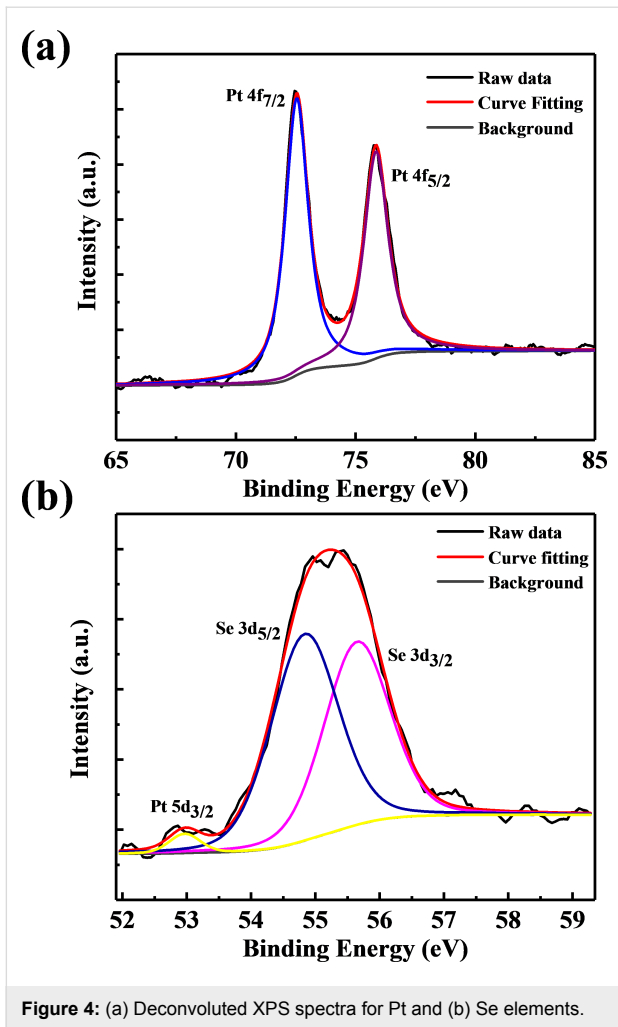


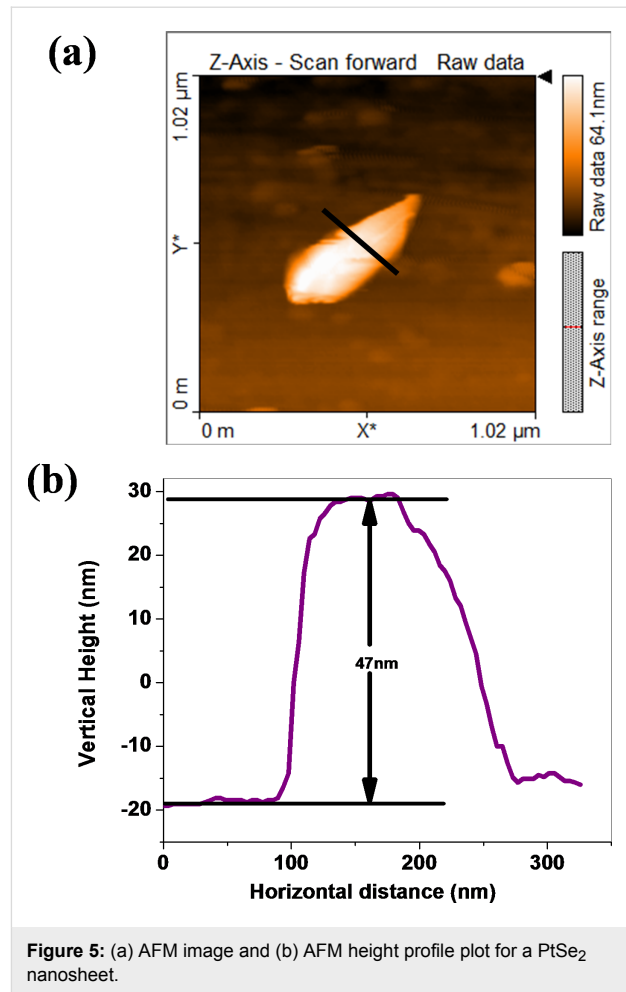
Figure 3: (a–c) Low-magnification TEM images and (d) a high-magnification TEM image, where the inset shows the selected area electron diffraction (SAED) pattern for the as-synthesized PtSe₂ nanosheets.



lower wavenumbers as the temperature increases from 100 K to 506 K. The Raman modes E_g and A_{1g} for $PtSe_2$ behave linearly within the temperature range 100–506 K. Furthermore, it was observed that the full width half maximum (FWHM) increases with an increase in temperature. The peak positions in the Raman spectra were calculated by fitting the Lorentzian function to the A_{1g} and E_g modes. The temperature coefficient can be calculated by Equation 1 [29]:

$$\omega(T) = \omega_0 + \chi T, \quad (1)$$

where ω_0 is the peak position of the A_{1g} and E_g mode at zero Kelvin, χ is the temperature coefficient of the A_{1g} and E_g modes, and ω is a Raman phonon frequency. The slope of the Raman modes vs temperature plot directly gives the value of the temperature coefficient and is given in Table 1. Further, it was clearly seen that the Raman peak position and peak broadening was affected by temperature. This change in Raman modes is mainly due to the contribution from the thermal anharmonicity.



The Raman phonon frequency as a function of volume and temperature is given by Equation 2 [30]:

$$\left(\frac{\partial \ln \omega}{\partial T}\right)_P = \left(\frac{\partial \ln V}{\partial T}\right)_P \left(\frac{\partial \ln \omega}{\partial \ln V}\right)_T + \left(\frac{\partial \ln \omega}{\partial T}\right)_V, \quad (2)$$

$$\left(\frac{\partial \ln \omega}{\partial T}\right)_P = -\frac{\gamma}{K} \left(\frac{\partial \ln \omega}{\partial P}\right)_T + \left(\frac{\partial \ln \omega}{\partial T}\right)_V$$

where γ is the volume thermal coefficient and K represents the isothermal volume compressibility. The first term on the right hand side, $-\gamma/K (\partial \ln \omega / \partial P)_T$, represents the volume contribution at a constant temperature. The second term, $(\partial \ln \omega / \partial T)_V$, represents the temperature contribution at constant volume. In single-layer TMDCs due to the direct band gap, the double resonance phenomenon is useful to explain the change in FWHM, intensity and the peak shift as a function of temperature. The double resonance phenomenon can be attributed to several process including absorption of an incident photon, creation of a hole pair,

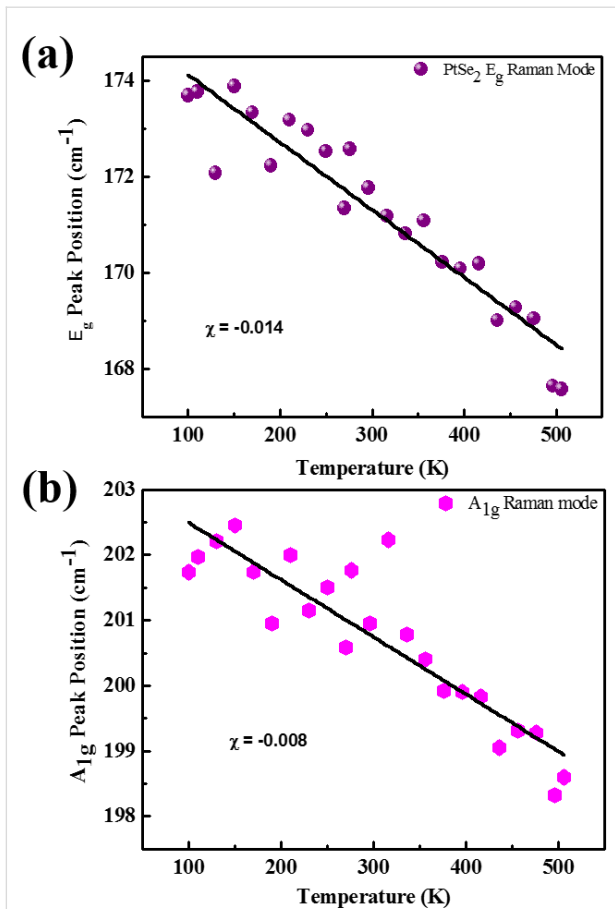


Figure 6: Temperature-dependent Raman spectra analysis for PtSe₂ nanosheets for the (a) E_g mode and the (b) A_{1g} mode as a function of temperature.

Table 1: Temperature coefficient values for the A_{1g} and E_g modes in a PtSe₂ nanosheet sample.

Material	Raman modes	Temperature coefficient (χ)	$\Delta\omega$ (cm ⁻¹)
PtSe ₂ nanosheet	E _g	-0.014	6.11
	A _{1g}	-0.008	3.14

double scattering of a created hole pair by phonon, and recombination of an electron–hole pair with emission of phonon. The temperature coefficient for the E_g and A_{1g} modes was found to be -0.014 and -0.008, respectively. The nature of the temperature dependence of the Raman spectra of PtSe₂ nanosheets is found to be similar in nature to that of graphene and other 2D materials such as MoS₂, WS₂, MoSe₂, WSe₂, BP, TiS₃, multi-layer graphene, and MoTe₂ [29,31–34]. A comparison of the temperature coefficient values corresponding to various 2D materials are shown in Table 2. The value of $\Delta\omega$ for both E_g and A_{1g} modes was found to be 6.11 cm⁻¹ and 3.14 cm⁻¹, respectively.

Table 2: Temperature coefficient values for various 2D materials.

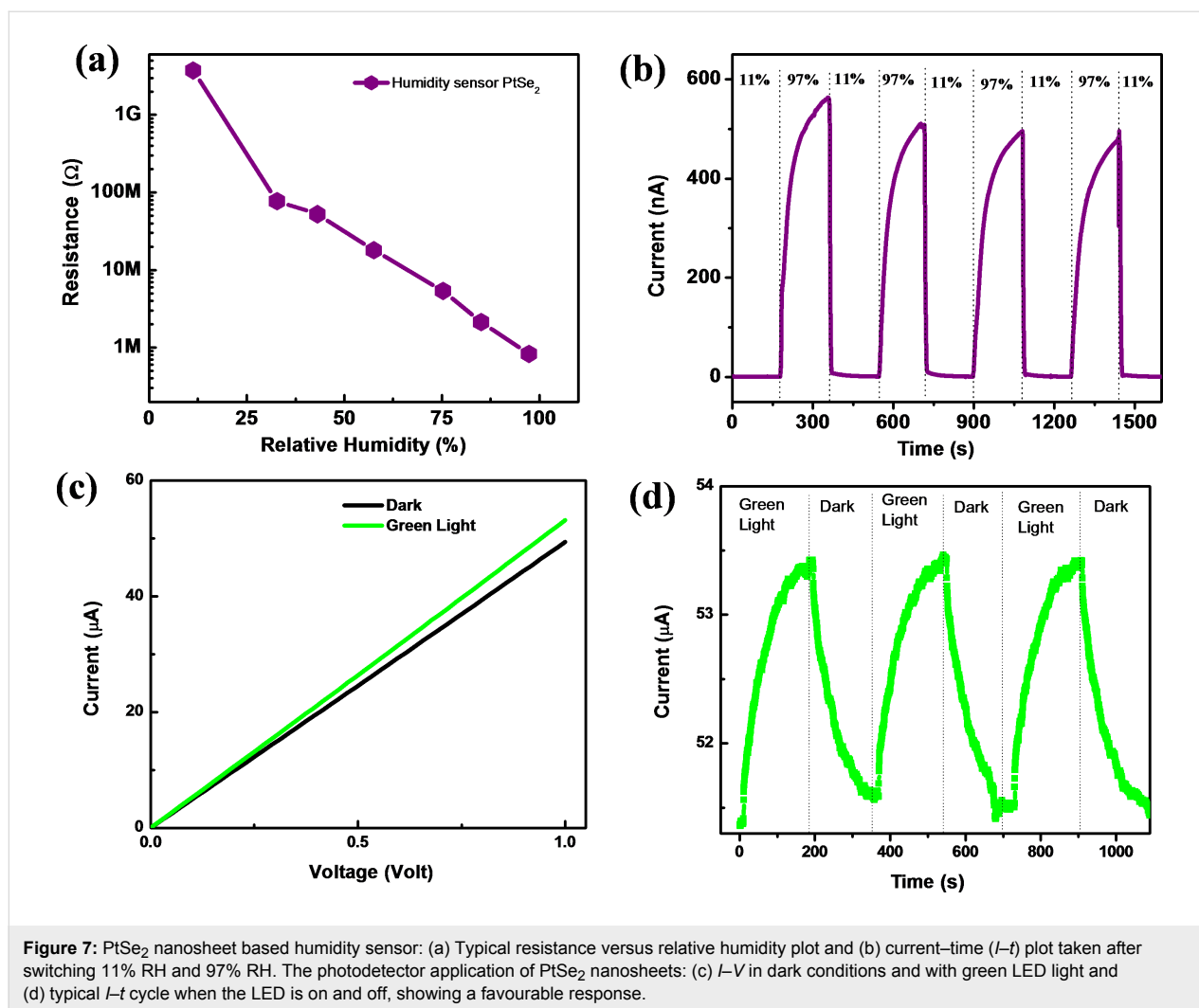
TMDCs	Raman modes	Temperature coefficient (χ)	$\Delta\omega$ (cm ⁻¹)	Ref.
MoSe ₂	A _{1g}	-0.0096	4.75	[29]
WSe ₂	A _{1g}	-0.0071	3.81	[29]
MoS ₂	E _g	-0.0136	8	[29]
	A _{1g}	-0.0113	6.11	
WS ₂	E _g	-0.0098	4.51	[29]
	A _{1g}	-0.014	6.43	
black phosphorous	A _{1g}	-0.008	4.39	[31]
	B _{2g}	-0.013	8.14	
	A _{2g}	-0.014	8.63	
TiS ₃	A _{1g}	-0.022, -0.025, -0.024, -0.017	–	[32]
		single-layer graphene	G	-0.0162
bilayer graphene	G	-0.0154	–	
MoTe ₂ (bilayer)	E' _{2g}	-0.0116	–	[34]
	B' _{2g}	-0.0181	–	
PtSe ₂	E _g	-0.014	6.11	this work
	A _{1g}	-0.008	3.14	

Humidity sensor and photodetector based on few-layer PtSe₂ nanosheets

Figure 7a shows the typical resistance of the sensor device vs relative humidity plot. The resistance is significantly decreased from 3.75 G Ω to 0.83 M Ω . The humidity sensing mechanism for the PtSe₂ sensor can be explained as follows. When the PtSe₂ nanosheet sensor device was exposed to water molecules/vapors, a charge transfer between the water molecules and the PtSe₂ nanosheets occurs. This results in the decrease in resistance of the PtSe₂ nanosheet sensor device with an increase in the relative humidity. The interactions among the water molecules (electron donor) and the PtSe₂ nanosheets results in an enhancement in the conductivity of the sensor device, similar to that observed for other 2D materials such as SnSe₂ [35], MoS₂ [36], BP [26], and MoSe₂ [37]. Figure 7b shows a typical current–time (*I*–*t*) plot where cycles of 11.3% and 97.3% RH levels were used to calculate the response and recovery time. The response and recovery time for the PtSe₂-based humidity sensor device was found to be 118 s and 5 s, respectively. The advantage of the PtSe₂-based humidity sensor device is its rapid recovery and its functionality at room temperature. Figure 7c shows a typical *I*–*V* plot in dark conditions and under green light illumination. Figure 7d shows the *I*–*t* plot for the photodetector based on PtSe₂ nanosheets with a response time of \approx 110 s and a recovery time of \approx 129 s.

Conclusion

In conclusion, we report on a wet chemistry method to grow PtSe₂ nanosheets. The SEM and TEM analysis confirm the for-



mation of PtSe₂ nanosheets. Further, the XRD, Raman and SAED pattern results were used to analyze the crystal structure and to confirm the formation of the PtSe₂ phase. Temperature-dependent Raman spectroscopy investigations were carried out on PtSe₂ nanosheet films grown on Si substrates between 100–506 K. The temperature coefficient for the E_g and A_{1g} modes was found to be –0.014 and –0.008, respectively. A room temperature humidity sensor based on the PtSe₂ nanosheets demonstrated an excellent recovery time of ≈5 s, indicating the great potential of PtSe₂-based sensors for future nano-electronics and sensor devices.

Supporting Information

Supporting Information File 1

Additional figures.

[<https://www.beilstein-journals.org/bjnano/content/supplementary/2190-4286-10-46-S1.pdf>]

Acknowledgements

This research work was supported by the SERB Government of India under the SERB Research Scientist scheme provided to Dr. D. J. Late.

ORCID® iDs

Mahendra S. Pawar - <https://orcid.org/0000-0002-3642-3158>

Dattatray J. Late - <https://orcid.org/0000-0003-3007-7220>

References

- Geim, A. K.; Novoselov, K. S. *Nat. Mater.* **2007**, *6*, 183–191. doi:10.1038/nmat1849
- Grigorenko, A. N.; Polini, M.; Novoselov, K. S. *Nat. Photonics* **2012**, *6*, 749–758. doi:10.1038/nphoton.2012.262
- Stankovich, S.; Dikin, D. A.; Dommett, G. H. B.; Kohlhaas, K. M.; Zimney, E. J.; Stach, E. A.; Piner, R. D.; Nguyen, S. T.; Ruoff, R. S. *Nature* **2006**, *442*, 282–286. doi:10.1038/nature04969
- Zhao, X.; Zhang, Q.; Chen, D.; Lu, P. *Macromolecules* **2010**, *43*, 2357–2363. doi:10.1021/ma902862u

5. Pawbake, A. S.; Mishra, K. K.; Machuno, L. G. B.; Gelamo, R. V.; Ravindran, T. R.; Rout, C. S.; Late, D. J. *Diamond Relat. Mater.* **2018**, *84*, 146–156. doi:10.1016/j.diamond.2018.03.021
6. Liu, W.; Luo, X.; Bao, Y.; Liu, Y. P.; Ning, G.-H.; Abdelwahab, I.; Li, L.; Nai, C. T.; Hu, Z. G.; Zhao, D.; Liu, B.; Quek, S. Y.; Loh, K. P. *Nat. Chem.* **2017**, *9*, 563–570. doi:10.1038/nchem.2696
7. Wang, Q. H.; Kalantar-Zadeh, K.; Kis, A.; Coleman, J. N.; Strano, M. S. *Nat. Nanotechnol.* **2012**, *7*, 699–712. doi:10.1038/nnano.2012.193
8. Peng, B.; Ang, P. K.; Loh, K. P. *Nano Today* **2015**, *10*, 128–137. doi:10.1016/j.nantod.2015.01.007
9. Li, H.; Shi, Y.; Chiu, M.-H.; Li, L.-J. *Nano Energy* **2015**, *18*, 293–305. doi:10.1016/j.nanoen.2015.10.023
10. Jariwala, D.; Sangwan, V. K.; Lauhon, L. J.; Marks, T. J.; Hersam, M. C. *ACS Nano* **2014**, *8*, 1102–1120. doi:10.1021/nn500064s
11. Shi, J.; Ma, D.; Han, G.-F.; Zhang, Y.; Ji, Q.; Gao, T.; Sun, J.; Song, X.; Li, C.; Zhang, Y.; Lang, X.-Y.; Zhang, Y.; Liu, Z. *ACS Nano* **2014**, *8*, 10196–10204. doi:10.1021/nl503211t
12. Voiry, D.; Salehi, M.; Silva, R.; Fujita, T.; Chen, M.; Asefa, T.; Shenoy, V. B.; Eda, G.; Chhowalla, M. *Nano Lett.* **2013**, *13*, 6222–6227. doi:10.1021/nl403661s
13. Splendiani, A.; Sun, L.; Zhang, Y.; Li, T.; Kim, J.; Chim, C.-Y.; Galli, G.; Wang, F. *Nano Lett.* **2010**, *10*, 1271–1275. doi:10.1021/nl903868w
14. Tongay, S.; Zhou, J.; Ataca, C.; Lo, K.; Matthews, T. S.; Li, J.; Grossman, J. C.; Wu, J. *Nano Lett.* **2012**, *12*, 5576–5580. doi:10.1021/nl302584w
15. Zhang, Y.; Chang, T.-R.; Zhou, B.; Cui, Y.-T.; Yan, H.; Liu, Z.; Schmitt, F.; Lee, J.; Moore, R.; Chen, Y.; Lin, H.; Jeng, H.-T.; Mo, S.-K.; Hussain, Z.; Bansil, A.; Shen, Z.-X. *Nat. Nanotechnol.* **2014**, *9*, 111–115. doi:10.1038/nnano.2013.277
16. Mak, K. F.; Lee, C.; Hone, J.; Shan, J.; Heinz, T. F. *Phys. Rev. Lett.* **2010**, *105*, 136805–136808. doi:10.1103/physrevlett.105.136805
17. Sundaram, R. S.; Engel, M.; Lombardo, A.; Krupke, R.; Ferrari, A. C.; Avouris, P.; Steiner, M. *Nano Lett.* **2013**, *13*, 1416–1421. doi:10.1021/nl400516a
18. Guo, G. Y.; Liang, W. Y. *J. Phys. C: Solid State Phys.* **1986**, *19*, 995–1008. doi:10.1088/0022-3719/19/7/011
19. Wang, Y.; Li, L.; Yao, W.; Song, S.; Sun, J. T.; Pan, J.; Ren, X.; Li, C.; Okunishi, E.; Wang, Y.-Q.; Wang, E.; Shao, Y.; Zhang, Y. Y.; Yang, H.-t.; Schwiery, E. F.; Iwasawa, H.; Shimada, K.; Taniguchi, M.; Cheng, Z.; Zhou, S.; Du, S.; Pennycook, S. J.; Pantelides, S. T.; Gao, H.-J. *Nano Lett.* **2015**, *15*, 4013–4018. doi:10.1021/acs.nanolett.5b00964
20. Zhao, Y.; Qiao, J.; Yu, Z.; Yu, P.; Xu, K.; Lau, S. P.; Zhou, W.; Liu, Z.; Wang, X.; Ji, W.; Chai, Y. *Adv. Mater. (Weinheim, Ger.)* **2017**, *29*, 1604230. doi:10.1002/adma.201604230
21. Sattar, S.; Schwingschlögl, U. *ACS Appl. Mater. Interfaces* **2017**, *9*, 15809–15813. doi:10.1021/acsami.7b00012
22. O'Brien, M.; McEvoy, N.; Motta, C.; Zheng, J.-Y.; Berner, N. C.; Kotakoski, J.; Elibol, K.; Pennycook, T. J.; Meyer, J. C.; Yim, C.; Abid, M.; Hallam, T.; Donegan, J. F.; Sanvito, S.; Duesberg, G. S. *2D Mater.* **2016**, *3*, 021004. doi:10.1088/2053-1583/3/2/021004
23. Grønvold, F.; Haraldsen, H.; Kjekshus, A.; Söderquist, R. *Acta Chem. Scand.* **1960**, *14*, 1879–1893. doi:10.3891/acta.chem.scand.14-1879
24. Yim, C.; Lee, K.; McEvoy, N.; O'Brien, M.; Riazimehr, S.; Berner, N. C.; Cullen, C. P.; Kotakoski, J.; Meyer, J. C.; Lemme, M. C.; Duesberg, G. S. *ACS Nano* **2016**, *10*, 9550–9558. doi:10.1021/acsnano.6b04898
25. Ali Umar, A.; Md Saad, S. K.; Mat Salleh, M. *ACS Omega* **2017**, *2*, 3325–3332. doi:10.1021/acsomega.7b00580
26. Erande, M. B.; Pawar, M. S.; Late, D. J. *ACS Appl. Mater. Interfaces* **2016**, *8*, 11548–11556. doi:10.1021/acscami.5b10247
27. Yu, X.; Yu, P.; Wu, D.; Singh, B.; Zeng, Q.; Lin, H.; Zhou, W.; Lin, J.; Suenaga, K.; Liu, Z.; Wang, Q. J. *Nat. Commun.* **2018**, *9*, 1545. doi:10.1038/s41467-018-03935-0
28. Zhang, K.; Yan, M.; Zhang, H.; Huang, H.; Arita, M.; Sun, Z.; Duan, W.; Wu, Y.; Zhou, S. *Phys. Rev. B* **2017**, *96*, 125102. doi:10.1103/physrevb.96.125102
29. Pawbake, A. S.; Pawar, M. S.; Jadhkar, S. R.; Late, D. J. *Nanoscale* **2016**, *8*, 3008–3018. doi:10.1039/c5nr07401k
30. Late, D. J.; Maitra, U.; Panchakarla, L. S.; Waghmare, U. V.; Rao, C. N. R. *J. Phys.: Condens. Matter* **2011**, *23*, 055303. doi:10.1088/0953-8984/23/5/055303
31. Late, D. J. *ACS Appl. Mater. Interfaces* **2015**, *7*, 5857–5862. doi:10.1021/am509056b
32. Pawbake, A. S.; Island, J. O.; Flores, E.; Ares, J. R.; Sanchez, C.; Ferrer, I. J.; Jadhkar, S. R.; van der Zant, H. S. J.; Castellanos-Gomez, A.; Late, D. J. *ACS Appl. Mater. Interfaces* **2015**, *7*, 24185–24190. doi:10.1021/acscami.5b07492
33. Calizo, I.; Balandin, A. A.; Bao, W.; Miao, F.; Lau, C. N. *Nano Lett.* **2007**, *7*, 2645–2649. doi:10.1021/nl071033g
34. Late, D. J. *Appl. Mater. Today* **2016**, *5*, 98–102. doi:10.1016/j.apmt.2016.09.013
35. Pawar, M.; Kadam, S.; Late, D. J. *ChemistrySelect* **2017**, *2*, 4068–4075. doi:10.1002/slct.201700261
36. Late, D. J.; Huang, Y.-K.; Liu, B.; Acharya, J.; Shirodkar, S. N.; Luo, J.; Yan, A.; Charles, D.; Waghmare, U. V.; Dravid, V. P.; Rao, C. N. R. *ACS Nano* **2013**, *7*, 4879–4891. doi:10.1021/nn400026u
37. Late, D. J.; Doneux, T.; Bougouma, M. *Appl. Phys. Lett.* **2014**, *105*, 233103. doi:10.1063/1.4903358

License and Terms

This is an Open Access article under the terms of the Creative Commons Attribution License (<http://creativecommons.org/licenses/by/4.0>). Please note that the reuse, redistribution and reproduction in particular requires that the authors and source are credited.

The license is subject to the *Beilstein Journal of Nanotechnology* terms and conditions: (<https://www.beilstein-journals.org/bjnano>)

The definitive version of this article is the electronic one which can be found at: [doi:10.3762/bjnano.10.46](https://doi.org/10.3762/bjnano.10.46)

Cite this: *Nanoscale Adv.*, 2021, 3, 4799

MoS₂ and CdMoS₄ nanostructure-based UV light photodetectors†

Mahendra S. Pawar,^{ab} Sunil R. Kadam,^c Bharat B. Kale^{id}*^c
and Dattatray J. Late^{id}*^{abd}

We have developed MoS₂ nanosheets and CdMoS₄ hierarchical nanostructures based on a UV light photodetector. The surface morphologies of the as-prepared samples were investigated *via* field emission scanning electron microscopy (FESEM) and transmission electron microscopy (TEM). The performance parameters for the present photodetectors are investigated under the illumination of UV light having a wavelength of ~385 nm. Upon the illumination of UV light, the CdMoS₄-based photodetector device showed a better response to UV light compared to the MoS₂ device in terms of photoresponsivity, response time (~72 s) and recovery time (~94 s). Our results reveal that CdMoS₄ hierarchical nanostructures are practical for enhancing the device performance.

Received 3rd May 2021
Accepted 3rd July 2021

DOI: 10.1039/d1na00326g

rsc.li/nanoscale-advances

Introduction

Photodetectors based on nanostructured materials are the significant components in nanoelectronic and optoelectronic devices.^{1–4} Photodetectors with quick photoresponse and high photoresponsivity are in much demand for real-world applications such as optical imaging and communication.^{2,5} To date, photodetectors from numerous nanomaterials (0D, 1D, and 2D) with remarkable response time and high responsivity have been reported to have excitation wavelengths ranging from ultraviolet to near-infrared region.^{6–12} For the development of high-performance photodetectors, semiconducting materials with an appropriate bandgap and nanostructured morphology are highly desirable and important. Although two-dimensional (2D) graphene has attracted significant interest in numerous nanoelectronic systems due to its outstanding electronic, thermal, and mechanical properties, further development has been restricted in optoelectronic devices due to its zero bandgap or semimetallic nature.¹³ In previous reports, researchers have developed a strategy to create a bandgap in graphene and utilized it for broadband photodetector application.¹⁴ However,

the presence of favourable bandgap in other 2D inorganic layered materials such as MoS₂, WS₂, MoSe₂, SnSe₂ and black phosphorous suggests great promise in the fabrication of large scale photodetector devices.^{15–23} These 2D materials also possess a layer-dependent tunable bandgap, *i.e.*, direct bandgap in monolayer and indirect bandgap in the bulk form. It makes these materials a potential candidate in numerous applications such as field effect transistors, solar cells, gas sensors, and energy storage devices.^{24–28} Due to the strong light absorption in the visible to near-infrared region, MoS₂ is widely used in optoelectronic systems. In 2012, Zhang *et al.* reported a single-layer MoS₂ phototransistor for the first time and obtained maximum photoresponsivity of ~7.5 mA W⁻¹ at an applied gate voltage (V_g , 50 V).¹² Jason *et al.* reported near-infrared photo-detection using bilayer MoS₂, where they have injected hot electrons into MoS₂ in order to originate sub-bandgap photocurrent results into photogain of the order of ~10⁵. This photogain leads to a photoresponsivity of 5.2 A W⁻¹ at 1070 nm, which is much higher than that of Si-based photodetectors.²⁹ Also, another report from Zhai *et al.* on monolayer MoS₂ coupled with an organic molecule showed a fast response time of 8 ms and maximum photoresponsivity of ~430 A W⁻¹ after Al₂O₃ passivation.³⁰ In addition, reports on MoS₂-based photodetectors show that it reduces the recombination rate of charge carriers along with photoabsorber, thus leading to an increase in the photocurrent.^{31–33} Herein, we report the fabrication of 2D MoS₂ nanosheets and 3D CdMoS₄ nanoflowers based on UV light photodetectors. The solvothermal route was implied for the synthesis of these structures, followed by structural and morphological investigation. We also demonstrated the device performance of these samples under UV light illumination and their cyclic response.

^aPhysical and Material Chemistry Division, CSIR – National Chemical Laboratory, Pune, 411008, Maharashtra, India. E-mail: datta099@gmail.com; djlate@mum.amity.edu

^bAcademy of Scientific and Innovative Research (AcSIR), Ghaziabad 201002, India

^cCentre for Materials for Electronics Technology (C-MET), Department of Electronics and Information and Technology (DeitY), Pune, 411008, Maharashtra, India. E-mail: bbkale@cmet.gov.in

^dCentre for Nanoscience & Nanotechnology, Amity University Maharashtra, Mumbai-Pune Expressway, Bhatan, Post – Somathne, Panvel, Mumbai, Maharashtra 410206, India

† Electronic supplementary information (ESI) available. See DOI: 10.1039/d1na00326g



Experimental method

Synthesis of MoS₂ nanosheets

Initially, we dissolved 2 mmol of ammonium molybdate in (40–50 ml) methanol with the help of a stirrer. To this mixture, we added dissolved thiourea in methanol dropwise, followed by stirring for 15 min. The whole solution was then transferred into a Teflon-lined stainless steel autoclave at 150 °C for 48 h. The precipitate was obtained using a Whatman filter paper, followed by washing with ethanol several times and then heated in an oven at 80 °C for 4 h. The MoS₂ powder sample was then annealed at 400 °C for 4 h in an N₂ atmosphere.

Synthesis of CdMoS₄ nanoflowers

For the CdMoS₄ nanoflowers synthesis, we have taken 2 mmol of cadmium nitrate and dissolved it in 40–50 ml methanol. Also, we prepared a 20 ml ammonium molybdate solution by dissolving a ammonium molybdate precursor in methanol with the help of a stirrer and continued for 10 min. To this solution, we added a dissolved cadmium nitrate solution dropwise under constant stirring for 10 min. Next, dissolved thiourea was added dropwise to it, and the solution mixture was stirred further for 15 min. The solution was then transferred into a Teflon-lined stainless steel autoclave at 150 °C for 48 h. After completion of the reaction, the reactor was allowed to cool down to room temperature naturally, followed by washing the product with distilled water and filtered using a Whatman filter paper. The precipitate obtained was washed with ethanol several times and then heated in an oven at 80 °C for 4 h. The CdMoS₄ powder sample was then annealed at 400 °C for 4 h in an N₂ atmosphere.

Both the products were further analysed using numerous microscopy and spectroscopy techniques. The details on the synthesis of MoS₂ nanosheets and CdMoS₄ nanoflowers were reported previously.³⁴

Material characterizations

The structural investigations were carried out *via* X-ray powder diffraction technique (XRD-D8, Advance, Bruker-AXS) and Raman spectrometry (HR-800, Horiba Jobin Yvon, France) at an excitation laser wavelength of 632.8 nm with a power density of 6.37×10^7 W cm^{-1.2} The surface morphologies of the as-prepared samples were characterized using a field emission scanning electron microscope (FESEM, Hitachi, S-4800) and transmission electron microscope (TEM, JEOL, 2010F Instrument).

Device fabrication and electrical measurements

The devices were fabricated on a indium tin oxide (ITO)-coated glass substrate with a source-drain separation of 500 μm. The central region of the conducting surface was etched with the zinc dust and concentrated HCl treatment. Then, we drop-casted our prepared material in this nonconducting region of the ITO substrate. Further, we annealed the device at 200 °C for 8 h in vacuum in order to obtain good adhesion of the as-

prepared material with the glass substrate. The electrical characterizations of the fabricated devices for MoS₂ and CdMoS₄ samples were carried out using a Keithley 2612A source meter, which was connected to a computer through a GPIB 288A interface. All the measurements were done at room temperature.

Results and discussion

XRD of MoS₂ and CdMoS₄

The phase formation of the as-synthesized MoS₂ and CdMoS₄ samples were confirmed by XRD and depicted in Fig. 1(a and b). The XRD patterns of the MoS₂ samples synthesized at 400 °C for 4 h are shown in Fig. 1(a), which match with the JCPDS data card no. 00-009-0312, confirming the formation of a pure hexagonal phase of layered MoS₂ and match well with the earlier report.³⁵ Fig. 1(b) shows the XRD pattern for the CdMoS₄ sample annealed at 400 °C for 4 h. Indexing of the annealed CdMoS₄ sample was carried out using the Powder 4-DICVOLE software, which validated the formation of the monoclinic structure of CdMoS₄.

Raman spectroscopy of MoS₂ and CdMoS₄

In view of this, the as-prepared samples were characterized *via* Raman spectroscopy and are shown in Fig. 1(c) and (d). The two Raman peaks assigned to the MoS₂ sample correspond to the E_{2g}¹ (in-plane) and A_{1g} (out-of-plane) vibration mode, as shown in Fig. 1(c).

These two Raman modes E_{2g}¹ and A_{1g} appear at 382.5 and 406 cm⁻¹, respectively. The separation of 27.56 cm⁻¹ between these two peaks specified the presence of the few-layer nature of MoS₂. The intense Raman peaks at 125, 150, 182, 238, 285, 307, 398, 664, 754, 819, 860 and 890 cm⁻¹ were observed for annealed CdMoS₄ sample shown in Fig. 1(d).

FESEM and TEM of MoS₂

In order to investigate the surface morphology of the as-synthesized MoS₂ and CdMoS₄ samples, FESEM analysis was

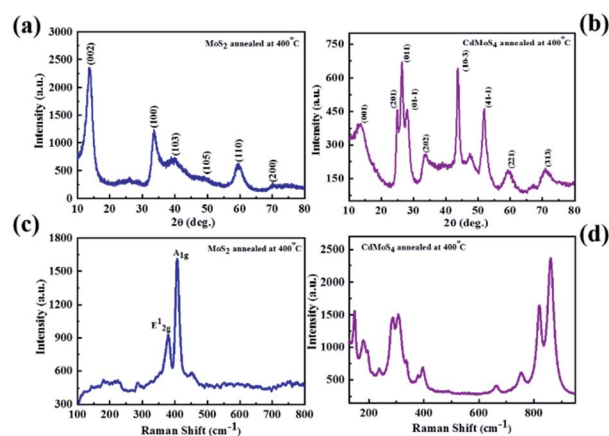


Fig. 1 XRD pattern of (a) MoS₂ and (b) CdMoS₄ samples annealed at 400 °C, Raman spectra of (c) MoS₂ and (d) CdMoS₄ samples annealed at 400 °C.



carried out and the results are depicted in Fig. 2 and 3, respectively. We observed some brake petals of MoS₂ sheets of different sizes located on the long sheet shown in Fig. 2(a and b). The long honeycomb-like sheets measured up to 10 μm and the thickness was found to be ~200 nm (Fig. 2(a and b)). The pore size of the honeycomb sheet is 40–50 nm, and the thickness of the single cell is ~10 nm. The TEM image depicted in Fig. 2(c and d) represents the sheet-like structure of MoS₂ and matches well with the FESEM results. The MoS₂ samples were entirely honeycomb-like sheets without aggregation.

XPS of MoS₂

The X-ray photoelectron spectroscopy (XPS) was carried out for MoS₂ sheets, and core-level XPS spectra for Mo 3d and S 2p are shown in Fig. 2(e and f). Fig. 2(e) displays few characteristic peaks corresponding to the orbital of Mo²⁺, Mo⁴⁺ and Mo⁶⁺ observed at 232.29/229.05, 234.86/231.57 and 236.07/233.03 eV, respectively. In addition, one peak for S 2s is observed at 226.4 eV, which specifies the presence of bridging S²⁻.³⁶ The two peaks at binding energies of 161.8 eV and 163 eV are detected for S 2p, which can be attributed to S 2p_{3/2} and 2p_{1/2}, respectively, as shown in Fig. 2(f). One minor peak for S at a higher binding energy of 168.52 eV appeared due to surface oxidation of MoS₂ sheets.³⁷

FESEM and TEM of CdMoS₄

The surface morphology of CdMoS₄ samples is shown in Fig. 3(a–c). Fig. 3(a and b) shows the FESEM images that clearly show the formation of a porous nanoflower-like surface

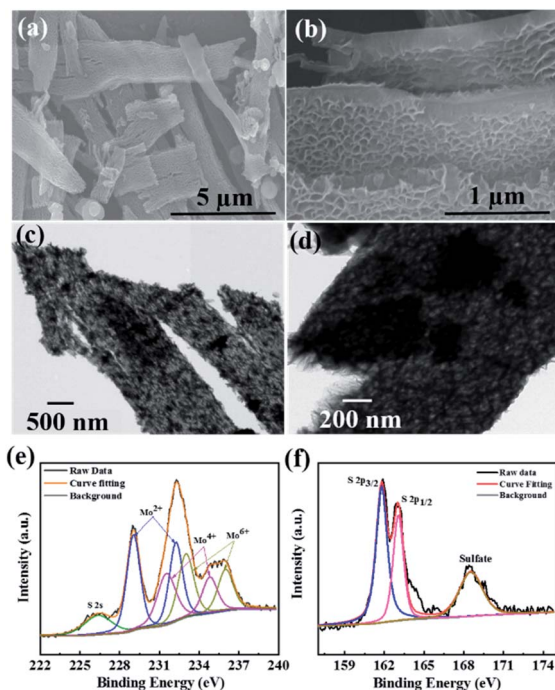


Fig. 2 (a and b) FESEM images, (c and d) TEM images and (e and f) deconvoluted XPS spectra for Mo 3d and S 2p elements of the MoS₂ samples annealed at 400 °C.

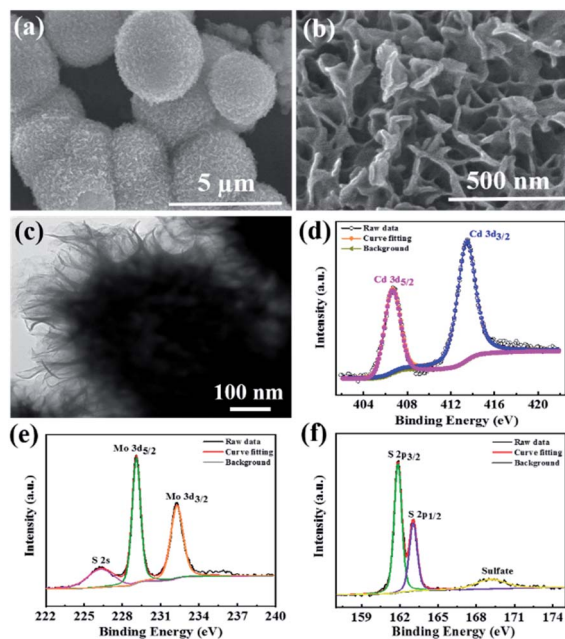


Fig. 3 (a and b) FESEM images, (c) TEM image and (d–f) deconvoluted XPS spectra for Cd 3d, Mo 3d, and S 2p of the CdMoS₄ nanoflowers annealed at 400 °C.

morphology of the CdMoS₄ sample. The average size of the nanoflower was observed to be ~3 μm and thickness ~50 nm. This kind of porous nano flower-like structure of CdMoS₄ provides a fair amount of surface area, thus enabling easy transportation of generated electron-hole to the surface and enhancing the photodetector activity. Fig. 3(c) shows the TEM image for the as-prepared CdMoS₄ sample. An original CdMoS₄ nanoflower in Fig. 3(c) shows a marigold flower-like microstructure of ~2 μm. The uniform hierarchical nanostructures consist of well-organized independent nano petals with a length of 20–30 nm (Fig. 3(c)).

XPS of CdMoS₄

Fig. 3(d–f) present the XPS spectra for Cd 3d, Mo 3d and S 2p elements of CdMoS₄ annealed at 400 °C. The Cd 3d doublet peaks at 413.4 eV and 406.6 eV are observed for Cd 3d_{3/2} and 3d_{5/2}, respectively, as shown in Fig. 3(d). Fig. 3(e) displays two prominent peaks at 232.24 eV and 229.1 eV for Mo 3d, indicating the presence of a +4 oxidation state for Mo. The S 2p spectra in Fig. 3(f) also show two peaks at 163.1 eV and 161.8 eV, assigned to S 2p_{1/2} and S 2p_{3/2}, respectively. Our XPS results match well with the earlier reports and further confirm the existence of Cd, Mo and S in CdMoS₄ nanoflowers. It is apparent that the surface of CdMoS₄ is made up of comparatively smooth sheets.

The UV-visible spectroscopy has been carried out for MoS₂ and CdMoS₄ annealed samples to investigate the optical properties presented (see in ESI Fig. S1†). The red plot shows the broad absorption for CdMoS₄ nanoflowers in the UV region compared to MoS₂ (black color).



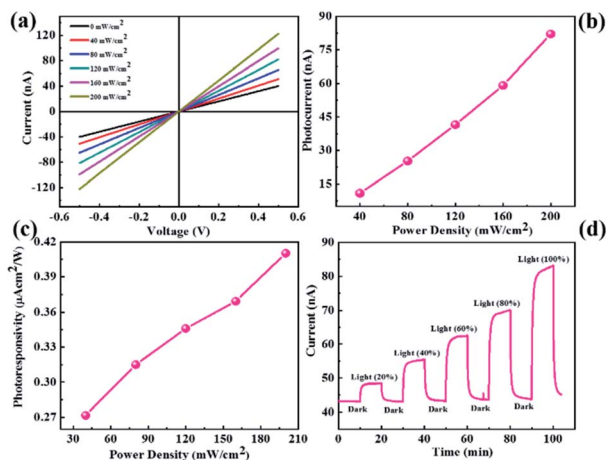


Fig. 4 MoS₂ nanosheet-based photodetector device. (a) current–voltage (I – V) characteristics, (b) photocurrent as a function of power density, (c) photoresponsivity vs. power density and (d) current–time (I – t) plot.

Photoresponse study of MoS₂

The as-synthesized MoS₂ and CdMoS₄ samples were further used for UV light photodetection. The experimental setup used for the measurement of UV light photodetection is shown in ESI Fig. S2.† Fig. 4(a) shows the I – V characteristics of the MoS₂ nanosheet sensor device for numerous power densities under UV light ranging from 0–200 mW cm^{–2}. We observed that the current increases with the increase in the power density of UV light. Photocurrents as a function of the power density plot are shown in Fig. 4(b), which indicates that the photocurrent increases with an increase in the power density. The photocurrent is calculated using the formula shown in eqn (1).

$$I_p = I_{\text{illumination}} - I_{\text{dark}} \quad (1)$$

Fig. 4(c) shows the photoresponsivity vs. power density plot, whereby photoresponsivity is defined as the ratio of photocurrent to power density. We observed that the photoresponsivity increases with the increase in the power density. The photocurrent response of the MoS₂ nanosheet photodetector is shown in Fig. 4(d), which is measured under light illumination and dark conditions at an applied bias voltage of 0.5 V. The response time and recovery time with the MoS₂ nanosheet-based sensor were ~118 s and ~123 s, respectively.

Photoresponse study of CdMoS₄

Similarly, we have performed the UV light photodetector measurements for the CdMoS₄ device shown in Fig. 5. Fig. 5(a) shows the I – V characteristics of the CdMoS₄ nanosheet sensor device at various power densities of UV light ranging from 0–200 mW cm^{–2}. We observed the increment in the current value with the increase in power density. The photocurrent as a function of power density is shown in Fig. 5(b). Upon increasing the power density, the photocurrent also increases. The photoresponsivity vs. power density plot is depicted in Fig. 5(c). The obtained

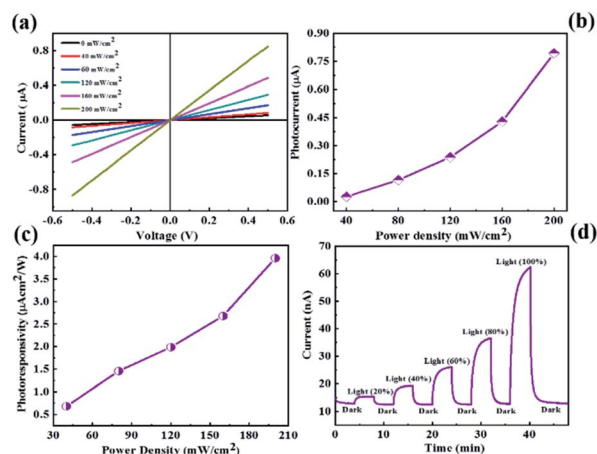


Fig. 5 CdMoS₄ nanoflower-based photodetector device (a) current–voltage (I – V) characteristics, (b) photocurrent as a function of power density, (c) photoresponsivity vs. power density and (d) current–time (I – t) plot.

maximum photoresponsivity was ~4 μA cm² W^{–1} at a power density of 200 mW cm^{–2}, which is much higher than that of the MoS₂-based device. The response time and recovery time for the CdMoS₄-based device are calculated from the I – t plot shown in Fig. 5(d). The values are found to be ~74 s and ~94 s, respectively, which are lower than those of the device fabricated for the MoS₂ nanosheet sample.

The proposed mechanism details under biasing and light illuminations using ITO electrodes, as shown in ESI Fig. S3(a) and (b).† The role of Cd was to produce impurity energy levels into the material, which shifts the absorption edges toward a longer wavelength, resulting in the enhancement in the properties of the photodetector. The enhanced photoexcited carrier density of the CdMoS₄ sample suppressing the electron–hole recombination helps in improving the performance of the photodetector. In addition, the self-assembled nanoflowers from thin petals and the high surface area required for the absorption of light results in a higher number of charge carriers. The electron transfer becomes faster because of the thin petal-like morphology of the CdMoS₄ sample, which also inhibits charge recombination. The comparative photodetector performance of MoS₂ and CdMoS₄ with previously reported Mo-based devices is presented in ESI Table 1.† The cyclic photoresponse study for the annealed MoS₂ and CdMoS₄ samples was carried out for more than 2000 s, and the various cycles have been recorded in light and dark conditions. The current–time (I – t) plots for the MoS₂ and CdMoS₄-based devices are shown in ESI Fig. S4(a) and (b),† respectively. Both the devices displays good photoresponse stability and reproducibility under UV light illumination. The results reveal that the CdMoS₄ device showed good cyclic stability without showing any change in the photocurrent value compared to the MoS₂ device for a long periods.

Conclusion

In conclusion, the structural and morphological investigation of as-synthesized MoS₂ nanosheets and CdMoS₄ nanoflowers



were investigated *via* spectroscopy and microscopy techniques. The UV photodetector devices were fabricated on ITO (indium tin oxide)-coated glass substrates. The CdMoS₄ nanoflowers device showed a better response to UV light compared to pristine MoS₂ nanosheets in terms of photoresponsivity, whereby the response time was 74 s and the recovery time was 94 s. Our results reveal that the device performance of CdMoS₄ materials can be improved by making composite or heterostructures using other 2D materials or by functionalization.

Author contributions

MSP has carried out the experimental work on device fabrication, analysis and first writing of the draft; SRK synthesized the materials and performed the XPS measurements; BBK and DJL supervised the overall work with comments on the first draft, writing, reviewing and editing.

Conflicts of interest

There are no conflicts of interest to declare.

Acknowledgements

M. S. Pawar acknowledges CSIR-Delhi [File No: (31/11(1084)/2019-EMR-I)]. Authors thank Director-CSIR-National Chemical laboratory, Pune (India) for the research facilities.

Notes and references

- G. Konstantatos and E. H. Sargent, *Nat. Nanotechnol.*, 2010, **5**, 391.
- A. Pospischil, M. Humer, M. M. Furchi, D. Bachmann, R. Guider, T. Fromherz and T. Mueller, *Nat. Photonics*, 2013, **7**, 892.
- L. Tang, S. E. Kocabas, S. Latif, A. K. Okyay, D. S. Ly-Gagnon, K. C. Saraswat and D. A. Miller, *Nat. Photonics*, 2008, **2**, 226.
- J. S. Jie, W. J. Zhang, Y. Jiang, X. M. Meng, Y. Q. Li and S. T. Lee, *Nano Lett.*, 2006, **6**, 1887.
- T. Mueller, F. Xia and P. Avouris, *Nat. Photonics*, 2010, **4**, 297.
- D. C. Oertel, M. G. Bawendi, A. C. Arango and V. Bulović, *Appl. Phys. Lett.*, 2005, **87**, 213505.
- S. A. McDonald, G. Konstantatos, S. Zhang, P. W. Cyr, E. J. Klem, L. Levina and E. H. Sargent, *Nat. Mater.*, 2005, **4**, 138.
- L. Hu, J. Yan, M. Liao, L. Wu and X. Fang, *Small*, 2011, **7**, 1012.
- C. Lan, C. Li, Y. Yin, H. Guo and S. Wang, *J. Mater. Chem. C*, 2015, **3**, 8074.
- M. S. Pawar, P. K. Bankar, M. A. More and D. J. Late, *RSC Adv.*, 2015, **5**, 88796.
- P. Hu, Z. Wen, L. Wang, P. Tan and K. Xiao, *ACS Nano*, 2012, **6**, 5988.
- Z. Yin, H. Li, H. Li, L. Jiang, Y. Shi, Y. Sun, G. Lu, Q. Zhang, X. Chen and H. Zhang, *ACS Nano*, 2012, **6**, 74.
- I. Meric, M. Y. Han, A. F. Young, B. Ozyilmaz, P. Kim and K. L. Shepard, *Nat. Nanotechnol.*, 2008, **3**, 654.
- Y. Shi, W. Fang, K. Zhang, W. Zhang and L. J. Li, *Small*, 2009, **5**, 2005.
- J. Y. Wu, Y. T. Chun, S. Li, T. Zhang, J. Wang, P. K. Shrestha and D. Chu, *Adv. Mater.*, 2018, **30**, 1705880.
- S. H. Yu, Y. Lee, S. K. Jang, J. Kang, J. Jeon, C. Lee, J. Y. Lee, H. Kim, E. Hwang, S. Lee and J. H. Cho, *ACS Nano*, 2014, **8**, 8285.
- H. Tan, Y. Fan, Y. Zhou, Q. Chen, W. Xu and J. H. Warner, *ACS Nano*, 2016, **10**, 7866.
- N. Perea-López, A. L. Elías, A. Berkdemir, A. Castro-Beltran, H. R. Gutiérrez, S. Feng, R. Lv, T. Hayashi, F. López-Urías, S. Ghosh and B. Muchharla, *Adv. Funct. Mater.*, 2013, **23**, 5511.
- Y. H. Chang, W. Zhang, Y. Zhu, Y. Han, J. Pu, J. K. Chang, W. T. Hsu, J. K. Huang, C. L. Hsu, M. H. Chiu and T. Takenobu, *ACS Nano*, 2014, **8**, 8582.
- W. Zhang, M. H. Chiu, C. H. Chen, W. Chen, L. J. Li and A. T. S. Wee, *ACS Nano*, 2014, **8**, 8653.
- X. Zhou, L. Gan, W. Tian, Q. Zhang, S. Jin, H. Li, Y. Bando, D. Golberg and T. Zhai, *Adv. Mater.*, 2015, **27**, 8035.
- M. Buscema, D. J. Groenendijk, S. I. Blanter, G. A. Steele, H. S. Van Der Zant and A. Castellanos-Gomez, *Nano Lett.*, 2014, **14**, 3347.
- L. Ye, H. Li, Z. Chen and J. Xu, *ACS Photonics*, 2016, **3**, 692.
- C. Guo, Z. Tian, Y. Xiao, Q. Mi and J. Xue, *Appl. Phys. Lett.*, 2016, **109**, 203104.
- M. L. Tsai, S. H. Su, J. K. Chang, D. S. Tsai, C. H. Chen, C. I. Wu, L. J. Li, L. J. Chen and J. H. He, *ACS Nano*, 2014, **8**, 8317.
- D. J. Late, Y. K. Huang, B. Liu, J. Acharya, S. N. Shirodkar, J. Luo, A. Yan, D. Charles, V. Waghmare, V. P. Dravid and C. N. R. Rao, *ACS Nano*, 2013, **7**, 4879.
- C. Hao, B. Yang, F. Wen, J. Xiang, L. Li, W. Wang, Z. Zeng, B. Xu, Z. Zhao, Z. Liu and Y. Tian, *Adv. Mater.*, 2016, **28**, 3194.
- R. Bhandavat, L. David and G. Singh, *J. Phys. Chem. Lett.*, 2012, **3**, 1523.
- W. Wang, A. Klots, D. Prasai, Y. Yang, K. I. Bolotin and J. Valentine, *Nano Lett.*, 2015, **15**, 7440.
- Y. Huang, F. Zhuge, J. Hou, L. Lv, P. Luo, N. Zhou, L. Gan and T. Zhai, *ACS Nano*, 2018, **12**, 4062.
- C. Fang, H. Wang, Z. Shen, H. Shen, S. Wang, J. Ma, J. Wang, H. Luo and D. Li, *ACS Appl. Mater. Interfaces*, 2019, **11**, 8419.
- L. Wang, J. Jie, Z. Shao, Q. Zhang, X. Zhang, Y. Wang, Z. Sun and S. T. Lee, *Adv. Funct. Mater.*, 2015, **25**, 2910.
- W. Zhang, C. P. Chuu, J. K. Huang, C. H. Chen, M. L. Tsai, Y. H. Chang, C. T. Liang, Y. Z. Chen, Y. L. Chueh, J. H. He and M. Y. Chou, *Sci. Rep.*, 2014, **4**, 3826.
- S. R. Kadam, D. J. Late, R. P. Panmand, M. V. Kulkarni, L. K. Nikam, S. W. Gosavi, C. J. Park and B. B. Kale, *J. Mater. Chem. A*, 2015, **3**, 21233.
- X. Zhang, H. Tang, M. Xue and C. Li, *Mater. Lett.*, 2014, **130**, 83.
- C. Wu, D. Liu, H. Li and J. Li, *Small*, 2018, **14**, 1704227.
- N. Karikalán, R. Karthik, S. M. Chen, C. Karupiah and A. Elangovan, *Sci. Rep.*, 2017, **7**, 1–10.

